SCUOLA DI DOTTORATO
UNIVERSITÀ DEGLI STUDI DI MILANO-BICOCCA

Dipartimento di / Department of

Fisica “Giuseppe Occhialini”

Dottorato di Ricerca in / PhD program Fisica e Astronomia Ciclo / Cycle XXXIV

Curriculum in Astrofisica

BLACK HOLE OR NEUTRON STAR? THIS IS (ONE OF) THE QUESTION(S)

A VARIABILITY STUDY OF ULXs TOWARDS A BETTER COMPREHENSION OF THEIR PHYSICS

Salvaggio Chiara

Matricola / Registration number 736281

Tutor: Prof.ssa Monica Colpi

Supervisor: Dott.ssa Anna Wolter

Coordinatore / Coordinator: Prof.ssa Marta Calvi

ANNO ACCADEMICO / ACADEMIC YEAR 2020/2021

Contents

Introduction

During the 80s, point-like X-ray sources with luminosities in excess of 10^{39} erg s^{-1} have been observed for the first time in the images of nearby galaxies. Thanks to their variability properties in the X-ray band they have been interpreted as accreting compact objects. It was soon clear that they were a class of sources different from the Galactic X-ray binaries, due to their larger luminosities, above the Eddington limit for accretion onto a black hole (BH) of $\sim 10 M_{\odot}$. They are usually indicated as *Ultraluminous X-ray sources* (ULX) and while at first they were thought to host intermediate mass BHs, there are now evidences that most of them contain a stellar mass compact object, i.e. a stellar mass BH or a neutron star (NS), accreting at super-Eddington rates. Even if many progresses have been done towards the comprehension of the ULXs in the last years, many aspects of their physics are still matter of study. Just in few cases the nature of the compact object has been identified, but the relative fraction of BHs and NSs in ULXs and a detailed description of the super-Eddington accretion physics are still missing.

A key role in the understanding of ULXs can be played by variability studies. The variable X-ray emission is associated to the accreting matter, therefore variability can bring information to shed light onto the accretion mechanism powering ULXs. Individual high-statistics observations are useful to characterize a single spectral state and to study the short-term temporal variability typical of that configuration. Thus, combined spectral-timing studies have been used to investigate the properties of the accretion structures, e.g. accretion disc or outflows, to derive information about the physical mechanisms at stake in each spectral state. On the other hand, the weakness of such short-term studies is that they do not give us a complete view of the accretion cycle, fundamental for our understanding of the super-Eddington accretion processes, which instead can be obtained with a regular monitoring, as demonstrated by analogous studies of the sub-Eddington accretion cycle in Galactic X-ray binaries. Therefore, long-term variability studies of ULXs are very important in this context to obtain information about the timescales linked to each spectral regime and to spectral state transitions and have already given their first results, such as the discovery of super-orbital periodicities, possibly linked to a precession motion, or of bimodal flux distributions, proposed to indicate propeller phases and thus an indirect method to individuate NS candidates.

As a consequence of these considerations, we focused on a long-term variability study of a sample of ULXs in spiral galaxies. We interpret our results in the context of super-Eddington accretion, with the accretion disc expected to become geometrically thick inside the spherization radius, where the Eddington limit is reached, and to be characterized by advection and outflows.

In addition, we investigated both the short and long-term variability in another sample of ULXs in a ring galaxy, the Cartwheel, which contains the largest number of ULXs in a single galaxy and therefore is particularly suitable for a population study.

Chapter 1

Ultraluminous X-ray sources

Ultraluminous X-ray sources (ULXs) are defined as point-like, non-nuclear extragalactic sources, with luminosities larger than 10^{39} erg s^{-1} in the X-ray band. The most luminous ULXs reach luminosities of 10^{41}–10^{42} erg s^{-1} (see e.g. Kaaret et al. 2017). They are usually interpreted as accreting compact objects, i.e. neutron stars (NSs) or black holes (BHs), in binary systems, thus they are particularly luminous X-ray binaries. The luminosity threshold of 10^{39} erg s^{-1}, used to identify such objects, was chosen because it is the Eddington luminosity for accretion onto a $\sim 10 M_{\odot}$ BH, assuming spherical hydrogen accretion. The Eddington luminosity, L_{Edd}, is the maximum luminosity which can be emitted from a system maintaining an equilibrium between gravity and radiation pressure. Assuming spherical accretion of ionised hydrogen and a dominant Thomson scattering process, it is expressed as:

$$L_{Edd} = \frac{4\pi G M m_p}{\sigma_T}, \tag{1.1}$$

where c is the speed of light, G the universal gravitational constant, M the mass of the source considered, m_p the proton mass and σ_T is the Thomson cross section. Overcoming the Eddington luminosity in an accreting system would imply a larger radiation pressure exerted on the accreting matter with respect to gravity, with a consequent interruption of accretion.

The easiest way to explain such objects was with sub-Eddington accretors, similar to the X-ray binaries observed in our Galaxy, but with a larger mass and consequently a larger L_{Edd}, allowing to reach the observed luminosities without overcoming the Eddington limit. For a long time ULXs have been supposed, by the scientific community, to be the place where intermediate mass black holes (IMBHs) could be host (e.g. Colbert and Mushotzky 1999). IMBHs are BHs with masses between those of the stellar mass BHs, originating from stellar evolution, and those of supermassive BHs (SMBHs), with masses of millions/billions times the solar mass and observed in the center of galaxies. The IMBHs may have been the seeds for the formation of SMBHs, which were already present in the early universe as demonstrated by the discovery of AGNs (active galactic nuclei) at high redshifts (e.g. Fan et al. 2003, Bañados et al. 2018).

ULXs have been discovered thanks to the advent of imaging X-ray astronomy. The first X-ray satellite able to resolve the images of external galaxies (e.g. Long et al. 1981, Fabbiano 1989) was the *Einstein Observatory*. These images revealed some non-nuclear X-ray sources, with luminosities larger than 10^{39} erg s^{-1} (e.g. Fabbiano 1989). In the 90s, with *ROSAT* and *ASCA*, the first spectra of ULXs have been obtained. In order to have high quality spectra, it was necessary to wait until the 2000s, with the launch of *Chandra* and *XMM-Newton*.

Only in a small fraction of ULXs, the compact object has been firmly identified. In 2014, Bachetti et al. discovered coherent pulsations, emitted by M82 X-2, confirming for the first time the presence of a NS in a ULX. We refer to such pulsating ULXs as PULXs. This implies that the accretion should happen in a super-Eddington regime. Thus, the ULXs may be super-Eddington accretors containing stellar mass BHs, with masses between ~ 3 and $100\ M_{\odot}$ or NSs, which have even smaller masses of $\sim 1.4 - 3\ M_{\odot}$. There are also other observational evidences supporting the super-Eddington accretion

scenario: the discovery of a new spectral state in ULXs, the *ultraluminous state* (e.g. Roberts 2007, Gladstone et al. 2009); the detection of nebular emission around ULXs in optical, radio and X-rays (e.g. Pakull and Mirioni 2002, 2003, Pakull et al. 2010, Abolmasov 2011, Cseh et al. 2012, Belfiore et al. 2020), which is an indirect evidence of the winds expected in super-Eddington accretion systems (Shakura and Sunyaev 1973); and the direct evidence of the existence of such winds thanks to the detection of emission and absorption lines in the high resolution X-ray spectra of some ULXs (e.g. Pinto et al. 2016, Kosec et al. 2018a). Sub-Eddington accretion onto IMBHs still remains a possibility for some of the most luminous ULXs.

By now, the only direct method to confirm the nature of the compact object in a ULX is the detection of pulsations. No methods are currently available to identify BHs in ULX systems. Indirect methods have been suggested to identify NSs, also in absence of pulsations. A possibility is the detection of a cyclotron line, which can be only emitted by a NS (e.g. Walton et al. 2018a, Brightman et al. 2018). Also the long-term light curves of ULXs can be used to identify candidate NSs (e.g. Earnshaw et al. 2018, Song et al. 2020): if a bimodal flux distribution, with large flux difference between the two flux levels, is observed, it could indicate propeller phases, during which accretion stops and matter is ejected from the system (e.g. Tsygankov et al. 2016, Grebenev 2017). This mechanism is caused by the magnetosphere of highly magnetized NSs, thus cannot be produced by BH accretors. Also the spectra of ULXs may give information about the accretor: Pintore et al. (2017) found that the spectra of the known PULX are among the hardest spectra in the ULX population, thus the hardest ULXs may be considered as PULX candidates.

We are still far from a satisfactory description of the ULXs, regarding which there are many open questions. The aim of this thesis is to study the variability properties of ULXs. We will focus on a systematic analysis of the long-term temporal variability in ULXs samples. X-ray emission and its variability are thought to be produced by the accreting matter. Therefore, a systematic study of the variability may be used to derive information useful to characterize the accretion processes in ULXs, which are still not fully understood.

Before focusing on the variability (see Chapter 2), in the rest of this chapter we summarize the known properties of the ULXs.

1.1 Neutron stars and black holes in binary systems

ULXs may host neutron stars (NSs) or black holes (BHs). BHs are usually observed in two mass ranges: below 100 $M_\odot$[1] we find the stellar mass BHs (sMBHs) and above 10^6 $M_\odot$ there are the supermassive BHs (SMBHs). The existence of a third class of BHs with intermediate masses between sMBHs and SMBHs has been supposed for a long time and has been confirmed thanks to the gravitational waves (GWs) detection. The existence of IMBHs is also supported by studies on tidal disruption events (TDE). The GWs have shown evidence of BH masses around $\sim 10^2$ $M_\odot$ (e.g. Abbott and et al. 2020a), thus just at the lower end of the mass range expected for IMBHs. Some TDE have instead suggested a BH mass of 10^4–$10^5 M_\odot$ (e.g. Maksym et al. 2013, Donato et al. 2014, Lin et al. 2018), covering the upper end of the mass range for IMBHs.

Neutron stars and stellar mass black holes: NSs and sMBHs are the final product of stellar evolution. During its life, a star is sustained by the radiation pressure, released by the nuclear reactions that occur in the nucleus of the star, which is directed outwards and balances the pressure of gravity, the latter directed towards the center of the star. When a sufficiently massive star ends the nuclear burning, there is nothing which can oppose to the gravity of its particles. The star core, composed of iron, begins to collapse towards its center, becoming very compact and rich of neutrons. A shock waves propagates from the core to the envelope, the external layers of the star, which expands outwards, in a spectacular explosion: a core collapse supernova. The remnant compact core is a NS. Part of the material launched during the supernova may fall back onto the compact nucleus, inducing further collapse, if the infalling matter makes the core mass larger than the Chandrasekar limit. What

[1] $M_\odot$ is the mass of the Sun, i.e. 1.99×10^{33} g

remains is an extreme compact object: a stellar mass BH. NSs originate from stars with initial mass between 9 – 10 and 20 – 25 $M_\odot$ (e.g. Heger et al. 2003), while stellar mass BHs originate from stars with initial stellar mass larger than $\sim$ 20 – 25 $M_\odot$ (e.g. Heger et al. 2003) and their mass is < 100 $M_\odot$. sMBHs are sometimes divided in two sub-categories: ordinary sMBHs, the ones originating by fallback after a supernova explosion as previously explained (M_{BH} < 20 $M_\odot$, which may be larger in low metallicity environments; e.g. Heger et al. 2003) and massive sMBHs (40 $M_\odot$ < M_{BH} <100 $M_\odot$; e.g. Belczynski et al. 2010). The latter may form through direct collapse of low metallicity stars, with initial mass above 40 $M_\odot$ (e.g. Belczynski et al. 2010, Heger et al. 2003) and may power the ULXs (e.g. Zampieri and Roberts 2009, Mapelli et al. 2009).

Super massive BHs: (SMBHs), with masses > 10^6 $M_\odot$ (e.g. Ferrarese and Ford 2005), are observed in the center of galaxies. They were already present in the early universe, thus they must have formed in a "short" time: the formation channels of SMBHs are still matter of study (e.g. Inayoshi et al. 2021). SMBHs are not thought to be hosted in ULXs, so we do not treat them in details.

Intermediate mass BHs: (IMBHs) are BHs with masses between 100 $M_\odot$ and 10^6 $M_\odot$, filling the mass gap between the other two BH categories. They appeared to be the easiest way to explain the luminosities emitted by the ULXs, without the need of introducing an accretion physics different from that usually observed in Galactic X-ray binaries, i.e. a super-Eddington process. ULXs should then simply represent a class of X-ray binaries similar to the Galactic X-ray binaries, but with larger accretors masses, which allows to reach higher luminosities through sub-Eddington accretion. The existence of IMBHs has remained for a long time only an hypothesis without direct evidences.

Thanks to the observation of the merger event GW190521, the LIGO and Virgo collaborations detected, through the gravitational waves signal, the first evidence of an IMBH. The remnant of the event is $\sim$ 140 $M_\odot$ and the progenitors masses are $\sim$ 85 and 66 $M_\odot$ (Abbott and et al. 2020a,b). How more massive IMBH, with masses of the order of 1000 $M_\odot$ or more, whose existence is suggested by TDE studies (see e.g. Greene et al. 2020, Gezari 2021), forms is still an open question. IMBHs may have played a role in the formation of the SMBHs: a possible explanation for the presence of SMBHs in the young universe is accretion onto IMBHs (e.g. Volonteri 2010, Inayoshi et al. 2021).

Some scenarios have been proposed as possible formation channels for IMBHs, such as mergers or accretion in dense environments, i.e. star clusters, or direct collapse of very massive stars, which may form in low metallicity environments, where less mass is lost through stellar winds (e.g. Vink 2011). In dense star clusters, very massive stars may form through mergers; the collapse of such massive stars would form IMBH (e.g. Portegies Zwart and McMillan 2002). Mergers of lighter BHs (Miller and Hamilton 2002) and gas accretion (Vesperini et al. 2010), which could increase up to one hundred times the initial BH mass, in dense globular clusters may be a channel of formation for IMBHs. In low metallicity environments, very massive stars with masses larger than 260 $M_\odot$ – stars with masses in the range 140–260 $M_\odot$ are completely disrupted in the supernova, due to the electron-positron instability, without leaving any remnant (e.g. Ober et al. 1983, Heger and Woosley 2002) – may form and produce IMBHs through direct collapse (e.g. Heger et al. 2003).

1.1.1 Accretion in X-Ray Binaries and Ultraluminous X-ray sources

Both neutron stars and black holes may be in X-ray binaries, which are indeed binary systems composed of a compact object, a BH or NS, accreting mass from a companion star. The compact object assumes the role of *accretor* and the companion star is called the *donor*.
Galactic X-ray binaries are divided in two main classes:
- High Mass X-ray Binaries (HMXBs): the donor star has larger mass than the accretor. They are thought to be mainly wind-fed systems.
- Low Mass X-ray Binaries (LMXB): the donor mass is smaller than the accretor mass. They are thought to accrete through Roche-Lobe overflow.
If ULXs contain IMBHs they might be powered by the same sub-Eddington accretion processes in act in the Galactic X-ray binaries. In case of stellar mass accretors, ULXs would need a different accretion mechanism allowing them to reach super-Eddington luminosities.

Bondi-Hoyle-Lyttleton (BHL) model for wind accretion:
The usually adopted model to explain the wind accretion is the Bondi-Hoyle-Lyttleton model (see Edgar 2004 for a review). It is assumed that a steady and uniform supersonic wind moves towards the accretor. When the wind reaches the accretion radius (r_a), the matter is accreted by the compact object. It is also possible that an accretion disc forms (e.g. Karino et al. 2019, Hirai and Mandel 2021), thanks to the transportation of angular momentum coming from the orbital motion.

Roche-Lobe overflow (RLOF):
The Roche surfaces are equipotential surfaces around the binary system. The surfaces around each component of the binary system, which meet in the *inner Lagrangian point*, form a limit surface. The limit equipotential surface encloses the space around each of the elements of the binary and the enclosed volumes are called *Roche lobes*. Inside the lobe, the material is gravitationally bound only to the star inside the lobe. In the case of the X-ray binaries, when the companion star becomes larger than its *Roche lobe*, a transfer of matter towards the compact object, through the inner Lagrangian point, begins. The accreting matter starts to orbit around the compact object, forming a disc structure: the accretion disc.

Wind-Roche-Lobe overflow (WRLOF): A proposed mechanism for accretion in ULXs is a wind RLOF (El Mellah et al. 2019, Wiktorowicz et al. 2021). In this case the accretor gravitationally drives the stellar wind towards the inner Lagrangian point (L1), causing a transfer of material similar to the case of RLOF. Wiktorowicz et al. 2021 estimated that wind-fed ULXs, which could accrete through BHL mechanism or WRLOF, are a fraction of 49-89%, which can increase in favorable conditions, such as in very young stellar environments, where they become the dominant component. The ULXs population is dominated by sources with luminosities $< 3{\times}10^{39}$ erg s^{-1}, which may be both RLOF or wind-fed systems, accreting through BHL or WRLOF mechanisms. The most luminous ULXs instead, if they are wind-fed systems, may be powered through WRLOF only (Wiktorowicz et al. 2021).

1.1.2 Super-Eddington accretion

Assuming that ULXs host stellar mass compact objects, the accretion process in act must be at least apparently super-Eddington to justify the observed luminosities.

Magneto-hydrodynamical simulations (e.g. Ohsuga and Mineshige 2007, Ohsuga et al. 2009, Ohsuga and Mineshige 2011) have shown that, if the spherical symmetry is not present, e.g. for disc accretion, moderately super-Eddington accretion rates, of a factor ~ 5 above the Eddington accretion rate $\dot{M}_{Edd}$, may be sustained producing an apparent luminosity by up to 22 L_{Edd}.

One way to obtain an apparently super-Eddington accretion onto a BH is anisotropic emission. If the X-ray emission is along our line of sight, the object would appear super-Eddington, even if it has a sub-Eddington accretion rate (King et al. 2001). There are two types of beamed emission: relativistic and geometric beaming. In the case of relativistic beaming, we expect the formation of jets, similar to those observed in the blazars or in gamma ray bursts (GRB), where the emission is dominated by relativistic electrons which produce synchrotron radiation. We would see the binary along its jet, as in the case of blazars, which would make the ULXs microblazars (Körding et al. 2002). This scenario can be ruled out by observations: for every ULX with $L_x \sim 10^{40}$ erg s^{-1}, there should be ~ 30 ULXs with $L_x \sim 10^{39}$ erg s^{-1} (Davis and Mushotzky 2004), considering the ULXs pointing at other directions than our line of sight, and this is not observed (e.g. Feng and Soria 2011, Walton et al. 2011). If the relativistic beaming is the main mechanism driving ULXs, we would also expect X-ray power-law spectra, typical of beamed jets, but they are not usually observed in ULXs data (Kaaret et al. 2017). On the other hand, the observations of nebular emission observed in the optical, radio and X-ray bands, around some ULXs (e.g. Pakull et al. 2010, Cseh et al. 2012, Belfiore et al. 2019, see also figure 1.1), suggest the presence of a quasi-isotropic X-ray emission.

The geometrical or mild beaming originates when structures in the accretion disc limit the escape of the X-ray photons in preferentially directions (King et al. 2001). This effect can arise in super-

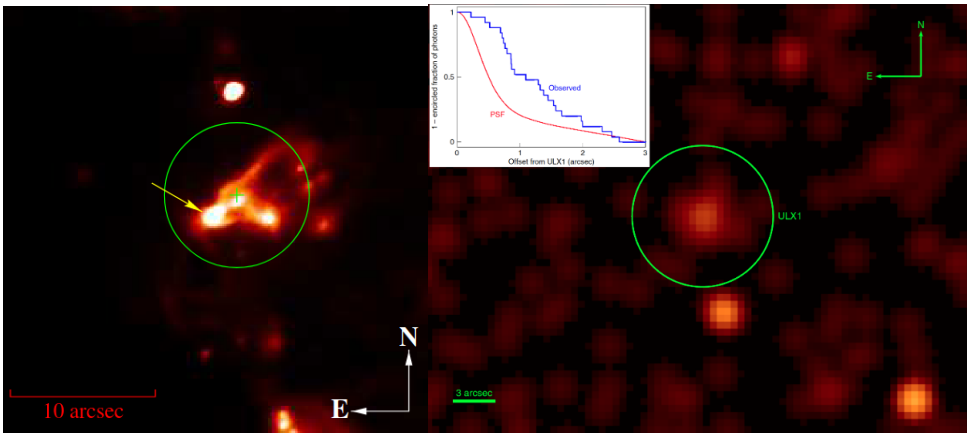

Figure 1.1: Nebular emission around ULXs. Left: H_α image of the **foot** nebula around Holmberg II X-1 (from Pakull and Mirioni 2002). Right: the X-ray bubble around NGC 5907 ULX-1 (from Belfiore et al. 2020).

Eddington accretion discs, not in standard sub-Eddington discs. A super-critical accretion disc (Shakura and Sunyaev 1973) is expected to form when the accretion rate is larger than the Eddington accretion rate ($\dot{M}_{Edd} = 48\pi GM/c\kappa$, where M is the accretor mass, c is the velocity of light, κ is Thomson opacity and G is the universal gravitational constant; Poutanen et al. 2007). An important radius in this situation is the spherization radius (Shakura and Sunyaev 1973, King 2008):

$$R_{sp} = \frac{27}{4}\frac{\dot{M}}{\dot{M}_{Edd}}R_s, \tag{1.2}$$

$\dot{M}$ is the accretion rate, $\dot{M}_{Edd}$ is the Eddington accretion rate, $R_s = \frac{2GM}{c^2}$ is the Schwarzschild radius. The spherization radius is the radius where the emitted luminosity is equal to the Eddington value and where the vertical component of the gravitational force equals the force of the radiation pressure. At the spherization radius, the disc height becomes equal to the distance from the accretor. Inside the spherization radius the disc becomes geometrically thick and the mass in excess is not accreted but ejected from the system through powerful winds (e.g. Poutanen et al. 2007, Ohsuga and Mineshige 2011). Another model proposed for supercritical accretion discs is the *Polish Doughnut* or slim disc model (Jaroszynski et al. 1980, Abramowicz et al. 1988). This model assumes that all the accretion matter in the disc reaches the BH. The photons are trapped in the disc (at distances less than the trapping radius, i.e. where the photon diffusion is equal to the accretion time-scale) and most of the gravitational energy is advected into the black hole. The bolometric luminosity is larger than the Eddington one and is related to the mass accretion rate ($\dot{m}$, which is expressed in Eddington units) by a logarithmic relation: $L_{bol} \sim L_{Edd}(1 + \ln\dot{m})$. The real situation may be between the Shakura and Sunyaev (1973) supercritical disc and the slim disc model, but the mechanisms at the base of supercritical accretion are still not well understood (Poutanen et al. 2007).
Observations have confirmed the existence of powerful winds around ULXs (see the next paragraphs for more details), similar to those observed around SS433, which is an X-ray binary in the Milky Way, powered by super-Eddington accretion (e.g. Fabrika 2004). The emitted wind assumes the shape of a funnel, as derived from the simulations (e.g. Kawashima et al. 2012) and, depending on our line of sight, we can see the hard inner radiation directly or through the wind, in the latter case a softer emission would be seen. Thus, a combination of geometrical beaming and super-Eddington accretion may explain the large luminosities emitted by ULX systems.

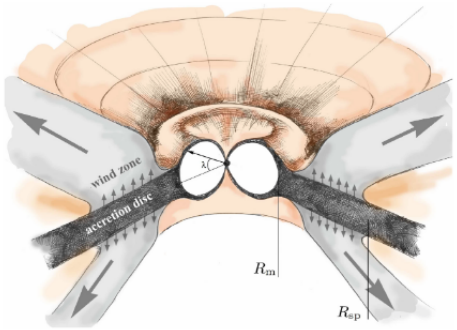

Figure 1.2: Artistic impression of a highly magnetized NS ULX. The accretion disc is truncated at the magnetospheric radius and the accreting matter is funneled onto the magnetic poles. Image taken from Mushtukov et al. 2019.

1.1.3 Accretion in NS systems

A fraction of ULXs is now known to host NS accretors (e.g. Bachetti et al. 2014, Israel et al. 2017b). NSs may have large magnetic fields (10^{12}–10^{14} G), which produce a magnetosphere around the compact star. NSs are usually born as rotating objects, because the rotation of the star, which evolves into a NS, is amplified, for angular momentum conservation, during the collapse which follows the interruption of the nuclear burning inside the star core. The magnetosphere plays a role in the accretion onto a NS. An accretion disc forms around the compact object, as for BHs, but it is interrupted by the magnetosphere at the magnetospheric radius (Basko and Sunyaev 1976, see also figure 1.2). The accretion matter is dragged towards the magnetic poles of the NS, where an accretion column is formed, which is sustained by the magnetic pressure (Lyubarskii and Syunyaev 1988). The radiation is emitted perpendicular to the direction of the accretion flux, from the side wall of the column (Basko and Sunyaev 1976). For high accretion rates, larger than 10^{19} g s^{-1}, it is possible to reach luminosities of the order of 10^{40} erg s^{-1}, but assuming a magnetic field larger than 10^{14} G (Mushtukov et al. 2015). As pointed out by Israel et al. (2017a) other conditions are needed for a NS to emit super-Eddington luminosities: the accretion has to be mediated by an accretion disc, which allows the radiation to be emitted in a range of directions, the accretion disc has to be geometrically thin down to the magnetospheric radius, implying that the emission from the disc remains sub-Eddington, the angular speed of the disc has to be larger than the NS one, so that gravity exceeds the force exerted onto the accretion matter by the magnetic field lines and can reach the NS surface. If the magnetic axis of the NS is misaligned from the rotational axis, we would see the radiation emitted from the accretion column only when one of the magnetic poles is directed towards us. This results in a pulsed X-ray emission.

The magnetospheric radius (r_m), where the magnetic field begins to control the accreting plasma, is a fraction of the Alfvèn radius, the distance where the magnetic pressure is equal to the pressure exerted by the accreting matter.

$$r_m = \frac{\zeta \mu^{\frac{4}{7}}}{\dot{M}^{\frac{2}{7}} (2GM)^{\frac{1}{7}}} \tag{1.3}$$

where $\mu = \frac{Br^3}{2}$ is the magnetic dipole, B is the magnetic field, M is the NS mass, $\dot{M}$ the accretion rate, ζ is a numerical factor <1 which indicates the fraction of the Alfvèn radius occupied by the magnetosphere, G is the gravitational constant.

The accretion disc exerts a torque onto the NS, which accelerates in a "spin-up" phase. When the magnetospheric radius becomes larger than the corotation radius, ($r_{co} = (GMP^2/4\pi^2)^{\frac{1}{3}}$, P is the spin period of the pulsar), i.e. the distance where the Keplerian speed of the matter in the accretion disc is equal to the rotation speed of the NS, a centrifugal barrier prevents matter from accretion. The accreting matter is ejected from the system in a so called "propeller phase".

The propeller mechanism (e.g. Illarionov and Sunyaev 1975) is an inhibition of accretion, caused by the magnetospheric radius becoming larger than the corotation radius of the matter in the accretion disc of a neutron star. During the accretion a "spin-up" happens: the accretion disc exerts a torque on the NS, which is accelerated in the rotation around its rotational (or "spin") axis. Also the magnetosphere, which corotates with the NS, is accelerated and when its dimension becomes larger than the corotation radius, a centrifugal force emerges, creating a gravitational barrier. The effect is that the accreting matter experiences a force outwards and it is ejected from the system. As a result of the interruption of the accretion, the X-ray luminosity of the system is drastically reduced and the system leaves the ultraluminous regime. When no accretion happens, the NS decelerates, during a "spin-down" phase, until the magnetospheric radius becomes smaller than the corotation radius. The accretion disc can form again and accretion is restored.

1.1.4 ULX as gravitational waves progenitors

Gravitational waves are perturbations of the space-time, generated by accelerated masses, which propagate as waves in the empty space. During their propagation, at the speed of light, they deform the space-time itself and everything inside it.

On September 14, 2015 the first gravitational wave signal was detected by the LIGO interferometers (Abbott and et al. 2016). The gravitational waves were produced by the merger of two BHs, with masses of $\sim$ 36 and 29 $M_{\odot}$. The first double NS merger was instead observed on August 17, 2017 with the Advanced LIGO and VIRGO detectors (Abbott and et al. 2017).

ULXs could evolve in gravitational waves progenitors. Considering double BH mergers, originating from very massive stars, when the primary star has evolved in a BH, the mass transfer can be high, causing an ultraluminous phase (Belczynski et al. 2014). This stage should be short, considering that both stars are massive.

Mondal et al. 2020a considered the formation channels of merging double compact objects (DCOs): BH-BH, BH-NS and NS-NS, that have an ultraluminous X-ray phase. They discovered that $\sim$50% of the progenitors of BH-BH mergers evolved through a ULX stage. They also derived that a fraction of 5–40% of the observed ULXs will evolve in merging DCOs, the exact fraction depending on the common envelop model assumed and on metallicity.

Wiktorowicz et al. 2021 studied the wind-fed ULXs, finding a large fraction of systems powered by wind accretion: $\sim$75–96% of wind-fed systems are expected in young star forming environments (<100 Myr). About 46% of wind-fed ULXs will form a DCO, but only $\sim$6% of them can evolve in merging DCOs, in the other cases the system will be too wide to merge in a time < 10 Gyr.

1.2 Observational properties of ULXs

1.2.1 Hyperluminous sources (HLX)

Some ULXs are found to reach luminosities larger than 10^{41} erg s^{-1} and have been labelled as *hyperluminous sources* (HLX). According to the recent catalog of ULXs candidates (Walton et al. 2022), the HLX represent $\sim$ 4% of the whole ULXs number. They constitute the most extreme subclass in the ULX population and are the best group of sources where to look for IMBHs, which could explain the emitted radiation with standard sub-Eddington accretion. However, one of the HLXs is NGC 5907 ULX-1, which is a confirmed PULX, indicating that also NSs can reach such extreme luminosities (Israel et al. 2017b).

Among the HLX, there are M82 X-1, ESO 243-49 ULX-1 (HLX-1), which have often been considered as good IMBH candidates (e.g. Kaaret et al. 2017), and N10 in the Cartwheel galaxy (Wolter and Trinchieri 2004, Pizzolato et al. 2010), compatible with a massive stellar mass BH, formed from a low metallicity star.

ESO 243-49 ULX-1, or HLX-1, has a peak luminosity of $\sim 10^{42}$ erg s^{-1} (Farrell et al. 2009) and a spectrum consistent with a hard state in some observations and a thermal state in others, which

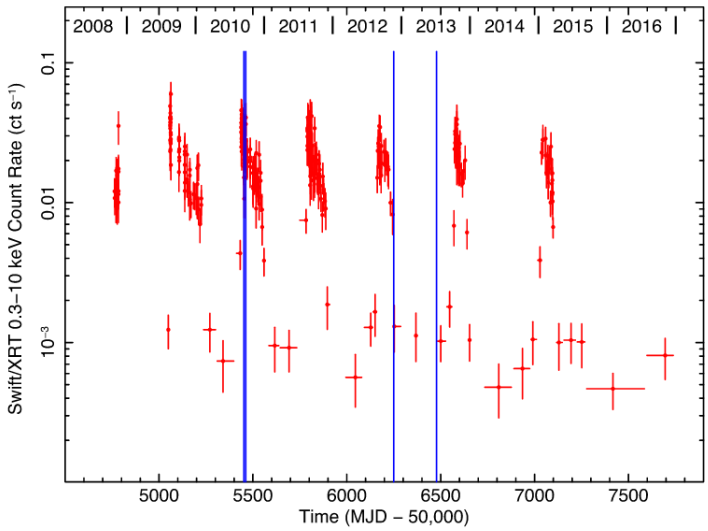

Figure 1.3: *Swift*/XRT light-curve of ESO 243-49 ULX-1 (HLX-1) where the quasi-periodicity trend of the outbursts is visible. The image is taken from Soria et al. 2017. The vertical blue lines indicate HST observations also analysed in the cited paper.

are typical states of the Galactic BH binaries (Servillat et al. 2011). In addition, the disc luminosity has been found to scale with the fourth power of its inner temperature, as expected for a standard accretion disc (Servillat et al. 2011). Many estimations for the mass of the BH in ESO 243-49 ULX-1 have been made; for example Straub et al. 2014 estimated a value of ~ 6,000–200,000 $M_{\odot}$, in accordance with the IMBH hypothesis. HLX-1 has quasi-periodic outbursts (e.g. Lasota et al. 2011; see figure 1.3) with an increasing recurrence time (e.g. Soria et al. 2017, Lin et al. 2020); the time separation between the outbursts is of the order of hundreds of days. Different explanations have been proposed for the quasi-periodicity of the outbursts, such as an enhanced accretion due to a tidal stripping at the periastron position of a star in a very eccentric orbit (Lasota et al. 2011), an oscillation in the accretion rate linked to wind emission from the inner disc regions (Soria et al. 2017) or a disc precession induced by tidal interactions (Lin et al. 2015).

M82 X-1, with peak luminosity of ~ 10^{41} erg s^{-1} (e.g. Kaaret et al. 2006), shows twin-peaked HF-QPOs (see section 2.1.5) which led to a mass estimate of 428±105 $M_{\odot}$ (Pasham et al. 2014). In the spectrum observed during a flaring episode, Feng and Kaaret (2010) found that the luminosity of the disc was proportional to the disc inner temperature at the fourth, using a standard thin disc model. They derived from the spectral analysis a BH mass of 200–800 $M_{\odot}$, assuming a rapidly rotating BH. Brightman et al. (2016b) instead modelled the spectrum of M82 X-1 as a slim disc, estimating a mass of 20–573 $M_{\odot}$ depending on the BH spin and inclination angle. So, with the actual knowledge, the BH in M82 X-1 may be interpreted both as a massive stellar BH or as an IMBH.

Pizzolato et al. (2010) showed that N10 in the Cartwheel galaxy has a (0.5-10) keV peak luminosity of ~ 1.2×10^{41} erg s^{-1}. From their spectral analysis, they found that it is compatible with a BH mass of ~ 100 $M_{\odot}$. A similar mass may be explained through the stellar evolution of a massive star in a low metallicity environment.

1.2.2 ULX spectra

The first low quality spectra of ULXs, such as those obtained in the 90s with *ROSAT* and *ASCA*, may be fit with single component models (see figure 1.4 left).

With the launch of *Chandra* and *XMM-Newton*, in the 2000s high quality spectra of ULXs have been obtained for the first time.

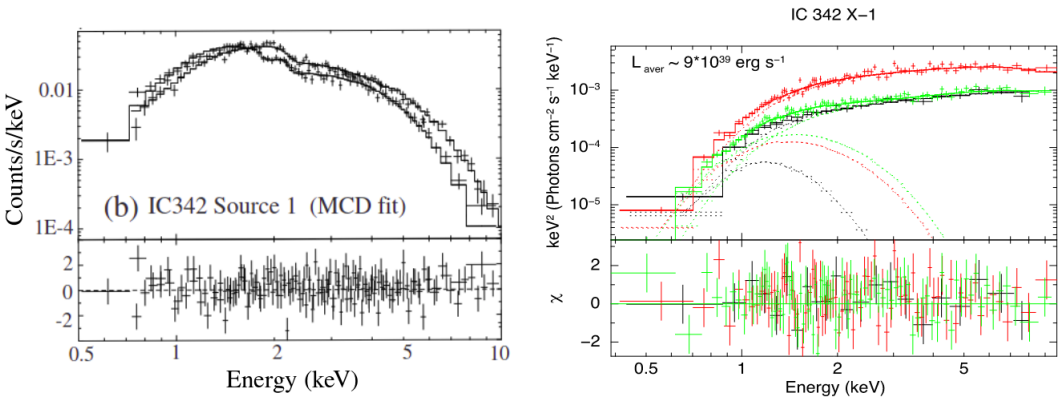

Figure 1.4: Left: ASCA spectra of IC 342 X-1, in two different epochs, fitted with a single component model: a multicolour blackbody disc. Image taken from Makishima et al. 2000. Right: IC 342 X-1 spectrum of the *XMM-Newton* EPIC cameras, fitted with a two components model: a multicolour blackbody disc plus a Comptonizing component. Image taken from Pintore et al. 2014.

Thanks to high quality data, two typical features can be identified in the ULXs spectra: an excess at soft energies and a curvature at 2–5 keV (see e.g. Stobbart et al. 2006, Roberts 2007, Gladstone et al. 2009). Such spectra are not consistent with IMBHs models, but can be explained with extreme accretion onto stellar mass compact objects. Gladstone et al. (2009) tried to fit high quality spectra (i.e. with more than 10000 counts) of ULXs with single component models, a power-law or a multicolor blackbody disc, obtaining non-acceptable fits in most cases and contrasting results between the two models: the power-law fits suggested the presence of IMBHs in at least some of the analysed sources, while the disc model temperatures suggested sMBHs accreting at high rates. They concluded that a good description of the ULXs can be obtained with at least two components models (see figure 1.4 right). One possible scenario is that we see the cool emission of the outer disc regions, while the inner regions are obscured by an optically-thick corona, that is possible to form thanks to the extreme accretion rates (Roberts 2007). Another possibility, proposed by Gonçalves and Soria (2006), is that we see a negligible emission from the disc and a dominant power-law component modified by absorption from a ionised and fast outflow. From the spectral analysis of ULXs with a two components model, composed of a multicolor blackbody disc and a power-law, Gladstone et al. (2009) found either a hot disc, as expected for a stellar mass BH accreting at or above its Eddington limit, but with a soft excess never observed before, or a cool disc with a high-energy tail, not observed in the spectra of the Galactic X-ray binaries. Gladstone et al. (2009) named this new spectral state observed in ULXs, i.e. a cool disc plus a broken harder component, the *ultraluminous state* and they interpreted this new state as a signature of extreme accretion onto stellar mass BHs. To better characterize the *ultraluminous state*, they substituted the power-law with a more physical model: a Comptonization model. This resulted in a cool optically thick corona, different from the hot and optically thin one, usually found in Galactic X-ray binaries in standard sub-Eddington accretion states: the optically thick corona represents the high energy spectral component, while the cool disc, i.e. the low energy component, was interpreted as the soft emission coming from the external regions of the accretion disc. The thickness of the corona in ULXs, can derive from the winds launched when there are super-Eddington accretion rates (Poutanen et al. 2007, Gladstone et al. 2009). Alternatively, the soft component could originate from the wind photosphere, while the hard component may be the hot emission of the inner disc regions (Middleton et al. 2011a). Sutton et al. (2013) suggested an empirical classification for ULXs based on the spectral shapes observed: a *broadened disc*, appearing at around the Eddington limit, and two ultraluminous regimes, *hard ultraluminous* and *soft ultraluminous*, at increasing luminosities, with two components and a peak respectively in the high energy or low energy component. In figure 1.5 (from Kaaret et al. 2017) the

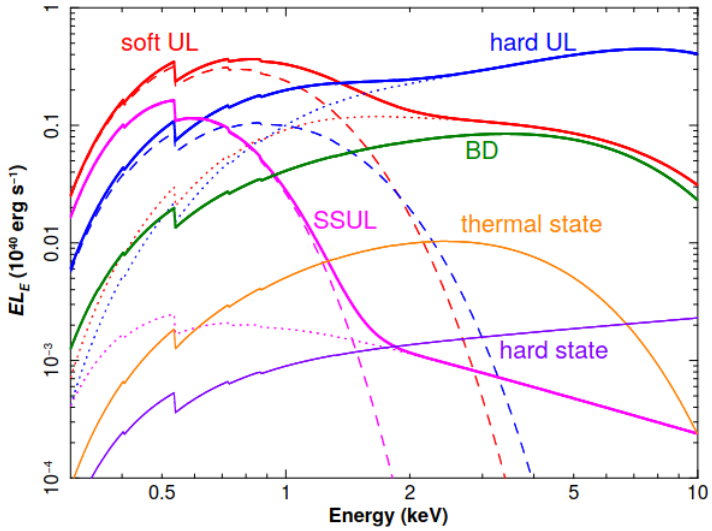

Figure 1.5: Comparison of ULX and Galactic BH binaries (GBHB) spectral states. Red solid line: ULX soft ultraluminous (soft UL); blue solid line: ULX hard ultraluminous (hard UL); green solid line: ULX broadened disc (BD); magenta solid line: ULX super-soft ultraluminous (SSUL); orange solid line: GBHB thermal state; purple solid line: GBHB hard state. Dashed and dotted lines represent respectively the two components of the ultraluminous regimes, modeled with a multicolour disc and an optically thick corona. Image from: Kaaret et al. 2017.

ULX and Galactic BH binaries spectral states are compared. The ultraluminous regimes represent the same kind of system, seen at different angles. The angular dependence comes both from the inclination of the system and from the presence of an outflowing wind, originating at super-Eddington accretion rates, which assumes the shape of a funnel (e.g. Poutanen et al. 2007, Kawashima et al. 2012). So, if the ULX is seen face-on, we can detect the hard emission of the inner regions, while with an edge-on system we see it through the wind's photosphere, resulting in a softer emission. When the accretion rate increases, the wind's opening angle becomes narrower (the beaming factor b is proportional to $\dot{m}^{-2}$, $b \propto 73/\dot{m}^2$, with $\dot{m}$ the accretion rate in Eddington units; King 2009) and the wind may intercept the observer line of sight. So, especially when the ULX is seen at intermediate angles, it is possible to see a transition between the two ultraluminous regimes, if there is a change in the accretion rate and consequently in the wind opening angle.

In many ULXs an additional third spectral component is needed to model an hard excess in the emission above 10 keV. This emission could originate in the accretion column and could indicate a NS accretor (e.g. Walton et al. 2018c).

The relation between the luminosity (L) and the temperature (T) of the disc component for sub-Eddington accretors, with a standard thin disc (Shakura and Sunyaev 1973), is $L \propto T^4$. Some ULXs show a different relation between L and T, such as $L \propto T^2$ (e.g. Mondal et al. 2021a), which is expected for a slim disc (Watarai et al. 2000), or an anti-correlation with $L \propto T^{-4}$ (e.g. Robba et al. 2021), supporting the presence of stellar mass super-Eddington accretors.

1.2.3 Observational evidences for outflows

X-ray spectra: Low energy residuals have been identified in ULX spectra (Gladstone et al. 2009) and Sutton et al. (2015) showed that they are probably associated with the ULX, at least in the case of NGC 5408 X-1. Middleton et al. (2014) studied the *XMM-Newton* / EPIC spectra of NGC 5408 X-1 and NGC 6946 X-1 and found that the soft residuals can be modeled by absorption from an

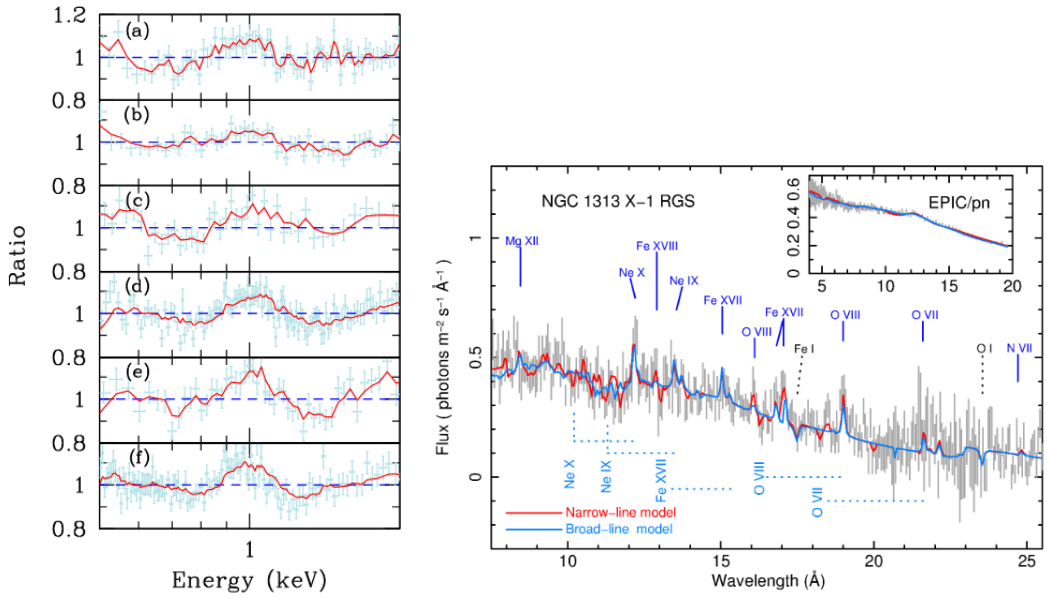

Figure 1.6: Left: *XMM-Newton* EPIC-pn spectral residuals for a sample of ULXs fitted with a multicolour blackbody disc plus a Comptonization model. Image taken from Middleton et al. 2015c. Right: *XMM-Newton* RGS spectrum of NGC 1313 X-1. The model indicated with a red solid line represents rest-frame absorption and emission with a relativistically-outflowing and photoionized absorber, with $v = 0.2c$. The blue line includes also a broadened absorber, with $v = 0.25c$. The insert represents the EPIC-pn spectrum. Image taken from Pinto et al. 2016.

outflowing wind, partially ionized and optically thin, with a velocity of $\sim 0.2c$. The shape of the residuals has been found to be the same in a sample of sources (see figure 1.6 left), suggesting that they have a common origin. From the analysis of NGC 1313 X-1, it was found that the strenght of the emission or absorption features anticorrelates with the spectral hardness, which is in agreement with a scenario of atomic transitions in a wind associated with an outflow (Middleton et al. 2015c).

These residuals have been resolved for the first time by Pinto et al. (2016), using the high resolution spectra, taken with the RGS (Reflecting Grating Spectrometer) on board *XMM-Newton*. The emission lines, originating from a strongly ionized iron, oxygen, neon (Fe XVII, O VIII, Ne X are significantly detected in the case of NGC 1313 X-1; see figure 1.6 right), are consistent with rest-frame emission, maybe associated with a shock between the outflowing wind and the surrounding gas. The blushifted absorption lines (Ne IX, O VIII, O VII) are associated with the fast outflowing wind and the derived velocity is $\sim 0.2c$. Such winds have been identified in a growing number of ULXs (e.g. Pinto et al. 2017, 2021, Kosec et al. 2018a,b, 2021), with velocities of $\sim 0.1 - 0.3c$.

Optical, radio and X-ray bubbles around ULXs: Many ULXs are surrounded by a nebula (or bubble) emitting in optical or in radio (e.g. Pakull and Mirioni 2002, 2003, Pakull et al. 2010, Abolmasov 2011, Cseh et al. 2012; see figure 1.1 left). Most of these bubbles are powered by shocks, originated from the interaction between the outflows of the ULX and the surrounding medium; in some cases the nebula is powered by photoionization. They extend by up to hundreds of parsecs and the shock-ionized nebulae are powered by outflows, which could be subrelativistic winds, relativistic jets emitted continuosly or relativistic particles ejected episodically (e.g. Kaaret et al. 2017, Cseh et al. 2014, 2015).

Belfiore et al. (2020) discovered the first X-ray emitting bubble around an ULX. The ULX is NGC 5907 ULX-1, which is also the most luminous known PULX, with a peak luminosity larger than 10^{41} erg s^{-1}, in excess of ~ 500 times its Eddington limit. The diffuse X-ray emission was detected

during a low state of the PULX and has a diameter of $\sim$ 200 pc and a luminosity of $\sim 2{\times}10^{38}$ erg s^{-1}. Belfiore et al. (2020) interpreted this emission as an expanding nebula fed by the ULX wind. The mechanical power to obtain such luminosity is $1.3{\times}10^{41}$ erg s^{-1}, the derived age of the bubble is $\sim$ 70,000 yr and the velocity of the wind $\gtrsim 0.1c$, consistent with the outflows velocity obtained for other sources from the high resolution spectral analysis (e.g. Pinto et al. 2016).

1.2.4 Ultraluminous Supersoft Sources

Some ULXs, named ultraluminous supersoft sources (ULSs), show almost no emission above 1 keV. They are in the so called *supersoft ultraluminous state* (SSUL) (Feng et al. 2016). This spectral state is characterized by a cool blackbody component, with temperature < 140 eV, which dominates the spectrum and the hard component, if present, is very weak (e.g. Pinto et al. 2021). Their blackbody radii are $\sim 5{\times}10^3$–10^5 km and their luminosities a few 10^{39} erg s^{-1} (Urquhart and Soria 2016a). The blackbody radius changes between observations and this is consistent with the photosphere of an optically-thick outflow, with an increase in the photosphere radius when the outflow becomes thicker. ULSs can be interpreted as ULXs seen at high inclination angles and very high accretion rates, which causes the outflow to become very thick and to absorb completely and reprocess the hard emission of the inner regions (Urquhart and Soria 2016a). This scenario has been observationally confirmed by the detection of rest-frame emission and of blueshifted absorption lines, indicating powerful winds, in the high resolution grating spectra of some sources that appear as soft ULX or ULS in different epochs (NGC 55 ULX, NGC 247 ULX-1; Pinto et al. 2017, 2021).

1.2.5 Optical counterparts

Out of about 400 known ULXs (see e.g. Walton et al. 2011, Earnshaw et al. 2019b; recent catalogues contain even more candidate ULXs: 629, Kovlakas et al. 2020; 1843, Walton et al. 2022; 779 Bernadich et al. 2021) only in few cases, about 20, the optical counterpart has been uniquely identified (Tao et al. 2011, Gladstone et al. 2013), usually appearing as a giant or supergiant OB type (e.g. Zampieri et al. 2004, Soria et al. 2005). The small number of identifications depends on the difficulty of this kind of observations. ULXs are often observed in crowded field, hence for the identification of the optical counterparts it is often needed the use of both the *Hubble Space Telescope*, for the optical imaging, and *Chandra* for the X-ray localization (Kaaret et al. 2017). Most ULXs counterparts have optical apparent magnitudes in the range $m_v \sim$ 21–24 (Tao et al. 2011, Gladstone et al. 2013), while the V-band absolute magnitudes are in the range $M_v \sim$ (–3) – (–8) (Kaaret et al. 2017). The variability of the optical counterparts of ULXs are usually smaller than 0.1 – 0.2 magnitudes (Tao et al. 2011), except for some sources with a large variability in the X-ray band (factor of hundred or more) which show a strong variability also in the optical range (up to several stellar magnitudes) (Fabrika et al. 2021, Soria et al. 2012, Motch et al. 2014). The flux ratio of ULXs between the X-ray and the optical band, defined as $B_0 + 2.5\log(f_x)$ (B_0 is the dereddened B magnitude and f_x is the flux in 2–10 keV in microjanskys), is usually high (> 100–200) and similar to those observed in LMXBs (Kaaret et al. 2017, Fabrika et al. 2021). This finding suggests that the ULXs optical emission is mainly dominated by the light reprocessed by the accretion flow, while the contribution from the companion star may be very small. The flux ratios found in ULXs can be used to distinguish between ULXs and AGN (active galactic nuclei), the latters have flux ratios usually smaller than 10, except in some cases where they reach a factor $\sim$ 100, due to the large absorption in the host galaxy (Aird et al. 2010, Della Ceca et al. 2015, Fabrika et al. 2021). The colours of the optical counterparts of ULXs tend to the blue, with a power spectral energy density distribution (SED) $F_\nu \propto \nu^\alpha$, with $\alpha \sim 1 - 2$ (Tao et al. 2011, Vinokurov et al. 2013). These slopes agree with the emission expected from hot winds emitted by supercritical discs, with small emission from the companion star (Fabrika et al. 2015). In conclusion, the determination of the companion star through the study of the emission of the optical counterpart is usually very difficult. NGC 7793 P13 is an exception: in this case absorption lines have been detected in the optical spectrum, allowing a classification of the companion star which is a supergiant B9Ia, with a mass of $18 - 23\ M_\odot$ (Motch et al. 2014). Also in M101 ULX-1 (labelled M101 28ULX in this thesis) optical spectral features,

in this case absorption lines, have been detected from the donor star which is probably a Wolf-Rayet (WR) star (Liu et al. 2013).
In addition to the optical study of the ULXs, also near infra-red (NIR) data have been used to find information about the companion star in ULXs. Heida et al. (2014) found the NIR counterparts for a sample of ULXs, 11 of which not previously detected in the optical or infrared band. Some other NIR candidate counterparts have been detected from other single sources (Heida et al. 2015, 2016, 2019) and are usually consistent with red supergiant donor stars.

1.2.6 ULX populations

ULXs are found in all galaxy types. The most luminous of them are in spiral and irregulars, while ULXs in elliptical galaxies are usually less luminous (e.g. Swartz et al. 2004, Feng and Soria 2011). One third of the ULXs in spiral galaxies have luminosities > 4–5×10^{39} erg s^{-1} and $\sim$10% have luminosities $> 10^{40}$ erg s^{-1} (Walton et al. 2011, Earnshaw et al. 2019b). ULXs are often associated with star forming regions (e.g. Grimm et al. 2003), but sometimes they are found in non- or faint star forming regions, suggesting that they turn on after the lifespan of an HII region, $\sim$10–20 Myr (Swartz et al. 2009, 2011). The number of ULXs correlates with recent star formation, implying a larger number of ULXs in star forming galaxies and this is confirmed by the discovery of many ULXs in interacting galaxies (e.g. the Antennae, Zezas et al. 2002, Zezas and Fabbiano 2002; the Cartwheel, Gao et al. 2003, Wolter and Trinchieri 2004), which have a large star formation rate.

Are there ULXs in the Milky Way and in the Magellanic Clouds? The only binary system in our Galaxy able to accrete persistently at super-Eddington rates is SS433 (e.g. Fabrika 2004). Even if its luminosity is always smaller than 10^{39} erg s^{-1}, i.e. its X-ray luminosity is usually 10^{35} – 10^{36} erg s^{-1}, it is thought to be an edge-on ULX: an inclination of $\sim$ 78.8 deg has been derived for this system (Margon and Anderson 1989). In addition, jets and a super-critical disc with outflows have been discovered in SS433 (e.g. Fabian and Rees 1979, Fabrika 1997), which cover the hot inner accretion regions. An intrinsic X-ray luminosity $\geq 10^{37}$ erg s^{-1} has been estimated for the system, implying an apparent luminosity $> 10^{39}$ erg s^{-1} for an hypothetical face-on observer and confirming the ULX nature (Middleton et al. 2021). In addition, some transient ULX NSs, which occasionally accrete at super-Eddington luminosities have been observed. The first evidence for a pulsating super-Eddington accretor is indeed a transient NS, A0538-66 (peak luminosity $\sim 8\times10^{38}$ erg s^{-1}), in the Large Magellanic Cloud (Skinner et al. 1982). While the first ULX NS in the Milky Way is Swift J0243.6+6124, which has reached a peak luminosity of $\sim 2\times10^{39}$ erg s^{-1} (Wilson-Hodge et al. 2018). Other similar objects are SMC X-3 (Townsend et al. 2017, Tsygankov et al. 2017), with peak luminosity of $\sim 1.2\times10^{39}$ erg s^{-1}, SMC X-1 and GRO J1744-28 (Lucke et al. 1976, Kouveliotou et al. 1996).

ULXs in globular clusters: A number of ULXs are associated with globular clusters (GCs); Dage et al. (2019) analysed a sample of 9 GC ULXs. They found that their spectra are well fit with a single power-law or disc, unlike usually found in spiral galaxies where ULXs are well fit with two components models. Sources with a power-law best fit show none or little variability in the power-law index and in luminosity. The sources best fitted with a disc divide in two groups, i.e. with inner temperature larger or much smaller than 0.5 keV. The sources with inner temperature smaller than 0.5 keV show strong variability in luminosity but not in the disc temperature. Dage et al. (2019) also suggest a possible correlation between disc temperature and the presence or not of optical emission: the optical spectra of low temperature sources have forbidden emission lines, while a number of the high temperature sources show no emission. Dage et al. (2020) analysed other 7 sources in GCs candidates in M87 finding luminosities between 1 and 4 $\times10^{39}$ erg s^{-1} and their spectra are well fit with single component models as found also in the previous sample analysed by the same authors. Irwin et al. (2003) suggested that the population of ULXs in elliptical galaxies is different from the sources observed in spiral galaxies, usually associated with young stellar populations. In GCs in ellipticals the stellar environment is usually old, thus the companions of the ULXs are likely low mass donors.

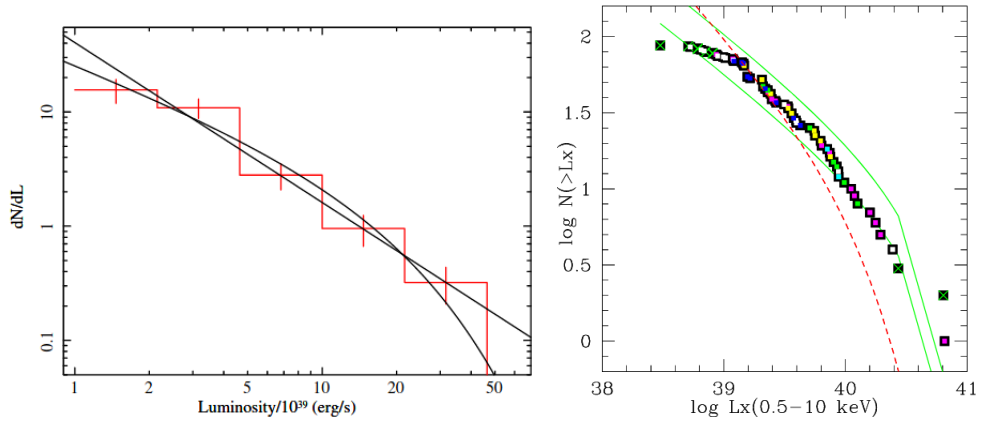

Figure 1.7: Left: Differential XLF of a sample of ULXs, with superimposed the best-fitting model obtained with a power-law and with a cut-off power-law. Image taken from Swartz et al. 2011. Right: Cumulative XLF for a sample of ring galaxies. The solid green line is the Grimm et al. 2003 model normalized to a SFR of 35 and 50 $M_{\odot} yr^{-1}$, respectively for the lower and upper curve. The red dashed line is the Swartz et al. 2011 model. Image taken from Wolter et al. 2018.

XLF: the Luminosity Function (LF) of a class of objects, describes the distribution in luminosity of the sources included in the considered sample. The LF may be constructed in a cumulative form, where each luminosity bin contains the sources with luminosity smaller than a reference value, or in a differential form, where the sources are grouped in luminosity bins and each bin is divided by its width. The X-ray LF (XLF) is a LF constructed in the X-ray band. For example, Swartz et al. (2011) studied the XLF of ULXs in star forming galaxies (see figure 1.7 left) and observed a break at (1–2)×10^{40} erg s^{-1}, while Wang et al. (2016), considering a larger sample of ULXs, found a break around 4×10^{40} erg s^{-1}. The XLF for ULXs is consistent with the high energy tail of HMXBs (e.g. Wolter and Trinchieri 2004, Zezas et al. 2007, Wolter et al. 2015), given its continuous shape among different luminosities. This scenario suggests the presence of the same population of sources both at low and high luminosities, and thus favours stellar mass accretors instead of IMBHs, with the latters possibly powering a minority of objects in the ULX population (e.g. Zezas et al. 2007).

Grimm et al. (2003) found a relation between the XLF shape of HMXBs in late type galaxies and the Star Formation Rate (SFR), which is known as the *universal XLF for HMXBs*. A similar relation was derived also by Mineo et al. (2012). Wolter and Trinchieri (2004) and Wolter et al. (2015) found that the XLF of the Cartwheel galaxy and of NGC 2276, both containing a large number of ULXs, is consistent with the respective SFRs, through the universal relation of Grimm et al. (2003). The same conclusion was derived for a sample of ULXs in ring galaxies in Wolter et al. 2018, with the suggestion of a larger luminosity cut-off for the ring galaxies XLF (see figure 1.7 right). The link between the number of ULXs in a galaxy and its SFR was also found, based on different arguments, by some authors, e.g. Mapelli et al. (2009, 2010), who also found a possible anticorrelation between the number of ULXs and the metallicity of the host galaxy, to be confirmed.

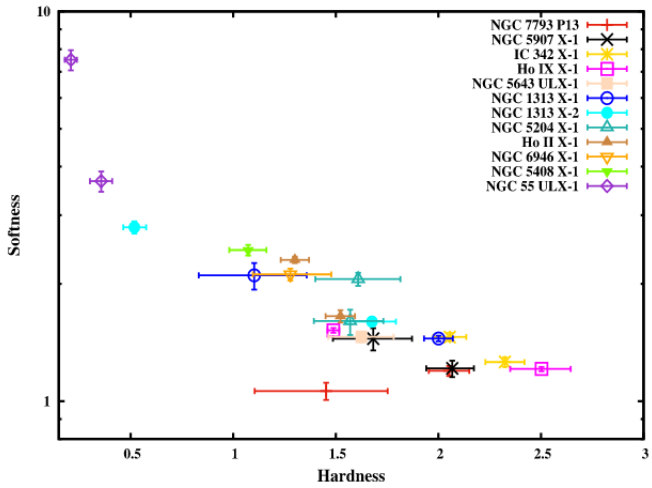

Figure 1.8: Colour-Colour diagram which shows the hardness for a sample of ULXs. The diagram has been constructed by using the flux ratios in the energy bands 2–4, 4–6, and 6–30 keV. Image from Pintore et al. 2017.

1.3 Which is the nature of ULXs?

As explained before, because of their large luminosities in the X-ray band, for a long time ULXs have been supposed to be the ideal place where IMBHs could be host (e.g. Colbert and Mushotzky 1999). The picture was drastically redrawn after the discovery of coherent pulsations in the ULX M82 X-2 (Bachetti et al. 2014), which was the proof of the presence of a NS in a ULX: the first PULX (pulsar ULX) was found. This discovery confirmed that super-Eddington accretion can be sustained for long periods of time and can happen in PULX systems.
After that first PULX, other pulsating objects have been found (Israel et al. 2017a,b, Fürst et al. 2016, Carpano et al. 2018, Sathyaprakash et al. 2019, Rodríguez Castillo et al. 2019), confirming that at least a fraction of ULXs contains NSs, but the relative fraction of NSs and BHs in ULXs is still unknown. Considering that only for $\sim$ 20 ULXs there are data with enough statistics to detect pulsations (e.g. Earnshaw et al. 2019b, Song et al. 2020), the NSs may be very common among ULXs.
Some indirect methods have been proposed to find NSs in ULXs. One possibility is the search for cyclotron lines, that can be only produced by a NS, as happened in the case of NGC 300 ULX-1 (Walton et al. 2018a) and M51 ULX-8 (Brightman et al. 2018).
In the long-term light curve of ULXs a bi-modal flux distribution or a transient behaviour is sometimes observed. These patterns have been taken as possible indicators of propeller phases (Grebenev 2017, Tsygankov et al. 2016, Earnshaw et al. 2018).

Another method to select potential candidates NS ULX comes from the spectral analysis: Pintore et al. (2017) suggested that PULXs are the hardest sources in the ULX population. This conclusion was based on hardness ratio studies, applied on a sample of sources with data in the energy band 2–30 keV. They constructed a colour-colour diagram for a sample of ULXs: the known PULX occupy the region with the highest hardness in the diagram (see also fig. 1.8).

On the other hand, no methods are currently known to confirm the presence of a BH in a ULX. Even if most ULXs are now thought to host stellar mass compact objects, the possibility that some systems host IMBHs has not been ruled out.

The thesis is organised as follows. In Chapter 2 we focus on the variability, which is also the central subject of our data analysis. We present the variability properties of ULXs from the literature, describing short and long-term features, pulsations, spectral variability and the statistical methods

for data analysis used in this work. Chapters 3 and 4 are dedicated to the data analysis done in this thesis, with a presentation of the obtained results. In Chapter 3, we present the long-term study of a sample of ULXs monitored with the *Swift* Observatory, with the aim of expanding the knowledge of the ULXs characteristics, with particular attention to their variability properties. Variability in the X-ray band is thought to generate from the super-critical accretion processes which power ULXs, thus variability studies together with spectral properties are useful to derive physical information about the accretion mechanisms in act. In Chapter 4, we instead report the analysis of the variability of point-like sources and of their luminosity function in a population of ULXs in a single ring galaxy: the Cartwheel galaxy. We report the conclusions and future perspectives of this work in Chapter 5.

Chapter 2

Variability in ULX: state of the art

The accreting matter around compact objects releases gravitational energy in form of radiation, which reaches high temperatures, of the order of keV, and thus the emission is observed in the X-ray band. This means that the X-ray emission from accreting compact objects, often found to be variable, is linked to the accretion flow. Thus, variability studies of the X-ray emission may allow us to investigate the physics of the accretion processes in act in the considered systems. Both Galactic X-ray binaries (GXBs) (e.g. Remillard and McClintock 2006) and AGNs (e.g. Padovani et al. 2017) have shown variability in the X-ray band. Also ULXs often show variability in their emission (e.g. Heil et al. 2009, Earnshaw et al. 2018), which can be used to determine the timescales of the physical processes producing the high luminosities observed in these sources. The luminosities emitted by the ULXs are intermediate between those observed in the GXBs and in the AGNs, but their masses are not necessarily intermediate: only some ULXs, possibly containing IMBHs, would be in the mass gap between GXBs and AGNs masses, while those containing sMBHs or NSs (e.g. Bachetti et al. 2014), would have masses comparable to those of the GXBs. The variability properties of the GXBs have been used together with their spectral analysis to identify their canonical sub-Eddington spectral states (e.g. Remillard and McClintock 2006). The ULXs spectra are different from those typical of GXBs and are characterized by a different spectral state, an *ultraluminous state* (Gladstone et al. 2009), produced by a different accretion mechanism, which occurs at super-critical rates. AGNs are SMBHs, which may have needed a period of super-critical accretion to reach their large masses (e.g. Volonteri et al. 2003, Volonteri and Rees 2005). Thus, both AGNs and ULXs may be powered by super-Eddington accretion, which suggests that the same physical processes may be present in these two classes of objects, but on different mass- and time-scales. Therefore, a detailed characterization of the super-Eddington accretion processes in ULXs may also be useful to better understand accretion onto SMBHs.

Variability in an accreting system may be linked to variations in the mass accretion rate, deriving from changes in the emitted wind of the companion star. Stellar winds from massive stars are thought to contain dense clumps (e.g. Puls et al. 2008). For example, Lupie and Nordsieck (1987) studied a sample of 10 OB supergiants and found random variability in the polarization on timescales of days to months, in seven of the analysed objects. The randomness of the variability has been attributed to an inhomogeneous structured wind. The accretion onto a compact object in a wind-fed system of such stellar winds can be used to study the physical properties of the winds and the massive clumps (e.g. Orlandini et al. 2015). The clumpiness in the stellar wind may produce variability in the emitted radiation, with an increase in the X-ray emission when a dense clump is accreted. The situation in the ULXs may be more complex, considering the presence of a disc which mediates the accretion, preventing us to directly observe the result of the accretion of a single dense wind clump. On the other hand, we suggest that inhomogeneous injection of material in the accretion disc may produce the aperiodic variability observed in many ULXs.

In binary systems with a massive companion, the tidal forces exerted by the compact object onto the companion star produce an enhanced stream of wind in the direction of the compact object (Blondin et al. 1991). As a result, inhomogeneous accretion structures form in the vicinity of the

compact object and an enhanced absorption in some directions produces variability in the observed X-ray emission.

In a super-Eddington accretion flow, as in the case of most ULXs, powerful outflows/winds are ejected from the accretion disc (Shakura and Sunyaev 1973, Poutanen et al. 2007). Variability may be produced by variations in the ejected flow of matter, thus variability may also be used to obtain physical information about the outflows.

Furthermore, the orbital motion or the precession of structures in the accretion flow may produce some kind of variability, which in this case is expected to be periodic. The study of periodicities in ULXs may therefore bring information about the orbital parameters or the accreting structures.

Both short-term (minutes to hours; e.g. Roberts and Colbert 2003) and long-term variability (months to years) are often taken as evidence of accretion onto compact objects (e.g. Makishima et al. 2000; Fabbiano et al. 2003; Wolter et al. 2006, Crivellari et al. 2009). Also spectral variability has been used to support the idea that ULXs are accreting objects, as happened with the discovery of spectral state transitions in the ULXs of IC 342 (Kubota et al. 2001).

Temporal flux variability on different timescales or spectral variability of specific spectral components may be caused by different physical processes. In the following sections the main variability properties observed in ULXs, within their physical implications, are described.

2.1 Short-term variability

Flux variability is observed in ULXs on different timescales. Here we refer to short-term variability considering timescales from minutes to hours. This kind of variability can be studied within a single observation with a good statistics.

2.1.1 Short-term aperiodic variability

The variability properties of ULXs on short timescales are different from those observed in Galactic X-ray binaries or in AGNs. Heil et al. (2009) found some variable sources and a suppressed variability in other ULXs. They proposed that the lack of variability can be due to the limited energy or frequency bandpass of the ULXs data, or alternatively that the ULXs are intrinsically less variable compared to BH binaries and AGNs. This could depend on the reprocessing of the variable, scattered emission of the hard inner disc through an optically thick layer of inflowing/outflowing material, resulting in a dilution of the variability (e.g. Middleton et al. 2015a, Mushtukov et al. 2019, see figure 2.1).

The stochastic variability on short timescales can be caused by the winds launched by the accretion disc. If the wind has a clumpy structure (e.g. Middleton et al. 2011a, Takeuchi et al. 2013) we can observe a variable emission caused by the wind blobs intersecting our line of sight and stochastically obscuring the hard emission from the inner regionsof the accretion flow. In the framework of the spectral analysis of Sutton et al. (2013), a source can appear in the *hard ultraluminous* regime, when the inner regions are directly visible to the observer but, with an increase in the accretion rate and a consequent narrowing in the wind opening angle, the wind can intercept our line of sight, with a transition in the *soft ultraluminous* regime. In this situation the clumpy wind would produce short-term variability, by obscuring the emission of the inner accretion flow. This implies that the flux variability should be observed mostly in the soft regime. This hypothesis is confirmed by the study of the fractional variability (F_{var}), which is usually larger for sources in the *soft ultraluminous* regime (Sutton et al. 2013). On the other hand, not all the soft sources are variable in all the observations, which may complicate the scenario. Variability, when present, is usually dominated by the hard band, above 1 keV, while the flux below 1 keV is usually more stable, as seen both from F_{var} (see section 2.5.3 for a definition) studies (e.g. Sutton et al. 2013) and from the covariance spectra (e.g. Middleton et al. 2015a) and could be explained with the obscuration of the inner hard emission by the wind and the puffed disc, expected in a scenario of super-Eddington accretion (e.g. Middleton et al. 2015a, Pinto et al. 2017).

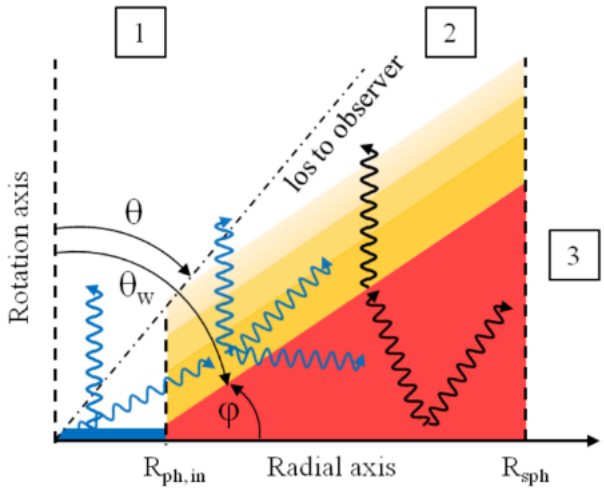

Figure 2.1: Supercritical accretion in ULXs. An optically thick outflow is launched from the region between R_{sph} and $R_{ph,in}$. Depending on the observer orientation, and thus on θ, the emission from the inner regions, i.e. $R < R_{ph,in}$, may be boosted (position 1) because of scattering into the observer line of sight, or reduced (position 2) through scattering out of the line of sight and Compton down scattering. Position 3 corresponds to supersoft ULXs or to sources which mainly emit at lower energies than the X-ray band, i.e. in UV. Image taken from Middleton et al. 2015a.

2.1.2 Flaring activity

A forest of narrow peaks is observed in the light curve of some ULXs (e.g. Earnshaw et al. 2019a, Kara et al. 2020, Pintore et al. 2021, Motta et al. 2020, D'Aì et al. 2021; see also figure 2.2 left). These flux peaks are not so commonly observed in ULXs and usually last on timescales of ~ minutes–hours. For example, in the case of NGC 4559 X7 (Pintore et al. 2021) a period of flaring activity was observed in the data taken with *XMM-Newton* and *NuSTAR* in 2019. The duration of the flares was between 5 and 10 ks and the flux increased of a factor ~ 3–4 during flares, with respect to the pre-flare flux. Usually there is not a (quasi-)periodic recurrence of the flares; an exception is represented by ULX 4XMM J111816.0-324910 in NGC 3621 (Motta et al. 2020; see figure 2.2 right), where a quasi-periodic appearance of ~ 3500 s is observed, but the origin of the periodic behaviour is still unclear. The quasi-periodic flares observed in NGC 3621 4XMM J111816.0-324910 are reminiscent of the variability observed in some other objects: GRS 1915+105 (a galactic BH binary; Belloni et al. 2000), IGR J17091–3624 (probably powered by a sMBH; Altamirano et al. 2011), MXB 1730–335 (a confirmed NS, also known as the Rapid Burster; Hoffman et al. 1978) and the AGN GSN 069 (Miniutti et al. 2019). In the latter, QPEs (quasi-periodic eruptions) have been observed, with a longer quasi-periodicity than all the other sources indicated, i.e. ~ 9 hr, probably linked to the larger BH mass, and with symmetric peaks. The peaks in the other sources have instead an asymmetric structure with a low-flux plateau and a shoulder before the main peak, which has a slower rise and a fast decay. See also Arcodia et al. 2021, 2022 for a discussion on QPEs from the nuclei of low-mass galaxies.

If the flares are rare (e.g. in the case of NGC 4559 X7; Pintore et al. 2021) or have a large cadence with respect to the typical observation exposures, the probability to detect flaring activity with a small number or short observations is quite low.

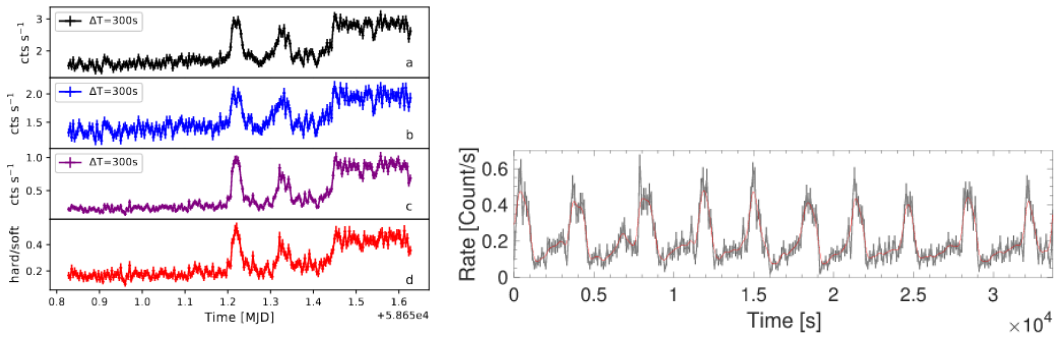

Figure 2.2: Left: Flares in the stacked EPIC-pn/MOS1/MOS2 light curve of NGC 4559 X7, in the energy band 0.3-10 keV (a), 0.3-2 keV (b), 2-10 keV (c). Panel d shows the hardness ratio. Image taken from Pintore et al. 2021. Right: *XMM-Newton* EPIC light curve of NGC 3621 4XMM J111816.0-324910, which show "heartbeats" variability. Image taken from Motta et al. 2020.

2.1.3 Flux dips

Some ULXs show dips in their light curve, caused by a drastic flux reduction (e.g. Stobbart et al. 2004, Pinto et al. 2021, Vasilopoulos et al. 2021, Hu et al. 2021, Alston et al. 2021, D'Aì et al. 2021). The duration of the dips varies in different sources: e.g. in NGC 55 ULX the dips duration is of ∼ 100–300 s (Stobbart et al. 2004), while in M51 ULX-7 the dips last ∼ 9 hours (Vasilopoulos et al. 2021, Hu et al. 2021). Also the amplitude of the flux reduction spans a large range of values: e.g. a reduction of 80–90% was observed in NGC 55 ULX; while 20–30% was found in the case of M51 ULX-7. Absorption dips have been observed in a number of Galactic X-ray binaries (e.g. Parmar et al. 1986, Díaz Trigo et al. 2009), more frequently in LMXBs, appearing at the same orbital phases and rarely are transient phenomena (e.g. Galloway et al. 2016), than in HMXBs where usually they are not periodic (e.g. Naik et al. 2011). They usually cause a reduction of the soft X-ray flux and induce a spectral hardening (e.g. D'Aì et al. 2014). Different causes may be at the origin of these dips features.

In the case of Roche-Lobe overflow fed systems, usually in the LMXBs, the dips could be caused by an obscuring effect from structures in the outer regions of the accretion disc (e.g. White and Swank 1982). The deformation of the disc in the outer regions may be caused by the interaction between the accretion flow and the external disc regions (e.g. White and Holt 1982). The dips in these systems are usually periodic and related to the orbital period of the binary system (e.g. White and Swank 1982).

In wind-fed systems, usually in the HMXBs, the dips can be explained with the eclipses caused by the extended atmosphere of the companion star. In fact, the companion star may be illuminated by the strong X-ray radiation, inducing the formation of a "shadow wind": if the emitted X-ray radiation is large, the gas on the portion of the surface of the companion star exposed to the X-rays will be highly photoionized, preventing the formation of a wind from that part of the star (Blondin 1994). The wind can escape from the other side of the stellar surface, producing a large column density at some directions and orbital phases. When the X-ray emission intercepts the regions with enhanced column density, it is shadowed by the dense material and flux dips are observed in the light curve.

Mechanisms similar to those described and usually observed in standard Galactic X-ray binaries, or maybe a combination of different processes, may cause the flux dips observed in the ULXs.

2.1.4 Eclipses

We define an X-ray eclipse as an obscuration of the compact object by the companion star, the latter being interposed between the telescope and the compact object along the line of sight. This implies

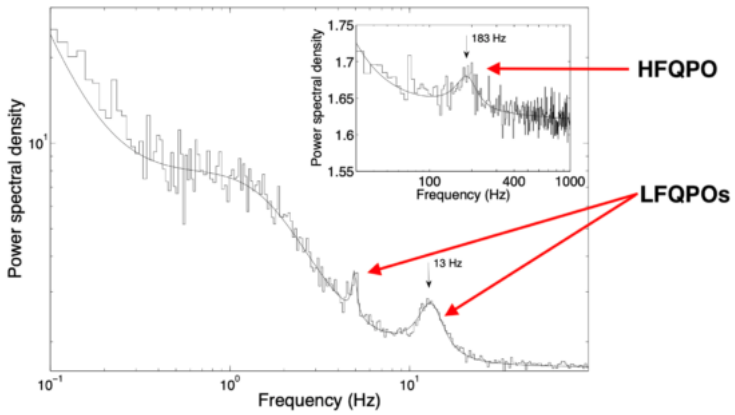

Figure 2.3: Examples of QPOs in the BH XTE J1550-564, from Motta et al. 2014.

an occurrence of one eclipse per orbital period. The effect is the same observed in flux dips: a drastic reduction of the X-ray flux in the X-ray light curve. Eclipses have been observed in some ULXs: CG X-1 (Qiu et al. 2019) and four ULXs in M51 (Urquhart and Soria 2016b, Wang et al. 2018). For three of the ULXs, the eclipses have been used to derive the orbital period: $P_{CGX-1} \sim$ 7.2 hr, $P_{M51ULX-1} \sim$ 6.3 d or 12.5-13 d, $P_{M51S2} \sim$ 52.75 hr (Qiu et al. 2019, Urquhart and Soria 2016b, Wang et al. 2018). An eclipse does not necessary induce a null flux emission. A residual X-ray emission may be detected during the eclipses: different mechanisms could cause the observed residual emission (e.g. Qiu et al. 2019). A possible scenario is that the observed emission originates in the collision between the wind of the stellar companion and the wind of the accretion disc, around the compact object. This picture requires a strong and fast wind both from the star and the disc wind, an assumption satisfied by the Wolf-Rayet ULX CG X-1. Another possibility is emission from the photosphere of the optically thick outflows launched by the super-Eddington accretor. The photons emitted from the outflow are scattered many times before propagating towards us and the last scattering surface radius results larger than the photosphere dimension (Qiu et al. 2019); otherwise the wind photosphere may extend on a scale comparable to, or larger than the companion star size and the emission comes directly from the external part of the outflow (Urquhart and Soria 2016b). Another possible explanation is that the X-ray radiation, emitted through the polar funnel, is down scattered by the wind into our line of sight at a distance larger then the dimension of the companion star (e.g. Qiu et al. 2019).

2.1.5 QPOs

Quasi periodic oscillations (QPOs) are features (peaks) observed in the power spectrum of the Galactic X-ray binaries (XRBs) light curves (see Ingram and Motta 2019 for a review; see fig.). They are classified in low frequency (LF) QPOs, for frequencies smaller than 30 Hz and high frequency (HF) QPOs, for frequencies higher than 60 Hz, in BH systems, while in NSs there are also additional QPO classes. HF QPOs in BHs are connected with the particles motion near the innermost stable circular orbit (ISCO; e.g. Morgan et al. 1997) and they are rare features. The LF QPOs are divided in 3 types, usually linked to the canonical spectral states observed in Galactic XRBs. The most common are type C QPOs, which appear in all the accretion states typical of X-ray binaries: low-hard, hard-intermediate, soft-intermediate and high-soft state (see e.g. Belloni 2010). They are narrow and have rms $\sim$ 20% and frequency between mHz and 30 Hz. Type B appear in the soft intermediate state and are narrow features with rms ~5% and frequency of 5–6 Hz. Type A are weak and broad features, appearing in the soft state with frequency 6–8 Hz.

QPOs have been observed in some ULXs (e.g. Mucciarelli et al. 2006, Strohmayer and Mushotzky 2009). The QPOs in ULXs were initially used to derive the mass of the accreting BH, assuming a

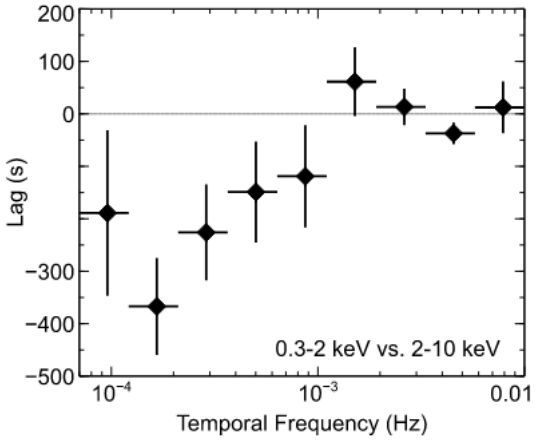

Figure 2.4: The soft time lag in NGC 1313 X-1. The image is taken from Kara et al. 2020.

different order of magnitude caused by larger BH masses with respect to the galactic BH binaries: for example Pasham et al. 2014 considered the QPOs they had discovered in M82 X-1 analogous to the HF QPOs of the XRBs and they used them to derive a mass for the accretor, which resulted of ~ 400 $M_{\odot}$. The PULX M82 X-2 also showed a QPO (Caballero-García et al. 2013) which was suggested to be a type-C QPO analogue, but considering that the ULX is a NS, the feature observed could be simply an analogue of the mHz QPOs of Galactic XRBs, or a different class of QPOs, possibly associated with super-Eddington accretion.

2.1.6 Time lags

Time lags are delays in the emission between different energy bands. The emission in different energy bands is associated with the spectral components of the ULXs, which may usually be modelled with two thermal components (e.g. Stobbart et al. 2006). The soft component models the emission from the outer disc or the wind photosphere and the hard component is instead emitted by the inner regions of the accretion disc (e.g. Middleton et al. 2011a). Time lags are a useful tool to study the casual connection between the two spectral components and may help to understand the emission mechanism in ULXs (e.g. Kara et al. 2020).

Some ULXs – NGC 5408 X-1, NGC 55 X-1, NGC 1313 X-1, NGC 7456 ULX-1 (Heil and Vaughan 2010, Pinto et al. 2017, Kara et al. 2020, Mondal et al. 2021b) – have shown a delay in the emission of the soft band with respect to the hard band, a soft or negative lag, at frequency $\sim$ 10 mHz, 0.1 mHZ, 0.1–0.5 mHz and 0.07 mHz respectively. Soft lags are thought to derive from the reprocessing of the hard photons, emitted from the inner accretion flow, through the optically thick base of the outflowing wind (e.g. Pinto et al. 2017, Pintore et al. 2021). In addition, NGC 5408 X-1 and NGC 4559 X-7 have also shown a low frequency hard lag at $\sim$0.1 mHz (Hernández-García et al. 2015, Pintore et al. 2021) of $\sim$ 1 ks and $\sim$ 300 s, respectively. NGC 4559 X-7 showed also a weak soft lag. The amplitudes of the soft lags observed in the ULXs are different e.g. $\sim$ 1000 s in NGC 55 X-1 (Pinto et al. 2017) and $\sim$ 5 s in NGC 5408 X-1 (De Marco et al. 2013). Given the different soft lag amplitudes observed, it is not clear if the origin is the same in all the sources. Kara et al. (2020) noted that the amplitudes of the soft lags observed in NGC 5408 X-1 and NGC 1313 X-1 are $\sim$ 5% of the average variability timescale of each source, while in NGC 55 X-1 the percentage is closed to but larger, $\sim$ 10–30%, than for the other sources. They proposed that the three sources time lags can have the same origin, but while for NGC 5408 X-1 and NGC 1313 X-1 they are mostly

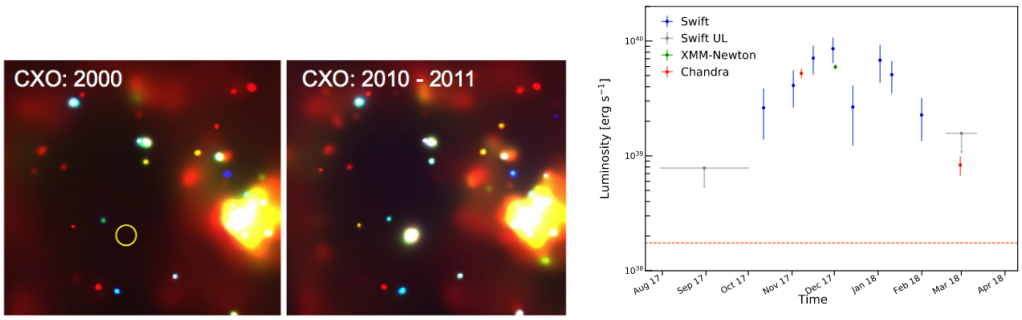

Figure 2.5: Left: *Chandra* image of the region of M83 where a transient ULX has been discovered. No emission was detected in the yellow region in the image taken in 2000, while a clear emission is visible in the image taken with 2010-2011 data. Image from Soria et al. 2012. Right: X-ray light curve of the transient ULX NGC 5907 ULX-2, taken from Pintore et al. 2018a.

produced by the hotter spectral component, suggesting that they are linked to the inner accretion flow, for NGC 55 X-1 both the colder and hotter components contribute. Pinto et al. (2017) attributed the variability observed in NGC 55 X-1 to fluctuations in the inner disc (hard component) and to the reprocessing of radiation through the wind (soft component) and proposed a different origin for long and short time lags, suggesting that the long ones are related to processes in the outer regions (e.g. interactions in/with the wind), while the short ones may be linked to processes in the inner regions of the accretion flow.

2.2 Long-term variability

Long-term variability (days to months timescales) is often observed in ULXs. Different patterns have been identified in the long-term light curves of ULXs, which may be linked to periodic or aperiodic variability. Studying the long-term variability of ULXs is useful to understand the physical mechanisms responsible for the observed emission, especially because some features might help to shed light on the nature of the compact object in the observed source. For example features indicating possible propeller phases can be used to individuate candidate NSs (e.g. Earnshaw et al. 2018, Song et al. 2020). In the following, the patterns observed in the long-term light curves of ULXs will be analysed in detail.

2.2.1 Transient behaviour

In the context of ULXs, a transient source is defined as an object with at least one detection and one non-detection in different observations. Examples of transient ULXs (see fig. 2.5) are CXOU 133705.1-295207 in M83 (Soria et al. 2012), NGC 5907 ULX-2 (Pintore et al. 2018a) or M51 ULX-7 (Terashima and Wilson 2004). While some transient ULXs remain bright for months or years after their first brightening (e.g. Soria et al. 2012), other objects have been detected in just a single observation (e.g. Isobe et al. 2008). Their outburst may originate from an unstable mass transfer from the companion star. A transient behaviour could also be caused by propeller phases, if the accretor is a strongly magnetised NS. The fact that the number of transient ULXs is increasing, makes the monitoring of galaxies very important in order to discover new ULXs, i.e. already known sources which had previously shown only sub-Eddington luminosity, or sources that have been never detected before, and suggests that the number of ULXs will further increase in the next years. Having the possibility of studying larger samples of sources, repeatedly observed, would be very useful to characterize the long-term properties of this class of still elusive objects, considering the fact that the transients are not detected in every observation.

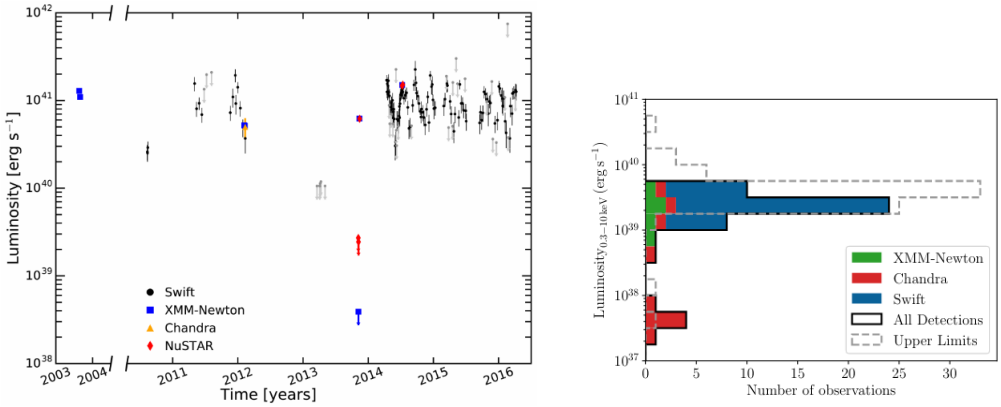

Figure 2.6: Left: Light curve of the PULX NGC 5907 showing its bimodal flux behaviour. From: Israel et al. 2017a. Right: Histrogram for the luminosity of M51 ULX-4, which shows a bimodal distribution. From: Earnshaw et al. 2018.

2.2.2 Bimodal flux distribution

A bimodal flux distribution is observed in the light-curves of some ULXs (e.g. Grebenev 2017, Tsygankov et al. 2016), in particular it is usually observed in the PULXs and can be explained in terms of the on set and switch off of the propeller mechanism. This means that two different flux states can be found in the light-curves: an *high state* in which the source has a large luminosity in the ultraluminous range and a *low state*, in which the source flux is reduced of orders of magnitudes (e.g. Earnshaw et al. 2018). In some cases, during the *low state*, the source luminosity goes under the detection threshold of the X-ray telescope that was observing the ULX; other times the source is observed with a luminosity under the ultraluminous threshold (1×10^{39} erg s^{-1}). A bimodal flux distribution is sometimes observed also in non-pulsating ULXs, such as M51 ULX-4, NGC 5194 ULX-4, NGC 628 ULX-1, rendering them candidate PULXs, for which pulsations have not been already discovered (Earnshaw et al. 2018, Song et al. 2020), if the two flux states are compatible with the propeller mechanism.

A transient behaviour and a bimodal flux distribution could indicate the same physics. In fact, a detection or a non-detection depends also on the quality of the observation. If the low state of a source is under the detection threshold of the instrument used to observe the ULX, the source would appear as a transient and the low state of the source would not be observed. Long high statistics observations of the sources are very useful in this case, to determine the low flux level of the X-ray emission and disentangle this degeneracy.

2.2.3 Long-term periodicities

Some ULXs show periodicities or quasi-periodicities in their long-term light curves (e.g. Foster et al. 2010). The detected periods are usually found on timescales from days to months. They could derive by an orbital or super-orbital modulation. In the former case we would see a flux modulation depending on the orbital period of the binary system. Often, the flux modulation observed in the long-term light curves of ULXs turn out to be longer than the orbital period of the binary system, suggesting a super-orbital origin (e.g. Brightman et al. 2020). A (super-)orbital periodicity can be confused with a flux bimodality, due to limited coverage in the observations, as happened for M82 X-2 (see Tsygankov et al. 2016, Brightman et al. 2019). Super-orbital modulations are also typical of PULXs (e.g. Walton et al. 2016, Israel et al. 2017a).

The origin of the super-orbital periodicity is still matter of study. Among the proposed explanations, there is the precession of a tilted and warped accretion disc (e.g. Motch et al. 2014, Hu et al. 2017) which would obscure different portions of the inner regions emission during its rotation. An-

other possibility is a Lense-Thirring precession (Bardeen and Petterson 1975). The Lense-Thirring effect is a vertical oscillation of particles, orbiting around a rotating body. This happens when the accretion disc is not in the equatorial plane of the rotating body. In this case, the orbital and the vertical frequencies of the orbiting particle are different and this inequality generates a torque which causes a precession of the accretion flow. In the scenario of super-critical accretion, the disc becomes geometrically thick inside the spherisation radius and can precess as a solid body, causing a super-orbital periodicity (e.g. Middleton et al. 2018). Middleton et al. (2019) proposed a possible method to obtain an indication of the compact object mass and spin, based on the precession timescale and on the temperature of the soft spectral component, by assuming that both the super-orbital periodicities and the mHz QPOs sometimes observed in ULXs are produced by a Lense-Thirring precession. The explanation of such (quasi-)periodicities with a precession of the accretion flow/disc is supported by the observations. The periodic flux modulation is often more evident in the hard band (e.g. Weng and Feng 2018), which would be covered in some phases of the precession cycle by the accretion structures, while the soft emission coming from the winds or the outer disc would remain more stable. Also the precession of the NS and of its magnetic dipole (Lipunov and Shakura 1980), in the case of PULX, is considered a possible cause of the super-orbital modulations observed (e.g. Fürst et al. 2017, Mushtukov et al. 2017), but this scenario would explain the periodicities of few months observed in PULXs, only in case of magnetar-like magnetic fields. Such large magnetic fields (B $\sim 10^{14}$–10^{15} G) have been proposed to explain the large X-ray emission in some PULX (e.g. Israel et al. 2017a, Brightman et al. 2018), while other authors have proposed weaker magnetic fields (e.g. King and Lasota 2016, B $\leqslant 10^{11}$ G; Kluzniak and Lasota 2015, B $\sim 10^{9}$ G).

2.2.4 Flaring activity and flux dips in the long-term light curves

Usually the long-term monitorings of ULXs are made with the *Swift* observatory, which allows us to perform regular monitorings, on a year baseline, with short exposures pointings of 1–2 ks. Should the duration of the flares be larger than or comparable to the typical observation exposure (e.g. in the cases presented in Pintore et al. 2021, Motta et al. 2020), or of shorter duration but with a very large increment in the flux, we could identify the flares as flux peaks (with respect to the average flux usually observed) in the long-term light curves. Also dips can be seen in the long-term light curves of ULXs, for example Grisé et al. (2013) discovered and studied dips in the *Swift*/XRT long-term light curve of NGC 5408 X-1.

2.3 Pulsations

It is now known that a fraction of ULXs contains NSs. In six sources, and possibly in another one (NGC 7793 ULX-4; Quintin et al. 2021), coherent pulsations have been detected (M82 X-2, NGC 7793 P13, NGC 5907 ULX-1, NGC 300 ULX-1, M51 ULX-7, NGC 1313 X-2; see Bachetti et al. 2014, Israel et al. 2017a,b, Fürst et al. 2016, Carpano et al. 2018, Rodríguez Castillo et al. 2019, Sathyaprakash et al. 2019) confirming that they contain a pulsating neutron star (NS) and they are indicated as PULXs (pulsar ULXs). See table 2.1 for their properties. In addition, the detection of a transient cyclotron line suggests the presence of a NS in another source (M51 ULX-8, Brightman et al. 2018). Considering the small number of ULXs having data with sufficient statistics to detect pulsations, about 20 sources at the time of writing (e.g. Earnshaw et al. 2019b, Song et al. 2020), NSs may constitute a large fraction among ULXs (e.g. Walton et al. 2018c, Pintore et al. 2017).

The first evidence for a pulsating super-Eddington accretor is the transient A0538-66, in the Large Magellanic Cloud. It is a pulsar with a spin period of $\sim$ 69 ms and a peak luminosity of $\sim 8{\times}10^{38}$ erg s^{-1}, below the empirical luminosity threshold typically used to define a ULX, but larger than the Eddington limit for a NS (Skinner et al. 1982).

There is also a claim for a galactic ultraluminous pulsating object, reaching a luminosity of $2{\times}10^{39}$ erg s^{-1} (Wilson-Hodge et al. 2018) and for a PULX in the Small Magellanic Cloud (Tsygankov et al. 2017).

The pulsation period of the PULX spans the range ~ 0.5–30 s and the pulsation profile is usually quasi-sinusoidal in shape. The pulsed fraction, i.e. the ratio between the semi-amplitude of the sinusoid and the average number of counts, has values of ~ 5–70% and usually increases with energy. Pulsations have not been detected in all the observations of the known PULXs, which suggests that other ULXs may be NSs, even if coherent pulsations have not been observed. The pulsation period is not constant in PULXs but it varies between the observations and also inside a single observation and its long term derivative is usually in the range $10^{-11} < \dot{P} < 10^{-7}$. The PULX periods, cannot therefore be detected with standard software, but it is necessary to include a correction for the derivative of the pulsation period and for the effects of the orbital motion (e.g. Israel et al. 2019, Rodriguez Castillo and Israel 2020). For example, the detection of pulsations in the PULX M51 ULX-7 used the software PASTA and SOPA, the former corrects for the spin period derivative, while the latter takes into account the orbital motion (Rodríguez Castillo et al. 2020). An automated search for periodicities in the X-ray band has been developed in the context of the EXTRAS project (De Luca et al. 2021), which focuses on the search for variability in the 3XMM-Newton catalog and brought to the discovery of pulsations in many X-ray sources including the ULXs NGC 5907 ULX-1 and NGC 7793 P13 (Israel et al. 2017a,b).

Some authors proposed possible explanations for the lack of pulsations. In order to see pulsations, the magnetospheric radius (R_M) should be only slightly smaller than the spherisation radius (King et al. 2017, Walton et al. 2018c). In this way the accreting matter reaches the magnetospheric radius with a super-Eddington rate and the thick inner disc has a narrow extension in radius. The consequence is a small contribution to the emission from the disc component and a stronger relative contribution from the accretion column, which favours the detection of the pulsed emission. Other authors suggested an alternative scenario (Mushtukov et al. 2017, Koliopanos et al. 2017); in this picture, the hot thermal component originates from a "curtain" just inside R_M, an envelope formed by the accreting matter, which follows the magnetic field lines, while the cool thermal component corresponds to the inner regions of the accretion disc, just outside R_M. The emission of the accreting column is reprocessed by the "curtain", which becomes closed and optically thick at high accretion rates, resulting in a multi-colour blackbody emission. Depending on the viewing angle and on the inclination of the "curtain", it is possible to detect pulsations, with a smoother profile than that usually observed in X-ray pulsars, due to the reprocession of the pulsed emission through the extended envelope. Walton et al. (2018c) noted that the scenario proposed by Mushtukov et al. (2017) cannot explain the emission of NGC 7793 P13 (Walton et al. 2018b), where the radius of the cooler spectral component is similar to the co-rotation radius (R_{co}). In fact, should the cooler spectral component correspond to R_M, the system would be in the situation $R_M \sim R_{co}$, which is the condition for the beginning of a propeller stage, with a consequent interruption of the accretion onto the NS.

PULXs show high flux variability on long timescales, which is typical of transient sources: their variability could reach several orders of magnitude. The bi-modal flux distribution, observed in the long-term light curves of some ULXs, and often present in the PULXs light curves, may be explained by the onset and the switch-off of the propeller stage, implying a strong magnetised NS accretor (see Grebenev 2017, Tsygankov et al. 2016). In addition, Mushtukov et al. (2017) suggested that the super-orbital period in NS systems could be linked to the precession of the neutron star caused by the interaction between the magnetic dipole and the accretion disc.

2.4 Spectral variability

In addition to the flux temporal variability, some ULXs also show variability in their spectral shape (see figure 2.7).

ULXs spectra in the energy band (0.3-10) keV are usually well modelled with two spectral components: a soft component plus a high energy tail (e.g. Gladstone et al. 2009). The broadband spectra of ULXs, with data above 10 keV, often require an additional third high energy component (e.g. Walton et al. 2018c), which models the hard emission of the inner accretion flow, originating from the accretion column for highly magnetised NSs (e.g. Brightman et al. 2016a, Walton et al. 2018b) or from a Comptonising corona for non-magnetic NSs or BHs (e.g. Reis and Miller 2013).

Src	P_{spin} s	P. frac. %	$\dot{P}$ ss^{-1}	P_{orb} d	P_{sup} d	L_{max} 10^{39} erg s^{-1}	ΔL_{max}
M82 X-2	1.4	$5\text{-}23^{n}$	-2×10^{-10}	2.5	60	18	~ 100
NGC7793 P13	0.4	$10\text{-}40^{x}$	$<5\times10^{-11}$	65	67/1500?	6	~ 100
NGC5907 ULX-1	1.1	$12\text{-}20^{x+n}$	-5×10^{-9}	5.3	78.1	220	>1800
NGC300 ULX-1	31	$37\text{-}70^{x+n}$	-5.6×10^{-7}	>300?	–	4.7	~ 50
M51ULX-7	2.8	$5\text{-}20^{x}$	$-1\text{-}5\times10^{-10}$	2	38.5	7.1	~ 80
NGC1313 X-2	1.5	$\sim 5^{x}$	$\sim 1.2\times10^{-10}$	2-6?	–	11	~10
NGC7793 ULX-4	2.5	$\sim 12^{x}$	$3\text{-}5\times10^{-8}$	–	–	3.4	> 1500

Table 2.1: Properties of the confirmed PULXs. Source name, spin period, pulsed fraction, spin period derivative, orbital period, super-orbital period, maximum luminosity observed in the X-ray band in units of 10^{39} erg s^{-1}, maximum variability factor in the luminosity, i.e. L_{max}/L_{min}. The pulsed fraction is energy dependent; we indicate if the interval indicated refers just to *XMM-Newton* band (x) or *NuSTAR* band (n) or both ($x + n$).
Ref. Bachetti et al. 2014, Brightman et al. 2019, Israel et al. 2017b, Fürst et al. 2016, 2018, Israel et al. 2017a, Belfiore et al. 2020, Carpano et al. 2018, Vasilopoulos et al. 2019, Rodríguez Castillo et al. 2020, Brightman et al. 2020, 2022, Vasilopoulos et al. 2020, 2021, Heida et al. 2019, Sathyaprakash et al. 2019, Zampieri et al. 2012, Robba et al. 2021, Quintin et al. 2021

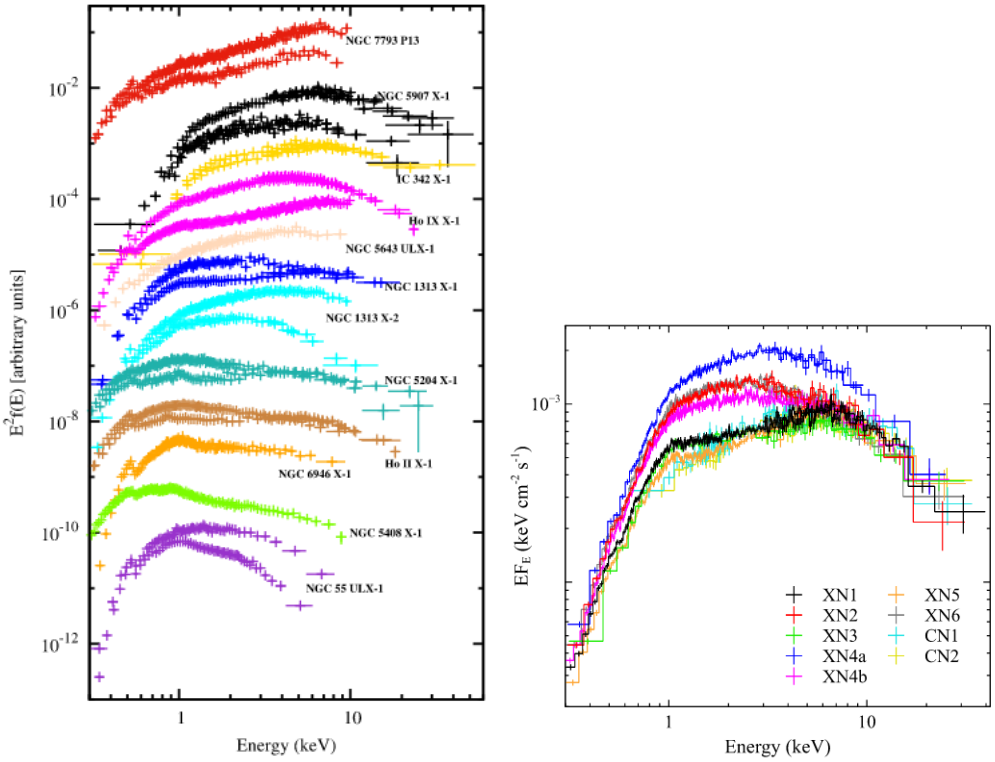

Figure 2.7: Left: Spectral variability seen in a sample of ULXs. Image taken from Pintore et al. 2017. Right: Different spectral shapes of NGC 1313 X-1, from Walton et al. 2020.

Spectral state transitions, between a low/hard and a high/soft state, have been observed for the first time in ULXs in IC 342 X-1 and X-2 (Kubota et al. 2001). Also NGC 1313 X-1 and X-2 have shown state transitions (Feng and Kaaret 2006): while NGC 1313 X-1 behaviour is similar to that observed in Galactic BH binaries (Feng and Kaaret 2006), considering the correlation between X-ray luminosity and power-law photon index, NGC 1313 X-2 has a opposite trend, showing a high/hard state.

Pintore et al. (2014) analysed a sample of ULXs, observed with *XMM-Newton*, modelling their spectra as a multicolor accretion disc plus a Comptonizing component, the latter resulting optically thick and cool. They suggested that the spectral variability observed on the hardness intensity diagram (HID) depends on the switch between accretion near and above the Eddington limit. They interpreted the observed trend with an increasing importance of a (soft) wind component linked to an increment in the accretion rate. Similar considerations have been previously presented in the work of Sutton et al. (2013), who explained the transitions between different spectral regimes, in terms of changes in the accretion rate, driving changes in the wind opening angle. In this framework, spectral variability and short-term flux variability may be linked: short-term variability may originate when a clumpy wind intersects our line of sight, as proposed by Middleton et al. (2011a).

Sutton et al. (2013) proposed an empirical method to classify the ULXs spectra in three regimes (*broadened disc, hard ultraluminous, soft ultraluminous*), based on the spectral parameters of a model composed of a multi-temperature blackbody disc and a power-law. The same source may change spectral regime among different observations.

Mondal et al. (2021a) studied spectral transitions in Circinus ULX-5, finding the source in three different spectral states, possibly linked to the source luminosity. Also for the source Holmberg IX X-1, a possible trend between the spectral evolution and the source luminosity has been found (Luangtip et al. 2016). Gúrpide et al. (2021a), studying the spectra of a sample of 17 ULXs, found that most of the softer sources – NGC 1313 X-1, NGC 55 ULX-1, IC 342 X-1 and Circinus ULX-5 – show three spectral states: one at high luminosity and the other two at similar low luminosities, but with different hardness ratios. They explained this finding in the context of a super-critical funnel: a source would result dim both at low mass transfer rates and when the gas in the funnel becomes optically thick obscuring the inner and bright regions of the accretion flow, which happens at high mass transfer rates. ULXs do not show the canonical spectral states observed in the galactic BH XRBs, among which they transit following an hysteresis cycle (e.g. Fender et al. 2004, Belloni 2010). Gúrpide et al. (2021b) discovered a spectral evolution cycle in the ULXs Holmberg II X-1 and NGC 5204 X-1, different from that of the galactic BH binaries. The two ULXs transit among the ULXs spectral regimes: hard, soft and supersoft, supporting the hypothesis that ULXs and ULSs are the same kind of system, but viewed at different inclinations.

2.5 Statistical methods to study ULXs variability

Different methods can be used to investigate variability and to quantify it. In the following paragraphs, the methods used in the data analysis, reported in the next chapters, are described.

2.5.1 Light curve deviation from a constant value

The first step to investigate variability is to look at the light curve, that is, the intensity of the source as a function of time and to verify if it is constant. One possibility is to calculate a χ^2 of the light curve count rates and the associated variability significance:

$$\chi^2 = \sum_{N=1}^{N_{obs}} \left(\frac{r_n - < r >}{\sigma_n} \right)^2 \tag{2.1}$$

where r_n is the count rate in the single observation, $< r >$ is the mean count rate and σ_n is the uncertainty on the count rate for each observation. The χ^2 statistics is not applicable in case of low counts statistics.

In such a case it is necessary to use the Cash statistics (Cash 1979):

$$C_{stat} = 2 \times \sum (counts_{exp} - counts_{obs} ln(counts_{exp})) \tag{2.2}$$

with $counts_{exp}$ = the counts expected in this case from a constant function equal to the average value of the light curve, while $counts_{obs}$ are the observed counts. The best fit is obtained in the case in which the expected counts are equal to the observed ones, so substituting $counts_{exp}$ with $counts_{obs}$ in equation 2.2, we obtain $C_{stat-best}$. The difference between C_{stat} and $C_{stat-best}$ distributes as a χ^2, with degrees of freedom equal to N_{obs} - 1. Evaluating the corresponding P_{value} it is possible to derive the corresponding significance of the variability for the analysed light curve.

2.5.2 Kolmogorov-Smirnov test

The Kolmogorov-Smirnov test compares the distribution of data with a reference distribution (one-sample test) or with another data sample (two-sample test). In this particular case, we compare the observed distribution of the arrival times of the photons with an equi-spaced distribution. This is a simple test to verify if a source is variable inside a single continuous observation. If the source flux is constant, the photons are expected to arrive on the detector at regular time intervals. This means that we can determine if a source is variable comparing the photons arrival times with a uniform distribution; if significant deviations from the uniform distribution are present the source may be considered variable.

2.5.3 Variability factors, normalised excess variance, fractional variability

The previously presented tests can be used to verify if a source has a significant variability in count rate, but do not give information about the amount of the variability. To quantify the variability it is possible to define a variability factor, i.e. the ratio between the highest and the lowest flux observed in the light curve. This is only a rough estimate of the variability, which does not take into account the uncertainties on the data. In order to account for the uncertainties, we can define the variability factor in a different way, as the ratio between the highest flux minus its error and the lowest flux plus its error. This method gives a more conservative estimation and permits to derive a lower limit on the maximum variability amplitude of the light curve. The derivation of a variability factor gives only information about the maximum variability amplitude observed, because it considers only two values: the lowest and the highest flux observed.

A good estimator for the variability, which takes into account all the detected points and their uncertainties, is the normalised excess variance, σ^2_{rms} (see e.g. Nandra et al. 1997), whose squared

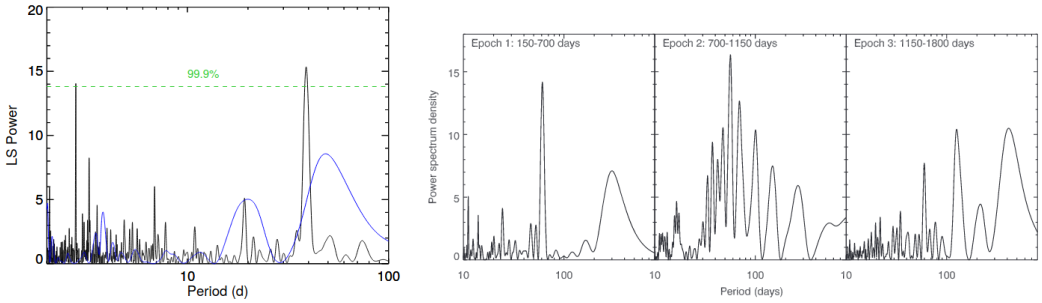

Figure 2.8: Examples of Lomb-Scargle periodograms. Power vs. period for the Lomb-Scargle periodogram of: Left: M51 ULX-7 (from Vasilopoulos et al. 2020); Right: M82 X-2 (from Brightman et al. 2019)

root is named fractional variability, F_{var} (see e.g. Vaughan et al. 2003, Edelson et al. 2002).

$$F_{var} = \frac{1}{\langle X \rangle} \sqrt{S^2 - \langle \sigma_{err}^2 \rangle}, \tag{2.3}$$

where $\langle X \rangle$ is the mean count rate, S^2 is the total variance of the count rate light curve, $\langle \sigma_{err}^2 \rangle$ is the mean error squared. The advantage of using F_{var}, instead of the normalised excess variance, is that it assumes values between 0 and 1 and can be expressed in percentage terms, which renders easy the comparison between different sources or epochs for the same source.

Allevato et al. (2013) studied the statistical properties of σ_{rms}^2 for processes in which red-noise is present, typical of accreting compact objects. When corrected for a bias, depending on the red-noise power spectral density slope and on the sampling pattern, σ_{rms}^2, or equivalently F_{var}, is a good estimator for deriving the amplitude of the variability of a light curve. They also found that, especially in case of sparse sampling, the estimates based on single light curves are highly uncertain, even if corrected for the bias, and they suggested to use an *ensemble estimate*. This approach is based on the evaluation of the estimator for many light curves of the same object, or of objects with the same variability properties. The obtained values are grouped in n bins and a mean is evaluated for each bin, here the formula given by Allevato et al. 2013, but adapted for F_{var}:

$$< F_{var} >= \sum_{i=1}^{n} \frac{F_{var,i}}{n}, \tag{2.4}$$

where $< F_{var} >$ is the mean F_{var}, $F_{var,i}$ is the fractional variability in the bin i, n is the number of bins. The mean of the distribution of $< F_{var} >$ is then the estimate for F_{var}.

2.5.4 Lomb-Scargle Periodogram

In order to look for periodicities in a light curve we have to derive the power spectral density (PSD) or power spectrum, which is defined as the modulus squared of the Fourier transform of the light curve. The Lomb-Scargle periodogram is an algorithm to derive the power spectrum in case of unevenly sampled light curves (Lomb 1976, Scargle 1982, VanderPlas 2018). If a high power peak appears in the periodogram, a periodicity is present in the analysed source. To asses the significance of the peak, we can compute the false alarm probability (FAP), which measures the probability that a peak with similar height is generated by a data set with no signal. So a large FAP value indicates that there is a large probability that the observed peak does not come from a periodic signal and that the peak in question has a very small significance. In general, the FAP assumes that only *white noise*, i.e. the spurious peaks are not correlated with frequency, is present. If there is *red noise*, i.e. noise with enhanced power toward low frequencies, which is often present in compact accreting objects (Vaughan et al. 2003), the FAP is not a good estimate for the peaks significance. In order to

assess the significance of the periodicity also when red noise is present, it is useful to run a Monte Carlo simulation. The basic idea is to simulate many light curves generated by a PSD affected by red noise, i.e. with a power-law shape with slope around 1–2 (e.g. An et al. 2016), but with similar characteristics to the observed light curve, i.e. same mean and sampling. For each simulated light curve the Lomb-Scargle method is applied and the obtained peaks are compared with the highest peak in the observed light curve: the significance of the peak is then based on the fraction of peaks with the same or higher significance in the simulations.

Chapter 3

Variability in ULXs: analysis of a sample of ULXs observed with Swift/XRT

Many efforts have been done in order to understand the variability properties of single sources (e.g. Heil and Vaughan 2010, Brightman et al. 2019, Gúrpide et al. 2021b, Robba et al. 2021, Walton et al. 2020, 2016, Pintore et al. 2015, Vasilopoulos et al. 2021, Pintore et al. 2021, 2016, Brightman et al. 2016a, 2020, Walton et al. 2013, Jithesh 2022, Hu et al. 2021, Motta et al. 2020, Urquhart et al. 2022, Ghosh et al. 2022), while a smaller number of studies exist on samples of sources (e.g. Heil et al. 2009, Crivellari et al. 2009, Sutton et al. 2013, Pintore et al. 2014, Earnshaw et al. 2018, Song et al. 2020, Bernadich et al. 2021, Dage et al. 2019, 2020, Gúrpide et al. 2021a). The analysis of the properties of ULXs samples is not an easy task. First of all, the ideal way to describe the common properties of a population of sources, would be the analysis of uniform data sets, with comparable quality and sampling properties. ULXs, besides often having exposures with different data quality – both considering the same source or comparing different objects – have also data often taken with different observation strategies. For example, observations taken with a telescope with large effective area, e.g. *XMM-Newton*, or a very good angular resolution, e.g. *Chandra*, are usually single exposures of long duration, suitable for spectral studies or for flux variability studies on short timescales, but not for analysing the long-term behaviour of the sources. On the other hand, the *Swift* observatory usually allows us to obtain long-term monitoring, with short exposures of typically 1–2 ks. These data are particularly useful to study the long-term behaviour of ULXs, but on the other hand do not allow us to analyse in detail the behaviour of a source inside a single exposure. In addition, while studying the variability properties of a source, the sampling pattern should be considered. The uniformity in the data sampling is very important: in particular with a uniform sampling it is easier to search for periodicities, which may be missed in highly sparse data samples. Also the aperiodic variability is influenced by the sampling pattern: different datasets may be sensible to different timescales, so the ideal way to compare datasets is to have sampling patterns as similar as possible.

Some ULXs studies which analyse samples of sources have been published in the literature. For example, the works of Gladstone and Roberts (2009) and Pintore et al. (2014, 2017) analysed the spectral properties in ULXs samples, in order to derive a common spectral description for the ULX population. Heil et al. (2009) worked on a sample of sources with the aim of deriving information about their short-term flux variability. Sutton et al. (2013) analysed a sample of ULXs and tried to give a uniform framework of their spectral and timing properties. Earnshaw et al. (2018) and Song et al. (2020) identified candidates propeller phases in ULXs data.

ULXs still remain elusive sources: studying their variability is an important tool to unveil the details of the accretion processes in act in these systems. Many aspects concerning the variability in

ULXs are still matter of study. Even if a trend between the variability on minutes to hours time-scales and the spectral regime of the source has been identified, i.e. the soft sources appear to be the most variable (Sutton et al. 2013), not all the sources in the soft ultraluminous regime present this kind of variability. In addition, short-term variability studies and the search for QPOs are often limited in ULXs by the low count rates (e.g. Urquhart et al. 2022). Also the long-term variability properties of ULXs are not well understood. Different hypothesis have been made about the origin of the long-term (super-)orbital periodicities observed in some ULXs, which are still matter of study. In addition, the sparse coverage, often present in the ULXs observations, may bring to miss a super-orbital modulation or to confuse it with a bimodality (see e.g. Tsygankov et al. 2016, Brightman et al. 2019). As a consequence it is not clear how many ULXs effectively have a super-orbital modulation of their flux, or if these modulations may have timescales different from the months timescales found so far. The long-term aperiodic variability is often observed in individual sources, but a systematic study of its properties in samples of ULXs is still lacking. Therefore, the aim of this project is to enlarge the physical description of the ULX population through the study of their long-term variability properties. For this reason, we have undertaken monitoring campaigns of a sample of ULXs with the *Swift* satellite. *Swift* is particularly suitable for such studies because it allows to perform weekly visits for a long time (e.g. for a year). Long-term studies of the ULXs have been published for a few bright sources of the ULX population (e.g. Kaaret and Feng 2009, Grisé et al. 2010, 2013, La Parola et al. 2015, Brightman et al. 2020). In addition, the number of known ULXs is increasing, also thanks to the *Swift*/XRT monitorings: the recent catalogue of Walton et al. (2022), which considers data taken with *Swift*, *XMM-Newton* and *Chandra* observatories, contains 1843 ULX candidates.

This chapter is organized as follows: we briefly introduce the X-ray satellites used to take the data analysed in this thesis. We describe the sample of sources monitored with the *Swift* observatory and present the data reduction and analysis in detail. The results obtained are then reported, followed by their discussion. We also include information on the additional analysis of the ULXs in NGC 925, which presented the most interesting results among the sample analysed and are the subject of a paper published in MNRAS (Salvaggio et al. 2022).

3.1 X-ray instrumentation

X-rays cannot be collected with telescopes on the Earth surface. Indeed, X-rays are absorbed by the Earth atmosphere and telescopes on board of satellites are needed to study X-ray sources.

X-rays represent a very energetic emission in the electromagnetic spectrum: they have a frequency in the band 10^{17} Hz $< \nu < 10^{19}$ Hz, higher than the frequency of the ultraviolet emission, but smaller than the frequency of the gamma rays. Because of the high frequency, X-ray radiation cannot be detected with normal incidence telescopes: the radiation would penetrate through the telescope mirrors, which would be unable to reflect the incoming photons onto the focal plane. X-ray radiation is detected thanks to the grazing incidence (incidence angles smaller than 2^o) onto mirrors made with dense materials: the mirror surface is quasi-parallel to the incoming radiation, thus the latter is not absorbed but reflected.

The most used configuration is *Wolter I* (Wolter 1952). In this configuration, the mirror is composed of a parabolic and an hyperbolic sections: the incoming photons will be reflected twice before reaching the focal plane, where the detectors are located. In order to increase the effective area and consequently the capability to collect more of the incoming X-ray photons, many nested mirrors are usually put in the telescope assembly.

3.1.1 The Neil Gehrels Swift Observatory

The *Swift* satellite[1][2][3] (Gehrels et al. 2004) was launched in November 2004, with the main mission of studying the Gamma Ray Bursts (GRBs). *Swift* hosts three scientific instruments: BAT (Burst Alert Telescope), XRT (X-Ray Telescope) and UVOT (Ultraviolet and Optical Telescope).

1. The XRT (Burrows et al. 2005) is an X-ray telescope working in 0.2–10 keV, with a focal lenght of 3.5 m and the mirrors configuration is Wolter I. The X-ray telescope has an effective area of 110 cm^2, a field of view (FOV) of 23.6 $arcmin^2$ and a Point Spread Function (PSF) of 18 arcsec at 1.5 keV (the PSF indicated is expressed in terms of half power diameter: the diameter of the circle containing half of the counts of the received radiation). The energetic resolution of the XRT (at launch) is 140 eV and the time resolution is 1.8 ms in WT mode, i.e. windowed-timing, with 1-dimensional spatial information, and 2.5 s in PC mode, i.e. photon counting, in two dimensions. The detectors are front-illuminated CCD detectors, with the same MOS design of the *XMM-Newton* EPIC MOS cameras (more details in section 3.1.2), and one pixel covers 2.36 arcsec on the field of view.

2. The UVOT (Roming et al. 2005) is an optical and UV telescope working in the energy band 170–650 nm with a micro-channel plate intensified CCD detector. The mirrors configuration is Ritchey-Chretien (two hyperbolic mirrors) with a third mirror inclined at 45°, which reflects the radiation towards the filter wheel containing a set of optical and UV filters. The telescope PSF is 0.9 arcsec FWHM and the field of view size is 17 arcmin.

3. The BAT (Barthelmy et al. 2005) is the instrument used to detect the GRBs and it is able to determine their initial position with an accuracy of 3 arcmin, in 20 s. It has a sensibility in the energy range 15–150 keV, an energetic resolution of 7 keV and a field of view of 2 steradians. When a GRB event has been detected, *Swift* autonomously slews to collect the soft X-rays and optical counterparts of the event.

In this work, we have used the data taken with the *Swift*/XRT instrument. In addition, to complete our analysis, we exploited the *XMM-Newton*, *Chandra* and *NuSTAR* archives. In the next section we describe the main features of the instruments used.

3.1.2 Other X-ray instruments

XMM-Newton:
The X-ray Multi-Mirror Mission[4], *XMM-Newton* (Jansen et al. 2001), is the bigger scientific X-ray satellite ever launched by the European Space Agency (ESA). It is as heavy as about 4 tons and 10 m long. *XMM-Newton* hosts three X-ray telescopes, each of them with focal lenght 7.5 m and composed of an assembly of 58 nested mirrors, in Wolter I configuration, which work by using the grazing incidence. The mirrors are made of gold and nickel.

The effective area of the *XMM-Newton* X-ray telescopes is maximum at 1.5 keV, with 1900 cm^2, while 1500 cm^2 are found at 2 keV and 900 and 350 cm^2 respectively at 7 and 10 keV; the spatial resolution (in the center of the field of view) is $5''$ in FWHM (or $15''$ in HPD) and the FOV is of $30'$ in diameter.

Here we use data taken with the European Photon Imaging Camera (EPIC). It is an instrument which comprises three cameras based on CCDs arrays: one of them is based on pn CCDs, with electrodes on both surfaces of the device, while the other two are MOS (Metal-Oxide-Semiconductor) CCD cameras. CCDs are solid state sensors, made with doped semi-conductors, able to convert the incoming photons into charged particles, whose number is proportional to the energy of the incoming photons. Potential wells collect the charged particles, in a depletion region free of majority charge

[1] https://swift.gsfc.nasa.gov/
[2] http://www.swift.ac.uk
[3] https://swift.asdc.asi.it/
[4] https://www.cosmos.esa.int/web/xmm-newton/technical-details

carriers. As a consequence, the excess charge is produced by the incoming radiation, which can be determined through the read-out register. MOS CCDs are composed of a thin oxide layer with electrodes (*gates*) above it, a silicon layer n-doped and a silicon substrate p-doped; they are sensible to energies between 0.2 and 10 keV. In the pn CCDs, which are backside illuminated three phases devices, there is a silicon substrate n-doped and the MOS gates are substituted by a pn junction. Thanks to the presence of electrodes on both the device surfaces a fully depleted region can be obtained in the pn CCDs and the sensibility is in the energy band 0.2-15 keV, larger than that of the MOS case.

Between the MOS detectors and the telescopes there are the Reflecting Gratings Spectrometers (RGS), so part of the radiation is deflected towards their detectors and only about 44% of the radiation reaches the MOS. The pn camera receives instead all the incoming flux. The nominal energy interval for the EPIC cameras is 0.15 – 15 keV.

On board *XMM-Newton* there is also an optical telescope, but we did not use its data for this thesis.

Chandra:
Chandra[5] (Weisskopf et al. 2000) is a satellite hosting an X-ray telescope composed of four couples of nested mirrors, each of them composed by an hyperbolic and a parabolic section, coated with iridium. The scientific instruments on board *Chandra* are an Advanced CCD Imaging Spectrometer (ACIS) and an High Resolution Camera (HRC), both in the focal plane and a Low Energy Transmission Grating Spectrometer (LETG) and a High Energy Transmission Grating Spectrometer (HETG), which are spectrometers. ACIS and HRC give information about the number, position, energy and arrival time of the X-ray photons and work nominally in the energy band 0.2-10 keV e 0.1-10 keV, respectively.

In this work we used data taken with ACIS, which has a very good angular resolution of $0.5''$ (HPD), better than any other X-ray satellite. ACIS-I is composed of 4 front illuminated CCDs, while ACIS-S is composed of 4 front illuminated and 2 back illuminated CCDs. The two ACIS instruments have respectively a field of view of $16'\times16'$ and $8'\times48'$.

NuSTAR:
NuSTAR[6] (Harrison et al. 2013) is a satellite working with the hard X-rays: it is sensible to 3 – 79 keV. It hosts two X-ray telescopes with 133 nested mirrors in a conic approximation of the Wolter I configuration. It has two detector units, each of them composed of four Cadmium-Zinc-Telluride detectors, able to convert high-energy photons into electrons. The energy resolution of the detectors is 0.4 keV. *NuSTAR* has an angular resolution of $43''$ HPD and its FOV is $13'\times13'$.

We have used the *NuSTAR* observations of NGC 925 to better characterize the ULXs spectra at high energies.

3.2 Swift/XRT monitoring campaigns: sample description

In order to obtain a sample of ULXs suitable for temporal variability studies, aimed at collecting information about the variability on timescales from days to months, and to search for new transients, our research group proposed the monitoring of a sample of nearby spiral galaxies, with the *Swift* satellite. The monitored galaxies have a distance < 15 Mpc and contain at least one known ULX. The selection criteria were the following: the galaxies had to contain at least one known ULX and they had to be only poorly monitored before our observation request. The limit on distance was chosen to guarantee the detection of known sources, at least when they are ultraluminous (L_x above 10^{39} erg s^{-1}), with observations of 1–2 ks exposure, which allowed us also to be sensible to new transients in the ultraluminous range.

The monitoring campaign began in 2019 and included the observations of seven galaxies with a two weeks cadence. This cadence allowed us to monitor the galaxies over an entire year and therefore to investigate the variability from weeks to months timescales. On the other hand, features on days

[5]http://chandra.harvard.edu
[6]https://www.nustar.caltech.edu

Galaxy	RA	Dec	Dist.(Mpc)	n.ULX	logd25	log(r_{maj}/r_{min})	area
Circinus	14:13:09.9	−65:20:20.8	4.2	6	1.94±0.02	0.31±0.04	0.016
M101	14:03:12.6	+54:20:56.7	7.0	6	2.38±0.02	0.02±0.03	0.189
NGC3486	11:00:24.1	+28:58:30.1	12.6	1	1.76±0.02	0.15±0.04	0.013
NGC3623	11:18:55.9	+13:05:32.5	13.3	1	1.88±0.03	0.59±0.05	0.019
NGC3627	11:20:15.0	+12:59:30.0	8.4	2	2.01± 0.03	0.35±0.04	0.022
NGC4945	13:05:27.3	−49:28:04.3	3.6	4	2.37±0.01	0.76±0.04	0.044
NGC5236	13:37:00.9	−29:51:56.1	4.7	4	2.13±0.02	0.01±0.03	0.028
NGC925	02:27:20.2	+33:34:12.8	8.9	3	2.03±0.02	0.27±0.03	0.028
NGC5055	13:15:41.4	+42:02:25.7	9.0	3	2.07±0.02	0.22±0.04	0.038
NGC4517	12:32:42.7	+00:06:54.9	8.6	1	1.96±0.02	0.80±0.02	0.006

Table 3.1: Sample of the observed galaxies. The coordinates (J2000) of the galaxies, logd25 (log of the apparent diameter in units of log(0.1arcmin)) and log(r_{maj}/r_{min}) (r_{maj} and r_{min} are the major and minor axis) are taken from HyperLeda (http://leda.univ-lyon1.fr/). The references for the distances are reported in the text. We indicate the number of the ULXs in each galaxy, including both the confirmed and the candidate ULXs. The galaxy area (in deg^2) is derived from the d25, except for M101, which is not completely included in the *Swift*/XRT image, does we used the area visible in the field of view.

timescales may be lost with such a cadence. In the following year, 2020, the monitoring of three of the galaxies, i.e. the ones containing the most variable and luminous ULXs, was extended: we asked for a denser sampling, with weekly cadence, to investigate variability on a smaller timescale and sometimes we asked for additional intra-week observations. In 2021, we extended the original sample monitoring other three galaxies: the final sample analysed comprises 10 galaxies, in which we detect 25 ULXs; some more ULXs are contained in the analysed galaxies but they are not detected or spatially resolved in these data. The tables containing the observations details are reported in the appendix (see appendix A). The main characteristics of each galaxy are reported in table 3.1. The coordinates of the ULXs detected in the *Swift*/XRT data are indicated in table 3.2, where we also indicate *Chandra* coordinates from the literature, when possible. The *Swift*/XRT observations are in PC mode.

We evaluated the number of background AGN expected at the fluxes considered in our analysis. The number of the extragalactic sources expected in a square degree was derived by the LogN-LogS relation given in Moretti et al. (2003), which corresponds to ~ 0.8 contaminants in the field of view of the sum of the areas of the observed galaxies.

Circinus galaxy

At a distance of 4.21 Mpc (Tully et al. 2013), Circinus galaxy is a spiral Sb galaxy and contains six ULXs (Bauer et al. 2001, Liu and Mirabel 2005, Winter et al. 2006, Ptak et al. 2006, Swartz et al. 2004, Walton et al. 2013). Four of them are near the nuclear region and cannot be resolved from the nucleus in *Swift*/XRT images and another one is a candidate ULX (indicated as 6ULX in this thesis), which is usually around and sometimes above 10^{39} erg s^{-1} in our *Swift*/XRT monitoring. Thus here we analyse just the two ULXs further from the nuclear region, i.e. 4ULX (ULX5 in the literature; Walton et al. 2013) and 6ULX (see table 3.2 for their coordinates).

M101

This galaxy is a face-on barred SABc spiral galaxy at a distance of 6.95 Mpc (Tully et al. 2013) and contains many point-like X-ray sources. Five of them have been classified as ULX (Pence et al. 2001, Colbert and Ptak 2002, Liu and Mirabel 2005, Liu and Bregman 2005, Heida et al. 2014); one of them (indicated as 24ULX in this thesis) was previously classified as an X-ray source, in particular a HMXB (Mineo et al. 2012), but reached ULX luminosities in our analysis in the *Swift*/XRT data.

Galaxy	name	RA Dec$_{Swift}$		RA Dec$_{Chandra}$		Ref.
Circinus galaxy						
	4ULX	14:12:39.0	−65:23:32.2	14:12:39.1	−65:23:32.7	(4)
	6ULX	14:12:53.6	−65:22:54.7	14:12:53.5	−65:22:54.7	(1)
	ULX1;CG X-1			14:13:12.3	−65:20:13.0	(2)
	ULX2;CG X-2			14:13:10.0	−65:20:44.0	(2)
	ULX3			14:13:10.3	−65:20:17.0	(2)
	ULX4			14:13:10.4	−65:20:22.0	(2)
M101						
	2ULX	14:02:48.2	+54:13:51.7	14:02:48.2	54:13:50.7	(3)
	16ULX	14:02:29.7	+54:21:18.1	14:02:29.9	+54:21:18.7	(4)
	24ULX	14:03:04.0	+54:27:35.9	14:03:03.9	+54:27:35.1	(5)
	27ULX	14:04:14.3	+54:26:03.6	14:04:14.2	54:26:04.5	(4)
	28ULX	14:03:32.4	+54:21:03.0	14:03:32.4	+54:21:02.8	(4)
	29ULX	14:03:14.3	+54:18:06.0	14:03:14.3	+54:18:06.2	(4)
NGC3486						
	ULX1			11:00:22.4	+28:58:18	(10)*
NGC3623						
	18ULX	11:18:58.5	+13:05:30.9	11:18:58.5	+13:05:31.0	(4)
NGC3627						
	5ULX	11:20:20.8	+12:58:46.0	11:20:20.9	+12:58:46.6	(4)
	23ULX	11:20:18.2	+12:58:58.9	11:20:18.3	12:59:00.3	(6)
NGC4945						
	4ULX	13:05:20.8	−49:28:23.1	13:05:21.9	−49:28:26.6	(1)
	6ULX	13:05:32.8	−49:27:34.1	13:05:32.9	−49:27:34.1	(1)
	Suzaku_J1305-4931			13:05:05.5	−49:31:39.0	(7)**
	41ULX***	13:04:56.1	−49:31:58.2			
NGC5236						
	58ULX	13:37:19.7	−29:53:48.9	13:37:19.8	−29:53:48.7	(4)
	79ULX	13:37:04.9	−29:52:07.6	13:37:05.1	−29:52:07.2	(8)
	9ULX	13:36:59.3	−29:49:59.5	13:36:59.5	−29:49:59.1	(4)
	82ULX	13:37:04.4	−29:51:23.0	13:37:04.4	−29:51:21.6	(4)
NGC925						
	ULX-1	02:27:27.5	+33:34:42.8	02:27:27.5	+33:34:43.0	(9)
	ULX-2	02:27:21.4	+33:34:59.1	02:27:21.5	+33:35:00.7	(9)
	ULX-3	02:27:20.1	+33:34:12.5			
NGC5055						
	ULX-1	13:15:19.5	+42:03:03.1	13:15:19.6	+42:03:02.3	(1)
	ULX-2	13:15:39.9	+42:01:51.8	13:15:39.3	+42:01:53.4	(1)
	ULX-3	13:16:01.9	+42:01:52.0	13:16:02.3	+42:01:53.6	(1)
NGC4517						
	ULX-1	12:32:42.8	+00:06:53.4			

Table 3.2: Sample of the studied ULXs; when a source was not detected in our analysis of *Swift*/XRT data, we reported the name from the literature. The reported coordinates come from the source detection onto the stacked *Swift*/XRT image. We indicate also the *Chandra* coordinates from the literature when possible. In the last column we indicate the reference for the *Chandra* coordinates. (1) Swartz et al. 2004; (2) Liu and Mirabel 2005; (3) Heida et al. 2014; (4) Chandra Source Catalog 2.0; (5) Mineo et al. 2012; (6) Swartz et al. 2009; (7) Isobe et al. 2008, ** the reported coordinates are from *Suzaku*; (8) Soria et al. 2012; (9) Swartz et al. 2011; (10) Foschini et al. 2002, * the reported coordinates are from *XMM-Newton*; *** see section 3.4.3

NGC 3486
It is a barred Sc spiral galaxy at a distance of 12.60 Mpc (Tully et al. 2016), containing one known ULX (Foschini et al. 2002). In our *Swift*/XRT monitoring the ULX was not detected. When we asked the observations we had used a slightly smaller distance for this galaxy. Thus the detection threshold in an average exposure of 1.5 ks was underestimated. The sensibility in the *Swift*/XRT observations, for a 3σ detection, corresponds to a luminosity of $\sim 5{\times}10^{39}$ erg s^{-1}.

NGC 3623
With a distance of 13.30 Mpc (Tully et al. 2016), NGC 3623 is the more distant galaxy in the sample. It is an Sa barred spiral galaxy, which hosts one known ULX (Liu and Bregman 2005).

NGC 3627
It is a barred Sb spiral galaxy, at a distance of 8.39 Mpc (Tully et al. 2016). Two ULXs are included in the D25, i.e. the apparent diameter of a galaxy, of NGC 3627 (Liu and Bregman 2005, Swartz et al. 2009).

NGC 4945
This barred spiral SBc edge-on galaxy has a distance of 3.55 Mpc (Tully et al. 2009). It contains three known ULXs, two of them are persistent (J130521.94-492826.6, J130532.89-492734.1; Swartz et al. 2004), while the third is a transient object, discovered with *Suzaku* (Suzaku J1305-4931; Isobe et al. 2008) and never detected in subsequent observations. In addition, a fourth object switched on and reached a ULX luminosity during the *Swift*/XRT monitoring analysed in this work (see section 3.4.3).

NGC 5236
NGC 5236, or M83, at a distance of 4.66 Mpc (Tully et al. 2013), is a barred Sc spiral galaxy with two known ULXs (Colbert and Ptak 2002, Soria et al. 2012) and one of them is a transient source. In addition, two sources, previously classified as X-ray sources (Berghea et al. 2008), sometimes exceed 10^{39} erg s^{-1} in the *Swift*/XRT data in our analysis.

NGC 925
It is a barred Scd spiral galaxy, at a distance of 8.9 Mpc (Tully et al. 2013) and hosts three ULXs. NGC 925 ULX-1 and ULX-2 (Swartz et al. 2011, Pintore et al. 2018b) are persistent sources, while ULX-3 (Earnshaw et al. 2020) is a transient object.

NGC 5055
This galaxy is a spiral, Sbc, at a distance of 9.04 Mpc (Tully et al. 2013) containing three ULXs (Roberts and Warwick 2000, Swartz et al. 2004).

NGC 4517
It is an egde-on Sc spiral galaxy, at a distance of 8.58 Mpc (Tully et al. 2013). The galaxy hosts one ULX (Swartz et al. 2011) and before our monitoring had never been observed with the *Swift* observatory.

3.2.1 *Swift*/XRT data reduction

We reduced data with standard procedures, running XRTPIPELINE[7], version 0.13.4 (release date: 2017-03-15). To detect the X-ray sources in each exposure, we ran XIMAGE[8], with a detection threshold of 3 sigma. We constructed a catalog of the known X-ray sources, for each galaxy in our sample,

[7]https://heasarc.gsfc.nasa.gov/ftools/caldb/help/xrtpipeline.html
[8]https://heasarc.gsfc.nasa.gov/docs/xanadu/ximage/ximage.html

consulting the literature and the astronomical databases Simbad[9] and NED[10] and compared the detected sources with the resulting catalog.

In addition, we constructed a stacked image with the *Swift*/XRT data of each galaxy. We report these images, with the regions corresponding to the ULXs super-imposed in figure 3.1. We also super-impose the optical contours of each galaxy from DSS. The ULX in the galaxy NGC 3486 is visible in the stacked image, even if it was not detected in the individual observations. We used all the available *Swift*/XRT exposures to construct the image, given the small number of counts in the observations. We also derived an average luminosity for NGC 3486 1ULX from the stacked exposures taken in 2019-2020, obtaining a value of $(3.7\pm0.6)\times10^{39}$ erg s^{-1}.

The spectra and light curves were extracted using 20″ regions, while the background was extracted from circular regions of 50″ radius, where no sources were present, but including part of the host galaxy to consider its contribution to the detected emission.

Light curves: The light curves of both sources and background, in each *Swift*/XRT observation, have been extracted using XSELECT (version 2.4) and have been corrected using XRTLCCORR, which takes into account the telescope vignetting, losses due to the point spread function (PSF) and to bad pixels/columns in the extraction region. We obtained a background subtracted light curve, using LCMATH, for each source in each observation. We used the light curves from the single observations to construct the light curve with all the analysed *Swift*/XRT exposures, for each ULX, using LCURVE from the XRONOS package for timing analysis version 5.22. We binned the light curves in 6 days bins, to have a common baseline for every ULXs while studying the variability. This ensures to include in the same bin additional intra-week observations, occasionally available for some ULXs, and to study the variability down to days timescales also in the first year of observations, when some additional exposures, with respect to our observations every two weeks, have been done, especially for Circinus galaxy.

Spectra: The *Swift*/XRT spectra of each source in each observation have been extracted using XSELECT. The exposure maps have been obtained with XRTEXPOMAP version 0.3.1 and the ancillary response files (ARFs) with XRTMKARF version 0.6.3. The Redistribution Matrix File (RMF) used (swxpc0to12s6_20130101v014.rmf) was downloaded from the more recent CALDB release[11]. Due to the low statistics in the individual short-exposure *Swift*/XRT observations, we have not grouped the single spectra to apply a spectral fit. We just assumed a spectral model to derive a flux from each *Swift*/XRT spectrum. See section 3.3.2 for more details.

3.2.2 *XMM-Newton* data reduction

We reduced archival *XMM-Newton* EPIC data data using the software SAS v.17.0.0. For the pn, we selected single pixel and double pixel events (PATTERN ≤ 4), for the MOS single and multiple pixel events (PATTERN ≤ 12). We cleaned the data removing high particle background time intervals, in which the count rate was > 1 cts s^{-1}, at energies > 10 keV. We extracted the spectra from circular regions of 20, 30 or 35″ radius, depending on the specific source, e.g. a smaller radius was chosen to avoid contamination between the sources in crowded field, a larger radius to include the emission of the most luminous or off-axis sources. The background was extracted from circular regions free of sources, in the same CCD quadrant and close to each source, with a radius of 50 or 60″. We grouped the spectra in 20 (or 25, depending on the source statistics) counts per bin. For the spectral analysis we used XSPEC version 12.10.1 (Arnaud 1996).

[9]http://simbad.u-strasbg.fr/simbad/

[10]https://ned.ipac.caltech.edu/

[11]https://www.swift.ac.uk/analysis/xrt/files/SWIFT-XRT-CALDB-09_v19.pdf

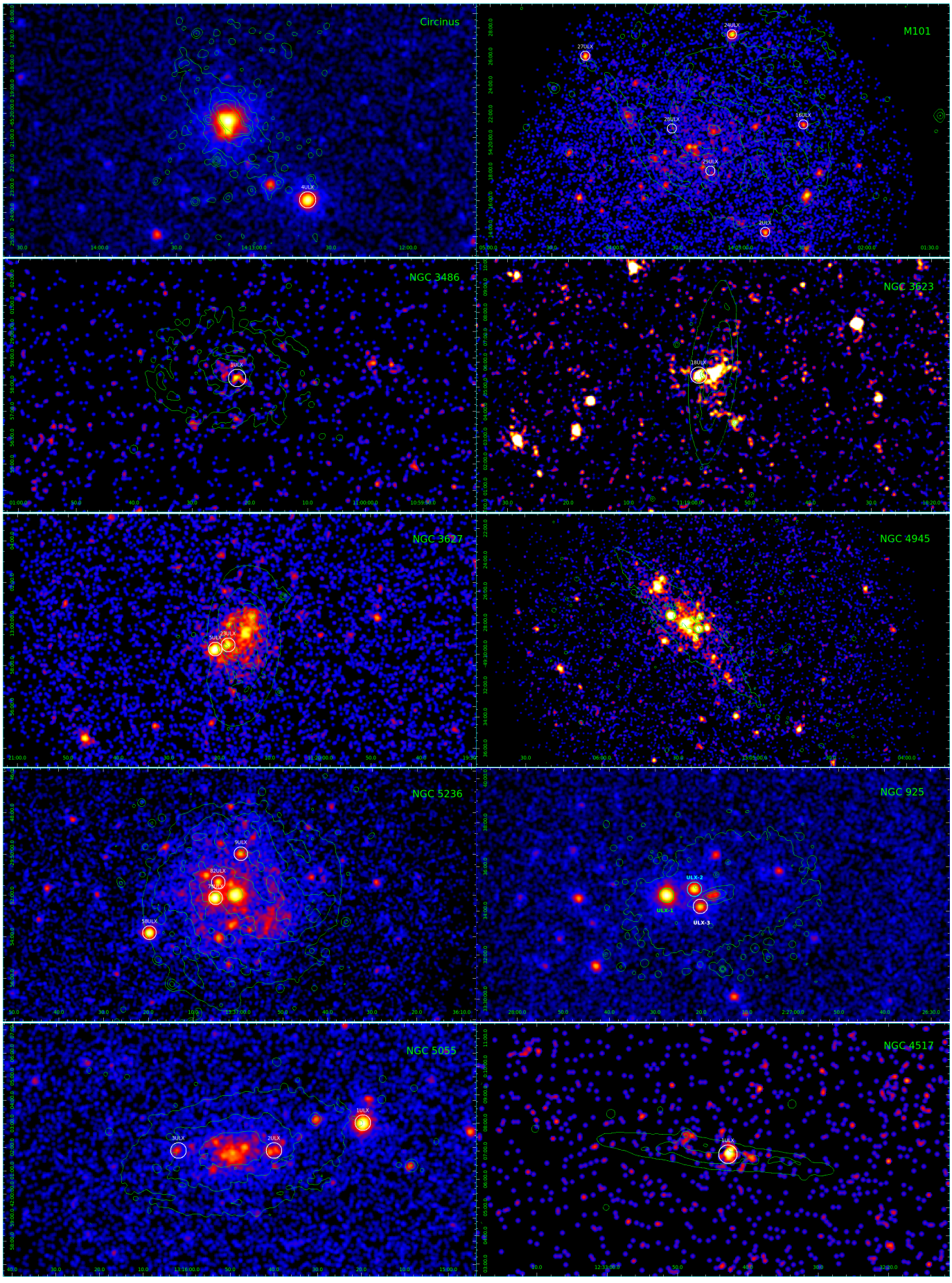

Figure 3.1: *Swift*/XRT stacked image for the observed galaxies. The ULXs positions are indicated with circles of 20″ radius and the optical contours from DSS of each galaxy are super-imposed with solid lines. Left (from top to bottom): Circinus galaxy, NGC 3486, NGC 3627, NGC 5236, NGC 5055. Right (from top to bottom): M101, NGC 3623, NGC 4945, NGC 925, NGC 4517.

Galaxy	ULX	σ_{var}	$F'^{ensemble'}_{var,[0.3-10]keV}$	$F'^{ensemble'}_{var,[0.3-1.5]keV}$	$F'^{ensemble'}_{var,[1.5-10]keV}$	t_{min} (days)	ΔF
Circinus galaxy	**4ULX**	>38	0.70±0.01	0.63±0.01	0.77±0.01	0.7 D	11.2
	6ULX	4.0	0.52±0.01	0.63±0.01	0.57±0.01	$0.4^{(*)}$ R	>6.7
M101	2ULX	2.74	–	–	–	–	>3.9
	16ULX	3.63	0.73±0.04	0.51±0.02	0.10±0.04	8.4 D	>3.7
	24ULX	4.15	0.36±0.01	0.47±0.01	0.45±0.01	5.8 R	5.4
	27ULX	6.14	0.59±0.01	0.59±0.01	0.59±0.03	7.8 D	3.7
	28ULX	0.96	–	–	–	–	>3.7
	29ULX	5.76	0.64±0.05	0.41±0.05	0.04±0.03	10.9 R	>6
NGC3486	1ULX	–	–	–	–	–	
NGC 3623	18ULX	0.46	–	–	–	–	>2.7
NGC 3627	5ULX	2.89	–	–	–	–	2.0
	23ULX	1.97	–	–	–	–	>2.5
NGC4945	**4ULX**	10.29	0.51±0.01	0.60±0.02	0.60±0.01	3.2 R	>11
	6ULX	6.46	0.41±0.01	0.65±0.02	0.54±0.01	4.4 R	>8.9
NGC5236	**9ULX**	3.18	0.52±0.01	0.53±0.02	0.63±0.02	2.3 D	>3.4
	58ULX	13.40	0.57±0.01	0.57±0.01	0.75±0.01	1.1 D	6.2
	79ULX	5.44	0.51±0.01	0.55±0.01	0.61±0.02	4.9 R	5.1
	82ULX	3.28	0.48±0.01	0.51±0.01	0.65±0.01	2.9 R	6.1
NGC925	**1ULX**	>38	0.63±0.01	0.62±0.01	0.69±0.01	5.4 R	10.4
	2ULX	5.8	0.39±0.01	0.42±0.01	0.54±0.01	–	4.2
	3ULX	29.8	0.77±0.01	0.65±0.01	0.72±0.01	2.0 R	>25
NGC5055	**1ULX**	18.41	0.66±0.01	0.57±0.01	0.92±0.01	1.6 R	9.6
	2ULX	3.41	0.51±0.02	0.48±0.05	0.45±0.10	0.8 R	>3.4
	3ULX	2.60	–	–	–	–	>3.5
NGC4517	1ULX	0.54	–	–	–	–	1.6

Table 3.3: The significance of the variability (σ_{var}) on timescales of days calculated using the Cash statistics; F_{var} for the variable ULXs in the total, soft (0.3–1.5) keV and hard (1.5–10) keV energy bands, in the studied sample; minimum half times (t_{min}) (using unabsorbed fluxes); maximum variability factor. We used the light curves with bins large six days for deriving F_{var} and the Cash statistics; the half times are instead derived considering the flux variation among the observations. We write 'D' if the minimum half time derived has been found during a flux decaying phase, or 'R' if it has been found during a rising phase.
(*) the model derived from the average values of the *XMM-Newton* fit is non-acceptable for the *Swift*/XRT average spectrum and no other acceptable fit has been found by modelling the average *Swift*/XRT spectrum. Thus the fluxes used to derive the half time may not always be correct.

3.3 Data analysis for the whole *Swift*/XRT sample

3.3.1 Temporal variability

To study the variability properties of the long-term light curves (stacked in six days bins) of the ULXs monitored with the *Swift* satellite, we applied the methods described in section 2.5.

For each ULX we verified if the light curve significantly differs from a constant value, by applying the Cash statistics (Cash 1979): the resulting significances are reported in table 3.3. To quantify the variability, we evaluated the F_{var} of the *Swift*/XRT data. We applied the "ensemble" approach proposed in Allevato et al. 2013, as described in section 2.5.3, which is more reliable than single estimates especially for sparse sampled light curves, as in this case. We simulated 5000 light curves, starting from the observed binned one, and we derived F_{var} for each of them. We grouped those values in bins of 50 points and derive a mean F_{var} for each bin. We then constructed the distribution of the obtained values and derived the "ensemble" estimate from the mean of the distribution (see table 3.3). The same method was used both to derive F_{var} in the total energy band (0.3-10 keV) and in the soft and hard energy bands, respectively below and above 1.5 keV.

The simulations were performed using a Monte Carlo approach. In case of a detection, a random

value was extracted from a Poissonian distribution centered on the observed total counts. We used the relative contribution of the observed source and background counts to derive the contribution of each component to the simulated total counts. We then obtained the net count rate dividing the obtained simulated source counts by the exposure time. We derived the uncertainty for each simulated count rate from the total counts: we used the Gehrels approximation (Gehrels 1986) if the total counts were less than twenty, and the square root of the counts otherwise. For the evaluation of F_{var} the upper limits are usually excluded and we did the same. As a consequence, when many significant upper limits are present in the light curve, F_{var} may be underestimated.

Given that the F_{var} calculation does not take into account the upper limits, we derived the maximum variability factor observed for each ULX, considering also the information provided by the upper limits. We report the results in the last column of table 3.3. We defined the variability factor (ΔF) as the ratio between the maximum and minimum flux of the source. We used the symmetric fluxes, i.e. we used the central value in the error bar for each flux, and we summed the flux error (i.e. half error bar) to the minimum flux value and subtracted the error to the maximum flux value before computing the ratio, in order to take into account the uncertainties. If the minimum value was an upper limit we report a ">", which indicates that the variability may be larger.

To derive information about the timescales of the variability, we also estimated the time needed to halve or double the flux of the sources significantly variable and with at least a factor two of variation among the observations; for this test we used the light curves with one observation per bin. The single *Swift*/XRT observations have not enough statistics to do a spectral analysis thus, to derive the fluxes, we used the spectral parameters from the fit of the average *Swift*/XRT spectrum or, when also the statistics of the average *Swift*/XRT spectrum was to low to do a spectral fitting, we used the average spectral parameters derived from the spectral analysis of the *XMM-Newton* data, which is reported in section 3.4.2, and we verified if they were a good fit also for the average *Swift*/XRT spectrum. We considered consecutive couples of fluxes and we summed the upper error to the smaller flux and subtracted the lower error to the larger flux. In this way we could verify if at least a variation of a factor two was present taking into account also the uncertainties. If the ratio between these two values was larger than 2, we evaluated the logarithm of the two values and derived the line connecting the two points. We determined the point on the line corresponding to a variation of a factor two and evaluated the time needed for this flux variation. We selected the minimum time interval found for each source and we report these values in table 3.3.

We also looked for flux periodicities by applying the Lomb-Scargle method to the *Swift*/XRT light curves (stacked in 6 d bins). No periodicities have been detected, except for one ULX: NGC 925 ULX-3. The details about this part of the analysis are included in section 3.5.1 and 3.5.2.

3.3.2 Spectral analysis

ULXs spectra have been modeled in the literature with different spectral models, e.g. power-law, disc-like or comptonizing models (e.g. Roberts et al. 2006, Middleton et al. 2011b, Walton et al. 2013, Brightman et al. 2016b, Pintore et al. 2016, Bachetti et al. 2013). Simple models, i.e. one component models, allow for good fits only for low statistics spectra; when the statistics of the spectrum is good, at least two components are usually needed to describe the complex spectral shape typically observed in ULXs (see e.g. Gladstone et al. 2009, Pintore and Zampieri 2011, Middleton et al. 2015a, Walton et al. 2020).

In the context of super-Eddington accretion, the two spectral components can be explained with an inflated disc inside the spherization radius (e.g. Poutanen et al. 2007), producing a complex structure composed of zones with different temperatures. The colder component may model the outer disc and/or the photosphere of the ejected winds (e.g. King and Pounds 2003); the hotter component may reproduce a hot inner accretion flow.

As a consequence of the above considerations, we decided to model the spectra with a cold blackbody model, BBODYRAD in XSPEC and a hotter multi-color blackbody disc, DISKBB (Mitsuda et al. 1984) in XSPEC. We also used an absorption component, TBABS, which models both the Galactic one and the local absorption, if present, thus we fixed a minimum to the absorption component equal to the Galactic absorption for each source.

Because of the low statistics in the short-exposure *Swift*/XRT data, they are not useful to study the spectral shape of the sources. So we used archival *XMM-Newton* data to characterize the ULXs' spectra. We also constructed an average *Swift*/XRT spectrum for each ULX and, when the statistics was enough to do a spectral analysis, we fit it with the same spectral model used in the fit of the *XMM-Newton* spectra (BBODYRAD + DISKBB, or just a DISKBB in some cases). See table 3.4 (3.7 for NGC 5055 ULX-2: in this case the *Swift*/XRT average spectrum was better modelled by a power-law). In some sources just one thermal component is sufficient to model the spectrum: in such cases we used just a DISKBB. We used the data of all the three EPIC cameras (pn, MOS1, MOS2) when possible. We excluded the data where the source of interest falls in a CCD gap or on a bad column. We considered the spectra in the energy range (0.3-10) keV and binned the data with a minimum of 20 (or 25, depending on the source statistics) counts per bin. We also consider a multiplicative constant in the model used for the spectral fit to take into account differences in the calibration of the instruments.

Sutton et al. (2013) proposed a method to classify the spectral shape of a ULX in three spectral regimes (soft ultraluminous, hard ultraluminous or broadened disc), based on the spectral parameters of a DISKBB+POWER-LAW model. Such spectral shapes are linked to different geometrical configurations of the system, i.e. a soft regime implies that a ULX is seen trough its wind, while a hard shape suggests a less inclined source where the emission of the inner regions is directly visible to the observer. In addition, the broadened disc shape is expected for sources around their Eddington limit, while the hard and soft ultraluminous regimes are expected for increasing accretion rates. Therefore this classification can be used to obtain information about the accretion configuration of the analysed sources. We thus fit the ULXs in our sample also with a TBABS*(DISKBB+POWER-LAW) model and used this model to classify the ULXs in our sample. The resulting parameters for this second spectral model are reported in table 3.7.

3.4 Results

3.4.1 Temporal variability on days timescales

We studied the variability of all the detected ULXs (see table 3.3), using a common binning of six days for the light-curves, in order to consider similar timescales while comparing the analysed sources. Some ULXs were not detected (NGC 3486 ULX1 and NGC4945 Suzaku_J1305-4931) or not spatially resolved (Circinus galaxy ULX1, ULX2, ULX3, ULX4) in the *Swift*/XRT data analysed in this work, while NGC 4945 41ULX was detected only once, so we brought the analysis on the other 24 sources. By applying the Cash statistics we found that 17/24 sources, which correspond to $\sim 71\%$ of the ULXs, result variable with at least a 3σ significance on days to months timescales. We further investigated their variability computing the fractional variability of the variable ones. This estimator gives us information about the fraction of flux involved in the variation: for each observed light curve we simulated 5000 light curves and used the simulated curves to compute the F_{var}, by applying an "ensemble" approach. First, we estimated the variability amplitude in the total energy band (0.3–10 keV), where all the sources have a F_{var} of at least 30%. In 12 sources the F_{var} value is larger than 50% in the total energy band. We then computed the F_{var} in the soft (0.3–1.5) keV and hard (1.5–10) keV energy bands. In 9 cases (~53% of the variable sources), the hard band dominates the variability. In M101 16ULX, M101 29ULX and NGC4945 6ULX, the variability is instead dominated by the soft band.

To derive information about the variability timescale, for each source which has varied its flux of at least a factor 2, we also evaluated the time needed to halve or double the flux. The results are shown in table 3.3: the obtained timescales are between $\sim$ 1 and 11 days. NGC 925 ULX-2 varies less than a factor 2 considering the uncertainties, in the data taken after 2019. Circinus 6ULX has instead a smaller t_{min} (~0.4 d), but we could not find a good fit for the average *Swift*/XRT spectrum, thus the fluxes used for the determination of the half time may not be correct. We fit the average *Swift*/XRT spectrum with both a power-law and a multicolour disc; both the fits are not statistically acceptable, but the disc model has a better fit statistics than the power-law one. We used the average

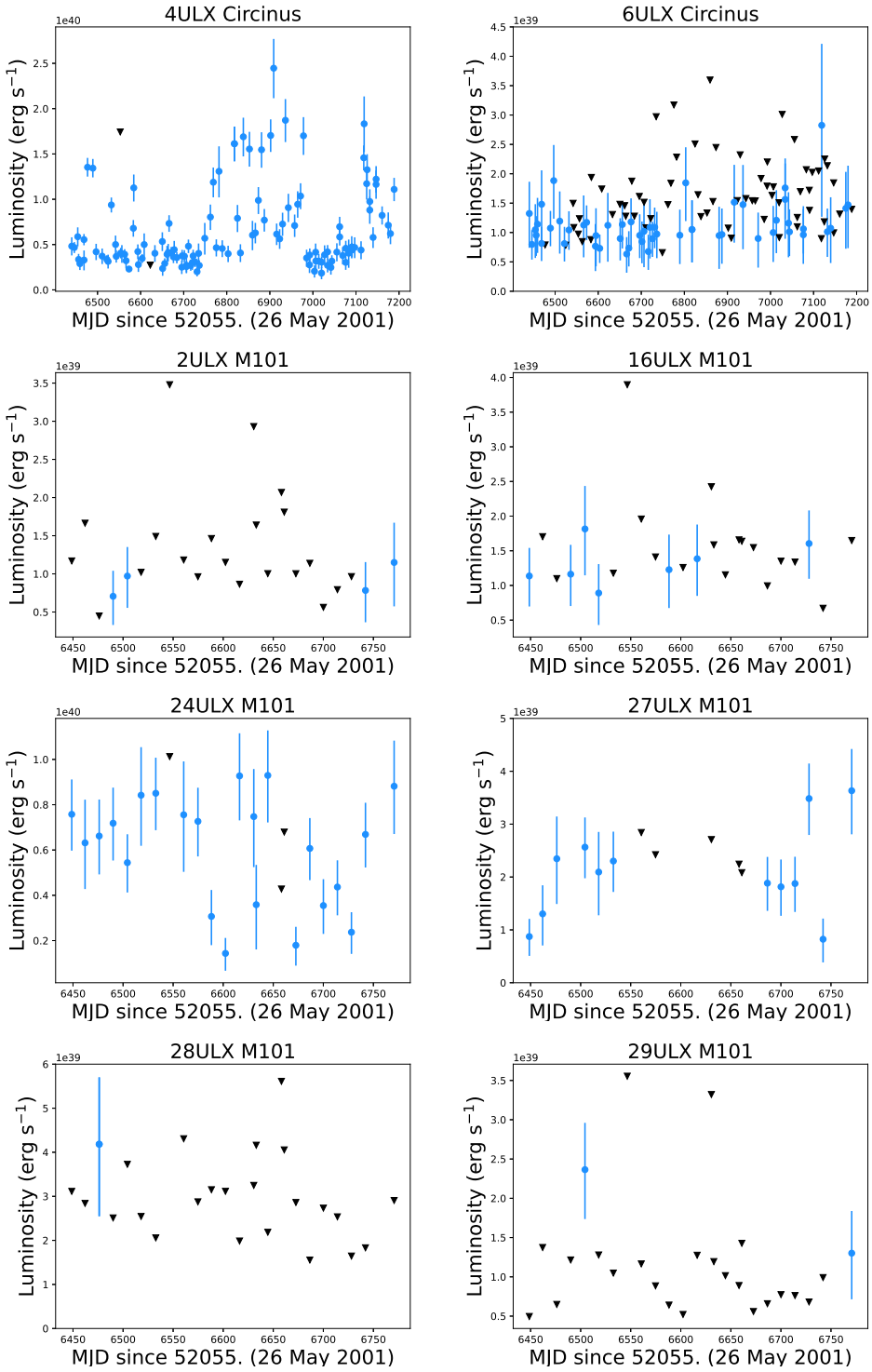

Figure 3.2: *Swift*/XRT light curves of the ULXs monitored for this work, with the observations taken after 2019. X-axis: time; Y-axis: unabsorbed luminosities in units of erg s^{-1} in (0.3-10) keV. The conversion from observed count-rate to luminosity has been done by assuming the average spectral-fitting with the model TBABS*(BBODYRAD+DISKBB) done with *XMM-Newton* data, which usually has a higher quality than the *Swift*/XRT one; when the model was not a good fit for the average *Swift*/XRT spectrum, we fit the average *Swift*/XRT spectrum.

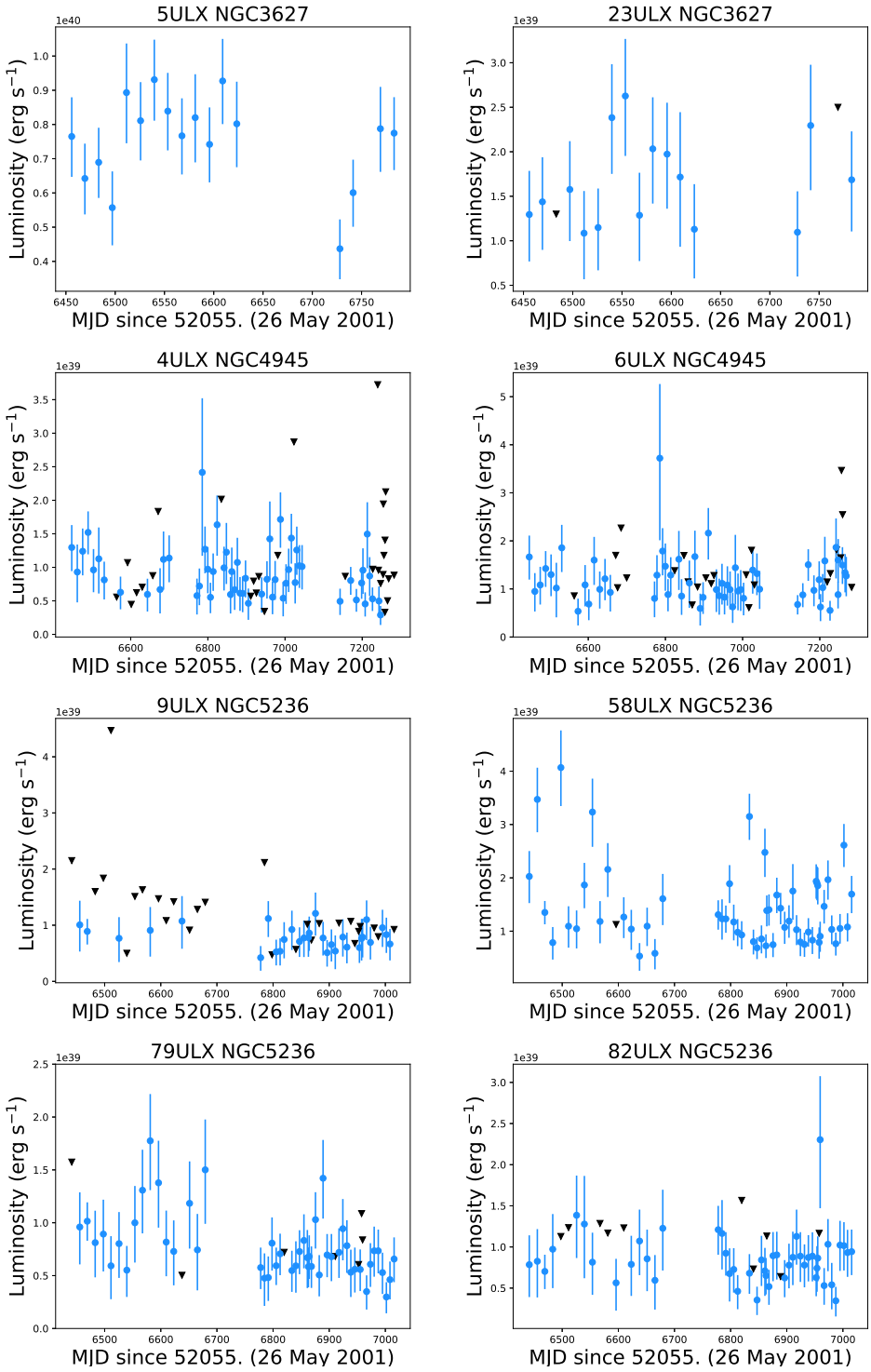

Figure 3.3: *Swift*/XRT light curves of the ULXs monitored for this work, with the observations taken after 2019. X-axis: time; Y-axis: unabsorbed luminosities in units of erg s^{-1} in (0.3-10) keV. The conversion from observed count-rate to luminosity has been done by assuming the average spectral-fitting with the model TBABS*(BBODYRAD+DISKBB) done with *XMM-Newton* data, which usually has a higher quality than the *Swift*/XRT one; when the model was not a good fit for the average *Swift*/XRT spectrum, we fit the average *Swift*/XRT spectrum.

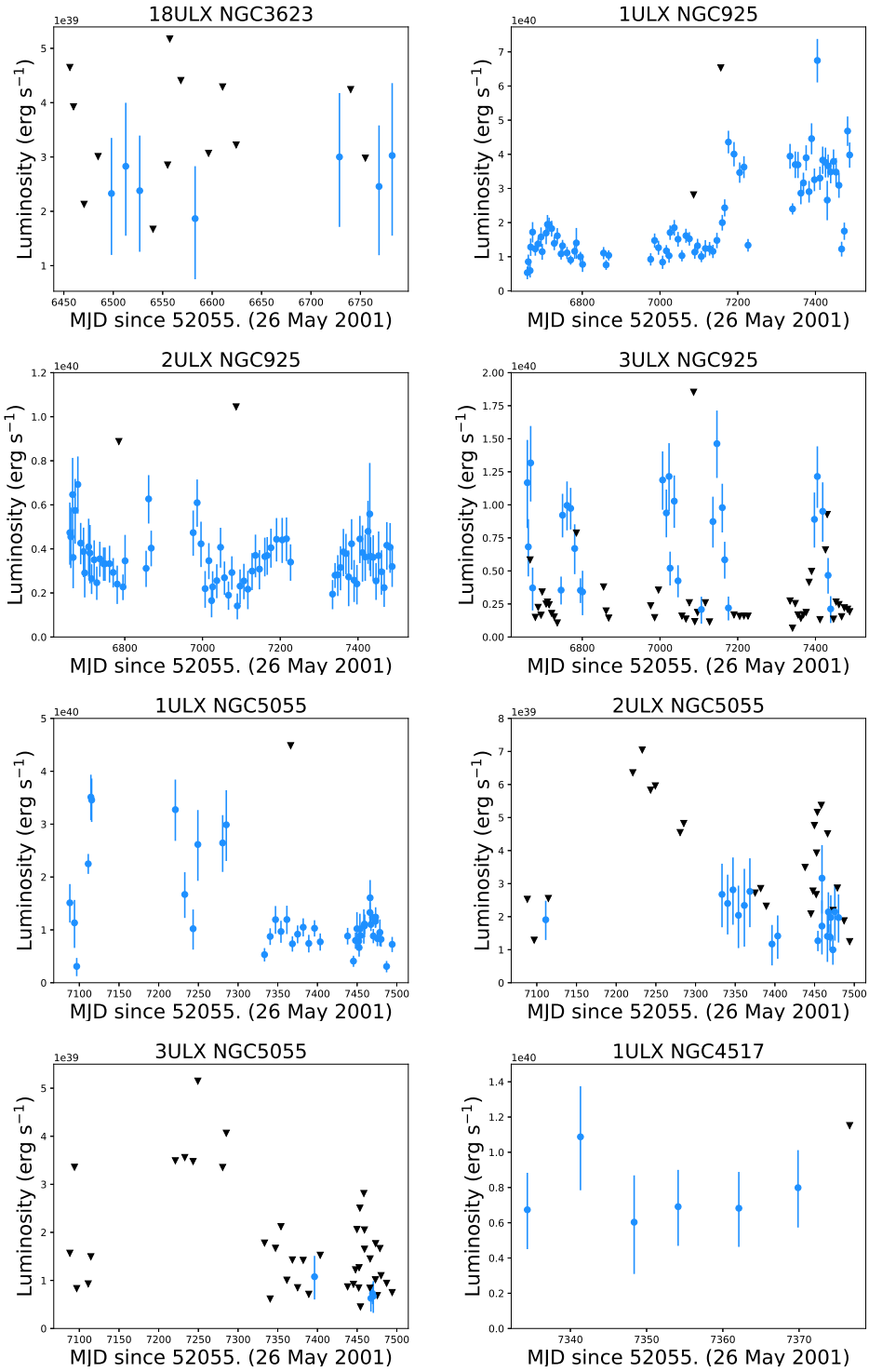

Figure 3.4: *Swift*/XRT light curves of the ULXs monitored for this work, with the observations taken after 2019. X-axis: time; Y-axis: unabsorbed luminosities in units of erg s^{-1} in (0.3-10) keV. The conversion from observed count-rate to luminosity has been done by assuming the average spectral-fitting with the model TBABS*(BBODYRAD+DISKBB) done with *XMM-Newton* data, which usually has a higher quality than the *Swift*/XRT one; when the model was not a good fit for the average *Swift*/XRT spectrum, we fit the average *Swift*/XRT spectrum.

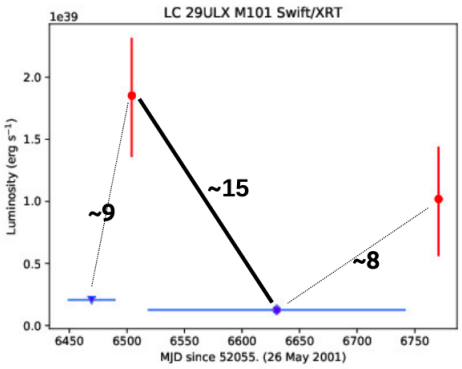

Figure 3.5: *Swift*/XRT light curve of M101 29ULX. We have stacked the upper limits to highlight the bi-modal behaviour of the source.

values from the *XMM-Newton* parameters of the disc model to derive the flux ($n_{\rm H} = 0.8{\times}10^{22}$ cm^{-2}, $kT_{in} = 0.74$). The fact that we could not find an acceptable model for the average *Swift*/XRT spectrum suggests the presence of spectral variability.

The long-term light curves of ULXs may also show diverse variability patterns, such as super-orbital periods and bi-modal flux distribution. Bi-modal flux distribution could in principle indicate a candidate PULX, because it can be produced by propeller stages. We have looked for these variability patterns in our data. NGC 925 ULX-3 (Salvaggio et al. 2022) has a flux modulation on a period of about four months, similar to the super-orbital periodicities found in other ULXs: more details are given in sections 3.5.1 and 3.5.2. Another source in the sample, M101 29ULX, has shown a bi-modal flux distribution. It has been detected only twice during the *Swift*/XRT monitoring. By stacking the upper limits between the detections, we found a flux variation of about an order of magnitude (see figure 3.5), which may be linked to propeller phases. Therefore we consider this source a candidate PULX. M101 29ULX is not spatially resolved from other X-ray sources in the *Swift*/XRT image, which may have influenced our results, thus further analysis is needed to confirm our findings. Urquhart et al. (2022) have analysed this source in the *Chandra* data, where it is resolved, and they suggest a fast-spinning NS to explain this source, but the nature of this ULX is still not confirmed. In the analysed sample, we also found a possible flaring activity in NGC 5236 58ULX: the source presents short high flux states, where it can increase its flux by up to a factor 5. We have asked for intra-week observations in order to track a flaring episode, but in none of those supplementary observations the source was caught in a peak of emission. Therefore, if the observed peaks correspond to episodes of flaring activity, we can only put an upper limit on the flares duration, which should be of the order of a week, otherwise we would have caught the source at high flux in consecutive observations.

3.4.2 Spectral analysis with archival *XMM-Newton* data

The best-fitting parameters, obtained from the analysis of archival *XMM-Newton* data with the model TBABS*(BBODYRAD+DISKBB), are reported in table 3.4 (the results for the ULXs in NGC 925 are instead reported in a dedicated table 3.10), where we also report the unabsorbed fluxes for the blackbody and disc component, in band 0.3-10 keV for each source. We also report the results for the average *Swift*/XRT spectrum, when the statistics was enough to obtain a spectral fit, or alternatively the average *XMM-Newton* parameters used to convert the *Swift*/XRT count rate to flux. The fluxes have been derived with the convolution model CFLUX. In the same table we also report the χ^2 over the degrees of freedom and the P_{value} of the fit. The latter indicates the null hypothesis probability, which is the probability that the data derive from the model. We consider the fits statistically acceptable when they have a P_{val} larger than 0.05, which corresponds to a confidence level $> 2\sigma$.

The unfolded *XMM-Newton* spectra of the ULXs, except for the sources in NGC 925, are displayed in figures 3.6, 3.7, 3.8 and 3.9 (the spectra are rebinned for display purposes, when needed). For each ULX we plot also the best-fit model for the observation with the larger statistics, to highlight the possible spectral variability in some sources. The spectra of the ULXs in NGC 925 are instead shown in figure 3.16, where we plot also *Swift*/XRT and *Chandra* data.

From the BBODYRAD and DISKBB normalizations it is possible to derive an estimate of the radius of the emitting region for each spectral component. The BBODYRAD emitting radius in km is equal to the $d \times \sqrt{\mathrm{norm_{bb}}}$, where d is the galaxy distance in units of 10 kpc. The DISKBB emitting radius in km is $\sqrt{\frac{\mathrm{norm_{disk}}}{cos(i)}} \times d$, where i is the inclination of the disc. The inner radius derived from the DISKBB component is an apparent radius; to derive the emitting region radius we have to apply corrections (e.g. Kubota et al. 1998, Vierdayanti et al. 2008) which take into account the physics of the disc atmosphere and a boundary condition. We thus have to multiply the resulting apparent radius by $f_{col}^2 \times \zeta$. $\zeta = 0.4$ is the boundary condition factor (e.g. Kubota et al. 1998), while f_{col} is the colour correction factor and it is usually taken equal to 1.7 for standard thin discs (e.g. Shimura and Takahara 1995). In case of super-Eddington accretion a better value for f_{col} is 3 (e.g. Watarai and Mineshige 2003) and the correction factor may be radial dependent (Soria et al. 2008). We derived the emitting regions for both the spectral components. For the disc component we derived the radii both assuming a colour correction equal to 1.7 and 3 and we assumed an average inclination of 60 degrees. The obtained values are indicated in table 3.5, we did not derive the radius when the normalization was not well constrained, i.e. when we derived an upper limit.

OBS. ID[(1)]	χ^2/dof[(2)]	$P^{(3)}_{val}$	$n_H^{(4)}$	$kT^{(5)}_{bb}$	$norm^{(6)}_{bb}$	$kT^{(7)}_{diskbb}$	$norm^{(8)}_{diskbb}$	$F^{(9)}_{bb}$	$F^{(10)}_{diskbb}$	instr.[(11)]	net counts[(12)]
			10^{22} cm^{-2}	keV		keV		10^{-13} erg s^{-1} cm^{-2}	10^{-13} erg s^{-1} cm^{-2}		
Circinus 4ULX			$N_{H,gal}$ = 0.53								
0111240101	318.54/364	0.96	$0.7^{+0.1}_{-0.1}$	$0.42^{+0.04}_{-0.1}$	$2.0^{+1.1}_{-0.6}$	$2.0^{+0.3}_{-0.2}$	$0.006^{+0.004}_{-0.003}$	6.7±0.3	17.91±0.04	**1**	11312.3
0656580601	413.01/422	0.61	$0.8^{+0.1}_{-0.1}$	$0.32^{+0.04}_{-0.04}$	$5.6^{+4.9}_{-2.4}$	$1.9^{+0.3}_{-0.2}$	$0.005^{+0.003}_{-0.002}$	5.9±0.3	13.9±0.5	**0**,1,2	6103.2
0701981001	1497.21/1478	0.36	$0.79^{+0.04}_{-0.04}$	$0.5^{+0.1}_{-0.1}$	$0.8^{+1.4}_{-0.4}$	$2.0^{+0.1}_{-0.1}$	$0.026^{+0.004}_{-0.004}$	3.7±0.4	74.1±0.1	**0**,2	39213.7
0780950201	359.79/327	0.1	$0.8^{+0.2}_{-0.2}$	$0.23^{+0.04}_{-0.03}$	$12.9^{+27.2}_{-8.8}$	$2.3^{+0.3}_{-0.2}$	$0.002^{+0.001}_{-0.001}$	3.7±0.5	11.9±0.1	**0**,1,2	1548.7
0792382701	319/78/335	0.72	$0.7^{+0.1}_{-0.1}$	$0.3^{+0.1}_{-0.1}$	$2.7^{+15.6}_{-1.9}$	$1.2^{+0.1}_{-0.1}$	$0.05^{+0.02}_{-0.02}$	1.8±0.4	22.8±0.5	**0**,1	7441.4
0824450301	1294.21/1240	0.14	$0.74^{+0.02}_{-0.02}$	$0.6^{+0.1}_{-0.1}$	$0.4^{+0.1}_{-0.1}$	$1.9^{+0.1}_{-0.1}$	$0.024^{+0.004}_{-0.004}$	5.5±0.3	66.53±0.04	**0**	93412.5
Swift/XRT av.	201.86/218	0.78	$0.6^{+0.1}_{-0.1}$	$0.4^{+0.1}_{-0.1}$	$1.6^{+3.4}_{-0.9}$	$2.0^{+0.4}_{-0.3}$	$0.009^{+0.006}_{-0.005}$	4.6±0.5	26.3±0.8	–	5606.0
Circinus 6ULX			$N_{H,gal}$ = 0.53								
0111240101	268.74/227	0.03	$0.9^{+0.1}_{-0.1}$	–	–	$0.70^{+0.03}_{-0.03}$	$0.08^{+0.02}_{-0.02}$	–	4.0±0.1	**0**,1	4028.1
0656580601	45.44/43	0.37	$0.7^{+0.1}_{-0.1}$	–	–	$0.8^{+0.1}_{0.1}$	$0.04^{+0.02}_{-0.01}$	–	3.2±0.2	**0**	1067.7
0701981001	161.47/183	0.87	$0.8^{+0.1}_{-0.1}$	–	–	$0.73^{+0.03}_{-0.03}$	$0.07^{+0.02}_{-0.01}$	–	3.6±0.2	**0**,1,2	2046.7
0780950201	90.69/86	0.34	$0.9^{+0.1}_{-0.1}$	–	–	$0.7^{+0.1}_{-0.1}$	$0.06^{+0.03}_{-0.02}$	-	3.0±0.3	**0**,1,2	327.5
0792382701	38.38/48	0.8	$0.6^{+0.2}_{-0.2}$	$0.4^{+0.1}_{-0.1}$	$0.5^{+0.6}_{-0.2}$	4.9(> 1.8)	<0.0005	1.6±0.1	1.3±0.3	**0**,1,2	733.6
XMM-Newton av.	–	–	0.8	–	–	0.74	0.06	–	–	–	–
M101 2ULX			$N_{H,gal}$ = 0.085								
0104260101	5.58/6	0.47	18^{+19}_{-8}	–	–	$1.0^{+0.8}_{-0.4}$	$0.04^{+0.01}_{-0.01}$	–	7.7±1.6	**1**,2	107.3
0164560701	11.7/14	0.63	$8.1^{+6.8}_{-3.4}$	–	–	$2.0^{+2.4}_{-0.8}$	$0.0006^{+0.0001}_{-0.0001}$	–	1.4±0.3	**0**,1,2	107.7
0212480201	27.72/19	0.09	$8.2^{+5.1}_{-2.5}$	–	–	5.1(>1.9)	$0.00004^{+0.00001}_{-0.00001}$	–	3.2±0.6	**0**,1,2	144.1
0824450501	44.19/32	0.07	12^{+4}_{-3}	–	–	$2.2^{+3.7}_{-0.7}$	$0.0011^{+0.002}_{-0.0007}$	–	5.1±0.6	**0**,2	311.7
XMM-Newton av.	–	–	14.5	–	–	1.3	0.01	–	–	–	–
M101 16ULX			$N_{H,gal}$ = 0.085								
0104260101	56.69/42	0.07	$0.25^{+0.1}_{-0.1}$	$0.15^{+0.02}_{-0.02}$	$47.8^{+123.2}_{-31.2}$	$0.8^{+0.6}_{-0.3}$	$0.0041^{+0.03}_{-0.0004}$	2.2±0.2	0.4±0.1	**1**,2	542.4
0164560701	34.75/31	0.29	$0.2^{+0.2}_{-0.1}$	$0.15^{+0.02}_{-0.02}$	$31.3^{+104.8}_{-21.1}$	$1.1^{+2.5}_{-0.6}$	<0.01	1.3±0.1	0.1±0.07	**0**,1,2	536.1

0212480201	5.91/8	0.66	$0.5^{+0.4}_{-0.3}$	–	–	$0.16^{+0.10}_{-0.04}$	87^{+81}_{-44}	–	5.7±0.9	**1**,2	161.5
0824450501	25.88/15	0.04	$0.5^{+0.4}_{-0.3}$	$0.11^{+0.04}_{-0.03}$	698^{+22624}_{-666}	$0.7^{+0.7}_{-0.3}$	$0.010^{+0.08}_{-0.009}$	7.0±0.9	0.5±0.1	**2**	337.1
XMM-Newton av.	–	–	0.18	0.15	31.2	0.97	0.006	–	–	–	–
M101 24ULX			$N_{H,gal}$ = 0.085								
0104260101	217.06/203	0.24	$0.13^{+0.1}_{-0.1}$	$0.2^{+0.3}_{-0.1}$	$1.5^{+17.2}_{-1.5}$	$1.4^{+0.5}_{-0.1}$	$0.006^{+0.002}_{-0.005}$	0.3±0.1	5.1±0.2	**0**,1,2	1331.1
0164560701	43.15/42	0.42	0.085	$0.3^{+0.1}_{-0.1}$	$0.4^{+0.3}_{-0.3}$	$1.4^{+0.6}_{-0.3}$	$0.003^{+0.005}_{-0.002}$	0.5±0.1	2.2±0.2	**0**	1133.3
0212480201	62.34/68	0.67	0.085	$0.4^{+0.1}_{-0.2}$	$0.3^{+0.3}_{-0.2}$	$1.9^{+0.7}_{-0.4}$	$0.002^{+0.003}_{-0.002}$	0.7±0.2	5.7±0.4	**1**,2	882.3
0824450501	320.94/309	0.31	$0.13^{+0.10}_{-0.03}$	$0.25^{+0.08}_{-0.06}$	$1.0^{+3.1}_{-0.7}$	$1.5^{+0.1}_{-0.1}$	$0.005^{+0.001}_{-0.001}$	0.4±0.1	5.3±0.2	**0**,1,2	4231.9
Swift/XRT av.	14/15	0.53	0.51(<1.36)	$0.12^{+1}_{-0.1}$	211(<26617)	$1.2^{+0.4}_{-0.3}$	$0.01^{+0.03}_{-0.01}$	2.7±1.4	5.6±0.5	–	420.5
M101 27ULX			$N_{H,gal}$ = 0.085								
0104260101	100.26/90	0.22	0.085	$0.16^{+0.02}_{-0.02}$	$15.4^{+12.0}_{-5.4}$	$0.8^{+0.1}_{-0.1}$	$0.03^{+0.03}_{-0.01}$	0.9±0.1	1.8±0.1	**0**,1,2	1283.6
0164560701	37.79/33	0.26	0.085	$0.21^{+0.02}_{-0.03}$	$8.0^{+3.5}_{-2.2}$	$1.1^{+150.7}_{-0.5}$	$0.005^{+0.05}_{-0.004}$	1.9±0.2	1.3±0.2	**1**,2	560.7
0212480201	72.35/89	0.9	0.085	$0.17^{+0.02}_{-0.02}$	$28.6^{+14.9}_{-8.5}$	$0.6^{+0.1}_{-0.1}$	$0.11^{+0.08}_{-0.05}$	2.2±0.3	3.5±0.3	**1**,2	1238.6
0824450501	370.25/340	0.13	0.085	$0.16^{+0.01}_{-0.01}$	$14.6^{+3.8}_{-2.7}$	$0.66^{+0.1}_{-0.04}$	$0.05^{+0.02}_{-0.01}$	1.0±0.1	1.8±0.1	**0**,1,2	5737.5
XMM-Newton av.	–	–	0.085	0.18	16.7	0.79	0.05	–	–	–	–
M101 28ULX			$N_{H,gal}$ = 0.085								
0164560701	(6.12/7)/(6.71/8)	0.53/0.6	<0.4/0.085	$0.07^{+0.02}_{-0.02}$/–	<245839/–	–/$0.09^{+0.01}_{-0.01}$	–/<572	0.6±0.1/–	–/0.34±0.06	**0**	158.7
0212480201	(29.63/39)/(29.61/39)	0.86/0.86	$0.2^{+0.1}_{-0.1}$/$0.2^{+0.1}_{-0.1}$	$0.06^{+0.01}_{-0.01}$/–	<114350/–	–/$0.06^{+0.01}_{-0.01}$	–/$374310.06^{+108870}_{-29527}$	7.5±0.4/–	10.0±0.1	**0**,1	964.3
XMM-Newton av.	–	–	0.14	–	–	0.08	187441	–	–	–	–
M101 29ULX			$N_{H,gal}$ = 0.085								
0104260101	114.33/100	0.16	0.085	$0.21^{+0.01}_{-0.01}$	$9.5^{+3.0}_{-2.2}$	$2.8^{+1.2}_{-0.7}$	$0.0003^{+0.0004}_{-0.0002}$	1.6±0.1	3.2±0.3	**1**,2	1304.7
0164560701	116.74/81	0.12	0.085	$0.19^{+0.02}_{-0.02}$	$6.2^{+2.9}_{-1.8}$	$2.2^{+0.8}_{-0.5}$	$0.0004^{+0.0006}_{-0.0002}$	0.8±0.1	1.5±0.1	**0**,1,2	1261.4
XMM-Newton av.	–	–	0.085	0.2	7.85	2.5	0.00035	–	–	–	–
NGC 5236 9ULX			$N_{H,gal}$ = 0.04								
0110910201	117.23/101	0.13	$0.2^{+0.2}_{-0.1}$	$0.13^{+0.03}_{-0.02}$	34^{+153}_{-31}	$1.9^{+0.4}_{-0.3}$	$0.0007^{+0.0006}_{-0.0003}$	1.2±0.1	1.6±0.1	**0**,1,2	1209.2
0503230101	26.21/11	0.13	$0.3^{+0.4}_{-0.2}$	–	–	$1.5^{+1.4}_{-0.6}$	<0.014	–	2.7±0.5	**2**	177.0
0552080101	15.44/1	0.22	0.04	–	–	$2.2^{+2.0}_{-0.8}$	<0.002	–	1.5±0.3	0	185.6

0723450101	21.61/21	0.42	0.04	$0.3^{+0.1}_{-0.2}$	<94.2	$2.2^{+2.9}_{-0.8}$	<0.002	0.22±0.06	1.3±0.1	**2**	529.5
0723450201	87.07/87	0.48	<0.23	$0.2^{+0.1}_{-0.1}$	$3.1^{+24.1}_{-2.5}$	$2.5^{+0.9}_{-0.5}$	<0.001	0.4±0.1	2.0±0.2	**1**,2	888.2
0729561001	49.88/44	0.25	0.04	$0.14^{+0.04}_{-0.03}$	$9.7^{+28.0}_{-6.6}$	$2.3^{+0.8}_{-0.5}$	$0.0004^{+0.0004}_{-0.0003}$	0.4±0.1	2.1±0.3	**1**,2	412.5
0729561201	75.75/109	0.99	<0.24	$0.2^{+0.1}_{-0.1}$	$2.0^{+26.9}_{-1.8}$	$1.9^{+0.4}_{-0.3}$	$0.0007^{+0.001}_{-0.0004}$	0.2±0.1	1.7±0.1	**0**,1,2	1189.6
0761620101	202.2/204	0.52	$0.06^{+0.1}_{-0.05}$	$0.16^{+0.03}_{-0.02}$	$7.3^{+13.2}_{-4.5}$	$2.1^{+0.2}_{-0.2}$	$0.0006^{+0.0003}_{-0.0002}$	0.48±0.04	2.4±0.1	**0**,2	3802.9
0761620201	127.18/141	0.79	<0.2	$0.26^{+0.04}_{-0.04}$	$6.3^{+45.4}_{-4.8}$	$1.7^{+0.4}_{-0.3}$	$0.001^{+0.001}_{-0.0005}$	0.39±0.08	1.7±0.1	**1**,2	1082.9
XMM-Newton av.	–	–	0.13	0.12	46.99	1.9	0.0007	–	–	–	–
NGC 5236 58ULX			$N_{H,gal}$ = 0.04								
0110910201	117.23/101	0.12	$0.2^{+0.2}_{-0.1}$	$0.14^{+0.03}_{-0.02}$	$34.0^{+153.3}_{-30.6}$	$1.9^{+0.4}_{-0.3}$	$0.0066^{+0.001}_{-0.0003}$	1.2±0.1	1.6±0.1	**0**,1,2	2748.1
0503230101	55.04/51	0.32	0.04	$0.33^{+0.03}_{-0.04}$	$3.3^{+1.2}_{-0.9}$	$2.4^{+7.4}_{-0.9}$	<0.007	3.9±0.3	7.0±0.7	**2**	1368.0
0552080101	36.88/39	0.57	0.04	$0.18^{+0.04}_{-0.04}$	$12.3^{+22.8}_{-6.4}$	$0.9^{+0.3}_{-0.2}$	$0.02^{+0.01}_{-0.01}$	1.1±0.2	2.7±0.3	**1**,2	537.2
0723450101	85.41/98	0.81	0.04	$0.23^{+0.03}_{-0.03}$	$3.5^{+1.8}_{-1.2}$	$1.0^{+0.1}_{-0.1}$	$0.02^{+0.01}_{-0.01}$	1.1±0.1	4.3±0.2	**2**	2722.3
0723450201	140.65/166	0.92	$0.05^{+0.05}_{-0.04}$	$0.23^{+0.05}_{-0.04}$	$4.7^{+9.0}_{-2.8}$	$1.0^{+0.1}_{-0.1}$	$0.03^{+0.01}_{-0.01}$	1.4±0.1	7.1±0.2	**1**	4865.6
0729561001	120.54/116	0.37	0.04	$0.19^{+0.02}_{-0.02}$	$7.6^{+3.2}_{-2.0}$	$1.0^{+0.1}_{-0.1}$	$0.011^{+0.01}_{-0.004}$	1.0±0.1	2.3±0.1	**0**,2	2129.7
0729561201	273.36/266	0.37	$0.05^{+0.03}_{-0.03}$	$0.24^{+0.03}_{-0.03}$	$4.7^{+3.5}_{-1.7}$	$1.0^{+0.1}_{-0.1}$	$0.02^{+0.01}_{-0.01}$	1.5±0.1	4.1±0.2	**0**,1,2	4459.5
0761620101	90.2/76	0.13	0.04	$0.21^{+0.02}_{-0.02}$	$5.0^{+2.5}_{-1.5}$	$1.2^{+0.2}_{-0.1}$	$0.006^{+0.004}_{-0.002}$	1.0±0.1	2.6±0.1	**0**,2	6237.5
0761620201	102.7/96	0.3	0.04	$0.23^{+0.02}_{-0.02}$	$4.1^{+1.3}_{-1.0}$	$1.3^{+0.3}_{-0.2}$	$0.004^{+0.004}_{-0.002}$	1.2±0.1	2.4±0.1	**1**	2426.2
Swift/XRT av.	65.73/53	0.11	0.04	$0.27^{+0.05}_{-0.08}$	$2.0^{+2.2}_{-1.1}$	$1.1^{+0.3}_{-0.2}$	$0.01^{+0.02}_{-0.01}$	1.0±0.2	4.5±0.3	–	1183.4
NGC 5236 79ULX			$N_{H,gal}$ = 0.04								
0723450101	496.31/602	0.99	$0.05^{+0.02}_{-0.02}$	$0.3^{+0.1}_{-0.1}$	$1.5^{+2.1}_{-0.8}$	$1.7^{+0.1}_{-0.1}$	$0.008^{+0.001}_{-0.001}$	0.7±0.1	11.7±0.2	**0**,2	13601.6
0723450201	217.93/201	0.20	$0.11^{+0.1}_{-0.1}$	$0.17^{+0.03}_{-0.02}$	$8.6^{+15.3}_{-5.2}$	$1.0^{+0.1}_{-0.1}$	$0.009^{+0.003}_{-0.003}$	0.7±0.1	2.0±0.1	**0**,2	3496.2
0729561001	110.14/120	0.73	<0.2	$0.17^{+0.07}_{-0.04}$	$6.1^{+33.9}_{-5.1}$	$1.2^{+0.1}_{-0.1}$	$0.008^{+0.004}_{-0.003}$	0.5±0.1	3.1±0.2	**0**,2	1888.9
0729561201	291.5/295	0.55	0.04	$0.22^{+0.03}_{-0.03}$	$3.3^{+1.6}_{-1.0}$	$1.5^{+0.1}_{-0.1}$	$0.008^{+0.002}_{-0.002}$	0.8±0.1	8.5±0.2	**0**,2	6086.0
0761620101	523.33/556	0.84	$0.04^{+0.02}_{-0.02}$	$0.21^{+0.03}_{-0.03}$	$3.1^{+3.1}_{-1.5}$	$1.4^{+0.1}_{-0.1}$	$0.009^{+0.001}_{-0.001}$	0.6±0.1	7.7±0.1	**0**,2	12202.3
0761620201	463.02/495	0.85	0.04	$0.21^{+0.02}_{-0.02}$	$3.6^{+1.2}_{-0.9}$	$1.4^{+0.1}_{-0.1}$	$0.008^{+0.001}_{-0.001}$	0.7±0.1	6.4±0.1	**0**,2	9035.3
Swift/XRT av.	24.29/35	0.91	0.04	$0.18^{+0.04}_{-0.04}$	$6.1^{+6.7}_{-3.2}$	$1.1^{+0.2}_{-0.2}$	$0.01^{+0.01}_{-0.01}$	0.8±0.2	2.9±0.2	–	790.4

NGC 5236 82ULX			$N_{H,gal}$ = 0.04								
0110910201	106.57/96	0.22	$0.19^{+0.2}_{-0.1}$	$0.14^{+0.1}_{-0.03}$	29^{+274}_{-26}	$0.8^{+0.1}_{-0.1}$	$0.02^{+0.01}_{-0.01}$	0.8±0.1	1.7±0.1	**0**,1	1372.3
0552080101	44.38/43	0.41	0.04	–	–	$0.96^{+0.1}_{-0.1}$	$0.012^{+0.01}_{-0.004}$	–	2.1±0.2	**0**,1,2	496.9
0723450101	35.99/43	0.77	0.04	–	–	$0.9^{+0.1}_{-0.1}$	$0.013^{+0.01}_{-0.003}$	–	2.1±0.1	**1**	1066.4
0723450201	232.74/220	0.27	$0.2^{+0.1}_{-0.1}$	$0.17^{+0.04}_{-0.03}$	$9.2^{+28}_{-6.6}$	$1.0^{+0.1}_{-0.1}$	$0.011^{+0.004}_{-0.003}$	0.7±0.1	2.0±0.1	**0**,1,2	3247.8
0729561001	106/103	0.4	$0.2^{+0.2}_{-0.1}$	$0.16^{+0.1}_{-0.04}$	$15.3^{+109.5}_{-13}$	$1.0^{+0.1}_{-0.1}$	$0.011^{+0.007}_{-0.005}$	0.9±0.1	2.1±0.2	**0**,1,2	1250.9
0729561201	19.76/27	0.84	0.04	–	–	$0.8^{+0.1}_{-0.1}$	$0.03^{+0.01}_{-0.01}$	–	2.3±0.2	**1**	677.6
0761620101	69.66/63	0.26	$0.3^{+0.3}_{-0.2}$	$0.14^{+0.1}_{-0.03}$	$125.4^{+1877}_{-123.9}$	$0.9^{+0.1}_{-0.2}$	$0.02^{+0.02}_{-0.01}$	3.8±0.4	2.8±0.2	**1**	1988.1
0761620201	313.2/288	0.15	$0.3^{+0.1}_{-0.1}$	$0.14^{+0.03}_{-0.02}$	$34.9^{+102.6}_{-26.2}$	$0.9^{+0.1}_{-0.1}$	$0.016^{+0.01}_{-0.004}$	1.3±0.1	2.1±0.1	**1**	1789.9
Swift/XRT av.	19.27/29	0.91	$0.34^{+0.4}_{-0.3}$	$0.12^{+0.07}_{-0.03}$	330.3^{+13177}_{-300}	$1.0^{+0.2}_{-0.2}$	$0.02^{+0.02}_{-0.01}$	4.0±0.6	2.9±0.3	–	686.2
NGC 3623 18ULX			$N_{H,gal}$ = 0.02								
0082140301	69.3/60	0.19	$0.1^{+0.2}_{-0.1}$	$0.3^{+0.2}_{-0.1}$	$0.3^{+3.6}_{-0.3}$	$1.5^{+0.3}_{-0.2}$	$0.001^{+0.0008}_{-0.0007}$	0.14±0.04	1.4±0.1	**0**,1,2	886.7
NGC 3627 5ULX			$N_{H,gal}$ = 0.02								
0093641101	25/32	0.81	0.02	$0.15^{+0.03}_{-0.03}$	$19.2^{+34.1}_{-11.3}$	$1.5^{+0.3}_{-0.2}$	$0.005^{+0.003}_{-0.002}$	0.9±0.2	4.7±0.5	**1**,2	473.2
Swift/XRT av.	36.9/49	0.9	0.04(<0.15)	$0.23^{+0.15}_{-0.04}$	$3.5^{+50}_{-3.3}$	$1.4^{+0.3}_{-0.2}$	$0.001^{+0.009}_{-0.008}$	1.0±0.3	11.1±0.6	–	1185.8
NGC 3627 23ULX			$N_{H,gal}$ = 0.02								
0093641101	18.97/23	0.7	0.02	–	–	$0.95^{+0.1}_{-0.1}$	$0.012^{+0.007}_{-0.004}$	–	1.9±0.2	**0**,1,2	337.2
NGC 4945 4ULX			$N_{H,gal}$ = 0.14								
0112310301	19.55/24	0.72	$0.3^{+0.2}_{-0.2}$	–	–	$1.0^{+0.2}_{-0.2}$	$0.009^{+0.009}_{-0.005}$	–	2.3±0.2	**1**,2	345.5
0204870101	135.58/150	0.79	$0.5^{+0.1}_{-0.1}$	–	–	$1.1^{+0.1}_{-0.1}$	$0.017^{+0.004}_{-0.003}$	–	5.8±0.2	**0**,1	3891.3
Swift/XRT av.	52.51/49	0.34	$0.28^{+0.09}_{-0.08}$	–	–	$1.4^{+0.2}_{-0.1}$	$0.007^{+0.004}_{-0.003}$	–	5.9±0.3	–	1094.0
NGC 4945 6ULX			$N_{H,gal}$ = 0.14								
0112310301	69.85/78	0.73	$0.6^{+0.3}_{-0.2}$	<0.9	<3.2	$1.9^{+1.1}_{-0.3}$	$0.002^{+0.002}_{-0.002}$	0.6±0.2	4.6±0.3	**1**,2	640.9
0204870101	132.75/147	0.9	$0.6^{+0.3}_{-0.1}$	$0.3^{+0.2}_{-0.1}$	$0.7^{+13.1}_{-0.6}$	$1.8^{+0.3}_{-0.2}$	$0.002^{+0.001}_{-0.001}$	0.5±0.1	4.2±0.2	**0**,1	2368.6
Swift/XRT av.	39.51/51	0.88	–	–	$0.69^{+0.2}_{-0.2}$	$1.4^{+0.2}_{-0.1}$	$0.009^{+0.005}_{-0.003}$	–	7.8±0.4	–	1112.6
NGC 5055 1ULX			$N_{H,gal}$ = 0.037								

0405080301	180.51/164	0.18	0.037	$0.19^{+0.01}_{-0.01}$	$28.6^{+6.7}_{-5.2}$	$1.4^{+0.2}_{-0.1}$	$0.011^{+0.01}_{-0.004}$	3.8±0.2	7.6±0.5	**0**,1,2	2248.6
0405080501	54.29/50	0.31	0.037	$0.19^{+0.02}_{-0.02}$	$22.8^{+9.9}_{-6.5}$	$1.6^{+0.3}_{-0.3}$	$0.006^{+0.01}_{-0.003}$	3.1±0.3	8.0±0.6	**0**	1439.3
Swift/XRT av.	90.84/84	0.29	0.037	$0.22^{+0.02}_{-0.02}$	$11.0^{+4.7}_{-3.2}$	$1.8^{+0.4}_{-0.3}$	$0.004^{+0.004}_{-0.002}$	3.0±0.2	9.3±0.5	–	2090.8
NGC 5055 2ULX			$N_{H,gal}$ = 0.037								
0405080301	16.61/10	0.08	0.037	–	–	$1.6^{+0.8}_{-0.4}$	$0.0009^{+0.001}_{-0.0006}$	–	1.1±0.2	**0**,1,2	179.9
0405080501	16.82/18	0.54	0.037	–	–	$1.3^{+0.3}_{-0.2}$	$0.002^{+0.002}_{-0.001}$	–	0.9±0.2	**0**,1,2	143.1
NGC 5055 3ULX			$N_{H,gal}$ = 0.037								
0405080501	3.71/3	0.3	0.037	–	–	$0.4^{+0.2}_{-0.1}$	<0.7	–	0.7±0.2	**2**	101.6
NGC 4517 1ULX			$N_{H,gal}$ = 0.02								
0203170301	456.85/493	0.88	$0.7^{+0.1}_{-0.1}$	$0.06^{+0.04}_{-0.03}$	<3e6	$1.6^{+0.1}_{-0.1}$	$0.006^{+0.001}_{-0.001}$	3.0±1.4	7.7±1.6	**0**,1,2	7159.1

Table 3.4: In this table: spectral-fitting of the *XMM-Newton* data with two thermal components: TBABS*(BBODYRAD+DISKBB) in XSPEC.
(1) Observation ID (2) Ratio between χ^2 and degrees of freedom (dof) (3) Null hypothesis probability for the spectral model: we consider a fit statistically acceptable when P_{val} >0.05, corresponding to $\sim 2\sigma$ (4) Hydrogen column density ($n_{\rm H}$) in units of $cm^{-2}\times10^{22}$; we imposed a minimum equal to the Galactic value, the latter is reported in the table for each galaxy (5) Black body temperature in keV units (6) Black body normalization (7) Inner disc temperature in keV units (8) Disc normalization (9) Black body flux in 0.3-10 keV, in units of 10^{-13} erg cm^{-2} s^{-1} (10) Disc flux in 0.3-10 keV, in units of 10^{-13} erg cm^{-2} s^{-1} (11) Instruments data used in the spectral analysis: 0=pn, 1=MOS1, 2=MOS2 (12) Net counts of pn or, when the source is not visible in the pn image, the MOS1 (or MOS2 when the source is visible only in the MOS2 image) net counts. We highlight in bold the instrument in column 11, to which the reported net counts correspond.
We also report the spectral parameters obtained from the spectral-fitting of the *Swift*/XRT average spectrum, when possible. In the other cases we just report the average parameters derived from the *XMM-Newton* best-fitting parameters, used to convert *Swift*/XRT count rate to flux.

Circinus 4ULX:
Circinus 4ULX is well fitted by two thermal components (a BBODYRAD + DISKBB). Variability is seen in the spectral parameters, especially in the blackbody temperature. In observation 0792382701, the ULX has a smaller inner disc temperature than in the other epochs and also a single DISKBB is an acceptable fit in this case.

Circinus 6ULX:
This source was indicated as a ULX in Swartz et al. (2004). In the considered *Swift*/XRT data it is found around 10^{39} erg s^{-1} with large error bars and only occasionally above it. In the *XMM-Newton* spectra just one thermal component, i.e. a DISKBB, is needed to fit data. The statistics of the two thermal components model is similar to that of the single component model. Just in one observation, 0792382701, the second thermal component, i.e. BBODYRAD, represent a significant improvement in the spectral model. In the *XMM-Newton* exposures the source is observed under the ultraluminous threshold.

M101 2ULX:
The statistics is scanty in the *XMM-Newton* observations, therefore we used just a DISKBB component to derive the fluxes from the *XMM-Newton* spectra of 2ULX.

M101 16ULX:
The statistics of the source is rather low. In observation 0212480201, with the smaller statistics, we used just a DISKBB to fit the data. In the other observations we applied the two components model (BBODYRAD + DISKBB). The fit is statistically acceptable both in observation 0164560701 and 0104260101, but in the latter the fit statistics is low. In observation 0164560701 the normalization of the hot component is an upper limit, which may suggest that this component is not needed, instead it is necessary to make the fit acceptable. In observation 0824450501 the two components fit is not an acceptable model for the data. Both in 0104260101 and 0824450501 some residuals are present around 1 keV, with a similar shape to that often found in ULXs where winds have been detected (e.g. Middleton et al. 2014, 2015c, Pinto et al. 2016, 2017). We found a large improvement to the fit by adding a thermal plasma component (APEC in XSPEC), with temperature ~ 1.2 keV. The low statistics in our data did not allow us to do a more detailed study.

M101 24ULX:
The two thermal components model (BBODYRAD +DISKBB) gives a good fit for M101 24ULX. The fit parameters are consistent among the observations within the uncertainties. In the two observations where we used the Galactic n_H for the fit we found a negligible additional intrinsic contribution of the order of 10^{10} and 10^{17} cm^{-2}.

M101 27ULX:
Both the thermal components, i.e. BBODYRAD and DISKBB are detected. The spectra are consistent among the observations, except for a possible variability in observation 0164560701, especially in the normalizations of the two components. For all the observations the additional contribution of the intrinsic n_H to the Galactic one is negligible ($< 10^{16}$ cm^{-2}).

M101 28ULX:
The statistics is low and most of the emission is below 1 keV. Just one thermal component, i.e. a DISKBB or a BBODYRAD, is needed to fit the data. The results for both models are reported in table 3.4. The temperature is smaller than 0.1 keV and this ULX is a supersoft ULX, or ULS, as already reported in the literature (Soria and Kong 2016, Urquhart and Soria 2016a). The characteristics of the ULS are described in section 1.2.4.

M101 29ULX:
We analysed only observations 0104260101 and 0164560701, with a BBODYRAD + DISKBB model,

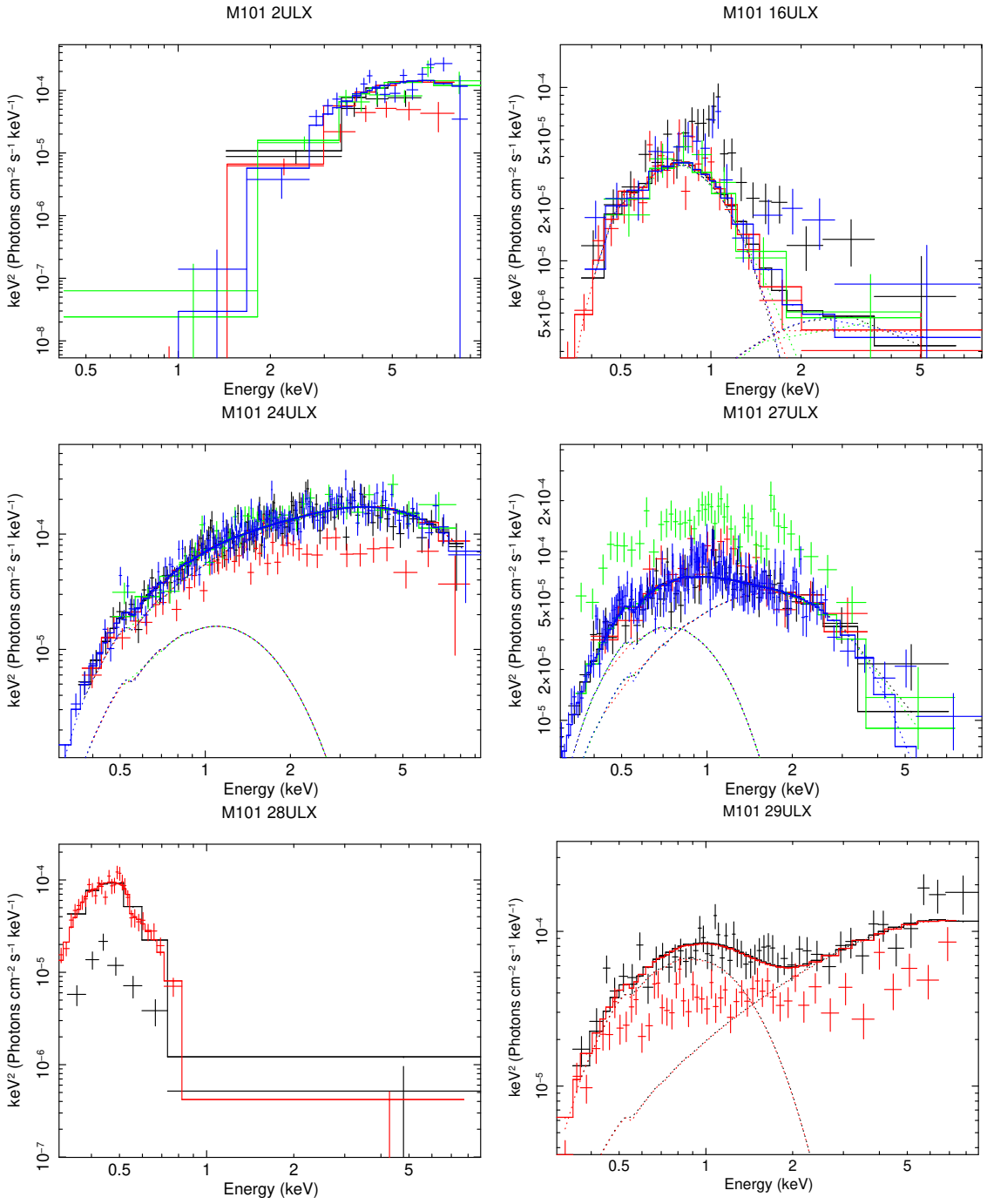

Figure 3.6: *XMM-Newton* spectra for each observation where the ULXs are detected. We report for each observation the data of the instrument highligthed in bold in column (11) of table 3.4. We also plot the model TBABS*(BBODYRAD+DISKBB) from the spectral fitting of the observation with the larger statistics. M101 2ULX: black: 0104260101, red: 0164560701, green: 0212480201, blue: 0824450501, model: 0824450501. M101 16ULX: black: 0104260101, red: 0164560701, green: 0212480201, blue: 0824450501, model: 0164560701. M101 24ULX: black: 0104260101, red: 0164560701, green: 0212480201, blue: 0824450501, model: 0824450501. M101 27ULX: black: 0104260101, red: 0164560701, green: 0212480201, blue: 0824450501, model: 0824450501. M101 28ULX: black: 0164560701, red: 0212480201, model: 0212480201. M101 29ULX: black: 0104260101, red: 0164560701, model: 0164560701.

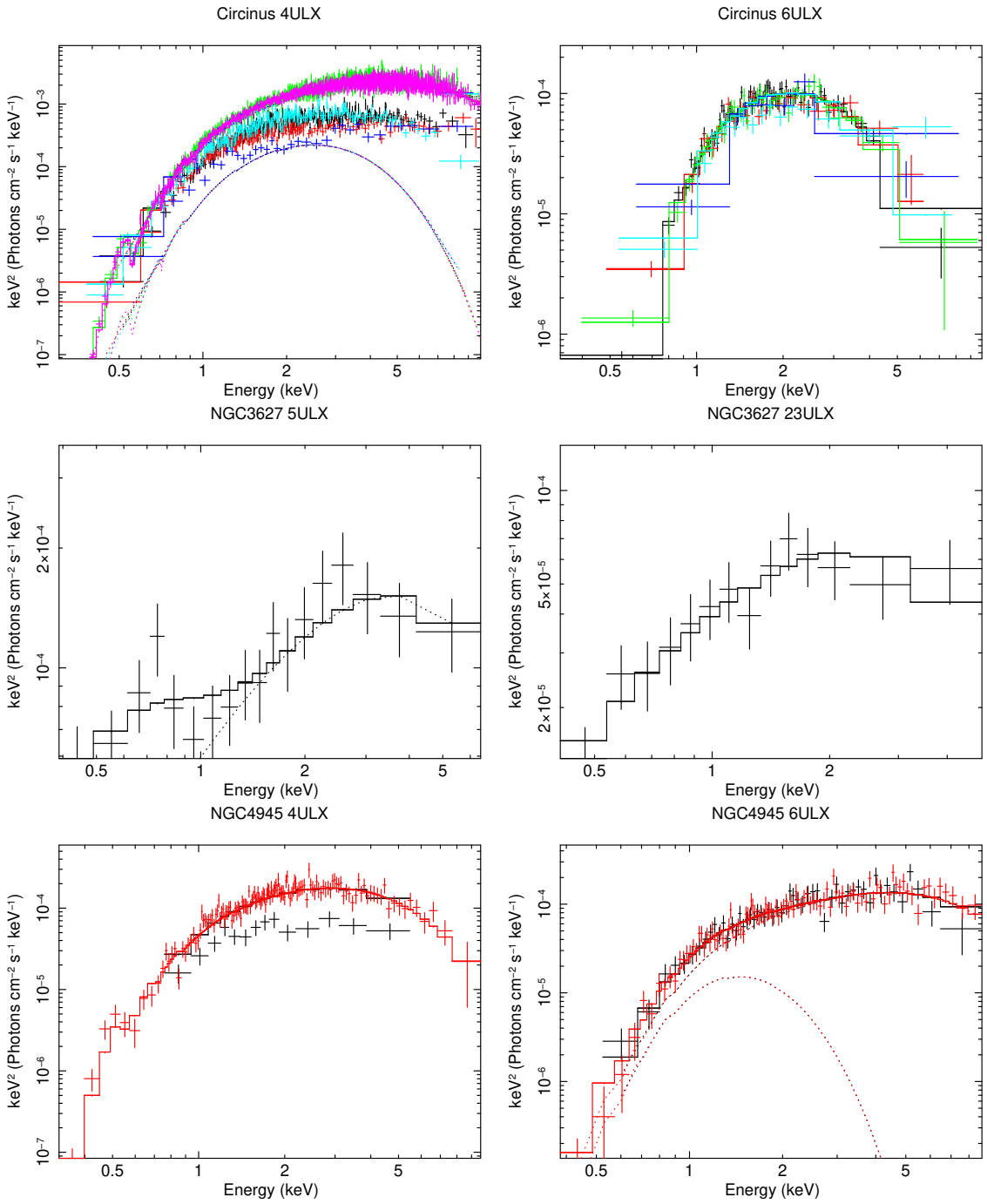

Figure 3.7: *XMM-Newton* spectra for each observation where the ULXs are detected. We report for each observation the data of the instrument highligthed in bold in column (11) of table 3.4. We also plot the model TBABS*(BBODYRAD+DISKBB) from the spectral fitting of the observation with the larger statistics. Circinus 4ULX: black: 0111240101, red: 0656580601, green: 0701981001, blue: 0780950201, cyan: 0792382701, magenta: 0824450301, model: 0824450301. Circinus 6ULX: black: 0111240101, red: 0656580601, green: 0701981001, blue: 0780950201, cyan: 0792382701, model: 0111240101. NGC 3627 5ULX and NGC 3627 23ULX: obsID 0093641101. NGC 4945 4ULX and NGC 4945 6ULX: black: 0112310301, red: 0204870101, model: 0204870101.

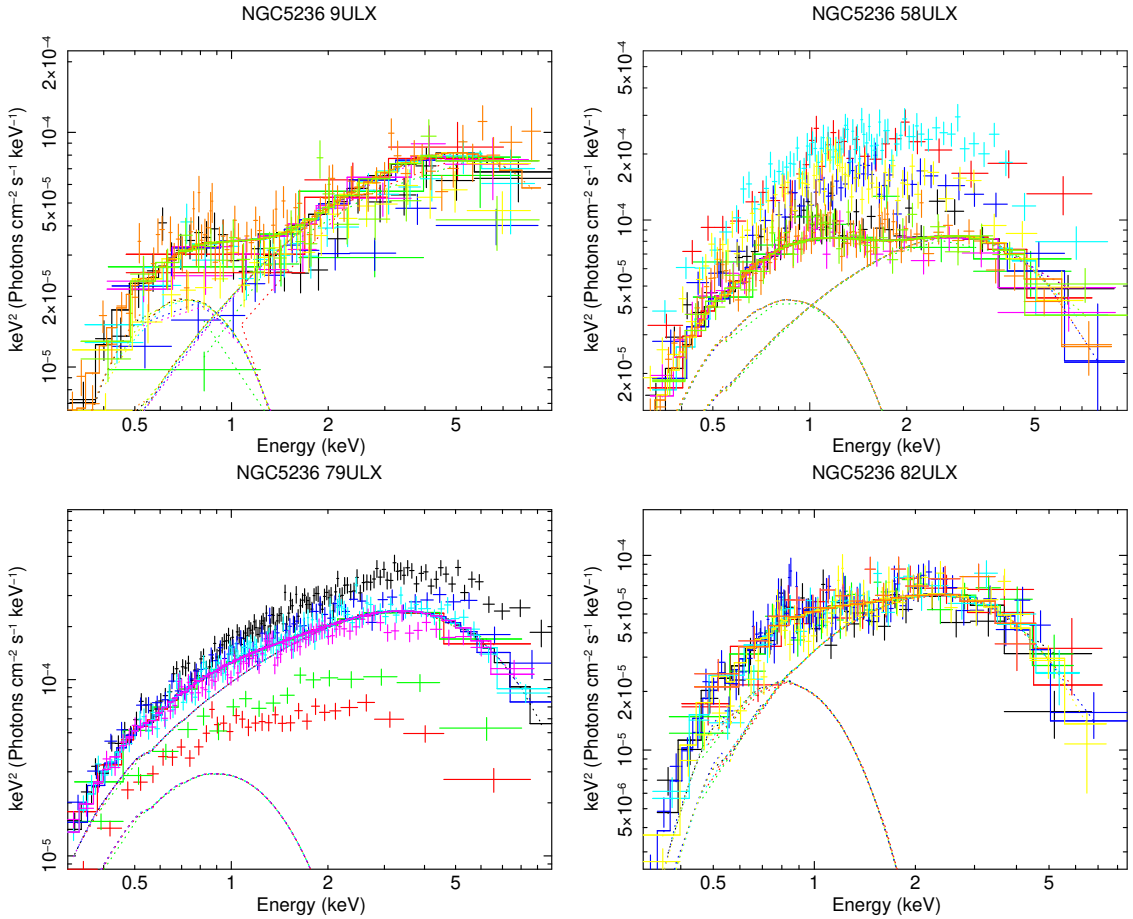

Figure 3.8: *XMM-Newton* spectra for each observation where the ULXs are detected. We report for each observation the data of the instrument highligthed in bold in column (11) of table 3.4. We also plot the model TBABS*(BBODYRAD+DISKBB) from the spectral fitting of the observation with the larger statistics. NGC 5236 9ULX and NGC 5236 58ULX: black: 0110910201, red: 0503230101, green: 0552080101, blue: 0723450101, cyan: 0723450201, magenta: 0729561001, yellow: 0729561201, orange: 0761620101, green2: 0761620201, model: 0761620101. NGC 5236 79ULX: black: 0723450101, red: 0723450201, green: 0729561001, blue: 0729561201, cyan: 0761620101, magenta: 0761620201, model: 0761620101. NGC 5236 82ULX: black: 0110910201, red: 0552080101, green: 0723450101, blue: 0723450201, cyan: 0729561001, magenta: 0729561201, yellow: 0761620101, orange: 0761620201, model: 0723450201.

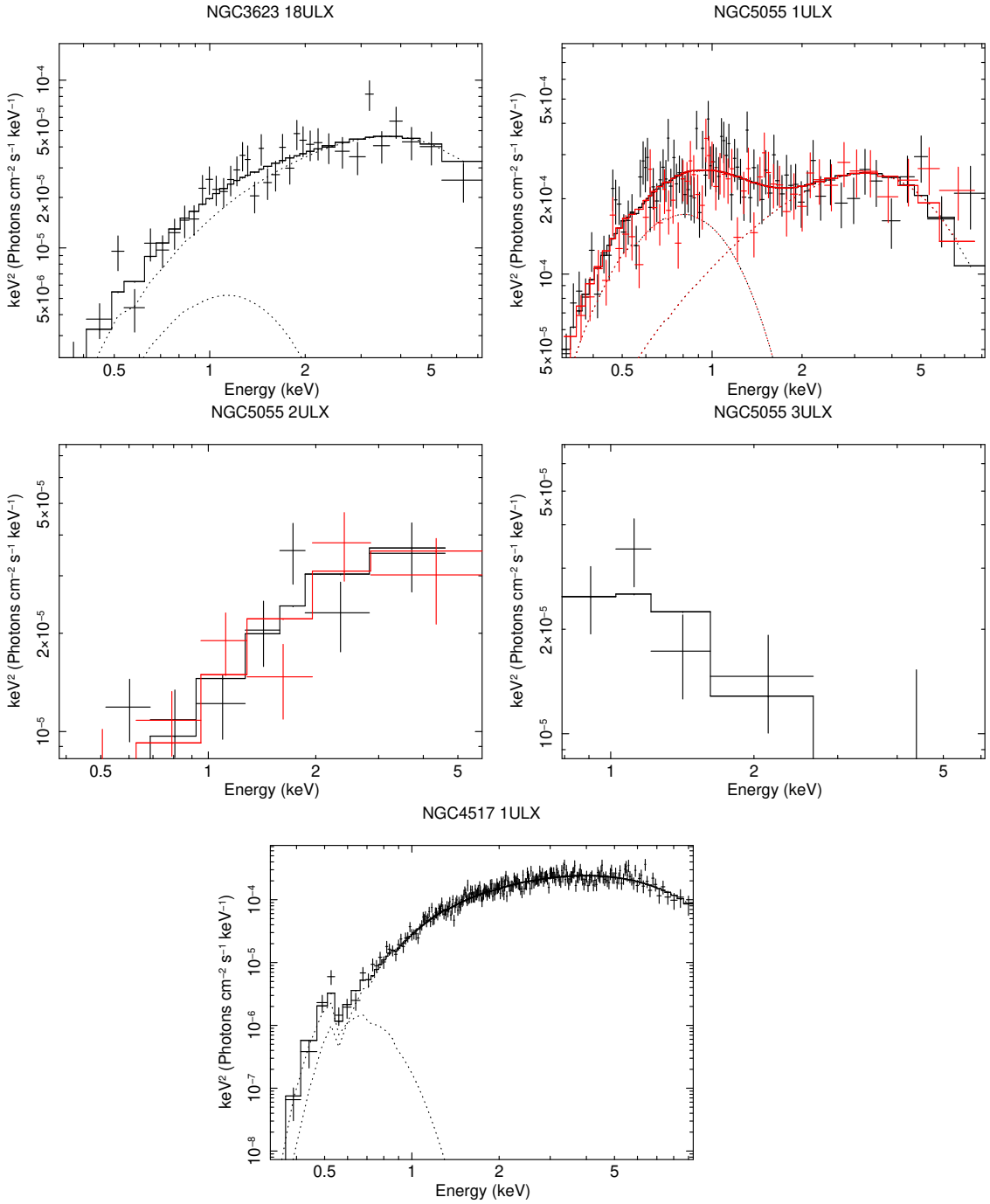

Figure 3.9: *XMM-Newton* spectra for each observation where the ULXs are detected. We report for each observation the data of the instrument highligthed in bold in column (11) of table 3.4. We also plot the model TBABS*(BBODYRAD+DISKBB) from the spectral fitting of the observation with the larger statistics. NGC 3623 18ULX: obsID: 0082140301. NGC 5055 1ULX and NGC 5055 2ULX: black: 0405080301, red: 0405080501, model: 0405080301. NGC 5055 3ULX: obsID: 0405080501. NGC 4517 1ULX: obsID: 0203170301.

because in the other observations the source was too weak or out of the field of view. No spectral variability is found in these data. The n_H is consistent with the Galactic one; the additional contribution of the intrinsic n_H would be smaller than 10^{16} cm^{-2}.

NGC 5236 9ULX:
The candidate ULX NGC 5236 9ULX is a source that occasionally overcomes the ultraluminous threshold of 10^{39} erg s^{-1}, in the *Swift*/XRT data. The two thermal components fit, i.e. BBODYRAD + DISKBB, is usually a good model. The n_H cannot always be constrained, which can influence the flux estimation. When we use the Galactic value for the n_H, the additional local contribution is smaller than 10^{15} cm^{-2}. In most of the *XMM-Newton* observations both the thermal components are present, except in the two observations with the smaller statistics, where we used just a DISKBB to fit the data, suggesting that it may really be an ultraluminous X-ray binary.

NGC 5236 58ULX:
Despite the large flux variability, we found only little spectral variability for this source. The blackbody (BBODYRAD) temperature shows some differences among the observations, while the disc (DISKBB) inner temperature is consistent among the observations within the uncertainties. The n_H is consistent with the Galactic one in some observations, with an upper limit on the additional local contribution of 0.01×10^{22} cm^{-2}.

NGC 5236 79ULX:
We applied the two thermal components fit (BBODYRAD + DISKBB), to all the *XMM-Newton* observations of this ULX. The blackbody temperature appears constant among the observations, inside the error bars. Some variations are seen instead in the disc temperature.

NGC 5236 82ULX:
It is a candidate ULX, occasionally overcoming 10^{39} erg s^{-1} in the *Swift*/XRT data. In the *XMM-Newton* observation 0761620101, NGC 5236 82ULX is ultraluminous, with a luminosity of $\sim1.6\times10^{39}$ erg s^{-1}. In some of the observations two thermal components (BBODYRAD + DISKBB) are present, while in others just one component (DISKBB) is needed to describe the spectrum. The observations where only one component is present are also low statistics observations, where the $n_{\rm H}$ is not well determined and thus we fixed it to the Galactic value, which may influence the overall fit. We found an upper limit of 0.03×10^{22} cm^{-2} on the additional intrinsic contribution.

NGC 3623 18ULX:
Just one *XMM-Newton* observation is available for this source. Both thermal components (BBODYRAD and DISKBB) are present in the spectrum, but the disc component dominates the source flux, contributing to ∼90% of the emission.

NGC 3627 5ULX:
Both thermal components (BBODYRAD and DISKBB) are present in the spectrum. There is only one *XMM-Newton* observation for this galaxy, thus we cannot search for spectral variability in the ULXs of NGC 3627 with the currently available data. The n_H is consistent with the Galactic value, while the local contribution is just of the order of 10^{15} cm^{-2}.

NGC 3627 23ULX:
We used only one thermal component, i.e. the DISKBB, to fit the spectrum of this source, which has a low statistics and it is in the ultraluminous range in the *XMM-Newton* data.

NGC 4945 4ULX:
The fits with the BBODYRAD+DISKBB model and with just a disc give similar statistics. In the double components fit the parameters are not well constrained in the lower statistics observation 0112310301; we thus report in the table the one component fit.

NGC 4945 6ULX:
We used the double thermal components model (BBODYRAD + DISKBB) with the Galactic n_H. We found an upper limit on the local absorption contribution of 0.03×10^{22} cm^{-2}. In observation 0112310301, which has a small statistics, the blackbody is not well constrained.

NGC 5055 1ULX:
1ULX is the most luminous of the three ULXs in the galaxy NGC 5055. Two *XMM-Newton* exposures are available and, in both, the ULX has two thermal components, i.e. BBODYRAD and DISKBB. No spectral variability is present among the two epochs. The absorption is consistent with the Galactic one, we found an upper limit of 0.01×10^{22} and 0.04×10^{22} cm^{22} on the local absorption in the two observations, 0405080301 and 0405080501 respectively.

NGC 5055 2ULX:
Just one thermal component is needed for modelling the spectrum, which has a scanty statistics. We thus used a DISKBB. The parameters in the two observations are consistent within the errors. The absorption is consistent with the Galactic $n_{\rm H}$, we found an upper limit of 0.05×10^{22} and 0.04×10^{22} cm^{-2} on the local absorption in observation 0405080301 and 0405080501 respectively.

NGC 5055 3ULX:
This source is visible in just one *XMM-Newton* observation and it is not ultraluminous in this epoch. In the recent *Swift*/XRT monitoring the source was detected only a few times, while in most of the observations it was below the detection threshold of the instrument. We modelled its *XMM-Newton* spectrum with a DISKBB. The $n_{\rm H}$ is consistent with the Galactic one, with a negligible contribution from the local absorption of the order of 10^{14} cm^{-2}.

NGC 4517 1ULX:
There is one *XMM-Newton* observation of NGC 4517, where the ULX is visible with all the three EPIC cameras. It is well modelled with the double thermal component fit (BBODYRAD + DISKBB).

NGC 925 ULX-1, ULX-2, ULX-3:
For the ULXs in NGC 925, the double thermal components model (BBODYRAD + DISKBB) is a good fit for the *XMM-Newton* data. In addition, we have also analysed *NuSTAR* and *Chandra* data for these sources. The results of the spectral fitting for the ULXs of NGC 925 are reported in table 3.10 and they are discussed in sections 3.5.2 and 3.5.3.

OBS. ID[(1)]	$R^{(2)}_{bb}$ km	$R^{(3)}_{diskbb,1.7}$ km	$R^{(4)}_{diskbb,3}$ km	$M^{(5)}_{BH}$ $M_\odot$
Circinus 4ULX				
0111240101	594^{+146}_{-97}	53^{+16}_{-16}	166^{+48}_{-49}	19
0656580601	994^{+367}_{-243}	49^{+13}_{-11}	151^{+40}_{-34}	17
0701981001	376^{+247}_{-110}	111^{+8}_{-9}	345^{+26}_{-28}	39
0780950201	1509^{+1151}_{-658}	31^{+7}_{-9}	96^{+22}_{-28}	11
0792382701	694^{+1104}_{-311}	154^{+28}_{-35}	478^{+88}_{-108}	54
0824450301	266^{+31}_{-36}	106^{+9}_{-9}	331^{+27}_{-29}	37
Circinus 6ULX				
0111240101	–	194^{+23}_{-26}	605^{+71}_{-81}	68
0656580601	–	137^{+31}_{-18}	428^{+96}_{-57}	48
0701981001	–	182^{+24}_{-14}	566^{+76}_{-42}	64
0780950201	–	168^{+38}_{-31}	524^{+118}_{-96}	59
0792382701	297^{+144}_{-67}	–	–	–
M101 2ULX				
0104260101	–	229^{+27}_{-31}	713^{+84}_{-96}	80
0164560701	–	28^{+2}_{-2}	87^{+7}_{-8}	10
0824450501	–	38^{+26}_{-15}	118^{+80}_{-47}	13

M101 16ULX				
0104260101	4840^{+4314}_{-1988}	73^{+138}_{-4}	228^{+430}_{-11}	26
0164560701	3916^{+4250}_{-1681}	–	–	–
0824450501	18494^{+88407}_{-14533}	114^{+229}_{-78}	356^{+713}_{-244}	40
M101 24ULX				
0104260101	857^{+2169}_{-857}	89^{+14}_{-53}	276^{+43}_{-163}	31
0164560701	443^{+143}_{-221}	63^{+40}_{-27}	195^{+124}_{-83}	21
0212480201	383^{+159}_{-162}	51^{+30}_{-51}	159^{+93}_{-159}	18
0824450501	700^{+717}_{-317}	81^{+8}_{-9}	252^{+24}_{-27}	28
M101 27ULX				
0104260101	2747^{+917}_{533}	198^{+82}_{-36}	617^{+256}_{-113}	69
0164560701	1980^{+394}_{-294}	81^{+188}_{-45}	252^{+584}_{-139}	28
0212480201	3744^{+873}_{-605}	380^{+119}_{-99}	1181^{+371}_{-309}	133
0824450501	2675^{+328}_{-260}	256^{+47}_{-27}	797^{+146}_{-84}	90
M101 29ULX				
0104260101	2158^{+317}_{-266}	20^{+9}_{-7}	62^{+33}_{-26}	7
0164560701	1743^{+369}_{-275}	23^{+13}_{-7}	71^{+41}_{-21}	8
NGC 5236 9ULX				
0110910201	1112^{+184}_{-149}	15^{+5}_{-5}	48^{+16}_{-14}	5
0723450201	828^{+1624}_{-464}	–	–	–
0729561001	1464^{+1422}_{-636}	15^{+6}_{-8}	48^{+20}_{-24}	5
0729561201	665^{+1862}_{-455}	20^{+11}_{-7}	63^{+35}_{-22}	7
0761620101	1270^{+858}_{-483}	19^{+4}_{-4}	59^{+13}_{-11}	7
0761620201	1180^{+2200}_{-604}	24^{+10}_{-7}	76^{+31}_{-22}	9
NGC 5236 58ULX				
0110910201	2741^{+3692}_{-1874}	62^{+5}_{-1}	194^{+14}_{-5}	22
0503230101	854^{+143}_{-126}	–	–	–
0552080101	1648^{+1136}_{-507}	109^{+24}_{-32}	338^{+76}_{-99}	38
0723450101	879^{+203}_{-167}	109^{+24}_{-32}	338^{+76}_{-99}	38
0723450201	1019^{+721}_{-371}	133^{+21}_{-24}	415^{+64}_{-76}	47
0729561001	1296^{+249}_{-184}	81^{+31}_{-16}	251^{+96}_{-51}	28
0729561201	1019^{+327}_{-205}	109^{+24}_{-32}	338^{+76}_{-99}	38
0761620101	1051^{+236}_{-172}	60^{+17}_{-11}	185^{+54}_{-34}	21
0761620201	952^{+141}_{-124}	49^{+20}_{-14}	151^{+63}_{-44}	17
NGC 5236 79ULX				
0723450101	576^{+316}_{-182}	69^{+4}_{-4}	214^{+13}_{-14}	24
0723450201	1378^{+979}_{-512}	73^{+11}_{-13}	227^{+35}_{-42}	26
0729561001	1161^{+1812}_{-691}	69^{+16}_{-14}	214^{+48}_{-45}	24
0729561201	854^{+187}_{-141}	69^{+8}_{-9}	214^{+25}_{-29}	24
0761620101	828^{+343}_{-233}	73^{+4}_{-4}	227^{+12}_{-13}	26
0761620201	892^{+138}_{-120}	69^{+4}_{-4}	214^{+13}_{-14}	24
NGC 5236 82ULX				
0110910201	2531^{+5650}_{-1717}	109^{+24}_{-32}	338^{+76}_{-99}	38
0552080101	–	84^{+30}_{-48}	262^{+93}_{-48}	30
072345101	–	88^{+29}_{-11}	273^{+90}_{-34}	31
0723450201	1426^{+1441}_{-668}	81^{+14}_{-12}	251^{+42}_{-37}	28
0729561001	1838^{+3412}_{-1126}	81^{+23}_{-21}	251^{+70}_{-65}	28
0729561201	–	133^{+21}_{-24}	415^{+64}_{-76}	47
0761620101	5263^{+15769}_{-4688}	109^{+45}_{-32}	338^{+140}_{-99}	38
0761620201	2777^{+2735}_{-1390}	97^{+27}_{-13}	303^{+83}_{-41}	34
NGC 3623 18ULX				
0082140301	729^{+1898}_{-729}	69^{+24}_{-31}	214^{+73}_{-97}	24
NGC 3627 5ULX				
0093641101	3681^{+2452}_{-1320}	97^{+26}_{-22}	302^{+80}_{-68}	34
NGC 3627 23ULX				
0093641101	–	150^{+39}_{-28}	469^{+121}_{-86}	53
NGC 4945 4ULX				
0112310301	–	56^{+23}_{-19}	174^{+72}_{-58}	20
0204870101	–	77^{+9}_{-7}	239^{+27}_{-22}	27
NGC 4945 6ULX				
0112310301	–	26^{+22}_{-26}	82^{+34}_{-82}	9
0204870101	301^{+1036}_{-187}	26^{+6}_{-8}	82^{+18}_{-24}	9
NGC 5055 1ULX				
0405080301	4813^{+534}_{-460}	154^{+59}_{-31}	481^{+183}_{-97}	54
0405080501	4297^{+849}_{-664}	114^{+72}_{-33}	355^{+225}_{-104}	40
NGC 5055 2ULX				
0405080301	–	44^{+20}_{-19}	138^{+62}_{-58}	16
0405080501	–	66^{+27}_{-19}	205^{+85}_{-60}	23
NGC 4517 1ULX				

0203170301	–	109^{+9}_{-10}	339^{+27}_{-30}	38
NGC 925 ULX1				
0784510301	2106^{+299}_{-239}	89^{+9}_{-9}	276^{+28}_{-27}	31
NGC 925 ULX2				
0784510301	933^{+356}_{-244}	21^{+9}_{-6}	64^{+27}_{-18}	7
NGC 925 ULX3				
0784510301	3766^{+2023}_{-1248}	36^{+37}_{-21}	111^{+111}_{-66}	13

Table 3.5: (1) Observation ID
(2) Emitting radius for the BBODYRAD component
(3) Emitting radius for the DISKBB component, assuming a colour correction factor 1.7
(4) Emitting radius for the DISKBB component, assuming a colour correction factor 3
(5) Hypothetical BH mass derived by $R_{diskbb,3}$, assuming that it corresponds to the ISCO of an accreting BH, in solar mass units

Emitting radii:
The hotter spectral component is thought to originate from the emission of the inner accretion flow, or alternatively may come from a corona covering the inner regions of the accretion flow. The colder spectral component is thought to arise from the emission of the wind photosphere or of the external regions of the accretion disc. We thus expect to find a large emitting radius for the colder component and a smaller radius for the hotter one, consistent with what we have found (see table 3.5), except for Circinus 4ULX while using a colour correction of 3, which results in comparable radii for the two components. This suggests that a smaller colour correction may be more appropriate in this source, or that the source is seen at an inclination angle smaller than 60 deg, which would imply a smaller radius for the hot spectral component. A small inclination for Circinus 4ULX is also consistent with the absence of a strong wind as reported in the analysis of the *XMM-Newton* RGS data done by Mondal et al. (2021a). One, in principle, could link the emitting region of the hot spectral component to the innermost stable circular orbit (ISCO) in case of a BH accretor, which is defined as a multiple of the Schwarzschild radius ($R_s = \frac{2GM}{c^2}$; $R_{ISCO} = 3R_s$ for a non-rotating BH). In the last column of table 3.5, we report the hypothetical mass for the central compact object estimated from the hotter emitting radius, should this distance correspond to the ISCO of a non-rotating BH and an $f_c = 3$. The values we obtained are all consistent with a stellar mass BH in each source. We have to note that the interpretation of the emitting radius derived from the spectral fitting as the inner edge of the accretion disc may not be correct, considering that we expect to have a super-Eddington accreting system and thus the spectral modelling with a multicolour blackbody disk is just a simplification of the real situation. Even if not corresponding to the inner edge of the accretion disc, which may be covered by the inflated disc and the winds, the derived radii are too small to be emitted by a system containing an IMBH, whose radius would be > 900 km. In some ULXs, i.e. Circinus 4ULX, M101 27ULX, NGC 5236 58ULX, NGC 5236 82ULX, the radius of the hot component is variable among the observations, thus difficult to interpret it simply as the inner edge of the accretion disc corresponding to the ISCO. Should the inner disc radius differ from the ISCO, we would need a truncation of the disc beyond the ISCO radius, which is improbable for these sources, as also discussed in Walton et al. (2013) in the case of Circinus 4ULX, because such truncations are only expected for very low accretion rates (e.g. Tomsick et al. 2009). The variability observed in R_{diskbb} may be associated to a variable f_c instead of a true geometrical change in the disc structure. Otherwise, it is possible that we see the inner regions of the accretion flow just in some of the observations, while the inner regions of the accretion flow are covered by the outflows or by a corona-like structure in the observations where we observe the larger radii. In such a case, we would expect a larger temperature in the observations when the hot inner accretion flow is visible and the emitting radius is smaller and a smaller temperature when we can see more external regions. We evaluated the Spearman correlation coefficient, by using the PYTHON library SCIPY.STATS.SPEARMANR, to look for any possible correlation among luminosity-temperature, radius-temperature and radius-luminosity, see table 3.6. For M101 27ULX, NGC 5236 58ULX, NGC 5236 82ULX (see figure 3.10) we found a strong anti-correlation among the DISKBB radius and its temperature as expected.

	COLD		HOT	
	coeff	P_{val}	coeff	P_{val}
Circinus 4ULX				
$L-T$	0.38	0.46	–0.32	0.53
$R-T$	–0.82	0.04	–0.62	0.19
$R-L$	0.15	0.78	0.83	0.04
Circinus 6ULX				
$L-T$	–	–	–0.11	0.90
$R-T$	–	–	–0.63	0.37
$R-L$	–	–	0.80	0.20
M101 24ULX				
$L-T$	1.0	0	0.99	0.05
$R-T$	–1.0	0	–0.63	0.37
$R-L$	–1.0	0	–0.40	0.6
M101 27ULX				
$L-T$	0.74	0.26	–0.95	0.05
$R-T$	–0.32	0.68	–1.0	0
$R-L$	0.20	0.8	0.95	0.05
NGC 5236 9ULX				
$L-T$	–0.50	0.39	0.37	0.54
$R-T$	–0.7	0.19	–0.92	0.03
$R-L$	0.3	0.62	0	1.0
NGC 5236 58ULX				
$L-T$	0.52	0.19	-0.60	0.12
$R-T$	-0.86	0.01	-0.75	0.03
$R-L$	-0.24	0.56	0.78	0.02
NGC 5236 79ULX				
$L-T$	0.56	0.25	0.99	0.0003
$R-T$	–0.88	0.02	–0.53	0.29
$R-L$	–0.15	0.77	–0.41	0.41
NGC 5236 82ULX				
$L-T$	–0.67	0.22	–0.17	0.70
$R-T$	–0.89	0.04	–0.94	0.0004
$R-L$	0.90	0.04	0.42	0.30

Table 3.6: Spearman's rank correlation coefficients for the cold (BBODYRAD) and hot (DISKBB) spectral component of the spectral model TBABS*(BBODYRAD+DISKBB). We indicate both the correlation and the corresponding P_{value}, for Luminosity-Temperature, Radius-Temperature, Radius-Luminosity for each of the components.

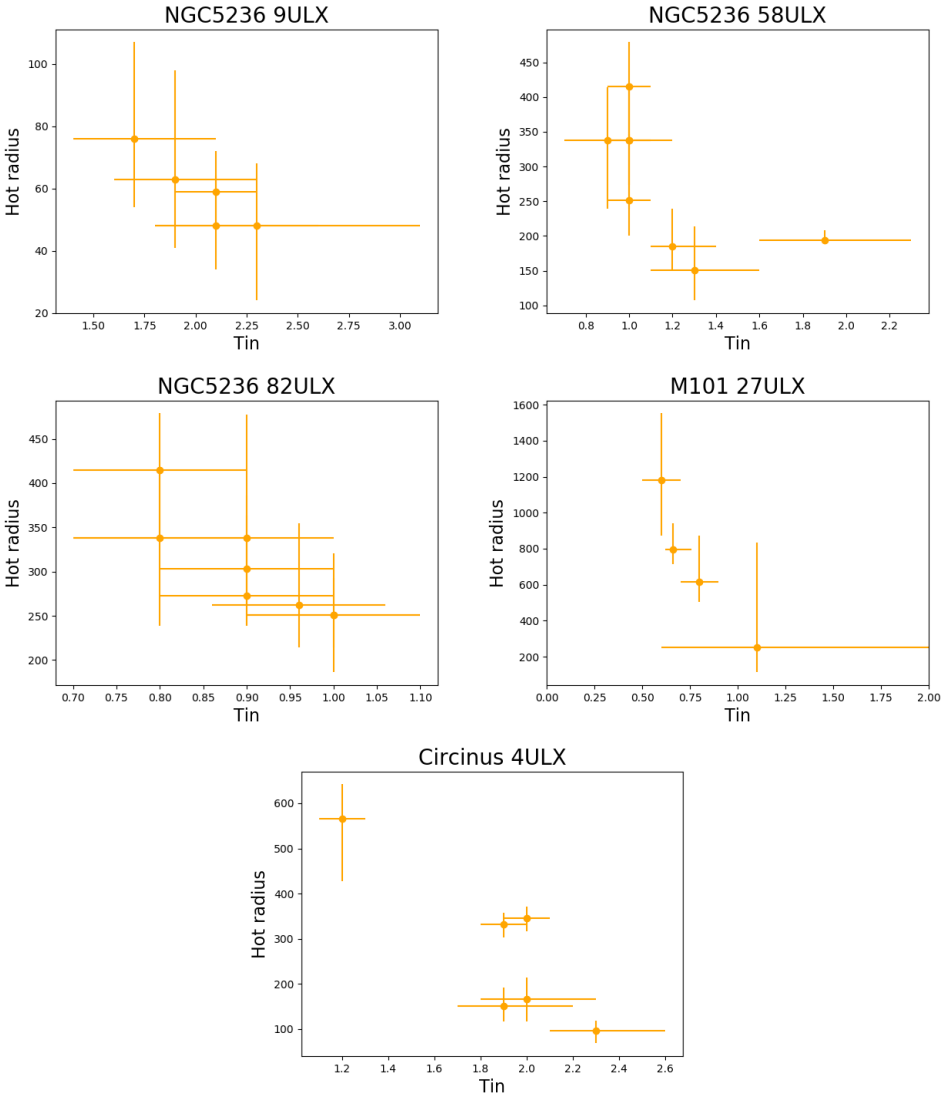

Figure 3.10: Anti-correlation among DISKBB radius and its inner temperature T_{in}.

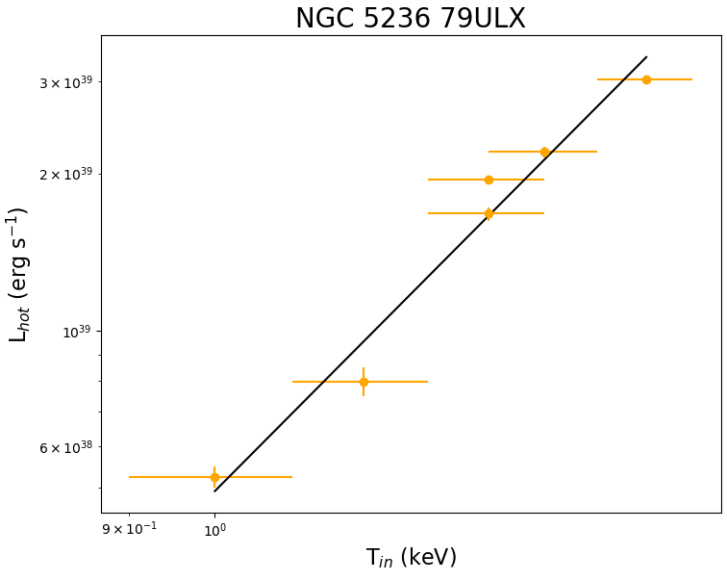

Figure 3.11: Luminosity of the DISKBB spectral component with *XMM-Newton* data in the band (0.001-10) keV vs. its inner temperature T_{in} in keV for NGC 5236 79ULX. We also plot the result of the fit with a power-law (solid black line): the best fit power-law index is ~ 3.6.

The anti-correlation seems evident by eye also for Circinus 4ULX, but the statistical significance is low ($P_{val} > 0.05$). The Spearman coefficient may have missed it because it does not consider the uncertainties in the calculation. An anti-correlation among DISKBB radius and temperature is also found for NGC 5236 9ULX. The relationship among bolometric luminosity (we use the luminosity in 0.001-10 keV) and temperature is useful to study the disc structure. A standard thin disc is expected to have $L \propto T^4$ (Shakura and Sunyaev 1973), while for an advection dominated disc the expected relation is $L \propto T^2$ (Watarai et al. 2000). In some ULXs an anti-correlation, i.e. $L \propto T^{-4}$ has been observed, usually in the soft spectral component, and suggests the influence of a strong wind (e.g. Walton et al. 2020, Robba et al. 2021, Gúrpide et al. 2021a). A significant correlation (or anti-correlation) between luminosity and temperature in our sample is present just for M101 24ULX, M101 27ULX and NGC 5236 79ULX. We fit the values obtained for these three sources with a power-law model to determine the power-law index and compare the resulting values with theoretical expectations. Unfortunately, the small number of points and the large error bars did not allow us to constrain the fitting parameters for M101 24ULX and M101 27ULX. For NGC 5236 79ULX we instead obtained a power-law index $\alpha = 3.6 \pm 0.4$, compatible with those usually found in sub-Eddington accretors (fig. 3.11). This suggests that NGC 5236 79ULX was not accreting at strongly super-Eddington rates in the considered observations and that the observed DISKBB radius may really correspond to the inner edge of the accretion disc, which is also consistent with the constant value found for R_{diskbb} in this case. In addition, if the accretion flow is not strongly super-Eddington the radii estimated with an $f_c = 1.7$ may be more reliable estimates, suggesting a light stellar mass BH with $M < 10\ M_{\odot}$. Considering the DISKBB radius and its luminosity, we found a significant positive correlation in sources Circinus 4ULX, M101 27ULX, NGC 5236 58ULX. A possible interpretation is that at the higher accretion rates, we cannot directly observe the inner regions of the accretion flow which may be covered by the outflows. In such a situation we could see the emission coming from an outer emitting radius with respect to epochs with a smaller contribution of the wind component. We have compared the derived radii with the radius of the ISCO for a non-rotating BH. The ISCO for an extreme co-rotating BH would be larger, with a maximum increase of a factor 12 (Zhang and Liu 2019), allowing in some cases the presence of an IMBH, but just with $f_c = 3$ and if we are really looking at the inner edge of

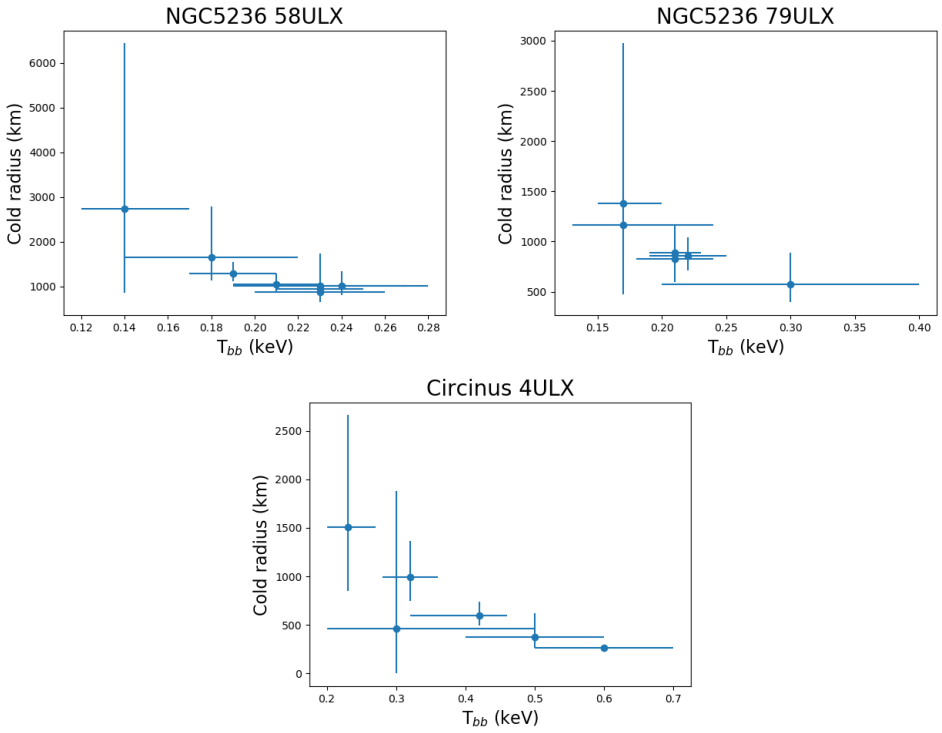

Figure 3.12: BBODYRAD radius vs. its temperature (*XMM-Newton* data) for NGC 5236 58ULX, NGC 5236 79ULX, Circinus 4ULX.

the accretion disc, which is improbable in super-Eddington accretors, while it is more probable that in most cases we are observing a slightly external region. To directly see the innermost regions of the accretion flow, uncovered by the outflows or the modified disc structure, we should have a nearly face-on line of sight, which would make the estimated emitting radii smaller, thus again in favour of stellar mass accretors, i.e. sMBHs or NSs.

The soft colder spectral component may be attributed to the emission of the wind photosphere or to the emission of the outer disc, expected to be a standard thin disc. An anti-correlation among the radius and temperature of the cold spectral component is present for Circinus 4ULX, M101 24ULX, NGC 5236 58ULX, NGC 5236 79ULX and NGC 5236 82ULX (fig. 3.12). This is consistent with an accretion disc, where we expect lower temperatures at increasing radii. When the accretion rate increases the spherization radius, , i.e. where the winds begin to be launched, becomes larger, thus such a trend may also indicate a wind launched from an external and thus colder region. On the other hand, no correlation is found among temperature and luminosity preventing us to draw any conclusion. The correlation among flux and radius in NGC 5236 82ULX is not reliable, because the ULX is constant in radius among the observations. Also the perfect correlations or anti-correlations found for the cold component in M101 24ULX are not reliable because both the radius and temperature are constant within the uncertainties.

OBS. ID	χ^2/dof	$n_{\rm H}$	kT$_{in}$	Γ	F$_{pow}$/F$_{disc}$	L$_x$/10^{39} erg s^{-1}	P$_{val}$	Spectral regime
		10^{22} cm^{-2}	keV		(0.3 – 1 keV)	(0.3 – 10 keV)		
Circinus 4ULX								
0111240101	321.43/364	$1.0^{+0.2}_{-0.1}$	$1.0^{+0.8}_{-0.2}$	$2.0^{+0.4}_{-0.4}$	16	7.2±0.1	0.95	hard/soft
0656580601	304.68/336	$1.2^{+0.3}_{-0.2}$	$0.2^{+0.1}_{-0.1}$	$2.2^{+0.1}_{-0.1}$	1.3	8.3±0.2	0.89	soft
0701981001	1495.45/1478	$0.9^{+0.2}_{-0.1}$	$1.9^{+0.1}_{-0.1}$	$1.9^{+1.0}_{-0.5}$	0.9	16.47±0.1	0.37	Disc
0780950201	361.2/327	$1.3^{+0.3}_{-0.3}$	$0.17^{+0.1}_{-0.03}$	$1.7^{+0.1}_{-0.1}$	0.21	7.6±0.4	0.09	hard
0792382701	318.99/335	$1.0^{+0.3}_{-0.2}$	$1.1^{+0.1}_{-0.1}$	$2.8^{+1.3}_{-0.8}$	3.7	7.7±0.2	0.73	Disc
0824450301	1301.14/1240	$0.81^{+0.06}_{-0.04}$	$1.7^{+0.1}_{-0.1}$	$1.5^{+0.5}_{-0.9}$	0.3	14.98±0.08	0.11	Disc
Circinus 6ULX								
0792382701	38.06/48	$0.9^{+0.3}_{-0.2}$	$0.6^{+0.2}_{-0.2}$	$0.7^{+1.7}_{-2.5}$	0.05	0.77±0.05	0.9	Disc
M101 16ULX								
0164560701	37.41/31	$0.3^{+0.2}_{-0.1}$	$0.17^{+0.04}_{-0.04}$	$2.2^{+1.8}_{-1.5}$	0.1	$1.6^{+0.1}_{-0.1}$	0.2	soft
M101 24ULX								
0104260101	214.16/203	$0.14^{+0.2}_{-0.06}$	$1.2^{+0.4}_{-0.2}$	$1.5^{+1.8}_{-3.9}$	0.6	3.2±0.1	0.28	Disc
0164560701	42.84/41	$0.11^{+0.19}_{-0.06}$	$0.9^{+0.5}_{-0.2}$	$1.3^{+1.5}_{-4.2}$	0.4	1.7±0.1	0.39	Disc
0212480201	60.68/67	$0.5^{+0.3}_{-0.1}$	$0.06^{+0.04}_{-0.05}$	$1.8^{+0.2}_{-0.2}$	0.3	10.8±0.6	0.69	hard/soft
0824450501	322.03/309	$0.3^{+0.2}_{0.1}$	$1.6^{+0.1}_{-0.3}$	$2.5^{+1.4}_{-0.9}$	2.6	3.9±0.1	0.29	Disc
M101 27ULX								
0104260101	95.64/89	$0.1^{+0.1}_{-0.1}$	$0.6^{+0.5}_{-0.2}$	$2.7^{+0.9}_{-0.8}$	5.4	2.0±0.1	0.3	hard/soft/Disc
0164560701	39.26/34	$0.4^{+0.1}_{-0.1}$	–	$3.5^{+0.4}_{-0.4}$	–	2.7±0.2	0.23	soft
0212480201	76.38/88	$0.3^{+0.1}_{-0.1}$	$0.6^{+0.1}_{-0.2}$	$3.7^{+0.9}_{-0.7}$	15.1	8.8±0.4	0.81	soft
0824450501	335.15/338	$0.2^{+0.1}_{-0.1}$	$0.5^{+0.1}_{-0.1}$	$2.9^{+0.3}_{-0.3}$	4.9	2.2±0.1	0.53	soft/Disc
M101 28ULX								
0164560701	6.71/8	0.085	$0.09^{+0.01}_{-0.01}$	–	–	0.19±0.03	0.57	SSUL
0212480201	29.61/39	$0.2^{+0.1}_{-0.1}$	$0.06^{+0.01}_{0.01}$	–	–	5.6±0.3	0.86	SSUL
M101 29ULX								

0104260101	83.09/99	0.085	$0.31^{+0.04}_{-0.04}$	$1.2^{+0.3}_{-0.3}$	0.3	3.0±0.1	0.88	hard
0164560701	89.8/81	0.085	$0.3^{+0.1}_{-0.1}$	$1.4^{+0.3}_{-0.4}$	0.5	1.4±0.1	0.24	hard
NGC 5236 9ULX								
0110910201	118.02/101	$0.5^{+0.2}_{-0.2}$	$0.12^{+0.03}_{-0.02}$	$1.7^{+0.2}_{-0.2}$	0.08	2.0±0.1	0.12	hard
0723450101	18.89/22	<0.2	–	$1.6^{+0.2}_{-0.2}$	–	0.4±0.1	0.65	hard
0723450201	93/90	0.04	–	$1.4^{+0.1}_{-0.1}$	–	0.62±0.04	0.39	hard
0729561001	58.75/46	0.04	–	$1.4^{+0.1}_{-0.1}$	–	0.64±0.07	0.1	hard
0729561201	83.06/111	$0.10^{+0.1}_{-0.04}$	–	$1.6^{+0.1}_{-0.1}$	–	0.56±0.04	0.98	hard
0761620101	220.82/205	0.04	$0.2^{+0.1}_{-0.1}$	$1.4^{+0.1}_{0.1}$	4.6	0.75±0.02	0.21	hard
0761620201	135.68/141	$0.2^{+0.3}_{-0.2}$	$0.14^{+0.2}_{-0.03}$	$1.6^{+0.2}_{-0.2}$	0.5	1.6±0.1	0.61	hard
NGC 5236 58ULX								
0110910201	202.57/196	$0.2^{+0.1}_{-0.1}$	$1.0^{+0.2}_{-0.3}$	$2.8^{+0.6}_{-0.3}$	11	1.5±0.1	0.36	soft
0503230101	53.58/50	$0.2^{+0.1}_{-0.1}$	0.5(<0.67)	$1.5^{+2.0}_{-2.3}$	0.65	3.4±0.2	0.34	Disc
0552080101	32.45/38	$0.2^{+0.4}_{-0.2}$	<0.14	$2.5^{+0.4}_{-0.3}$	1.8	2.1±0.2	0.72	soft
0723450101	88.93/97	$0.2^{+0.1}_{-0.1}$	$0.9^{+0.2}_{-0.2}$	$2.7^{+0.8}_{-0.6}$	5	2.1±0.1	0.71	soft/Disc
0723450201	151.22/166	$0.2^{+0.1}_{-0.1}$	$1.0^{+0.1}_{-0.2}$	$2.7^{+0.7}_{-0.6}$	4	3.1±0.1	0.79	Disc
0729561001	119.88/115	$0.2^{+0.1}_{-0.1}$	$1.1^{+0.2}_{-0.3}$	$3.0^{+0.8}_{-0.5}$	11	1.3±0.1	0.36	soft
0729561201	280.16/266	$0.3^{+0.1}_{-0.1}$	$1.0^{+0.1}_{-0.2}$	$3.0^{+0.6}_{-0.4}$	11.5	2.8±0.1	0.26	soft
0761620101	93.49/75	$0.2^{+0.1}_{-0.1}$	$1.3^{+0.5}_{-0.5}$	$2.7^{+1.1}_{-0.5}$	1	1.4±0.1	0.07	Disc
0761620201	103.63/97	$0.18^{+0.04}_{-0.04}$	–	$2.4^{+0.1}_{-0.1}$	–	1.4±0.1	0.29	soft
NGC 5236 79ULX								
0723450101	498.59/602	$0.12^{+0.06}_{-0.04}$	$1.6^{+0.1}_{-0.2}$	$2.0^{+0.6}_{-0.4}$	1.2	3.4±0.1	0.99	Disc
0723450201	229.67/201	$0.3^{+0.2}_{-0.1}$	$1.1^{+0.1}_{-0.1}$	$3.5^{+1.1}_{-0.8}$	12.5	1.40±0.04	0.08	soft
0729561001	113/120	$0.2^{+0.3}_{-0.1}$	$1.2^{+0.2}_{-0.3}$	$2.8^{+1.8}_{-0.9}$	3.7	1.2±0.1	0.66	Disc
0729561201	291.23/294	$0.1^{+0.1}_{-0.1}$	$1.5^{+0.1}_{-0.2}$	$2.1^{+0.7}_{-0.5}$	2.1	2.6±0.1	0.54	Disc
0761620101	543.22/556	$0.2^{+0.1}_{-0.1}$	$1.5^{+0.1}_{-0.1}$	$2.6^{+0.5}_{-0.4}$	2.3	2.46±0.04	0.64	Disc

0761620201	461.76/494	$0.14^{+0.06}_{-0.04}$	$1.4^{+0.1}_{-0.2}$	$2.4^{+0.6}_{-0.4}$	2.8	2.13±0.04	0.85	Disc
NGC 5236 82ULX								
0110910201	114.18/97	0.19	$0.9^{+0.1}_{-0.1}$	$2.9^{+0.5}_{-0.3}$	3.7	0.70±0.03	0.11	Disc
0723450201	245.46/221	0.2	$0.9^{+0.1}_{-0.1}$	$2.6^{+0.2}_{-0.2}$	4.5	0.82±0.03	0.12	Disc
0729561001	117.48/104	0.2	$0.9^{+0.2}_{-0.2}$	$2.4^{+0.4}_{-0.3}$	3.7	0.78±0.04	0.17	Disc
0761620201	322.7/289	0.3	$1.0^{+0.1}_{-0.1}$	$3.0^{+0.3}_{-0.2}$	9.7	1.12±0.04	0.08	soft
NGC 3623 18ULX								
0082140301	70.23/60	$0.4^{+0.5}_{-0.3}$	$1.5^{+0.3}_{-0.2}$	3.2 (<-5.4)	4.96	4.8±0.3	0.17	Disc/soft/hard
NGC 3627 5ULX								
0093641101	25.75/32	0.02	$1.7^{+0.9}_{-0.8}$	$2.4^{+1.1}_{-0.7}$	2.7	4.6±0.4	0.77	Disc/hard$^{(*)}$
NGC 3627 23ULX								
0093641101	12.02/20	$0.6^{+0.4}_{-0.5}$	0.1 (<1.5)	$2.2^{+0.5}_{-0.6}$	0.2	12.3±1.2	0.92	soft/hard
NGC 4945 6ULX								
0112310301	69.91/77	$0.7^{+0.6}_{-0.2}$	$1.5^{+0.5}_{-0.4}$	1.7< 4.6	1.1	0.85±0.04	0.7	Disc
0204870101	135.05/148	0.7	$1.7^{+0.3}_{-0.4}$	$2.0^{+0.7}_{-0.3}$	3.2	0.79±0.03	0.81	Disc
NGC 925 ULX-1								
0784510301	1095.25/1054	$0.34^{+0.1}_{-0.04}$	$0.21^{+0.1}_{-0.04}$	$1.71^{+0.04}_{0.04}$	2.9	27.7±0.4	0.18	hard
NGC 925 ULX-2								
0784510301	122.4/118	$0.3^{+0.1}_{-0.1}$	$0.3^{+0.1}_{-0.1}$	$1.7^{+0.3}_{-0.4}$	1.3	4.4±0.2	0.37	hard/soft
NGC 925 ULX-3								
0784510301	40.36/38	0.3	$0.13^{+0.03}_{-0.02}$	$2.0^{+0.5}_{-0.5}$	0.2	0.8±0.1	0.37	hard/soft
NGC 5055 1ULX								
0405080301	165.5/164	$0.10^{+0.1}_{-0.04}$	$0.3^{+0.1}_{-0.1}$	$2.0^{+0.2}_{-0.2}$	3.4	13.5±0.5	0.34	soft/hard
0405080501	53.54/49	$0.11^{+0.06}_{-0.09}$	$0.2^{+0.2}_{-0.2}$	$1.9^{+0.2}_{-0.3}$	2.2	12.9±0.6	0.3	hard/soft
NGC 5055 2ULX								
Swift/XRT av.	13.69/12	0.037	–	$1.8^{+0.2}_{-0.2}$	–	1.6±0.2	0.32	–
NGC 4517 1ULX								
0203170301	456.6/493	$0.8^{+0.2}_{-0.1}$	$1.6^{+0.1}_{-0.1}$	>4.7	7	12.2±0.3	0.88	Disc$^{(**)}$

Table 3.7: In this table: spectral classification with the spectral model TBABS*(DISKBB+POW). kT_{in} is the inner disc temperature, Γ is the power-law index, F_{pow} and F_{disc} are the fluxes for the power-law and disc component in (0.3-1) keV. The total luminosity is reported in units of 10^{39} erg s^{-1} in (0.3-10) keV. In the last column we indicate the spectral regime in which we classify the observation analysed. (*) The source is classified as a broadened disc by the disc plus power-law model, but a similar fit statistics is also given by a single hard power-law fit, with Γ = 1.7. (**) From the spectral parameters the source should be classified as SUL, but the spectrum is well fit also with just a disc. From a disc plus a comptonizing model we classify the source as a BD; see text for more details.

Spectral classification:
We derived a spectral classification for our sources, based on a multi-colour black body plus power-law model, to obtain some information about the accretion system configuration, following the empirical classification method from Sutton et al. (2013). For inner disc temperature < 0.5 keV, a source is classified as *hard ultraluminous* if the power-law index is < 2, as *soft ultraluminous* for a power-law index > 2. When the inner disc temperature is > 0.5 keV, if the flux ratio between the power-law and the disc in (0.3–1) keV is > 5, the source is in the *ultraluminous regime*, *hard* or *soft* determined by the power-law index. If the flux ratio is < 5, the spectrum is dominated by the disc and the source is defined as a *broadened disc*. We used the *XMM-Newton* archival data and the obtained results can be found in table 3.7; we report only the observations where the adopted model gives an acceptable fit. In the following, we group the ULXs with a similar classification and comment each of them. A summary of the classification is also reported in table 3.8, where we show how many times each ULX has been classified in each spectral shape, we report the overall classification (ST = the ULX shows spectral state transitions, D = the ULX has always or mostly a BD shape, UL = the ULX is usually in an ultraluminous regime, U = the spectral regime of the ULX remains unclassified). We also report the maximum difference in luminosity (ΔL) observed in the *XMM-Newton* observations, i.e. the ratio between the maximum and minimum luminosity observed, the minimum time in which a spectral state transition has been observed and the ΔL corresponding to the spectral transition.

Spectral state transitions: five sources are classified in different spectral regimes in at least two observations in the considered data. Circinus 4ULX shows spectral variability, with transitions among the ultraluminous and the broadened disc regimes. NGC 5236 58ULX has usually a soft spectral shape and transits between the soft ultraluminous and the broadened disc regimes. M101 24ULX, NGC 5236 79ULX and NGC 5236 82ULX have a broadened disc shape, but in one epoch their spectra are classified in the ultraluminous state. However, we note that NGC 5236 79ULX has a worse χ^2_ν and P_{val} in the observation where it appears with a softer shape than in the other observations. We will thus describe this ULX with the broadened disc sources. In the following we describe the other three cited sources in detail.

- **Circinus 4ULX:** This is a spectrally variable source, as found also from the spectral-fitting with the two thermal components model. Spectral variability was already found for this source in previous works (Circinus ULX5 in Walton et al. 2013, Mondal et al. 2021a). In particular, Mondal et al. (2021a) found the ULX in three different spectral states: a high flux disc-like spectrum, a low-flux power-law dominated spectrum and an intermediate state with a low flux and a dominant disc component. Here, we found both disc and power-law dominated observations. The source appeared in all the three spectral regimes proposed in the classification scheme of Sutton et al. (2013) and adopted here, i.e. broadened disc, soft ultraluminous and a hard ultraluminous. In addition, we derived the hardness ratio from the *XMM-Newton* data, has the ratio between the pn count rate in the energy bands (1.5-10) keV and (0.3-10) keV, which is always large (> 0.6); see figure 3.14. A clear trend is visible with an increasing hardness at high luminosities, where we find the two luminous disc dominated epochs, while at a smaller hardness and luminosity there are the epochs classified in the hard or soft ultraluminous regime and the observation with a dominant disc but a low luminosity, which seems to have an intermediate behaviour. Walton et al. (2013) and Mondal et al. (2021a), found that the short-term variability is not always present in this ULX and, when found it is always smaller than 20% in terms of F_{var}. Thus, we propose an intermediate/small inclination angle for Circinus 4ULX, where the wind sometimes intersects our line of sight, producing the observed flux and spectral behaviour, consistent also with our reasoning about the emission radii derived from the BBODYRAD+DISKBB spectral model. In addition, we suggest that the mass accretion rate plays an important role for this source, producing a variation in the wind opening angle and the strong long term-variability that we have found in the *Swift*/XRT data.

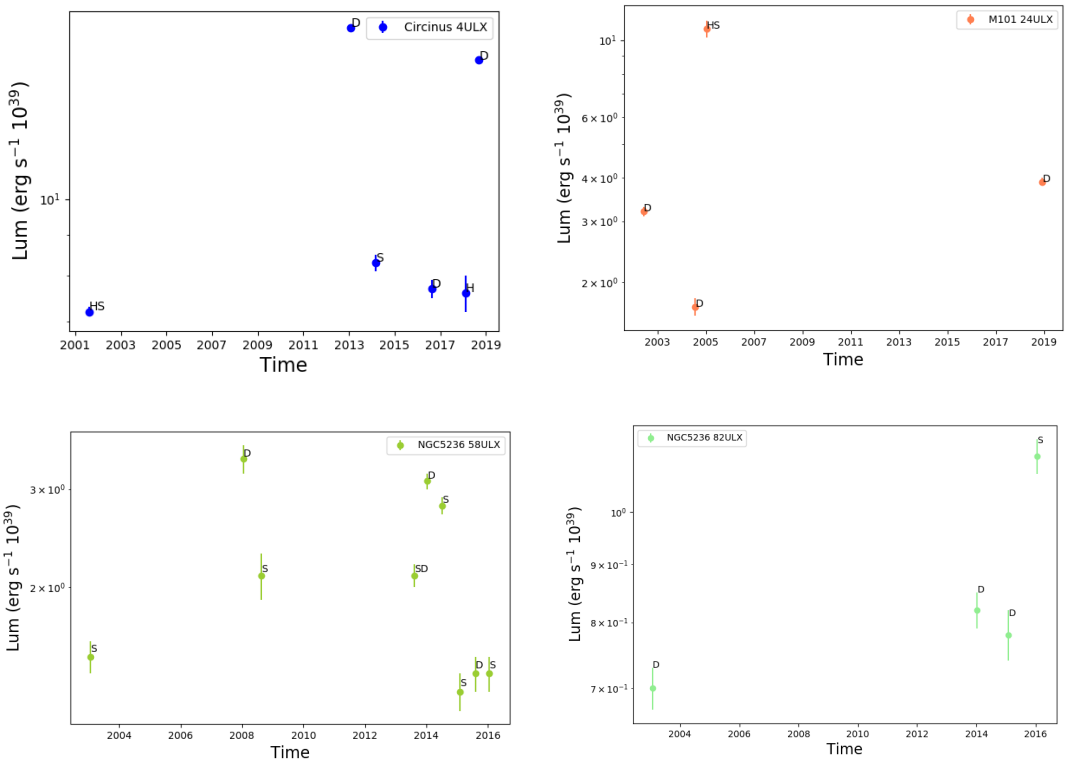

Figure 3.13: Light curves (luminosity in (0.3-10) keV in units of 10^{39} erg s^{-1} vs. year) of the *XMM-Newton* observations for the ULXs where spectral state transitions have been observed: Upper left: Circinus 4ULX; Upper right: M101 24ULX; Bottom left: NGC 5236 58ULX; Bottom right: NGC 5236 82ULX. The luminosities are derived from the spectral model TBABS*(DISKBB+POW). We also indicate the spectral regime as classified through the spectral-fitting with a TBABS*(DISKBB+POW) model: D = broadened disc, S = soft ultraluminous, H = hard ultraluminous, HS = between hard and soft ultraluminous. For NGC 5236 82ULX we just plot the epochs where the adopted spectral model gives a statistically acceptable fit.

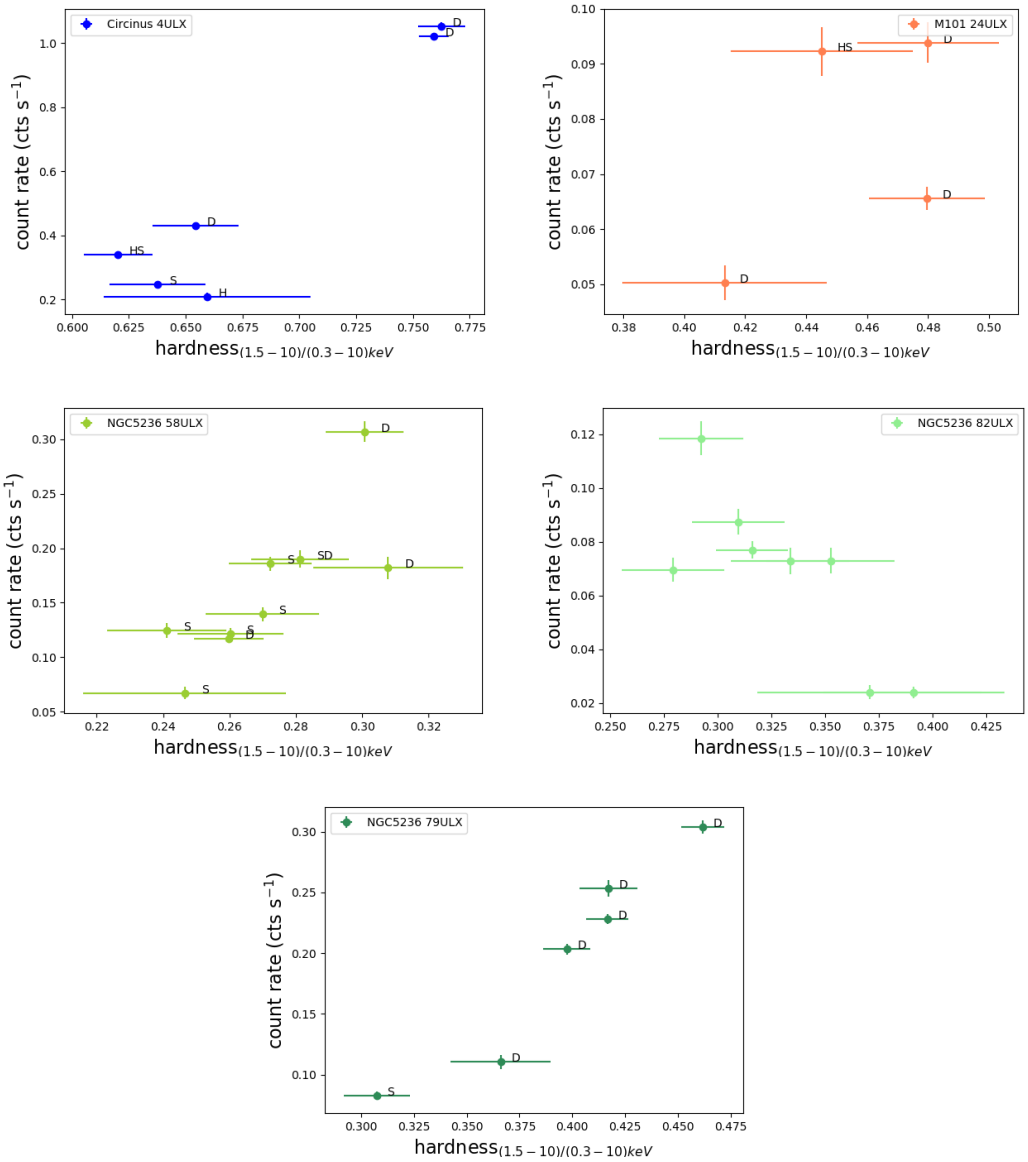

Figure 3.14: HID: count rate in the total band (0.3-10) keV vs. hardness ratio, evaluated as the ratio between the count rate in (1.5-10) keV and (0.3-10) keV. We used the *XMM-Newton* EPIC-pn count rates; when a source was not visible in the pn image we converted the MOS count rate to the expected pn count rate in the energy bands of interest. Upper left: Circinus 4ULX; Upper right: M101 24ULX; Middle left: NGC 5236 58ULX; Middle right: NGC 5236 82ULX; Bottom: NGC 5236 79ULX.

The minimum time in which a spectral state transition has been observed for this ULX is ~ 7 months and the corresponding change in luminosity is ~ 2 (see fig. 3.13).

- **NGC 5236 58ULX:** This ULX is on a spiral arm of the galaxy and it is characterized by a large variability, reaching a factor of 5 in flux variation in 2 weeks. Its fractional variability is larger than 50% in all the considered energy bands and 58ULX is able to change its flux of a factor 2 in about 1 day, but also on short timescales. We exploited the EXTraS archive (De Luca et al. 2016) to see if the ULX has shown variability also on short timescales and we found that the source is variable in some of the *XMM-Newton* observations. In particular, in observations 0503230101 and 0723450201 it is able to change its flux of a factor ~ 2 in ~ 50 min. In the *Swift*/XRT long-term light curve of this ULX, there are also some peaks that may indicate a flaring activity. Our monitoring was not sufficiently dense to track the flux rise and decay phases and constrain the typical duration of a flare.

  Some spectral variability is visible in the spectral parameters of this source. From the disc plus power-law model we classified this source in a soft ultraluminous regime and in some epochs as a broadened disc. This spectral and timing behaviour may be generated by a high inclined system, where the wind intersects our line of sight. The shorter state transition observed is of ~ 5.5 months, with no significant luminosity variation.

- **NGC 5236 82ULX:** It is a candidate ULX, occasionally above the ULX luminosity threshold. Just in four of the *XMM-Newton* observations the disc plus power-law model can be used to fit the data. The $n_{\rm H}$ resulted large and not well constrained, giving extremely large luminosities, highly unlikely for this source which is always around or below the the ultraluminous threshold in the long-term *Swift*/XRT monitoring. We therefore fixed the $n_{\rm H}$ to the values obtained with the two thermal model, to attempt a spectral classification. NGC 5236 82ULX is mainly classified as a broadened disc, but in one observation, where its luminosity exceeds 10^{39} erg s^{-1}, it has a softer shape. The spectral state transition happened in 11 months, with a luminosity variability factor of 1.4 among the two observations. The transition may have occurred in a shorter time: the two considered observations were not consecutive in this case because the intermediate observation was not possible to classify with the adopted model. In figure 3.13 we just plot the observations for which the spectral classification was possible.

- **M101 24ULX:** In three of the four available observations this ULX as a broadened disc shape. In observation 0212480201 it is instead classified in the hard ultraluminous regime, but also a soft regime is allowed by the spectral parameters. The transition among the BD shape and the ultraluminous regime happened on a timescale of ~ 6 months with a luminosity change of a factor 6.4.

Broadened disc sources: We classify some of the ULXs always or mostly in the broadened disc regime, suggesting that these sources are accreting at about their Eddington limit. Such sources are Circinus 6ULX, NGC 5236 79ULX, NGC 4945 6ULX and NGC 4517 1ULX.

- **Circinus 6ULX:** Except in one observation, the spectrum of Circinus 6ULX can be modelled with just a multi-color blackbody disc and also in the observation where two components are present the disc dominates the flux. This source was indicated as ULX in *Chandra* data by Swartz et al. (2004), but they determined the luminosity with two models and only one of them gave an ultraluminous value. In the spectra analysed here this source is always under 10^{39} erg s^{-1} and its spectrum is similar to the high/soft thermal state observed in Galactic BH binaries. Therefore, both the low luminosity usually observed in this source and its spectral shape suggest a sub-Eddington X-ray binary hosting a stellar mass BH, which may

sometimes accrete around its Eddington limit, entering the broadened disc regime, as happened in observation 0792382701.

- **NGC 5236 79ULX:** NGC 5236 79ULX, M83 ULX in the literature, is a transient ULX and has been suggested to be a LMXB (Soria et al. 2012). From the analysed spectra, we found some variations in the spectral disc temperature, considering the blackbody plus disc blackbody model. We classify this ULX as a broadened disc, in all the *XMM-Newton* observations, except in observation 0723450201, where the fit with the disc plus power-law suggests a softer spectral shape.
- **NGC 4945 6ULX:** The long-term variability of this source is dominated by the hard energy band. In observation 0204870101 the disc plus power-law model gives a very large value for the $n_{\rm H}$, with respect to the value obtained with the two thermal component model, which we considered unlikely. We thus repeated the fit by fixing the $n_{\rm H}$ to the value derived with the two thermal components fit. We classified 6ULX as a broadened disc. In both the observations the source has a luminosity smaller than 10^{39} erg s^{-1}.
- **NGC 4517 1ULX:** This is the only ULX detected in the galaxy NGC 4517, which was never observed with the *Swift* satellite before our monitoring campaign. We did not found flux variability in the *Swift*/XRT data, but we have to consider that this galaxy has been observed only seven times with the *Swift* satellite. The source was visible in one *XMM-Newton* observation. The source spectrum can be modelled both with a single disc or with two components and it is compatible with both a dominant disc and a soft regime of accretion. The statistics of the source is good enough to use a more complex model, i.e. a DISKBB+COMPTT in XSPEC. From this model we obtained a cold comptonizing component, with temperature ∼2 keV and optical depth ∼6 and this model favours a broadened disc classification. Given the high luminosity of $\sim 1.2\times10^{40}$ erg s^{-1} observed, this spectrum resembles the soft/high disc dominated state observed in Circinus 4ULX (Mondal et al. 2021a). New observations are needed to investigate the possible similarity with Circinus 4ULX and to possibly identify similar spectral state transitions.

Ultraluminous sources: Eight of the sources are mostly classified in the ultraluminous regime, suggesting that they are accreting at super-Eddington rates in the considered exposures. M101 27ULX is consistent with a soft ultraluminous regime; while M101 29ULX, NGC5236 9ULX and NGC 925 ULX-1 are classified in a hard ultraluminous regime. NGC 3627 23ULX, NGC 5055 1ULX, NGC 925 ULX-2 and NGC 925 ULX-3 are also classified in a ultraluminous regime, but we cannot distinguish between the hard and soft one.

- **M101 27ULX:** This ULX is classified as a soft ultraluminous source in two of the *XMM-Newton* observations. In one of them, both the disc and power-law components are detected, while in the other just a soft power-law is sufficient to model the spectrum. In the remaining two observations the classification is not unique, but the soft state is allowed in all the epochs. We thus suggest an intermediate/large inclination angle for this source, or alternatively the presence of a strong wind with a narrow opening angle.
- **M101 29ULX:** This source is the only ULX in our sample which shows a possible bi-modal flux distribution, rendering it a candidate PULX. It is spatially unresolved from other X-ray variable sources in the data analysed in this work, which can be resolved only in *Chandra* data and this fact may influence both the variability and spectral results obtained in this work. If most of the flux is accounted for by the ULX, 29ULX is a significantly variable source on days timescales and from its spectrum it can be classified as a hard source, in accordance with the PULX hypothesis.
- **NGC 5236 9ULX:** This source is a candidate ULX, which is usually observed at luminosities smaller than 10^{39} erg s^{-1}, but occasionally it is observed above this threshold. In the

XMM-Newton observations where a spectral classification is possible, it appears in the hard ultraluminous regime in three epochs. In other four observations just a single hard power-law gives a good fit for the data. The hard spectral shape may be explained with a small inclination angle for the system or with the absence of a strong wind.

- **NGC 3627 23ULX:** NGC 3627 23ULX is less luminous than the other ULX in the same galaxy, with a luminosity of the order of 10^{39} erg s^{-1} and sometimes even smaller. Its *XMM-Newton* spectrum is compatible both with a soft and a hard ultraluminous regime of accretion.

- **NGC 925 ULX-1:** NGC 925 ULX-1 results a *hard ultraluminous* source, suggesting that we are directly seen the hard emission of the inner regions of the ULX. Pintore et al. (2018b) proposed that the system is nearly face-on, with a small inclination angle, so that the inner emission is not covered by the winds launched by the accreting compact object in a *ultraluminous* accretion regime scenario.

- **NGC 925 ULX-2:** NGC 925 ULX-2 cannot be uniquely classified in the *XMM-Newton* observation, owing to the large uncertainties on the spectral-fitting parameters, which are compatible with both the *hard* and *soft ultraluminous* regime. The best fitting parameters allowed us to prefer the interpretation of the source in a *hard ultraluminous* regime. This is also in agreement with the HID (see section 3.5.2), where a linear trend, with an increasing ULX hardness at larger count rates, is present. This suggests that the source may be seen at a small inclination angle, closer to the face-on than to the edge-on orientation, with the inner accretion flow directly visible to the observer.

- **NGC 925 ULX-3:** In the case of NGC 925 ULX-3, the disc plus power-law model had spectral parameters with large uncertainties due to the low statistics in the *XMM-Newton* data, where the source is not seen above the ULX luminosity threshold. In particular, the $n_{\rm H}$ value resulted large and not well constrained. We thus fixed it at the value obtained with the blackbody plus disc model, to derive the spectral classification, but we found a doubtful classification (hard/soft). Considering the average *Swift*/XRT spectrum it appears a *hard ultraluminous* source. Our result is in agreement with the finding of Earnshaw et al. (2020), who noted that the spectrum of ULX-3 is softer at low luminosity and harder when the source is brighter. Earnshaw et al. (2020) also suggested that this trend may indicate propeller phases, during which the absence of accretion may cause a soft and dim state; otherwise, the *XMM-Newton* flux can be explained by the periodic flux modulation observed in the *Swift*/XRT light curve. In contrast, the hardness ratio is constant among the *Swift*/XRT observations (see figure 3.17).

- **NGC 5055 1ULX:** NGC 5055 1ULX, NGC 5055 X-1 in the literature (Mondal et al. 2020b), is the most luminous ULX in the galaxy NGC 5055, reaching luminosities of the order of 10^{40} erg s^{-1}. It is among the most variable ULXs in our sample, with a F_{var} larger than 50% in all the energy bands and of ∼90% in the hard one. In contrast to the long-term behaviour, Mondal et al. (2020b) did not found significant short-term variability. The source spectrum remains constant in the two *XMM-Newton* observations that we have analysed in this thesis and it can be classified as a ultraluminous regime of accretion: both the soft and hard regimes are allowed from the analysed data.

Unclassified sources: M101 2ULX, NGC 3623 18ULX, NGC 3627 5ULX, NGC 4945 4ULX, NGC 5055 2ULX, NGC 5055 3ULX and M101 16ULX allow both a disc or a ultraluminous spectral classification or the disc plus power-law model cannot be used to fit the spectrum.

- **M101 2ULX:** The scanty statistics of this source did not allow us to use the *XMM-Newton* data to obtain a spectral classification.

- **NGC 3623 18ULX:** It is visible in just one *XMM-Newton* observation, which allowed all the three possible spectral regimes of the Sutton et al. (2013) classification.

- **NGC 3627 5ULX:** No significant long-term variability has been found for this source in the data of our *Swift*/XRT monitoring. In the *XMM-Newton* observation the source appears to be a broadened disc source. It can also be fit with a single hard power-law, which suggests instead a hard ultraluminous spectral regime. The hard interpretation of the spectral shape and the luminosities above 10^{40} erg s^{-1} usually observed in the *Swift*/XRT data, may be explained with a low inclination, leaving the hot and hard inner emission directly visible. The absence of significant long-term flux variation may be explained with a rather constant mass accretion rate.

- **NGC 4945 4ULX:** The long-term lightcurve of this ULX is significantly variable. The spectral parameters are not well constrained in the *XMM-Newton* data when using two spectral components, therefore we did not derive a spectral classification.

- **NGC 5055 2ULX:** This source is variable on long timescales. We found no spectral variability and due to the low statistics we did not determine a spectral classification.

- **NGC 5055 3ULX:** This ULX has a low statistics in the analysed data and it is visible just in one *XMM-Newton* observation. Only one single component is needed for the spectral fitting, preventing us from spectrally classifying this source.

- **M101 16ULX:** The spectral-fitting of this source with the disc plus power-law model is statistically acceptable in just one observation, i.e. 0164560701, where the ULX resulted in a soft ultraluminous regime, while we could not classify the source in the other epochs. In two of the other *XMM-Newton* observations, i.e. 0104260101 and 0824450501, M101 16ULX shows residuals around at 1 keV in its spectrum when a two thermal components model is used and an improvement in the fit is obtained by adding a thermal plasma component. As already noted while discussing the double thermal model, this behaviour resembles the spectral features often observed in the ULXs (e.g. Middleton et al. 2015c, Pinto et al. 2016) in which an absorbing/emitting wind component has been detected. This picture suggests that a dominant wind component may be present also in 16ULX, suggesting a large inclination angle for this source and/or a large accretion rate, implying a narrow wind opening angle.

The ULS M101 28ULX:

- M101 28ULX, M101 ULX-1 in the literature, is the only supersoft ULX in our sample, with most of the emission below 1 keV, probably seen at a high inclination angle and/or at a high accretion rate. Its spectrum is modelled in the *XMM-Newton* data with a single thermal component, with a low temperature, <0.1 keV, as typical of the supersoft sources. Some residuals are seen in the hard part of the spectrum, suggesting a second spectral component, as also found in the literature (e.g. Soria and Kong 2016, Urquhart and Soria 2016a), but the low statistics of the data did not allow us to fit and constrain this component. This ULX is almost always undetected in the *Swift*/XRT monitoring, resulting with no sufficient statistics to study the long-term flux variability, which resulted non-significant.

3.4.3 A new ULX in NGC 4945?

On February 8th, 2021 a new X-ray source (not visible in previous observations taken with *Swift*/XRT or other X-ray satellites) switched-on in the galaxy NGC 4945 which was observed by *Swift*/XRT (Brightman 2021). The source position is RA=13:04:56.06, DEC=−49:31:58.2 (error radius 8.8″ at 90% confidence). Its count rate in the *Swift*/XRT observation was ∼0.02 cts s^{-1}. The spectrum, not well constrained, can be modelled with an absorbed power-law, with photon index ∼2 and $n_{\rm H}$ <2×10^{22} cm^{-2}. Assuming this spectral shape, the observed count rate corresponds to a luminosity of about 1.5×10^{39} erg s^{-1} at the galaxy distance, which is in the ultraluminous range. Both us and other researchers asked for other observations with *Swift*/XRT but the source was not detected, thus we could not deepen the study of this new source.

ULX	BD	SSUL	SUL	HUL	UL/BD	SUL/HUL	Class.	ΔL	t_{min}	$\Delta L(t_{min})$
Circinus 4ULX	3	–	1	1	–	1	ST	2.3	7	+2.0
Circinus 6ULX	1	–	–	–	–	–	D	–	–	–
M101 16ULX	–	–	1	–	–	–	UL	–	–	–
M101 24ULX	3	–	–	–	–	1	ST	6.4	6	+6.4
M101 27ULX	–	–	2	–	2	–	UL	4.4	–	–
M101 28ULX	–	2	–	–	–	–	UL	29.5	–	–
M101 29ULX	–	–	–	2	–	–	UL	2.1	–	–
NGC5236 9ULX	–	–	–	7	–	–	UL	5.0	–	–
NGC5236 58ULX	3	–	5	–	1	–	ST	2.6	5.5	1.0
NGC5236 79ULX	5	–	1	–	–	–	D	2.8	–	–
NGC5236 82ULX	3	–	1	–	–	–	ST	1.6	11	+1.4
NGC3623 18ULX	–	–	–	–	1	–	U	–	–	–
NGC3627 5ULX	–	–	–	–	1	–	U	–	–	–
NGC3627 23ULX	–	–	–	–	–	1	UL	–	–	–
NGC4945 6ULX	2	–	–	–	–	–	D	1.1	–	–
NGC925 ULX-1	–	–	–	1	–	–	UL	–	–	–
NGC925 ULX-2	–	–	–	–	–	1	UL	–	–	–
NGC925 ULX-3	–	–	–	–	–	1	UL	–	–	–
NGC5055 1ULX	–	–	–	–	–	1	UL	1.1	–	–
NGC4517 1ULX	1	–	–	–	–	–	D	–	–	–

Table 3.8: Spectral classification for the analysed ULXs, according to the spectral modelling with a DISKBB+POWERLAW model. We report the number of observations in which each ULX (column 1) has been classified in column: (2) broadened disc (BD), (3) super soft ultraluminous regime (SSUL), (4) soft ultraluminous regime (SUL), (5) hard ultraluminous regime (HUL), (6) compatible with both an ultraluminous regime or a BD shape, (7) compatible with both the SUL and HUL regimes. In column (8): overall classification for the ULX: ST = the ULX shows spectral state transitions, D = the ULX has always or mostly a BD shape, UL = the ULX is usually in an ultraluminous regime, U = the spectral regime of the ULX remains unclassified. In column (9): maximum luminosity variability factor derived in the *XMM-Newton* epochs. In column (10): minimum time interval, in months, among two different spectral states in consecutive observations (just for ULXs showing state transitions). In column (11): luminosity variability factor corresponding to the shorter spectral transition observed.

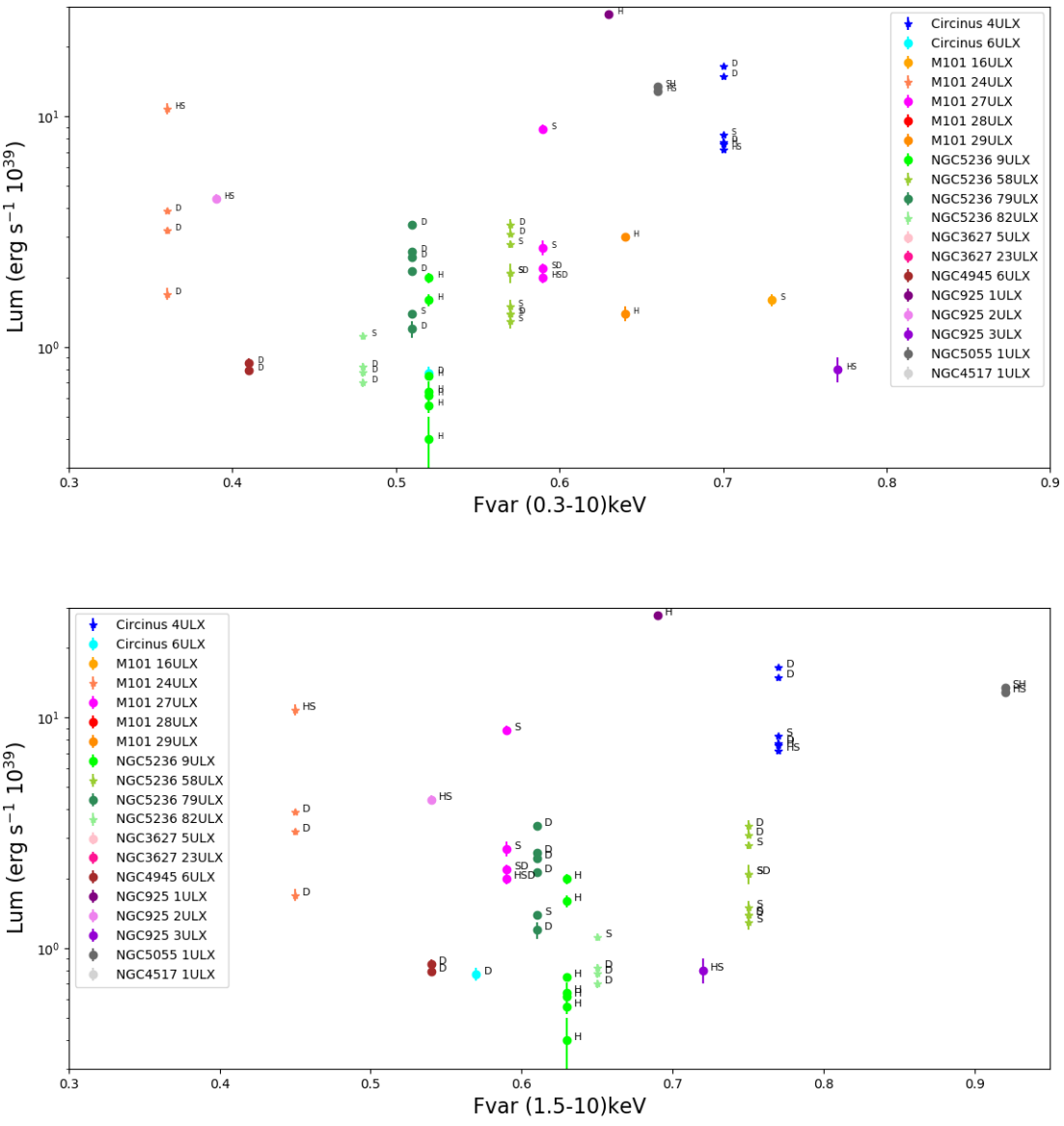

Figure 3.15: Luminosity in the *XMM-Newton* data in units of 10^{39} erg s^{-1} vs. fractional variability obtained from the *Swift*/XRT data for each ULX. We also indicate the spectral state classification, derived with the TBABS*(DISKBB+POW) model, for each point shown in the plot: D = broadened disc, S = soft ultraluminous, H = hard ultraluminous. Upper panel: luminosity in (0.3-10) keV vs. fractional variability in the total band (0.3-10) keV. Bottom panel: luminosity in (0.3-10) keV vs. fractional variability in the hard band (1.5-10) keV.

3.4.4 Discussion

Long-term variability is useful to characterize the properties of the X-ray binaries and thus also of the ULXs. Most of the sources analysed in this thesis, i.e. 71%, are variable on long timescales with at least a 3σ significance. In order to quantify the amplitude of the variability, we have derived the fractional variability for the significantly variable sources, i.e. the sources which vary with at least 3σ significance. The minimum timescale analysed here is 6 days and the maximum timescale is of the order of 1–3 years, depending on the specific source. We derived the fractional variability to quantify the variability. Following the prescription of Allevato et al. (2013), we used an "ensemble" approach, applied on simulated light curves, to derive a more reliable estimation of the F_{var}. We derived F_{var} both for the total energy band (0.3–10) keV and for the soft and hard bands, (0.3–1.5) and (1.5–10) keV, respectively. The emission in the soft and hard energy bands is associated respectively to the low (i.e. BBODYRAD) and high energy (i.e DISKBB) spectral component, which can be interpreted as the wind or the outer disc (soft) and the hot inner accretion flow (hard). This is the first sample of ULXs for which the fractional variability is derived systematically on long timescales. The typical behaviour observed in ULXs on short timescales (e.g. Sutton et al. 2013, Middleton et al. 2015a, Pintore et al. 2020) is that variability has usually a larger amplitude in the ULXs spectrally classified as soft sources and the amplitude of the variability is even larger in the hard energy band than in the soft one, when present. The same trend, i.e. larger amplitude in the hard band, has been observed on long timescales in many of the ULXs analysed here, where in at least 9/17 (53%) of the variable sources the variability is dominated by the hard band. The main exception is represented by M101 16ULX, M101 29ULX and NGC 4945 6ULX. In the remaining sources the variability is similar in the two energy bands.

The fact that the variability amplitude is usually dominated by the hard band, in the ULXs, is attributed to the obscuration of the inner accretion flow, which emits hard radiation, by the wind and the inflated disc (e.g. Middleton et al. 2015a). In the context of short-term variability, the wind blobs, assuming a clumpy wind (e.g. Middleton et al. 2011a, Takeuchi et al. 2013), which stochastically intersect our line of sight, produce the observed variability. This variability should mainly arise in the soft spectral regime, where the contribution of the wind to the emission is more important. The similar trend we observed on longer timescales can no longer be explained by the variation in the hard emission due to the individual wind blobs, which are usually linked to timescales of the order of seconds to thousands of seconds (e.g. Middleton et al. 2015a). In fact, on days timescales, we expect that the contribution to the variability of the individual blobs may be averaged out, deleting the effect observed on smaller timescales. Variability caused by a clumpy wind crossing our line of sight would happen on days timescales only for a BH with a very large mass, as those typical of the SMBHs powering the AGN (e.g. Takeuchi et al. 2013, Tombesi et al. 2012, Cappi et al. 2009, Braito et al. 2007), which is highly unlikely for the ULXs given the observed luminosities and the super-Eddington spectral shapes. In addition, if the same super-Eddington mechanisms were in act in both AGN and ULXs, we expect that the same physical processes would happen on much smaller timescales in the ULXs. Therefore, observing the same variability timescale in AGN and ULXs may be an indication that the variability in the two classes of objects has a different physical origin.

On the other hand, the propagation of fluctuations in the mass accretion rate through the disc may produce variability on longer timescales: Middleton et al. (2015a) estimated timescales of hours-days, by assuming a system similar to SS433, expected to be a Galactic super-Eddington accretor, and a BH accretor with mass of 10–100 $M_{\odot}$. If the assumptions made by those authors about the system characteristics are correct, such mechanism may explain the aperiodic variability on hours to days timescales, the latter comparable to the timescales analysed in this work, at least for BH accretors. As pointed out by Middleton et al. (2015a), this effect may produce variability in both the hard and soft spectral components: in the hard one by modulation of the high energy flux emitted by the inner disc, through scattering or directly; in the soft one by variations in the intrinsic emission of the wind, due to changes in the material column density. In addition, the variation in the soft component would act also on the wind opening angle. Therefore, when the wind opening angle narrows we would see the source through the wind, when it is larger we would see the hard emission directly. The switch between these conditions, or also among intermediate situations, may produce

the additional variability on days timescales that we have observed in the hard component of many ULXs in the analysed sample.

The timescale of the aperiodic variability observed in our *Swift*/XRT data is also similar to that observed in Holmberg II X-1 (Gúrpide et al. 2021b). In the latter, long-term variability has been attributed to the transitions between a bright/soft state and a dim/softer state (Gúrpide et al. 2021a,b), but it is not clear what drives repeatedly and rapid transitions among the SUL and SSUL regimes in Holmberg II X-1. Gúrpide et al. (2021a) suggested that the line of sight is grazing to the wind in the soft regime, thus a source precession may cause the spectral transitions. The same authors who proposed this explanation, in a following paper (Gúrpide et al. 2021b) argued that such a mechanism should cause periodic variability, in contrast with what they observed, and attributed the aperiodic variability to a combination of the narrowing of the opening angle of the wind funnel and the stochastic variability imprinted by the wind, which is in agreement also with the interpretation of our data.

To better characterize the timescales of the aperiodic variability observed, we also computed the minimum time in which a flux variation of a factor two is observed. The estimates are between 0.7 and 10.9 days (excluding Circinus 6ULX, for which we found 0.4 d, but the estimation may be wrong because we could not find an acceptable fit to the average *Swift*/XRT spectrum to assume when deriving the flux). The larger values have been found for the ULXs in M101, but this fact should be associated with the less dense *Swift*/XRT monitoring of this galaxy. In fact, M101 has been observed once every two weeks, while the other sources, showing at least a factor of two of variation in their flux, had also periods with a denser monitoring. This suggests that most of the significantly variable sources may change their flux on timescales of a week or even smaller. This is important in view of future monitoring campaigns: a cadence longer than one week may bring to lose possible variability features and in case of the most variable ULXs, timescales down to one day should be also considered.

According to the analysed *Swift*/XRT data, only one source in the sample has shown long-term periodic variability (Salvaggio et al. 2022): NGC 925 ULX-3 (see sections 3.5.1 and 3.5.2 for more details on the period search). This finding may suggest that the periodic variations, sometimes observed, are not so common in ULXs and may be caused by a process present only in some objects. On the other hand, deriving long-term periodicities is not easy, so we suggest that super-orbital periodicities may be present in many ULXs, but due to the low data quality of some ULXs they are not always found. Many factors may influence the periodicity detection. First of all, a source could be near the detection threshold of the instrument and, considering that often ULXs are variable sources, a ULX may be often non-visible in the observations. Having a small number of points makes the detection of a period difficult and the situation is still more complicated in case of a sparse sampling, which is often the situation that we find in ULXs data. In addition, the super-orbital periodicities observed in ULXs are not always stable: a shift in phase has been observed in some cases (see e.g. Brightman et al. 2019 for M82 X-2) and may be also the case for NGC 925 ULX-3, while a change in the period duration as been found in M51 ULX7 (see Brightman et al. 2021, Vasilopoulos et al. 2020).

In the ten galaxies analysed, just one new X-ray transient has been observed during our monitoring. The object was found in the galaxy NGC 4945, at ULX luminosity, but it suddenly switched off, preventing us from a detailed study.

Concerning the spectral analysis, through the study of archival *XMM-Newton* data we have observed different spectral regimes in four ULXs, Circinus 4ULX, M101 24ULX, NGC 5236 58ULX and NGC 5236 82ULX. Considering that for some sources just one or two *XMM-Newton* observations were available and that the statistics in some of the considered epochs was low, we suggest that state transitions are more common among the ULXs than what emerges in this work. We derived the minimum time in which a spectral transition has been detected in each source. We found the minimum value for NGC 5236 58ULX, where a state transition between a broadened disc shape and a soft ultraluminous regime happened in $\sim$ 5.5 months. The timescales observed for the spectral state transitions in the other ULXs analysed are similar, always months timescales. Considering that the analysed *XMM-Newton* observations are not so close in time, it is possible that the state

transitions found can happen in a smaller time interval. The months timescales we have derived from the spectral state transitions are similar to those usually derived for the super-orbital periodicities in ULXs. Given the similar timescales, we cannot exclude that the changes in spectral shape are linked to a super-orbital process. On the other hand, no periodicities have been identified so far in the *Swift*/XRT light curves of the sources which have shown state transitions. We found 13 sources in a ultraluminous accretion regime (hard or soft) at least in one epoch, including M101 28ULX which is the only source in our sample observed in a supersoft ultraluminous state (SSUL) and it was already known as a ULS (e.g. Soria and Kong 2016, Urquhart and Soria 2016a). We include also the ULS among the sources found in a ultraluminous state because it is thought that ULSs are standard ULXs, but seen at a high inclination angle. This is supported by the observations of systems that sometimes appear as a soft ULX and other times as a ULS, such as NGC 55 ULX (Pinto et al. 2017) or NGC 247 ULX-1 (Pinto et al. 2021). In addition, two ULXs, Holmberg II X-1 and NGC 5204 X-1, have been observed to transit through all the three ultraluminous regimes: hard, soft and supersoft (Gúrpide et al. 2021b). Other 4 ULXs in our sample have instead a broadened disc shape. The remaining 7 sources could not be uniquely classified and are compatible with both an ultraluminous regime or a dominant disc.

We derived the hardness ratio, as the ratio between the count rate in (1.5-10) and (0.3-10) keV, for the *XMM-Newton* data, for the sources with more then one observation, to look for possible trends among the epochs. In many cases the error bars were too large to detect any trend. We report in figure 3.14 the HID (hardness intensity diagram) for Circinus 4ULX, M101 2ULX, NGC 5236 58ULX, NGC 5236 82ULX and NGC 5236 79ULX. A clear trend is visible both in Circinus 4ULX and in NGC 5236 79ULX with an increasing hardness at the higher count rates. A similar trend seems to be present also in the HID of NGC 5236 58ULX and M101 24ULX, even if less evident, given the larger error bars. NGC 5236 82ULX may instead have the opposite behaviour, i.e. larger hardness at smaller count rates, but this is to be verified because also in this case the error bars are large and the ULX may have a roughly constant hardness ratio. A similar trend to that observed in Circinus 4ULX and NGC 5236 79ULX, i.e. a positive correlation between count rate and HID, has been also observed in the sources NGC 925 ULX-1 and NGC 925 ULX-2, with *Swift*/XRT data (see section 3.5.2).

We also compared the results of our temporal analysis, done with the *Swift*/XRT data, to the results of the spectral analysis, made with the *XMM-Newton* data. We highlight that the two datasets were not simultaneous, therefore we may have missed some correlations among the spectral and the timing behaviour. We did not find any correlation among the timescale of the variability (which we have estimated through an "half time" factor; see table 3.3) and the luminosity or spectral shape of the ULXs. In figure 3.15 we show the luminosity obtained from the spectral fitting in function of the fractional variability, during the *Swift*/XRT monitoring. We also indicate the spectral shape for the ULXs in each epoch. No obvious general trends among luminosity and spectral shape are visible in the plot. We observe all the spectral shapes at the highest luminosities (hard, soft and disc-like), while the lower luminosities, below $\sim 1{\times}10^{39}$ erg s^{-1}, are dominated by the broadened disc and the hard state. Two ULXs in our sample, i.e. M101 24ULX and NGC 5236 82ULX, enter in an ultraluminous regime at high luminosity, while they have a broadened disc shape at lower luminosity. Other sources, e.g. Circinus 4ULX, NGC 5236 58ULX, NGC 5236 79ULX, have a disc shape at both high and low luminosities and also enter the ultraluminous regime at low or intermediate luminosities. If we look at the plot in the upper panel, where we report the F_{var} in the total energy band, we see that the sources which reach luminosities of the order of 10^{40} erg s^{-1} (NGC 925 ULX-1, Circinus 4ULX, NGC 5055 1ULX) have all large F_{var}, > 0.6, with the exception of M101 24ULX, which reaches a luminosity in excess of 10^{40} erg s^{-1}, but it is the less variable ULX in the sample. NGC 925 ULX-1, Circinus 4ULX, NGC 5055 1ULX have also a variability factor of about one order of magnitude. Among the sources with peak luminosity below 10^{40} erg s^{-1} we observe different values for the F_{var}. A similar behaviour is also present if we consider the F_{var} in the hard band (lower panel of figure 3.15). Comparing the spectral regime with the fractional variability, we see a dominant disc shape at the lower F_{var} (below ~ 0.5 for F_{var} in (0.3-10) keV and below ~ 0.6 for F_{var} in (1.5-10) keV), while all the spectral shapes are observed at the higher F_{var} values.

3.5 NGC 925

The most interesting results have been obtained from the study of the ULXs in the galaxy NGC 925 (figure 3.1), which are reported in a paper submitted to MNRAS (Salvaggio et al. 2022). This galaxy is of particular interest because it contains three previously discovered ULXs, two of them are persistent sources (NGC 925 ULX-1 and NGC 925 ULX-2; Pintore et al. 2018b), while the third (NGC 925 ULX-3) is a transient ULX, only recently discovered (Earnshaw et al. 2020). NGC 925 ULX-1 is included in the 10% most luminous ULXs, with a luminosity reaching $\sim 5{\times}10^{40}$ erg s^{-1} in the data analysed for the paper (in a very recent observation the source has reached an even greater luminosity; see figure 3.4). NGC 925 ULX-3 is of particular interest among our sample of sources because it has a candidate super-orbital periodicity, that we investigated in detail thanks to the *Swift*/XRT monitoring.

The analysis reported in this section includes also *Swift*/XRT data taken previously than our monitoring campaign, resulting in 74 observations spanning $\sim$ 10 years. In addition, we used archival *XMM-Newton*, *Chandra* and *NuSTAR* data to analyse the ULXs spectra.

3.5.1 Data Reduction and Analysis

Swift/XRT

NGC 925 was observed with *Swift*/XRT 74 times between July 2011 and March 2021, see table 3.9. The observations lasted on average 2 ks. In this case we used the online tool for the XRT products[12] (Evans et al. 2009) to extract light curves and spectra. In such a way we verified that our procedure for the analysis gave consistent results with those obtained with the public tool. The light-curves are binned in six-days bin. We extracted the time averaged spectrum for each ULX, the spectra of the individual observations have too low statistics to attempt a spectral-fitting, and we applied a grouping of 20 counts per bin.

Chandra

The galaxy have been observed with *Chandra*/ACIS-S twice, on 25 November 2006 and on 1st December 2018 (Obs. ID: 7104, 20356), the observing time was of 2 and 10 ks. We used CIAO v.4.11 (Fruscione et al. 2006) to reduce data and the calibration files from CALDB v.4.8.3. To extract the source events, we used circular regions of 3″ radius, which was the smallest suitable radius considering the off-axis position of the sources, particularly in the first observation. The background was extracted using an annular region, with inner radius 6″ and outer radius 20″. Both the sources and background spectra have been extracted with the CIAO task SPECEXTRACT.

XMM-Newton

The only public *XMM-Newton* observation, at the time of the analysis, was taken on 18 January 2017. The details of the data reduction are reported in section 3.2.2. After the data cleaning we obtained a net exposure time of $\sim$ 32 ks and $\sim$ 42 ks, for pn and MOS respectively. The data were extracted from circular regions of 35″ radius (ULX-1) and 20″ radius (ULX-2 and ULX-3). The smaller extraction radius was chosen for ULX-2 and ULX-3 to avoid contamination between them, because of their small separation. The background radius was in this case of 60″. For ULX-2 we did not use the pn data, because the source falls in a CCD gap in the pn image.

NuSTAR

NuSTAR observed NGC 925 twice, in 2017 (exposure of $\sim$ 42 ks) and in 2019 (exposure of $\sim$ 53 ks). The 2017 observation began about twenty minutes before the *XMM-Newton* observation.

[12] https://www.swift.ac.uk/user_objects/

We reduced *NuSTAR* data with standard procedures, with the *NuSTAR* data analysis software NUSTARDAS v.1.3.0 in the Ftools v.6.16; we used the calibration files in CALDB v.20180312. For ULX-1 we used a circular extraction region of 50″ radius, while for ULX-2 we used a smaller radius of 30″, to avoid contamination from the closed sources. NGC 925 ULX-3 was not detected in 2017, while it was bright in 2019, but in the latter NGC 925 ULX-2 and ULX-3 contaminate each other. So we extracted both the spectra for ULX-1 and ULX-2 from the 2017 data, while we extracted only ULX-1 spectra from the 2019 data. We analysed ULX-1 2019 *NuSTAR* spectra with three *Swift*/XRT observations taken close in time (on 8, 13, 18 December 2019), the latters have been combined to obtain a stacked spectrum, quasi-simultaneous to the *NuSTAR* one.

	Instr.	Obs.ID	Start time	Stop time	Exposure
			[YYYY-MM-DD hh:mm:ss]		[ks]
1	*Swift*/XRT	00045596001	2011-07-21T09:26:28	2011-07-21T15:59:55	2.6
2	*Swift*/XRT	00045596002	2011-07-26T14:40:42	2011-07-26T14:54:55	0.8
3	*Swift*/XRT	00045596003	2011-07-27T00:03:18	2011-07-27T14:58:52	5.7
4	*Swift*/XRT	00045596004	2011-07-31T02:25:56	2011-07-31T23:19:55	0.3
5	*Swift*/XRT	00045596005	2011-08-02T00:58:52	2011-08-02T02:36:56	0.2
6	*Swift*/XRT	00045596006	2011-08-06T15:39:11	2011-08-06T15:43:56	0.3
7	*Swift*/XRT	00045596007	2011-09-07T03:33:50	2011-09-07T03:55:57	1.3
8	*Swift*/XRT	00045596008	2011-09-13T00:48:18	2011-09-13T12:09:56	3.6
9	*Swift*/XRT	00045596009	2012-08-23T22:06:46	2012-08-23T23:45:54	0.6
10	*Swift*/XRT	00045596010	2012-08-24T17:00:02	2012-08-25T14:00:55	5.3
11	*Swift*/XRT	00045596011	2012-08-27T20:28:20	2012-08-27T20:43:55	0.9
12	*Swift*/XRT	00045596012	2012-08-28T02:54:05	2012-08-28T20:28:55	4.4
13	*Swift*/XRT	00045596013	2012-08-29T01:16:16	2012-08-29T22:26:56	6.5
14	*Swift*/XRT	00045596014	2014-09-07T07:31:45	2014-09-07T09:19:54	2.1
15	*Swift*/XRT	00045596015	2017-11-19T05:59:52	2017-11-19T07:47:53	2.1
16	*Swift*/XRT	00045596016	2017-11-19T15:56:16	2017-11-19T17:27:52	1.9
17	*Swift*/XRT	00045596017	2017-11-21T07:45:23	2017-11-21T09:30:52	1.7
18	*Swift*/XRT	00045596018	2017-11-25T20:05:50	2017-11-25T22:00:54	1.8
19	*Swift*/XRT	00045596019	2019-08-18T16:33:23	2019-08-18T22:55:52	1.3
20	*Swift*/XRT	00045596020	2019-08-21T04:41:38	2019-08-21T05:02:52	1.3
21	*Swift*/XRT	00045596021	2019-08-25T18:33:26	2019-08-25T18:50:51	1.0
22	*Swift*/XRT	00045596022	2019-08-27T05:51:49	2019-08-27T21:57:53	1.5
23	*Swift*/XRT	00045596023	2019-09-01T05:20:20	2019-09-01T16:49:53	1.6
24	*Swift*/XRT	00045596024	2019-09-08T06:00:36	2019-09-09T03:01:52	2.4
25	*Swift*/XRT	00045596025	2019-09-15T13:27:33	2019-09-15T23:14:53	2.6
26	*Swift*/XRT	00045596026	2019-09-22T22:23:05	2019-09-22T22:47:52	1.5
27	*Swift*/XRT	00045596027	2019-09-25T22:05:20	2019-09-25T22:28:54	1.4
28	*Swift*/XRT	00045596028	2019-10-06T02:10:34	2019-10-06T21:28:54	1.2
29	*Swift*/XRT	00045596029	2019-10-09T11:29:11	2019-10-09T19:31:51	1.6
30	*Swift*/XRT	00045596030	2019-10-13T15:26:57	2019-10-13T17:28:52	2.9
31	*Swift*/XRT	00045596031	2019-10-20T06:55:11	2019-10-20T21:41:52	2.1
32	*Swift*/XRT	00045596032	2019-10-27T00:03:15	2019-10-27T22:35:52	2.5
33	*Swift*/XRT	00045596033	2019-11-03T18:17:09	2019-11-03T21:53:52	2.8
34	*Swift*/XRT	00045596034	2019-11-13T12:48:09	2019-11-13T22:33:53	2.8
35	*Swift*/XRT	00045596035	2019-11-17T06:02:31	2019-11-18T10:54:53	2.8
36	*Swift*/XRT	00045596036	2019-11-28T19:07:33	2019-11-28T22:43:54	2.5
37	*Swift*/XRT	00045596037	2019-12-08T03:37:33	2019-12-08T15:12:53	3.3
38	*Swift*/XRT	00089002001	2019-12-13T03:19:50	2019-12-13T05:02:54	1.9
39	*Swift*/XRT	00045596038	2019-12-18T12:12:51	2019-12-18T15:39:53	1.6
40	*Swift*/XRT	00045596039	2019-12-22T19:45:59	2019-12-22T19:53:53	0.5
41	*Swift*/XRT	00045596041	2020-01-02T09:15:03	2020-01-02T14:22:52	3.5
42	*Swift*/XRT	00045596042	2020-01-07T18:45:42	2020-01-07T22:06:52	1.2
43	*Swift*/XRT	00045596044	2020-03-01T21:11:49	2020-03-01T23:08:53	2.4
44	*Swift*/XRT	00045596045	2020-03-08T09:21:10	2020-03-08T11:21:09	2.4
45	*Swift*/XRT	00045596046	2020-03-15T00:37:12	2020-03-15T03:54:52	2.9
46	*Swift*/XRT	00095702001	2020-07-01T01:01:15	2020-07-01T09:06:53	2.1
47	*Swift*/XRT	00095702002	2020-07-11T04:45:24	2020-07-11T06:35:54	2.6
48	*Swift*/XRT	00095702003	2020-07-21T04:02:28	2020-07-21T13:45:53	1.9
49	*Swift*/XRT	00095702004	2020-07-31T17:17:45	2020-07-31T22:10:53	2.0
50	*Swift*/XRT	00095702005	2020-08-10T08:14:50	2020-08-10T10:28:53	2.6
51	*Swift*/XRT	00089004001	2020-08-17T07:32:05	2020-08-17T07:58:52	1.6
52	*Swift*/XRT	00095702006	2020-08-20T00:52:59	2020-08-20T16:55:52	2.8
53	*Swift*/XRT	00095702007	2020-08-30T17:18:07	2020-08-30T19:04:53	2.3
54	*Swift*/XRT	00095702008	2020-09-09T09:58:56	2020-09-09T12:04:52	2.5
55	*Swift*/XRT	00095702009	2020-09-19T10:41:53	2020-09-19T14:05:54	2.4
56	*Swift*/XRT	00095702010	2020-09-29T19:24:34	2020-09-29T21:16:52	2.5
57	*Swift*/XRT	00095702011	2020-10-08T13:35:29	2020-10-09T21:33:53	2.6
58	*Swift*/XRT	00095702012	2020-10-19T12:46:33	2020-10-19T12:48:54	0.1
59	*Swift*/XRT	00095702013	2020-10-22T12:09:32	2020-10-22T13:53:54	2.3
60	*Swift*/XRT	00095702014	2020-10-29T14:49:06	2020-10-29T16:32:52	1.9
61	*Swift*/XRT	00095702015	2020-11-08T10:40:54	2020-11-08T12:28:53	2.5
62	*Swift*/XRT	00095702016	2020-11-18T16:12:05	2020-11-18T22:50:54	1.5
63	*Swift*/XRT	00095702017	2020-11-29T13:15:24	2020-11-29T16:52:53	2.2
64	*Swift*/XRT	00095702018	2020-12-08T05:51:23	2020-12-08T07:48:53	2.0
65	*Swift*/XRT	00095702019	2020-12-18T11:15:01	2020-12-18T17:53:53	1.9
66	*Swift*/XRT	00095702020	2020-12-28T10:18:55	2020-12-28T10:20:26	0.1
67	*Swift*/XRT	00095702021	2021-01-01T06:37:39	2021-01-01T08:25:52	2.4
68	*Swift*/XRT	00095702022	2021-01-07T12:31:39	2021-01-07T16:08:52	2.5
69	*Swift*/XRT	00095702023	2021-01-17T02:01:45	2021-01-17T08:35:54	2.5
70	*Swift*/XRT	00095702025	2021-01-31T10:15:05	2021-01-31T13:37:53	2.3
71	*Swift*/XRT	00095702026	2021-02-06T13:58:46	2021-02-06T15:47:53	2.5
72	*Swift*/XRT	00095702027	2021-02-15T00:28:25	2021-02-16T13:37:54	2.6
73	*Swift*/XRT	00095702028	2021-02-26T01:04:10	2021-02-26T22:07:53	2.2
74	*Swift*/XRT	00095702029	2021-03-08T12:36:39	2021-03-08T14:33:53	2.4
75	*Chandra*	7104	2005-11-23T07:53:09	2005-11-23T08:57:05	2.2
76	*Chandra*	20356	2017-12-01T03:38:39	2017-12-01T07:04:06	10.0
77	*XMM-Newton*	0784510301	2017-01-18T19:45:14	2017-01-19T09:38:34	50.0
78	*NuSTAR*	30201003002	2017-01-18T19:36:09	2017-01-19T17:41:09	42.6
79	*NuSTAR*	90501351002	2019-12-12T05:31:09	2019-12-13T11:46:09	53.0

Table 3.9: Log of the observations of NGC 925, used in this section.

Source	Epoch	n_H 10^{22} cm^{-2}	kT_{diskbb} keV	N_{disc} 10^{-3}	$kT_{bbodyrad}$ keV	N_{bb}	$Flux_{diskbb}$ 10^{-13} erg s^{-1} cm^{-2}	$Flux_{bbodyrad}$	χ^2/dof	P_{val}
ULX1										
	XMM	$0.17^{+0.02}_{-0.02}$	$2.3^{+0.1}_{-0.1}$	$3.7^{+0.8}_{-0.7}$	$0.29^{+0.02}_{-0.02}$	$5.6^{+1.7}_{-1.2}$	18.5±0.4	4.1±0.1	1153.29/1131	0.32
	XMM/NuSTAR$^{(a)}$	$0.13^{+0.02}_{-0.02}$	$2.8^{+0.1}_{-0.1}$	$1.7^{+0.3}_{-0.3}$	$0.33^{+0.02}_{-0.02}$	$3.7^{+0.8}_{-0.6}$	18.0±0.4	4.7±0.1	1371.67/1269	0.02
	Chandra	0.17	$2.2^{+0.8}_{-0.4}$	$4.2^{+4.7}_{-2.8}$	$0.3^{+0.1}_{-0.1}$	$2.9^{+3.7}_{-1.6}$	19.0±2.0 / 18.8±1.1	2.3±0.7 / 2.5±0.6	70.89/63	0.29
	Swift average	0.17	$2.1^{+0.3}_{-0.2}$	$4.7^{+2.1}_{-1.6}$	$0.3^{+0.1}_{-0.1}$	$2.7^{+2.6}_{-1.2}$	17.4±0.5	1.8±0.2	181.47/206	0.81
	Swift/NuSTAR$^{(b)}$	0.17	$3.7^{+0.5}_{-0.4}$	$0.2^{+0.1}_{-0.1}$	$0.4^{+0.1}_{-0.1}$	$0.9^{+1.0}_{-0.6}$	5.3±2.1	3.5±0.8	87.18/79	0.25
ULX2										
	XMM/NuSTAR	$0.1^{+0.1}_{-0.1}$	$2.9^{+0.7}_{-0.5}$	$0.2^{+0.2}_{-0.1}$	$0.31^{+0.04}_{-0.04}$	$1.1^{+1.0}_{-0.5}$	2.6±0.2	1.1±0.1	145.27/139	0.34
	Chandra	0.1	$1.5^{+3.9}_{-0.5}$	$3.1^{+10.1}_{-3.0}$	$0.2^{+0.1}_{-0.1}$	$3.3^{+12.6}_{-2.7}$	3.2±0.9 / 3.1±0.4	0.8±0.6 / 1.0±0.3	4.23/9	0.90
	Swift average	0.1	$1.3^{+0.1}_{-0.1}$	$7.3^{+2.0}_{-1.6}$	$0.03^{+0.04}_{-0.03}$	>242.5	4.2±0.2	0.5±0.3	74.59/62	0.13
ULX3										
	XMM	$0.3^{+0.4}_{-0.3}$	$1.1^{+0.6}_{-0.3}$	$0.6^{+1.8}_{-0.5}$	$0.12^{+0.02}_{-0.02}$	$17.9^{+24.4}_{-9.9}$	0.26±0.04	0.3±0.1	40.55/38	0.36
	Chandra	0.3	$1.6^{+0.4}_{-0.3}$	$4.0^{+3.1}_{-2.4}$	$0.16^{+0.05}_{-0.04}$	$49.0^{+120.9}_{-37.4}$	– / 5.2±0.5	– / 2.6±0.7	17.98/18	0.46
	Swift average	0.3	$1.5^{+0.3}_{-0.2}$	$2.2^{+1.6}_{-1.0}$	$0.12^{+0.03}_{-0.02}$	$65.3^{+158.4}_{-43.4}$	1.9±0.2	1.2±0.2	34.43/32	0.35

Table 3.10: Spectral parameters for the spectra of NGC 925 ULX-1, ULX-2 and ULX-3: *XMM-Newton*2017, *XMM-Newton* / *NuSTAR* 2017, *Chandra*, *Swift*/XRT / *NuSTAR* 2019 and *Swift*/XRT average spectra. The spectral model used is CONST × TBABS × (BBODYRAD + DISKBB) in XSPEC. The uncertainties are at 90% confidence level. The unabsorbed X-ray fluxes reported are derived in the energy band 0.3–10 keV, in units of 10^{-13} erg s^{-1} cm^{-2}; the *XMM-Newton* fluxes in the table are from EPIC-pn, for NGC 925 ULX-1 and ULX-3, and from MOS1, for ULX-2. We fit the two *Chandra* observations together: the flux on the left refers to the observation 7104, while the flux on the right to the observation 20356. The n_H was fixed to the value obtained from *XMM-Newton* (for ULX-1 and ULX-3) or *XMM-Newton* / *NuSTAR* fit (for ULX-2).
In the last column we indicate the null hypothesis probability P_{val}, i.e. the probability for the observed data to be drawn from the model, given χ^2 and the degrees of freedom (dof). We consider acceptable the fits with $P_{val} \geq 0.05$, which corresponds to a confidence level larger than 2σ.
$^{(a)}$ The fit was not statistically acceptable: skewed residuals are present above 10 keV, suggesting a third spectral component; more details are reported in the text (section 3.5.2, Figure 3.19).
$^{(b)}$ For NGC 925 ULX-1 we fit also the *Swift*/XRT (average of 8, 13, 18 December 2019) together with the 2019 *NuSTAR* spectrum.

Spectral analysis

The spectral analysis was carried out with XSPEC v.12.10.1 (Arnaud 1996). We grouped the spectra in energy bins containing a minimum of 20 counts and we used the χ^2 statistics while doing the spectral analysis. We included an absorption component in all the spectral fits, which we modeled with TBABS.

As done for the whole sample of sources analysed we used the BBODYRAD + DISKBB model to fit the spectra. We first analysed the highest statistics data, *XMM-Newton* 2017 plus the simultaneous *NuSTAR* data, for ULX-1 and ULX-2, and only *XMM-Newton* data in the case of ULX-3. In some ULXs, a third component is needed to model the hard emission above 10 keV, which may arise from the accretion column, for NS accretors (e.g. Walton et al. 2018c), or from a comptonising corona, for BH or non-magnetic NS accretors (e.g. Reis and Miller 2013), which is the case for NGC 925 ULX-1. To account for differences in the flux calibrations between different instruments, we added a multiplicative constant (CONST in XSPEC): as expected from previous studies (see Madsen et al. 2017), the constants are consistent within 10%.

For consistency, we used the same model (BBODYRAD + DISKBB) with the poorer statistics data taken with *Chandra* and with the average *Swift*/XRT spectra. The absorbing column (n_H) was not constrained in some cases, so we fixed it to the best value of the *XMM-Newton* fit, which was larger than or comparable to the Galactic value, $n_{H,gal} = 7.26\times10^{20}$ cm^{-2}.[13] The best-fit spectral parameters are reported in Table 3.10. The unfolded spectra of each ULX are reported in Figure 3.16.

[13]https://heasarc.gsfc.nasa.gov/cgi-bin/Tools/w3nh/w3nh.pl

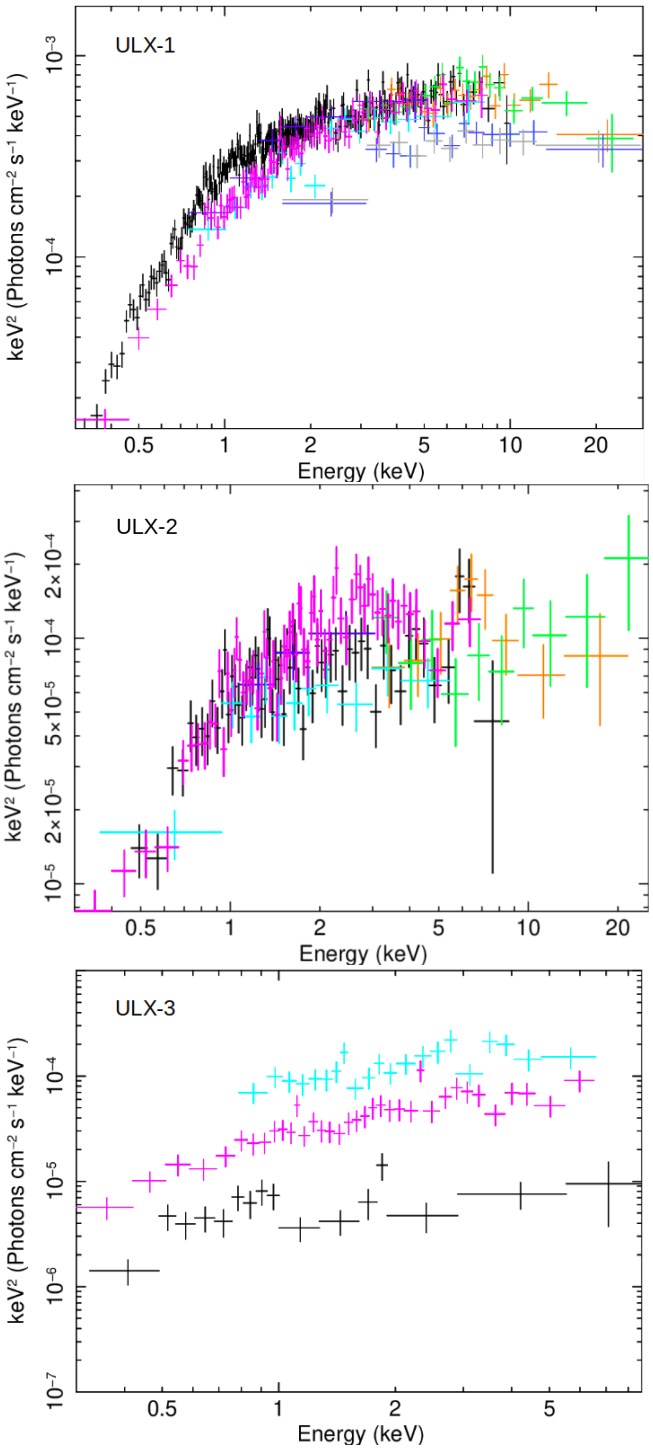

Figure 3.16: Unfolded spectra ($E^2 f(E)$), using a powerlaw model with photon index $\Gamma = 0$, to compare the spectral shapes without the influence of a particular spectral model, of the three ULX in NGC 925 (data are rebinned for display purposes). Data of *XMM-Newton* EPIC-pn are in black (for ULX-2 we have plot instead MOS1 data); *NuSTAR* FPMA/FPMB 2017 (orange/green); *NuSTAR* FPMA/FMPB 2019 (grey/light-blue); *Chandra* 7104 (blue); *Chandra* 20356 (cyan); average *Swift*/XRT (magenta).
Top panel: ULX-1; Middle panel: ULX-2; Bottom panel: ULX-3.

	$\text{soft}_{[0.3-1.5]keV}$	$\text{hard}_{[1.5-10.0]keV}$	$\text{total}_{[0.3-10.0]keV}$
ULX-1	0.54±0.01	0.59±0.01	0.54±0.01
ULX-2	0.26±0.05	0.59±0.02	0.35±0.02
ULX-3	0.57±0.01	0.38±0.01	0.63±0.01

Table 3.11: NGC 925 ULX-1, ULX-2, ULX-3 "ensemble" fractional variability, F_{var}. The uncertainties in the table derive from the standard deviation of the of the mean F_{var} distribution: more details are given in the text.

Hardness Ratio

For each *Swift*/XRT observation, we constructed the hardness-intensity diagram, HID (figure 3.17). We derived the hardness ratio as the count rates in the hard band (1.5-10.0) keV divided by the total energy band (0.3-10.0) keV. The threshold energy at 1.5 keV was chosen because the spectral components cross about at that energy; slight differences are present in the three sources, but we used the same threshold to directly compare the results. The error bars in the HID are large and did not allow us to identify any spectral evolution or trend with the count rate. To reduce the noise in the data, we binned the hardness ratio in function of the count rate. For ULX-1 and ULX-2, we grouped the data in at least 15 observations per count rate bin, while for ULX-3 every bin contains at least five observations, because the statistics is low.

From the binned HID a possible linear trend is visible both for ULX-1 and ULX-2, at low rates (count rate < 0.04 cts s^{-1}). To verify this hypothesis, we fit the binned count rate with the minimum least squares method. We comment the results for each source in section 3.5.2.

Timing analysis

To study the variability properties of the long-term light curves of the ULXs, we applied the methods described in section 2.5, as done for the whole sample of ULXs considered in this thesis. Besides evaluating the significance of the variability and the fractional variability, which in this case are evaluated on a longer light curve of $\sim$ 10 yr, we also determined a variability factor as the ratio between the highest and lowest flux detected in the *Swift*/XRT light curve. We notice that Allevato et al. (2013) determine also a bias on the estimate of the excess variance. The bias depends on the PSD slope, when data are affected by red noise as may be the case of accreting compact objects (see e.g. Vaughan et al. 2003), and on the sampling pattern. The red noise power spectrum has the shape of a power-law, with index $\sim$ 1–2 (see e.g. Press 1978). Should red noise be present in the analysed data, with slope $\sim$ 2, the fractional variability estimate may reduce of about 25%; for a slope $\sim$ 1, the effects of the irregular sampling pattern would instead dominate on those caused by the red noise and the F_{var} would increase of $\sim$ 10%. The obtained values for the F_{var} are reported in table 3.11.

Period search: We applied a Lomb-Scargle test (see section 2.5.4; Lomb 1976, Scargle 1982, VanderPlas 2018) on the long-term light curves to identify possible periodicities. The only ULX for which we found a periodicity is NGC 925 ULX-3.

We first analysed the observed light curve; we applied the *LombScargle* class of the subpackage *timeseries* in the astronomy Python package *astropy*[14]. As a first step, we derived the periodogram of the light curve considering the detections only. We then included the information brought by the upper limits, including them as points corresponding to half of the flux of the upper limit value and an error bar large the same amount. In this way we consider all the possible values allowed by the upper limit evaluation. Otherwise this method is affected by a bias: the central value of the error bar, i.e. half of the upper limit value, is implicitly assumed to be more probable than the other allowed values. So, to verify that the periodicity is not an artefact of our analysis, we used the Monte Carlo approach, as described above (see section 3.3.1). For the period search we also considered the upper limits in the simulations. For each upper limit in the observed light curve, we extracted a

[14]https://docs.astropy.org/en/stable/timeseries/lombscargle.html

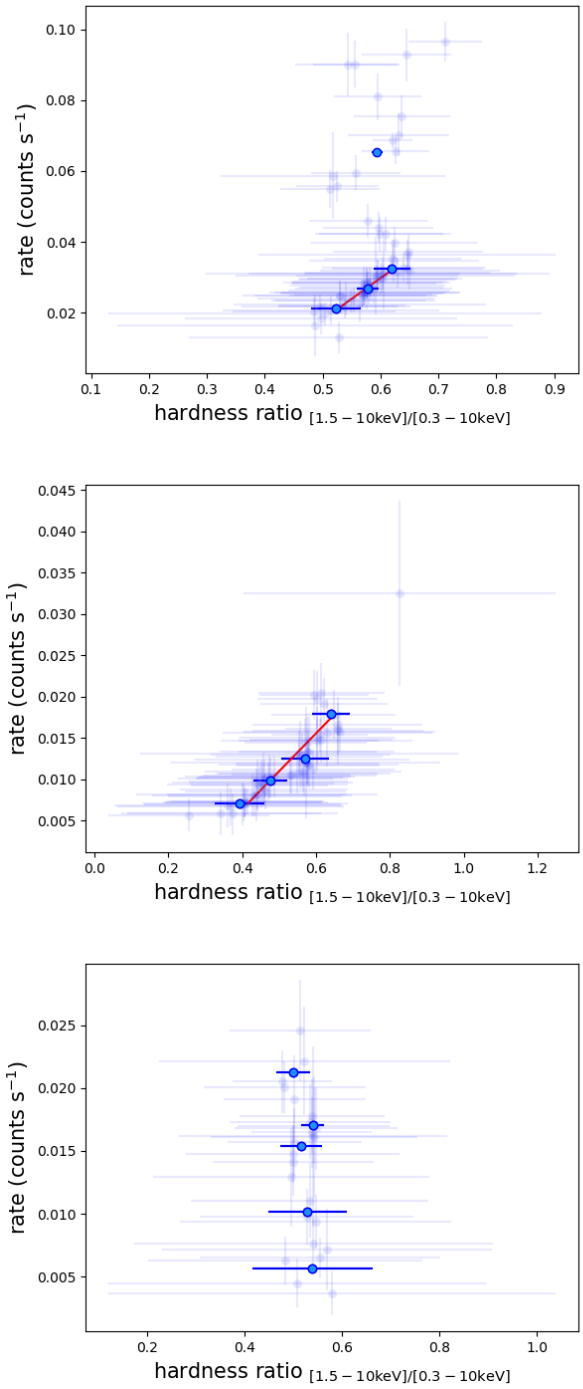

Figure 3.17: NGC 925 ULX-1 (top); ULX-2 (middle); ULX-3 (bottom) count rate vs. hardness ratio, with *Swift*/XRT data. The count rate is derived in the energy band (0.3-10) keV, in units of counts s^{-1}. The hardness ratio is calculated as the ratio between count rates in the (1.5-10) and (0.3-10) keV energy bands. The binned hardness ratios, as a function of the count rate,are indicated with blue dots, while the unbinned hardness ratios are represented with the transparent blue dots. The result of the linear regression, applied to the binned hardness ratios is super-imposed as a red solid line for: ULX-1 (top) using the hardness ratios at low count rates (< 0.04 cts s^{-1}); ULX-2 (middle), for all the binned points.

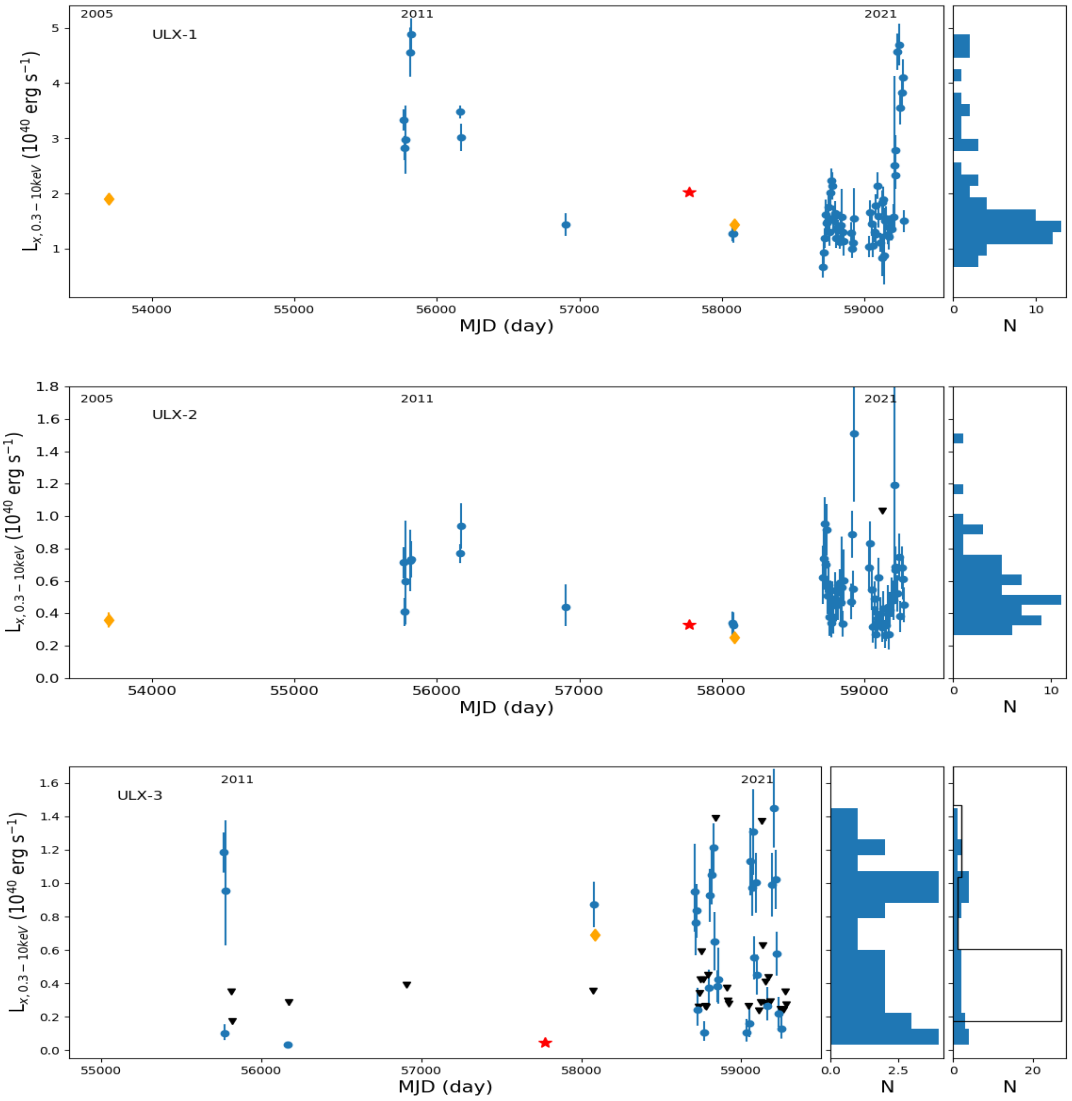

Figure 3.18: Light-curves and luminosity distributions for the three ULXs in the galaxy NGC 925, shown with six-day bins. The unabsorbed luminosities in units of 10^{40} erg s^{-1}, in the energy band (0.3-10) keV, are derived from the best-fitting model in table 3.10. *Swift*/XRT detections are indicated with blue dots; *Swift*/XRT upper limits are marked with black triangles; the *XMM-Newton* observation is represented with the red star; *Chandra* data are marked with orange diamonds. Top: NGC 925 ULX-1. - Left, light curve; right, the histogram of the *Swift*/XRT luminosity distribution. Middle: NGC 925 ULX-2. - Left, light curve; right, histogram of the *Swift*/XRT luminosity distribution. Bottom: NGC 925 ULX-3. - Left, light curve (note the different X-axis scale with respect to that used in the other two panels); middle, histogram of the *Swift*/XRT luminosity distribution; right, histogram of the *Swift*/XRT luminosity distribution, with upper limits superimposed with a black solid line.

random number from a uniform distribution of values between zero and the upper limit value, while the background rate was generated following the same procedure used in the observations where the source was detected. The uncertainty was derived in the same way used in case of detections.

3.5.2 Results

NGC 925 ULX-1

NGC 925 ULX-1, with a peak luminosity of $\sim 5\times10^{40}$ erg s^{-1} in the 0.3-10 keV energy band in the *Swift*/XRT data, is the most luminous of the ULXs in NGC 925. It is also included in the 10% most luminous ULXs known at the date (e.g Walton et al. 2011, Swartz et al. 2011, Earnshaw et al. 2019b, Walton et al. 2021, Bernadich et al. 2021). The variability significance of this source, on $\sim$ 6 d – 10 yr timescale, largely exceeds 3σ: the significance determined with the Cash statistics is $\sim 37\sigma$. Also the amplitude of the variability is high: we determined a variability factor of $\sim$ 8 and the F_{var} in the total energy band is $\sim$ 54%.

The spectral analysis of the *XMM-Newton* / *NuSTAR* spectrum with the BBODYRAD + DISKBB model leaves some residuals above 10 keV (see figure 3.19), suggesting that a third spectral component is needed. Often similar residuals are found in the spectra of the ULXs for which hard X-ray data, i.e. those taken with the *NuSTAR* satellite, are available (e.g. Walton et al. 2018c). We fit this excess with a cutoff power-law (CUTOFFPL in XSPEC), obtaining the following best fit parameters: $T_{bbodyrad}$ = 0.27±0.02 keV, $T_{diskbb} = 1.3^{+0.6}_{-0.2}$ keV, $\Gamma = 0.1^{+0.6}_{-2.7}$, HighECut = $5.2^{+1.9}_{-3.4}$ keV, with P value = 0.33 (see fig. 3.19). The one adopted here is a possible solution, but the statistics in the *NuSTAR* data is low, not enough to discriminate among different models. Indeed, also a two components model, i.e. an absorbed DISKBB + POWER-LAW, gives an acceptable solution. The *Swift*/XRT average spectrum is modelled by a black body, with temperature $\sim$ 0.3, and by a multi-colour disc, with inner temperature $\sim$ 2.1 keV.

In 0.3-10 keV band, the best parameters of the spectral-fitting obtained with the data of the different satellites are consistent inside the confidence intervals, which suggests only little spectral variability, while the flux variability is large.

The HID does not show an overall correlation. Only for rates smaller than 0.04 cts s^{-1}, i.e. the three lower count rate bins, there is a linear trend and from the minimum least squares fit we derived a large correlation coefficient of 0.98 (see fig. 3.17).

NGC 925 ULX-2

The variability significance of NGC 925 ULX-2 is $\sim 8\sigma$ and the flux variability factor derived, $\sim$ 5, is the smallest among the ULXs in NGC 925. The hard band dominates the F_{var}, with a value of $\sim$ 59%, while the soft band is less variable, with $F_{var} \sim$ 26%.

In the *Swift*/XRT spectral data, the BBODYRAD component is not significantly requested: it has a very small temperature of $\sim$ 0.03 keV and its normalisation is unconstrained. This is also confirmed by the statistics of the spectral-fitting: both the DISKBB component alone and the two components spectral-fitting give similar statistics. The inner temperature of the disc component assumes a value of $\sim$ 1.3 keV. The single component model is not statistically acceptable in the *XMM-Newton* / *NuSTAR* data, while it is a good model in the *Chandra* data. We suggest that both the spectral components are present in the data, but the ability to well constrain both of them, is limited by the data statistics. The *XMM-Newton* / *NuSTAR* and the *Chandra* spectral-fitting are consistent within 90% errors, while the differences with the *Swift*/XRT average spectrum suggest the presence of spectral variability.

From the HID of ULX-2, we see an evolution of the hardness with the count rate, which is always smaller than 0.04 cts s^{-1} in 0.3-10 keV. The trend is linear and from the linear fit with the least squares method we derived a correlation factor of $\sim$ 0.93 (see fig. 3.17). This indicates that the source becomes harder with increasing rates.

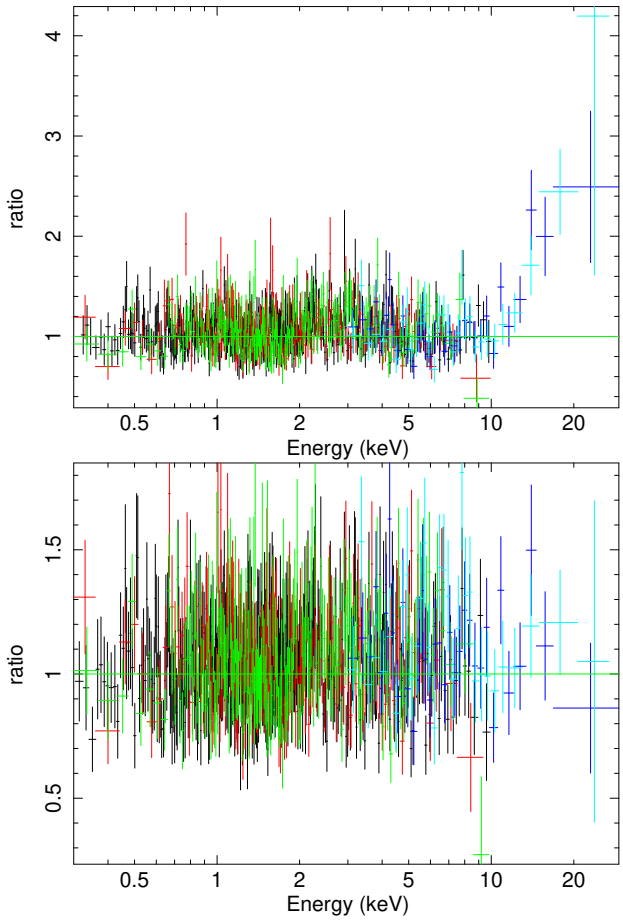

Figure 3.19: Top: NGC 925 ULX-1: *XMM-Newton* EPIC pn, MOS1, MOS2 (black, red, green), *NuSTAR* FPMA/FMPB (blue, cyan) residuals (data/model), for the model BBODYRAD + DISKBB: an excess is evident above 10 keV. Bottom: NGC 925 ULX-1 residuals with the BBODYRAD + DISKBB + CUTOFFPL model; the colours are the same of the top panel.

NGC 925 ULX-3

NGC 925 ULX-3 is a transient source discovered by Earnshaw et al. (2020). The variability significance of its *Swift*/XRT light curve is $\sim 22\sigma$, with a flux variability factor of ~ 7, which is only a lower limit on the variability. In fact, the *Swift*/XRT light curve of ULX-3 contains many upper limits and we found a variability factor > 25 considering also the *Swift*/XRT upper limits. Also Earnshaw et al. (2020), considering the lowest *Chandra* upper limit, found a larger variability factor of ~ 30.

ULX-3 has the highest fractional variability among the ULXs in NGC 925, with a value of $\sim 63\%$ in the total 0.3-10 keV energy band. In contrast with what is usually found in ULXs, at least on short timescales (e.g. Sutton et al. 2013, Pintore et al. 2020), the larger amount of variability is attributed to the soft band, below 1.5 keV (when considering also the more recent *Swift*/XRT observations the hard band is instead the more variable, see table 3.3). However, the spectral shape of this source changes around 1 keV: repeating the estimate of the variability with 1 keV as the energy threshold, we found the larger amount of variability associated with the hard component, implying that the variability mostly happens around 1–2 keV.

The average *Swift*/XRT spectrum is well fitted with the double component model (BBODYRAD + DISKBB) and the HID is constant within the uncertainties, with a mean value of ~ 0.5, in contrast with the behaviour of the other two ULXs in this galaxy (see fig. 3.17).

ULX-3 also shows a flux periodicity of about four months. We have analysed only the *Swift*/XRT data taken between the 2019 and March 2021, i.e. 58500 < MJD < 59300, because the monitoring was more regular and denser. In this way, we could exclude periods with long-term gaps, where the source behaviour was unknown, e.g. it might have faded.

The frequency range to which we applied the Lomb-Scargle periodogram is $[2\times10^{-3} - 0.08]$ d^{-1}, corresponding to the period range of [12-500] d. The smallest timescale considered corresponds to twice the time binning of the light curve (i.e. the Nyquist frequency), while the longest timescale to about the time window used for the search of the periodicity. Using only the *Swift*/XRT detections, several peaks are present in the power spectrum density (PSD), the highest corresponding to a ~ 126 d period. This peak was not statistically significant because the data are sparse and the detections cover only 3–4 cycles.

Considering also the upper limits (UL), to reduce the gap between the observations, we may have a more significant peak (see fig. 3.20). First, we included them in the observed curve as half of the UL value, with an uncertainty of the same amount, then we simulated 5000 light curves with a Monte Carlo approach, as explained in section 3.5.1. On each simulated light curve we applied the Lomb-Scargle algorithm to derive the periodogram. From the observed light curve, including both detections and UL, the peak corresponding to ~ 126 d is predominant. From the simulations, we constructed the distribution of the highest peak frequencies and we fit it with a Gaussian. The mean value of the distribution is 126.1 d and its standard deviation is 2.0 d, completely in agreement with the result obtained from the observed light curve. The light curve of ULX-3 with the best sinusoidal fit of the periodicity superimposed is shown in figure 3.21.

To derive the significance of the highest peak in the observed light curve and in the simulated periodograms, we applied the Baluev method (Baluev 2008), an analytical approximation to derive the False Alarm Probability (FAP), which is the probability to obtain a comparable to or higher peak than the considered one, in case only noise was present in the light curve. This method gives an upper limit on the FAP, so a lower limit on the detection significance. The FAP obtained for the observed curve is $\sim 10^{-8}$, which corresponds to a peak significance $> 5\,\sigma$. The FAP determination is reliable if only white noise is present, i.e. noise independent from the frequency (see e.g. VanderPlas 2018). In accreting compact objects, red noise is often present (e.g. Vaughan et al. 2003). To verify if the peak detection is significant in case of red noise, we adopted an approach similar to the one used in Walton et al. 2016. We simulated 5000 light curves from a red noise power spectrum, which we assumed to have a power-law shape with slope 1 or 2. The simulations have been performed with the *Simulator* object of the spectral timing Python library *Stingray*[15] (Bachetti et al. 2020 v.0.2), which applies the Timmer and Koenig (1995) algorithm; a library description can be found in Huppenkothen et al.

[15]https://docs.stingray.science

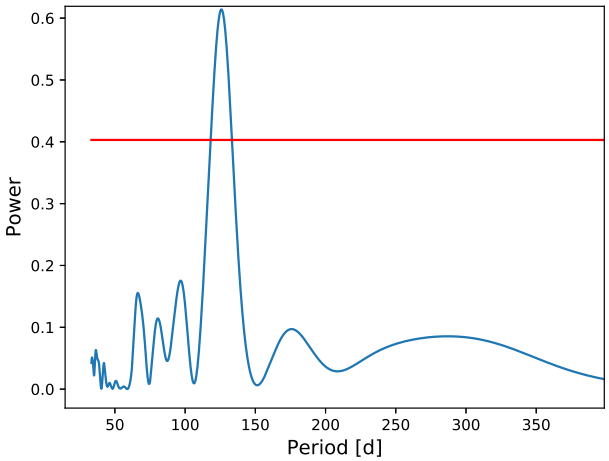

Figure 3.20: (Super-)orbital period for NGC 925 ULX-3. We plot the power vs. frequency, resulted from the Lomb-Scargle analysis. The 3σ significance level is indicated with a red line.

(2019a, 2019b). For each simulation, we generated a continuous light curve, with time resolution 2 ks, and then we selected only the time bins which correspond to the observed epochs. For each curve, we derived the Lomb-Scargle periodogram, obtaining peaks generated from random noise. For slope=2, which is the worst case, most of the generated peaks, about 70%, are found at periods longer (i.e. smaller frequencies) than half of the observed window. These are unreliable estimates because less than two cycles would be covered. We also observe that at frequencies comparable or larger than that of the periodicity observed, only 2-3 significant peaks ($\sim$ 0.05% of the generated peaks) are generated from the red noise. With slope=1, only 2 peaks, out of the 5000 simulations, are significant and both of them have frequency significantly smaller than the one corresponding to the periodicity. Should only white noise be present in the data, the Baluev method gives a reliable estimation of the FAP. With this assumption, the significance of the periodicity found is largely in excess of 5σ.

3.5.3 Discussion

From the analysis reported above, we derived the timing and spectral properties of the ULXs of NGC 925 in the X-ray band. In this section, we discuss the obtained results.

Temporal variability

All the three ULXs in NGC 925 are variable in flux on days to months timescales, but only one of them, ULX-3, shows a periodic modulation. We analysed their aperiodic variability by deriving the F_{var}, considering both our *Swift*/XRT monitoring and archival *Swift*/XRT data. In the context of ULXs, this estimator has been often used to study the variability inside individual observations, on timescales ranging from minutes to hours (e.g. Sutton et al. 2013, Pintore et al. 2020, Robba et al. 2021, Mondal et al. 2021a). This estimator can also be used to study long-term light curves, as often done in the literature for accreting compact objects such as blazars (e.g. Vagnetti et al. 2016, Aleksić et al. 2015, Schleicher et al. 2019). We used an "ensemble" approach, as explained in section 3.3.1. All the three ULXs in NGC 925 significantly vary on long-term timescales and they have a large fractional variability. In the total band F_{var} is higher than 50%, both for ULX-1 and ULX-3, while ULX-2 is less variable, with $F_{var} \sim 35\%$. In the latter, the variability is driven by the hard band, where F_{var} is higher than 50%. The same trend is present also in the other two sources, but it is

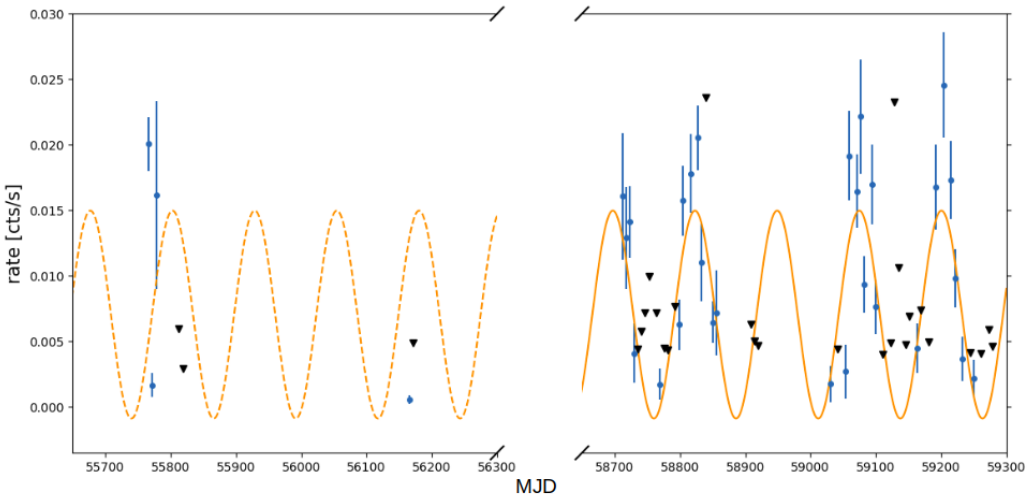

Figure 3.21: (Super-)orbital period of NGC 925 ULX-3 of 126 d. The light curve is binned in 6 days bins and the sinusoidal best-fit of the periodicity is superimposed. The period estimation has been done from the denser and more recent data (orange solid line) and it has been extrapolated to older data (orange dashed line). The *Swift*/XRT detections are marked with blue dots, while the upper limits with black inverted triangles.

less marked. This trend has been also observed on shorter timescales in other ULX systems (e.g. Middleton et al. 2015c, Walton et al. 2018b) and has been explained with the obscuration of the inner hard accretion flow by the outflowing winds.

We found a periodicity in NGC 925 ULX-3 of $\sim$ 126 d, which is consistent with the interval previously estimated by Earnshaw et al. (2020). From the superposition of the periodicity on the older dataset, we see that the period may not always be present in the ULX or it can be unstable, i.e. with shifts in phase or duration, as also found in other ULXs (see e.g. Vasilopoulos et al. 2020, 2021). Tens/hundreds of days periodicities, derived from flux variations in long-term light curves, have been discovered in other ULXs and have often been interpreted as super-orbital periods (e.g. Israel et al. 2017a, Fürst et al. 2018, Brightman et al. 2019). So we suggest that also the periodicity observed in the light curve of ULX-3 may be explained by a super-orbital modulation of the flux, possibly linked to a precession of a structure in the accretion flow, e.g. of the accreting disc, or of the magnetic dipole, in case of a NS accretor, but the available data did not permit to deepen the study of this point. On the other hand, we cannot exclude that the observed periodicity is caused by an orbital modulation of the flux, since the orbital period of the system is currently unknown.

No indications of a bimodal flux distribution are visible in the lightcurves of NGC 925 ULX-1 and ULX-2, which could indicate propeller phases and therefore a NS accretor. Furthermore, around ULX-1, Lara-López et al. (2021) identified a low-metallicity environment, where the formation of BHs with respect to NSs may be favoured, since low-metallicity stars are expected to lose smaller masses (e.g. Heger et al. 2003). In contrast, the residuals above 10 keV in ULX-1 *NuSTAR* data, may be modelled with similar parameters to that associated with the accretion columns above NSs magnetic poles (e.g. Walton et al. 2018c), but we remark the fact that the statistics is low and does not permit to discriminate among different spectral components, above 10 keV. ULX-3 is the only ULX in NGC 925 with a large number of significant upper limits. *Swift*/XRT observed the source only twice between MJD 56165 and MJD 57770 ($\sim$ 4 years) without detections before the *XMM-Newton* detection on MJD 57771. In this period, the source could have experienced a propeller stage, otherwise the two *Swift*/XRT non-detections may be simply explained by the (super-)orbital modulation of the flux. A high-metallicity environment has been found around ULX-3 (Lara-López et al. 2021), consistent with the formation of a NS.

Spectral classification

Using the *XMM-Newton* data, we classified the ULXs with the classification scheme proposed in Sutton et al. 2013, by using the spectral model DISKBB + POWER-LAW. Only one *XMM-Newton* observation was publicly available at the time of the analysis, not permitting us to search for transitions among different spectral regimes.

As reported in section 3.4.2, NGC 925 ULX-1 resulted in the *hard ultraluminous* regime in the available observation; we classified NGC 925 ULX-2 as a *hard ultraluminous* source, but also a *soft ultraluminous* classification is possible for this source; the spectral classification of the *XMM-Newton* spectrum of NGC 925 ULX-3 is also doubtful, but it resulted an *hard ultraluminous* source in the average *Swift*/XRT spectrum.

From a comparison with the known PULXs, typically found in the *hard ultraluminous regime* (e.g. Sutton et al. 2013, Pintore et al. 2017, Carpano et al. 2018), the ULXs in NGC 925 appear with similar disc temperatures (for the PULXs $\sim$ 0.04 – 0.2 keV), while the power-law index of the PULXs are sometimes similar and others harder ($\Gamma \sim 1$ – 1.9) than the sources in NGC 925.

Super-Eddington accretion

The normalizations of the spectral fitting components, BBODYRAD and DISKBB, see section 3.4.2 for a definition, give information on the apparent radius of the emitting areas. These radii might lack a physical meaning, but can be used to attempt a first characterization of the system accretion geometry.

We derived the emitting regions radii by using the *Swift*/XRT average spectrum, which may give an average estimation if spectral variability is present. The disc radius depends on the inclination

of the system: we assumed a reference value of 45° while estimating the radius of this component, given the quite hard spectral shape for the ULXs in NGC 925, suggesting rather low inclinations.

For ULX-1, the BBODYRAD and DISKBB radii are respectively 1452^{+588}_{-362} km and 75^{+14}_{-17} km, without assuming any colour or boundary correction factor. Such values are comparable to the radii observed in some other ULXs (e.g. Circinus ULX-5: Walton et al. 2020, Mondal et al. 2021a; 4X J1118: Motta et al. 2020). The source is in an ultraluminous regime of accretion, which implies a super-critical accretion disc (e.g. Shakura and Sunyaev 1973, Poutanen et al. 2007), characterized by outflows and advection (slim disc models). The disc would become geometrically thick, in the regions inside the spherisation radius[16]. From this radius, a fraction of the matter in the accretion flow is ejected from the disc through powerful winds. In the most external regions, the disc is instead expected to be geometrically thin. While the inner regions of the accretion flow are hot, the colder outer regions may contribute very little to the total emitted X-ray flux. The very inner regions may also be naked by the thick disc and the wind. In this scenario, some authors (e.g. Walton et al. 2015, Pintore et al. 2018b) proposed that the larger radius may represent the average dimension of the region where the outflows are launched, while the smaller radius may be interpreted as the inner disc size. Assuming an accreting, non-rotating BH, the inner disc radius would be equal to three Schwarzschild radii $\left(R_{in} = \frac{6GM}{c^2}\right)$. The apparent inner radius for NGC 925 ULX-1 results ~ 75 km, too small for an IMBH, which would require at least ~ 900 km in radius, for a minimum mass of $100 M_{\odot}$. This radius is also too small for a massive stellar BH of 30–100 $M_{\odot}$; we therefore propose a stellar mass BH, with mass < 10 $M_{\odot}$ or a NS, to be hosted in ULX-1. Considering the classification of the source in a super-Eddington accretion regime, it is reasonable to assume a colour correction factor equal 3 (e.g. Watarai and Mineshige 2003). By applying this f_{col} and a boundary correction factor $\zeta = 0.4$, the radius of the hot spectral component may increase to ~ 270 km, allowing a more massive BH of ~ 45 $M_{\odot}$, but still too small for an IMBH.

From the hot spectral component of ULX-2 *Swift*/XRT spectrum, we derived a radius of 89^{+12}_{-14} km, consistent with the estimation of Pintore et al. (2018b), derived from the *XMM-Newton* / *NuSTAR* spectrum. The colder region radius resulted > 13860 km. The same considerations carried out for NGC 925 ULX-1, also hold for ULX-2.

The colder region radius for ULX-3 is 7200^{+6100}_{-3000} km, the hotter component has instead a radius of 47^{+11}_{-14} km. In this case the compact object mass could be even smaller than for the other two sources.

[16] At the spherisation radius the vertical component of gravity and the force exerted by radiation pressure become comparable (Poutanen et al. 2007).

Chapter 4

The Cartwheel Galaxy

4.1 Introduction

In the context of the study of ULX variability, we also analysed the ULX population of a ring galaxy: the Cartwheel. The Cartwheel galaxy contains a large number of ULXs: Wolter and Trinchieri (2004) detected 16 ULXs, including source N10, which is a HLX. The large ULXs luminosity could be explained in terms of a collection of unresolved objects, due to the large distance. In subsequent works these sources have been discovered to be variable in flux (Crivellari et al. 2009; Pizzolato et al. 2010 for N10): a substantial temporal variability disfavours the interpretation as unresolved sources, pointing at a single accreting compact object. In fact a collection of unresolved object, also if they are variable, may result on average on a small or absent temporal variability. Thus, considering the large number of ULXs and that they are often variable, the Cartwheel is an interesting target to apply variability studies. In addition, the ULXs in the Cartwheel galaxy are likely associated to a single star formation burst (the same assumption has been also used in Wolter et al. 2018), which makes the Cartwheel ULXs the ideal target to carry out a population study.

Ring galaxies are irregular galaxies, with an annular shape. They are thought to form through roughly head-on collisions with a massive intruder galaxy, which is indicated as the bullet galaxy. As a consequence of the interaction between the two galaxies, a gravitational perturbation is induced and a shock wave forms. The wave propagates in the disc of the target galaxy and the result is the formation of a ring composed of gas and stars (e.g. Lynds and Toomre 1976).

The Cartwheel has a shape reminiscent of a wheel. It is located in a compact group (group radius 1.68 arcminutes) of 4 members (Iovino SGC 0035-3357; 2002): G1, G2, G3 and the Cartwheel galaxy. Its inclination is $50\pm10°$, its redshift is z=0.03 (Amram et al. 1998) and its distance $\sim$ 131 Mpc[1]. The particular shape of the Cartwheel originated in the impact with one of the companions (Higdon 1995), G3 (Higdon 1996) or G2 (Athanassoula et al. 1997). The consequence was the formation of two elliptical rings linked by spokes, the inner one has dust lanes crossing it (Struck et al. 1996). The linear diameter of the outer ring is $90''$ along the major axis, which is the largest physical diameter found in ring galaxies, and the inner one diameter is $18''$ (Amram et al. 1998): at a distance of 131 Mpc the diameters correspond respectively to 57 kpc and 11 kpc.

In the Cartwheel Galaxy there is the largest number of Ultra-Luminous X-Ray Sources (ULXs) contained in a single galaxy (Wolter and Trinchieri 2004, Gao et al. 2003). There is a claim for a larger number of ULXs, 34, in the galaxy NGC 2207 (see Walton et al. 2021), but the authors have used a distance for this galaxy of 34.6 Mpc, while the most recent estimations give a distance of about 17 Mpc for the same galaxy, which would give 7 ULXs instead of 34. In a previous work, Mineo et al. (2014) indicated 28 ULXs from both the interacting galaxies NGC2207 and IC2163. The high X-ray emission of the Cartwheel Galaxy is connected with the impact responsible for the formation

[1]Distances between ~129 and ~133 Mpc are indicated in NED (https://ned.ipac.caltech.edu); we adopt an intermediate value of 131 Mpc.

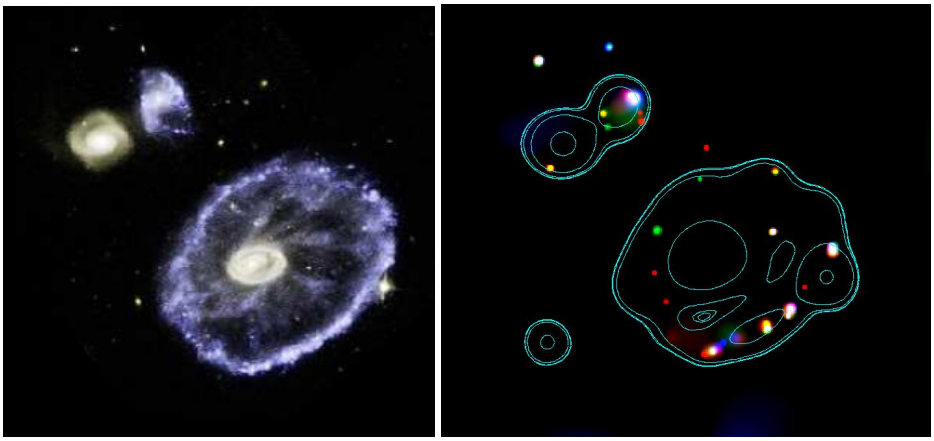

Figure 4.1: Left: Hubble Space Telescope (HST) optical image of the Cartwheel Galaxy (bottom). Two of the companions are visible in the upper part of the image: G1 (right) and G2 (left). G3 is further North, out of this field of view, but it has been observed in X-rays. Right: RGB image of the Cartwheel galaxy using *Chandra* data. Each epoch is represented with a colour: 2019 in red, 9531 in green and 9807 in blue. The data are smoothed with a Gaussian function ($3 \leq \sigma \leq 5$), with CSMOOTH.

of the ring and the star formation episode (e.g.Wolter et al. 1999, Higdon 1996, Mapelli et al. 2008). The southern part of the external ring contains most of the ULXs and yields more star formation than the other side. This observational evidence agrees with the hydrodynamical simulations conducted by Renaud et al. (2018). Simulations predicted a larger star formation in the part of the outer ring furthest from the nuclear region. This portion of the galaxy corresponds to the S-SW region of the outer ring, which contains massive and luminous HII regions (Higdon 1995).

The X-ray emission of the Cartwheel galaxy has already been studied in literature. Wolter et al. (1999) presented the first X-ray detection of the ring, the point sources and the X-ray Luminosity Function (XLF) have been studied in the work of Wolter and Trinchieri (2004), where the first *Chandra* observation of 2001 has been analysed; an extension of that work, with *XMM-Newton* data, was presented in Crivellari et al. (2009), which addresses both the Cartwheel and the companion galaxies; the most luminous source, N10, was studied in the works of Wolter et al. (2006) and Pizzolato et al. (2010), in which it was found to be variable.

We have analysed the *Chandra* and *XMM-Newton* pointings, with the aim of addressing the variability of the Cartwheel and of the companion galaxies ULXs. We also study the variability of the X-ray luminosity function (XLF) for the Cartwheel sources, considering them a single population of ULXs, comparing its shape at the three *Chandra* epochs. While all the sources have also been analysed in previous works, by using the first *Chandra* epoch and the *XMM-Newton* pointings, the second and third *Chandra* exposures have been previously used just to study the most luminous source N10.

4.2 The datasets

XMM-Newton observed the Cartwheel galaxy twice (see table 4.1), in 2004 and 2005 (Obs. IDs: 0200800101 and 0200800201). We analysed the EPIC-pn data. We reduced them with standard procedures, with SAS version 19.0 and we filtered the data as explained in section 3.2.2.

Chandra observed the Cartwheel galaxy three times, in 2001 and 2008 (Obs. IDs: 2019, 9531, 9807), with the instrument ACIS-S (see table 4.1). We reduced data with standard procedures, with CIAO version 4.11 and using the calibrations of the CALDB version 4.7.9.

Instrument	obs.Id	obs.Date	Exp. (ks)
Chandra	2019	26/27 May 2001	76.1
Chandra	9531	21 Jan 2008	51.4
Chandra	9807	09 Sep 2008	49.5
XMM-Newton	0200800101	14 Dec 2004	37.2
XMM-Newton	0200800201	21 May 2005	60.9

Table 4.1: Journal of observations with *Chandra* and *XMM-Newton* .

	9531-2019	*9807-2019*
α	−0.158	−0.099
δ	0.100	−0.078

Table 4.2: Average value of the differences between the right ascension (α) and the declination (δ) of observations 9531 and 9807, with respect to the observation 2019. All the differences are reported in arcsecond units.

We used the *Chandra* data, which have the smallest PSF, to detect point sources, both using the single exposures and a merged image of the three. We constructed the merged image, after the reprojection of each single image with the CIAO task REPROJECT_OBS, with the tool MERGE_OBS. The detection on the merged image allowed us to reach deeper fluxes.

The source detection has been run with WAVDETECT on scales 1, 2, 4, 8, 16 pixels, using a detection threshold of 6.58×10^{-7}, which has been derived from the pixels number in the analysed images. We created the PSF maps, necessary for the detection procedure, with the tool MAKEPSFMAP. In case of the merged image, we summed the single PSF maps with DMIMGCALC. The detected sources have very little counts, thus pile up is not present in the data.

4.3 Data analysis and Results

4.3.1 Point sources

We computed the differences in right ascension and declination of the three *Chandra* pointings, to verify if an astrometry correction was necessary. In particular, we derived the differences between the second and third exposures with respect to the first one. The resulting values found are reported in table 4.2, in arcsec units. The differences are smaller than the minimum of the PSF in the corresponding region, $\sim 0.9\ ''$, which allowed us to neglect them in the analysis. We used the coordinates of the first exposure, where most sources were visible. When a source was not detected in observation 2019, we instead used the coordinates from the merged image. More sources are visible in the first *Chandra* epoch than in the other exposures, because there was a decrease in the *Chandra* flux sensitivity during the years, which caused the first observation to be more sensitive than the others.

SOURCE	Position (J2000) Obs=2019		Position (J2000) Obs=9531		Position (J2000) Obs=9807		Position (J2000) Obs=Merged	
N1 (G2)	0:37:45.301	−33:42:28.684	0:37:45.283	−33:42:28.853	0:37:45.282	−33:42:28.550	0:37:45.300	−33:42:28.689
N2 (G1)	0:37:43.855	−33:42:09.810	0:37:43.855	−33:42:09.920	0:37:43.832	−33:42:10.010	0:37:43.850	−33:42:09.857
N3 (G1)	0:37:43.138	−33:42:04.223	0:37:43.097	−33:42:04.122	0:37:43.101	−33:42:04.272	0:37:43.098	−33:42:04.129
N4 (G1)	0:37:43.010	−33:42:06.155			0:37:43.006	−33:42:06.149	0:37:43.013	−33:42:06.099
N5 (G1)	0:37:42.802	−33:42:12.662					0:37:42.784	−33:42:12.679
N6	0:37:42.471	−33:43:04.262					0:37:42.492	−33:43:04.130
N7	0:37:41.081	−33:43:31.891					0:37:41.083	−33:43:31.780
N8	0:37:41.046	−33:42:21.358			0:37:41.063	−33:42:21.544	0:37:41.045	−33:42:21.534
N9	0:37:40.875	−33:43:30.972	0:37:40.865	−33:43:30.874	0:37:40.850	−33:43:31.177	0:37:40.876	−33:43:31.019
N10	0:37:39.390	−33:43:23.346	0:37:39.390	−33:43:23.373	0:37:39.393	−33:43:23.364	0:37:39.391	−33:43:23.284
N11	0:37:39.234	−33:42:50.322	0:37:39.217	−33:42:50.099	0:37:39.222	−33:42:50.298	0:37:39.222	−33:42:50.262
N12	0:37:39.171	−33:42:29.765	0:37:39.130	−33:42:29.680	0:37:39.158	−33:42:29.975	0:37:39.156	−33:42:29.691
N13	0:37:38.826	−33:43:18.551	0:37:38.796	−33:43:18.805	0:37:38.813	−33:43:18.894	0:37:38.805	−33:43:18.803
N14	0:37:38.741	−33:43:16.225	0:37:38.756	−33:43:16.347	0:37:38.736	−33:43:16.267	0:37:38.730	−33:43:16.303
N15	0:37:38.346	−33:43:09.006	0:37:38.354	−33:43:08.905	0:37:38.349	−33:43:08.989	0:37:38.347	−33:43:08.906
N16	0:37:37.606	−33:42:55.250	0:37:37.585	−33:42:54.860	0:37:37.595	−33:42:55.026	0:37:37.606	−33:42:55.158
N17	0:37:37.590	−33:42:57.207	0:37:37.591	−33:42:56.802			0:37:37.594	−33:42:57.024
N18	0:37:43.366	-33:43:12.753					0:37:43.380	−33:43:12.779
N19 (G1)	0:37:42.832	−33:42:09.68	0:37:42.835	−33:42:09.885			0:37:42.819	−33:42:09.800
N20	0:37:42.146	−33:43:13.961					0:37:42.142	−33:43:13.785
N21	0:37:41.261	−33:42:32.376	0:37:41.212	−33:42:32.484			0:37:41.211	−33:42:32.429
N22	0:37:40.439	−33:43:24.946					0:37:40.450	−33:43:24.697
N23	0:37:42.008	−33:43:26.917						
N24	0:37:40.178	−33:43:26.920			0:37:40.210	−33:43:26.196	0:37:40.261	−33:43:26.649
P25			0:37:42.403	−33:42:49.841	0:37:42.399	−33:42:49.732	0:37:42.393	−33:42:49.763
P26					0:37:40.589	−33:43:28.306	0:37:40.576	−33:43:28.351
P27							0:37:39.423	−33:43:21.198
P28							0:37:38.109	−33:43:05.615
P29					0:37:42.821	−33:43:14.264	0:37:42.863	−33:43:14.399
P30 (G1)			0:37:43.751	−33:42:14.516			0:37:43.754	−33:42:14.355
P31 (G1)	0:37:42.939	−33:42:04.178					0:37:42.937	−33:42:04.208
P32 (G3)	0:37:47.020	−33:39:53.158	0:37:47.042	−33:39:53.229	0:37:46.960	−33:39:52.951	0:37:47.013	−33:39:53.336
P33			0:37:40.749	−33:42:58.181			0:37:40.721	−33:42:58.328
P34							0:37:43.064	−33:43:22.606
P35							0:37:41.339	−33:43:31.455
P36							0:37:37.877	−33:42:53.140
P37	0:37:41.727	−33:42:35.426						

Table 4.3: Coordinates of the point sources in the Cartwheel Galaxy and in the companion galaxies (G1, G2, G3). The detection has been run with the task *wavdetect* of the CIAO threads. Source P25 is the *XMM-Newton* source XMM8 (Crivellari et al. 2009). The source detection has been run in each of the *Chandra* exposures and also in their merged image.

The detected point sources are listed in table 4.3 , with the same nomenclature used by Wolter and Trinchieri (2004), while the new sources are labeled with letter P and progressive numbers. Both the Cartwheel and the companion galaxies (G1, G2, G3) are included in the table. When a source was not detected in an image, no coordinates are reported in the table. Having used a different version of the software and calibration files with respect with the previously published analysis, we detected a slightly different number of sources, in the first *Chandra* observation, which was already analysed in Wolter and Trinchieri (2004), we detect sources P31, P32 and P37 not indicated in the previous analysis. The other two *Chandra* exposures were not previously analysed, except for the most luminous point-like source N10. Considering all the three *Chandra* pointings individually and their merged image, we detected 12 "new" sources, with respect to the previous analysis of observation 2019 of Wolter and Trinchieri (2004). Three of them (P31, P36, P37) were indicated in the analysis of Gao et al. (2003), who also detect a source at the position RA=0:37:38.97 Dec=−33:43:17.5, not detected in our analysis. We also detect, in the second and third *Chandra* exposures, the *XMM-Newton* source XMM8, which we named P25, while this source was not visible in the first *Chandra* observation. No nuclear source is visible in X-rays for the galaxy G1, but a number of sources are associated to it. We detect source N1 and P32, associated respectively with the galaxies G2 and G3. Both the nuclei of G2 and G3 are visible in the merged image. The nucleus of G2 is also detected in observation 9531, while that of G3 is visible in observation 2019.

For each of the detected sources we extracted the source counts from a circular region with 1″ radius, in the energy range 0.5 – 10 keV.

To highlight the sources variability among the exposures, we constructed a image of the three *Chandra* epochs combined, see figure 4.1.

The sources visible in *XMM-Newton* data are N6, N7+N9, N11, N12, N13+N14, N16+N17, N21 and P25 (see also Crivellari et al. 2009). We extracted the sources counts in the energy band 0.5–10 keV, from circular regions with radius 10″ (8″ for N12 which is near a CCD gap). The extracted counts are reported in table 4.5.

4.3.2 Spectral analysis

We extracted the *Chandra* spectra from circular regions with 1″ radius, using the SPECEXTRACT task of CIAO, with an annular background around each source.

Due to the little counts in most of the sources, we summed the spectra in the three *Chandra* exposures to improve the statistics (with the COMBINE procedure of CIAO) and analysed only those which resulted to contain more than 100 net counts. The sources in question are N9, N10, N11, N14, N16 and N17. We binned the spectra with at least 20 counts per bin and we applied the χ^2 statistics in the spectral analysis.

We used an absorbed power-law to describe the spectra (TBABS*POW in XSPEC).The model gave a statistically acceptable spectral-fitting for the six sources; the resulting parameters are reported in Table 4.4. The $n_{\rm H}$ was not well constrained for sources N16 and N17, thus we just give an upper limit. The power-law index Γ ranges from 1.4 to 2.7, which suggests that the analysed sources have different spectral hardness. Considering the Galactic absorption in the direction of the Cartwheel, i.e. $n_{\rm H} = 2.5{\times}10^{20}$ cm^{-2} (Kalberla et al. 2005), at least N10, N11 and N14 have an additional local absorption. Indeed, if we model their spectra with $n_{\rm H}$ fixed at the Galactic value, it results in a not statistically acceptable fit. The additional absorption found in some of the sources is not surprising. Absorbing material may be present in the vicinity of a ULX and may be ascribed to the diffuse gas visible in the Cartwheel ring (Wolter and Trinchieri 2004) or to the outflows that are sometimes observed around the ULXs (e.g. Middleton et al. 2015b, Pinto et al. 2016).

Source	$n_{\rm H}$ ($*10^{20}$cm^{-2})	Γ	$F_{(0.5-2.0)\rm keV}$ 10^{-15}erg cm^{-2} s^{-1}	$F_{(2.0-10.0)\rm keV}$ 10^{-15}erg cm^{-2} s^{-1}	$L_{(0.5-2.0)\rm keV}$ 10^{39} erg s^{-1}	$L_{(2.0-10.0)\rm keV}$ 10^{39} erg s^{-1}	χ^2/dof	$P_{\rm val}$
N9	$31.1^{+40.4}_{-28.9}$	$1.6^{+1.1}_{-0.9}$	3.6±0.5	8.2±1.1	6.7±1.0	15.9±2.1	2.2/3	0.53
N10	$43.9^{+11.6}_{-9.5}$	$2.1^{+0.3}_{-0.2}$	20.3±1.5	20.9±1.5	39.4±2.9	40.6±2.9	22.82/23	0.47
N11	$115.9^{+74.8}_{-54.3}$	$1.9^{+0.8}_{-0.7}$	7.5±1.1	9.7±1.5	14.6±2.1	18.8±2.9	0.84/3	0.84
N14	$30.5^{+18.4}_{-14.3}$	$2.7^{+0.6}_{-0.5}$	5.4±0.7	2.3±0.3	10.5±1.4	4.5±0.6	6.83/5	0.23
N16	<24.1	$1.4^{+0.2}_{-0.1}$	2.3±0.4	8.0±1.0	4.5±0.8	15.5±1.9	3.62/5	0.61
N17	<22.3	$2.1^{+1.0}_{-0.5}$	2.9±0.4	2.9±0.4	5.6±0.8	5.6±0.8	2.99/4	0.56

Table 4.4: Spectral fitting parameters: n_H, power-law index (Γ) and unabsorbed fluxes and luminosities in (0.5-2.0) keV and (2.0-10.0) keV, for the sources with more than 100 counts, in the sum of the three *Chandra* observations. We used an absorbed power-law model (*tbabs*pow* in XSPEC). The degrees of freedom (dof) are usually few because of the small number of counts in the spectra. The adopted model gives an acceptable fit at more than 2σ for all the sources, i.e. $P_{\rm val} > 0.05$.

For the sources with lesser counts we could not study the individual spectra, due to the low statistics. We analysed the average spectrum of all the sources with the *Chandra* data, excluding N10, i.e. the most luminous ULX, which may influence the result. By fitting simultaneously the three *Chandra* exposures, we obtained $n_H = 1.0^{+0.4}_{-0.3} \times 10^{21}$ cm^{-2}, $\Gamma = 1.7^{+0.1}_{-0.1}$. We used this model and a Bayesian code, BLike (A. Belfiore, private communication), to derive the fluxes. For consistency, also for the six sources with more than 100 counts, for which we have also studied the spectrum, we used the same model and method to derive fluxes in the single exposures. The luminosities derived with this spectral model are consistent with those obtained by using the spectral model from Wolter and Trinchieri (2004), i.e. $n_H = 1.9 \times 10^{21}$ cm^{-2} and $\Gamma = 2.2$. The difference on the luminosity estimation from the two model is smaller than 10%. We applied the same method also to derive *XMM-Newton* fluxes. We verified that the adopted model was statistically acceptable for the *XMM-Newton* sources with enough spectral counts and we assumed that it was an acceptable approximation also for the less luminous ULXs. For *XMM-Newton* we used an extraction radius of $10''$, except for source N12 for which we used a smaller radius of $8''$, because it was close to a CCD gap. *XMM-Newton* background was computed from an elliptical region including all the Cartwheel galaxy, but not the detected point sources. We derived the luminosity from the flux with the assumed distance of 131 Mpc.

4.3.3 Variability on short timescales

Some ULXs analysed in the literature have shown short-term variability, as explained in section 2.1.1. Due to the large distance of the Cartwheel galaxy and consequently the low statistics of the data, we searched for the short-term variability of the brightest sources only. Furthermore, Heil et al. (2009) did not find a large occurrence of short-term variability in the brightest sources, thus we do not expect to find short-term variability in many of the Cartwheel sources, considering also that we analyse only the most luminous of them. We selected the sources with at least 20 net counts in the single *Chandra* observation and we applied a Kolmogorov-Smirnov test on the photons arrival times. In absence of variability, the photons would arrive on the telescope at regular time intervals, so we compared the arrival times with an expected uniform distribution.

We found variability with at least 1σ significance only for three ULXs, in three single observations: N9 in observation 2019, N14 in observation 9807 and N22 in observation 9807. We interpret this fact as a lack of significant short-term variability for the Cartwheel sources, as often happens in ULXs (see e.g. Heil et al. 2009), but we note that the low statistics in the data may have influenced this finding.

4.3.4 Long-term variability

While studying the long-term variability, we first considered the same instrument by analysing the three *Chandra* epochs. The *Chandra* effective area decreased in the years, thus we had to correct the observed counts in the two 2008 observations to take into account this effect. We verified the significance of the long-term variability in the energy band 0.5-10.0 keV, by applying the Cash statistics (Cash 1979). The corrected counts and the statistics for each source are listed in table 4.5.

SOURCE	cts_{2019}	cts_{101}	cts_{201}	cts_{9531}	cts_{9807}	*Cash stat*	P_{val}	σ
N1(G2)	59			27.5	15.6	11.89	2.6e-03	**3.01**
N2(G1)	35			28.75	19.5	1.48	4.8e-01	0.71
N3(G1)	55			92.5	67.6	31.25	1.6e-07	**5.24**
N4(G1)	44			21.25	26	1.68	4.3e-01	0.79
N5(G1)	37			8.75	11.7	11.19	3.7e-03	2.90
N6	17	0	52.5	3.75	5.20	5.62/87.25	6.0e-02/5.1e-18	1.88/**8.65**
N7	59			12.50	9.10	30.60	2.3e-07	**5.18**
N8	19			6.25	11.7	2.95	2.3e-01	1.20
N9	60			67.5	32.5	13.23	1.3e-03	**3.21**
N7N9(XMM)	118	159.6	159.6	80	41.6	140.24	2.5e-29	**11.24**
N10	344	214.2	210	195	61.1	118.85/160.36	1.6e-26/1.2e-33	**10.66/12.09**
N11	61	52.5	52.5	43.75	35.10	0.68/12.42	7.1e-01/1.4e-02	0.37/2.44
N12	40	0	52.5	27.5	13	6.23/57.12	4.4e-02/1.2e-11	2.01/**6.78**
N13	34			27.5	32.5	2.44	2.9e-01	1.05
N14	78			50	62.4	2.20	3.3e-01	0.97
N13N14(XMM)	111	184.8	211.05	77.5	93.6	160.84	9.7e-34	**12.11**
N15	16			15	7.8	2.10	3.5e-01	0.93
N16	85			45	62.4	3.63	1.6e-01	1.40
N17	95			55	22.1	22.98	1.0e-05	**4.41**
N16N17(XMM)	179	78.75	132.3	92.5	84.5	8.39	7.8e-02	1.76
N18	7			3.75	2.6	0.65	7.2e-01	0.35
N19(G1)	12			18.75	10.4	5.47	6.5e-02	1.85
N20	6			0	0	10.13	6.3e-03	2.73
N21	7			20	9.1	12.8	1.7e-03	**3.14**
N21(XMM)	7	7	0	20	9.1	34.41	6.1e-07	**4.9**
N22	15			12.5	10.4	0.30	8.6e-01	0.18
N23	12			0	1.3	15.06	5.38e-04	**3.46**
N24	12			5	16.9	8.10	1.7e-02	2.38
P25	3	26.25	78.75	40	28.6	59.73/107.9	1.1e-13/2.0e-22	**7.43/9.74**
P26	4			3.75	40.3	65.53	5.9e-15	**7.81**
P27	25			16.25	7.8	3.98	1.4e-01	1.49
P28	3			10	9.1	8.99	1.1e-02	2.54
P29	5			3.75	11.7	7.66	2.2e-02	2.29
P30(G1)	2			20	3.9	27.42	1.1e-06	**4.87**
P31(G1)	31			21.25	22.1	0.12	9.4e-01	0.07
P32(G3)	9			10	7.8	1.19	5.5e-01	0.59
P33	2			8.75	3.9	7.65	2.2e-02	2.29
P34	3			3.75	3.9	1.01	6.0e-01	0.52
P35	6			11.25	6.5	4.35	1.1e-01	1.58
P36	10			7.5	1.3	5.39	6.8e-02	1.83
P37	10			3.75	1.3	4.50	1.08e-01	1.62

Table 4.5: Column 1: names of the sources; Columns 2, 3, 4, 5, 6: total counts in source regions in (0.5 - 10.0 keV); *Chandra* counts in observations 9531 and 9807, corrected for changes in the effective area; *XMM-Newton* counts corrected to account for the difference with respect to *Chandra* effective area. Columns 7, 8, 9: Cash statistics, P-value, significance of the variability, with *Chandra* data only. When a source was detected also with *XMM-Newton* the statistics with all data is reported at the right of '/'. The values obtained from the sum of the sources not individually resolved by *XMM-Newton* (N7+N9 + N13+N14, N16+N17) are also listed.

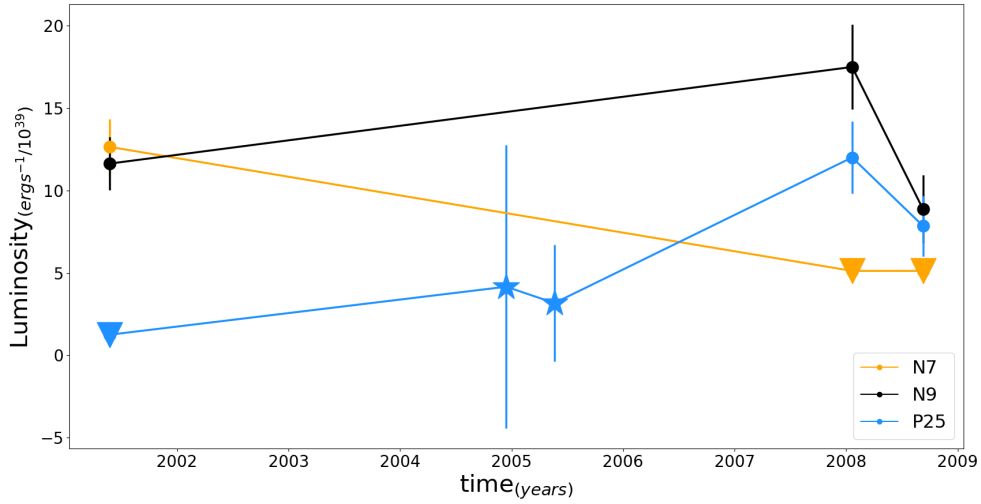

Figure 4.2: Light curves of sources N7 (orange), N9 (black), P25 (blue) in the Cartwheel galaxy. The *Chandra* observations are the 'dots', the *XMM-Newton* observations are the 'stars'. The 2σ upper limits, derived with the code BLIKE, are represented with 'inverted triangles'.

Some sources were not resolved in the *XMM-Newton* data. Thus, while considering also the *XMM-Newton* data we analysed the long-term variability of the following sources: N6, N10, N11, N12, N21, P25, N7+N9, N13+N14, N16+N17.

The effective areas of *Chandra* and *XMM-Newton* are different; we corrected the *XMM-Newton* counts in order to compare them with *Chandra* counts, considering the ratio of the effective areas. We applied the Cash statistics to the data of both satellites (table 4.5). The sources variable at least with a 3σ significance are highlighted in bold in the last column of the table.

It is not easy to conduct a systematic study with a small number of sources, thus we applied different methods to all the detected sources, to determine the range of total variability.

To estimate the total intensity variability, we computed the ratio between the maximum and minimum observed luminosity, L_{max}/L_{min}; we report the obtained ratios in Table 4.6. The luminosity has been estimated by using the most likely flux value, derived with BLIKE, and considering the assumed distance of 131 Mpc. In the ratio computation we used the symmetrical luminosity (L_{simm}), which is:

$$L_{simm} = L_{BLike} + \frac{err_{hi} - err_{lo}}{2}, \tag{4.1}$$

L_{BLike} is the luminosity derived from the most likely flux, err_{hi} is the upper error on luminosity and err_{lo} is the lower error on luminosity. When just one detection was present, we used the detection and the lower upper limit, deriving just a lower limit on the luminosity ratio.

The amplitude of the variability may be computed by deriving the fractional variability amplitude F_{var} (see section 2.5.3). We derived F_{var} for sources having a minimum of two detections and we computed a 3σ upper limit of the F_{var}, using the XRONOS task LCSTATS, when the fractional variability amplitude determination was not possible, because large uncertainties were present (see the results in table 4.6). F_{var} derived from single light curves and extremely sparse samplings may result in unreliable estimates, so we derived also the "ensemble" F_{var} for both the *Chandra* and *XMM-Newton* data. We proceeded with the simulations with the same Monte Carlo approach used in the previous chapter, for our *Swift*/XRT sample of ULXs. The resulting F_{var} is reported in the last column of table 4.6.

Considering only *Chandra* data, ~30% of the ULXs are variable with at least a 3σ significance.

The percentage is similar, ∼29%, considering the Cartwheel or G1 alone (table 4.5). Only one source for galaxy was detected in G2 and G3: N1, associated to G2, is significantly variable, while P32 in G3 has a variability significance smaller than 1σ.

When we include also the *XMM-Newton* data, the sources variable with a minimum of 3σ significance are 35% (table 4.5). Source N13N14 is variable at more than 3σ, but considering N13 and N14 separately in the *Chandra* data, their variability significance is $\sim 1\sigma$.

About 37% of the sources detected with *Chandra* have a luminosity ratio > 2 (excluding those for which the data did not permit the estimation); this should be considered as a lower limit on the number of sources which vary more than a factor 2, because for seven sources we obtained only a lower limit between 1.30 and 1.79 on the luminosity ratio, thus their variability factor may be larger. For two of the sources the lower limit on the variability factor is larger than 5 (> 9.6 for source P25 and >6.6 for source P26) which means that their variability may reach or overcome an order of magnitude. In the Cartwheel alone, the variability factor is larger than 2 for 50% of the sources (considering both *Chandra* and *XMM-Newton* data); for the galaxy G1 the percentage becomes 29%. We had to exclude some sources while estimating this percentage, because for those ULXs there were no detections in the *Chandra* observations or the source was detected only once and we found upper limits larger than the detection luminosity in the other epochs.

$F_{var,ensemble}$ is between 8 and 64% for the single *Chandra* sources and, for many of them, 33%, $F_{var,ensamble} > 30\%$, considering only the ULXs for which it was possible to derive F_{var}. Considering also *XMM-Newton* data this percentage of sources becomes ∼ 50% and in 18% of the sources $F_{var,ensamble} > 50\%$.

The long-term variability was found in many of the analysed sources, suggesting that variability on timescales of months to years is a characteristic feature of the ULX population in ring galaxies, in contrast with short-term variability, which seems often absent. The same behaviours, both on long and short timescales, are usually observed in the ULXs of non-ring galaxies, which are often variable on long timescales, while short-term variability appears to be suppressed in some sources and transient in others (see e.g. Gladstone and Roberts 2009, Song et al. 2020, Heil et al. 2009), rendering the detection of the short-term variability a difficult task if only few observations are available. Some of the Cartwheel and of its companions sources have a transient behaviour – they are not always detected in the observations – such as source P25, which was not visible in the first *Chandra* epoch, or source N7, which was visible in the first *Chandra* epoch and in the *XMM-Newton* observations but then turned off: in figure 4.2, we show the light curves of this two transient sources; in the same figure we plot for comparison the light curve of N9, which is a persistent source with a luminosity comparable with those of the transient P25 and N7. A transient source may be characterised by propeller stages, which may be caused only by a NS compact object. Otherwise, the non-detection in some observations may be caused by a flux under the instrument detection threshold.

Source	$L_{2019}^{(0.5-10.0keV)}$	$L_{101}^{(0.5-10.0keV)}$	$L_{201}^{(0.5-10.0keV)}$	$L_{9531}^{(0.5-10.0keV)}$	$L_{9807}^{(0.5-10.0keV)}$	L_{max}/L_{min}	F_{var}	$F_{var,ensemble}$
	10^{39}	10^{39}	10^{39}	10^{39}	10^{39}			
N1 (G2)	12.82±1.66			7.96±1.88	4.56±1.48	2.81	0.39±0.12	0.55±0.02
N2 (G1)	7.66±1.39			8.10±1.87	5.08±1.60	1.59	<0.55	0.17±0.03
N3 (G1)	11.35±1.61			28.41±3.26	18.70±2.73	2.50	0.40±0.08	0.33±0.01
N4 (G1)	9.20±1.45			6.74±1.71	6.95±1.77	1.36	<0.53	0.26±0.04
N5 (G1)	7.99±1.39			<5.10	<4.46	>1.79	–	–
N6	3.32±0.91	0	7.74±3.70	<4.14	<4.91	?/>2.33	–/<1.90	–/0.40±0.13
N7	12.64±1.68			<5.12	<5.12	>2.47	–	–
N8	3.87±0.99			<3.96	2.97±1.30	1.30	<0.96	0.17±0.06
N9	11.63±1.61			17.49±2.58	8.87±2.05	1.97	0.36±0.10	0.34±0.02
N7N9	24.24±2.33	66.93±7.46	35.78±4.47	20.11±2.84	11.01±2.44	6.07	0.70±0.06	0.76±0.01
N10	70.45±3.81	106.41±8.39	57.26±5.20	54.37±4.42	17.37±2.71	4.05/6.13	0.54±0.05/0.51±0.04	0.64±0.01/0.57±0.01
N11	13.24±1.72	11.40±6.17	1.92±3.39	11.98±2.18	9.96±2.05	1.33/6.90	<0.42/0.20±0.16	0.17±0.02/0.38±0.03
N12	7.78±1.31	0	3.87±3.42	7.57±1.77	<4.98	>1.56/>2.01	<0.62/<0.73	0.10±0.06/0.43±0.04
N13	7.14±1.26			10.99±2.09	10.26±2.18	1.54	<0.53	0.07±0.02
N14	16.29±1.86			14.51±2.36	18.37±2.81	1.27	<0.35	0.12±0.02
N13N14	23.43±2.24	97.98±8.33	52.04±5.19	25.48±3.16	28.64±3.56	4.18	0.69±0.05	0.75±0.01
N15	3.46±0.92			4.77±1.51	<4.63	1.38	<0.96	0.08±0.04
N16	19.82±2.13			13.04±2.23	19.75±2.84	1.52	0.13±0.10	0.21±0.02
N17	22.19±2.22			15.33±2.41	6.02±1.70	3.69	0.44±0.09	0.58±0.02
N16N17	41.71±3.07	21.47±5.79	26.27±4.18	28.21±3.27	26.05±3.31	1.94	<0.24	0.26±0.01
N18	<2.11			<2.45	<2.35	?	–	–
N19 (G1)	3.19±0.92			5.41±1.57	<5.03	1.69	0.51±0.23	0.30±0.06
N20	2.52±0.82			<1.09	<1.88	>2.31	–	–
N21	<2.64	0	2.22±3.44	6.05±1.69	3.06±1.30	>2.29/>2.73	0.47±0.25/<1.13	0.42±0.10/0.53±0.07
N22	2.35±0.82			<5.75	<5.26	?	–	–
N23	<3.23			<1.29	<2.20	?	–	–
N24	<3.12			<3.78	5.49±1.64	>1.76	–	–
P25	<1.25	4.16±8.59	3.17±3.54	12.00±2.20	7.85±1.84	>9.6/47.79	<0.64/<0.72	0.18±0.05/0.30±0.04
P26	<1.80			<1.81	11.98±2.28	>6.64	–	–
P27	4.59±1.04			5.32±1.53	<4.08	>1.30	<0.84	0.12±0.06
P28	<1.36			3.97±1.42	3.31±1.39	>2.92	<1.37	0.13±0.06
P29	<2.53			<3.49	3.94±1.41	>1.56	–	–
P30 (G1)	<2.30			6.40±1.66	<3.32	>2.78	–	–
P31 (G1)	6.08±1.21			5.68±1.60	5.85±1.65	1.07	<0.62	0.10±0.03
P32 (G3)	2.21±0.80			<4.93	3.19±1.39	1.45	<1.31	0.09±0.05
P33	<1.98			3.18±1.25	<4.61	>1.61	–	–
P34	<2.00			<2.36	<2.11	?	–	–
P35	<2.20			<5.00	<4.73	?	–	–
P36	<3.20			<3.32	<1.40	?	–	–
P37	2.40±0.81			<2.91	<1.65	>1.46	–	–

Table 4.6: Column 1: source name; Columns 2, 5, 6: ULXs luminosity in the *Chandra* observations; Columns 3, 4: ULXs luminosity in *XMM-Newton* observations, the luminosities are in (0.5 - 10 keV) and were derived assuming an absorbed power-law model ($n_{\rm H}$ = 1.9×10^{21} cm^{-2} and Γ = 2.2) and a distance of 131 Mpc. Column 7: ratio between maximum and minimum luminosity; Column 8: fractional variability (F_{var}). When the mean error squared is larger than the variance of the light curve we do not compute F_{var}. The count rates used for the computation of F_{var} have been corrected to account for the differences in the effective area of the instruments in each observation. When a source was detected also with *XMM-Newton* data, we report on the left the value obtained with *Chandra* data only, on the right, the value obtained by considering also *XMM-Newton* data. When a source was detected only once and the upper limits are higher than the detected luminosity, we cannot compute L_{max}/L_{min} and we report a '?'. Column 9: F_{var} derived with the "ensemble" approach for *Chandra* data. P34, P35 and P36 are included in the table for completeness, even if they were only detected in the merged image in our analysis.

4.3.5 Luminosity function

Many ULXs resulted highly variable in flux among the observations. We studied the X-ray luminosity function (XLF) of the Cartwheel, in order to verify if the flux variability of its sources may influence the shape of the XLF.

Binder et al. (2017) studied the effects of variability on the shape of the XLF of the X-ray binaries in NGC 300. They could not distinguish the effects caused by Common Envelope phase from those deriving from the sources variability, thus they did not obtain any firm conclusion.

Zezas et al. (2006) studied the variability of the Antennae X-ray point sources and they concluded that, despite the flux variability by up to a factor 2-6, observed in many sources in months to years timescales, no changes in the total XLF shape were visible.

We constructed the cumulative X-ray luminosity function (XLF) of the Cartwheel in each of the *Chandra* observations, which span 8 years, in the energy band (2.0-10.0) keV, the energy band was chosen to allow a direct comparison with the analysis of Grimm et al. (2003). The cumulative XLF of the Cartwheel, in the first *Chandra* epoch, only for the sources in the ring, has already been studied in Wolter and Trinchieri (2004). They assumed a Star Formation Rate (SFR) of 20 $M_{\odot}$ yr^{-1} for the Cartwheel and they found that the XLF was in agreement with the "universal" LF of the High Mass X-ray Binaries (HMXBs) (Grimm et al. 2003). The authors noted a flattening at low luminosity in the XLF and they attributed this effect to detection incompleteness, but they did not present a corrected version of the XLF considering the incompleteness. The corrected Cartwheel XLF is plotted in Figure 6 of Wolter et al. (2015) and the same analysis was presented also in Wolter et al. (2018), considering only the sources in the Cartwheel ring. We computed the XLF for the three epochs and by using all the detected sources associated with the Cartwheel, also those not in the ring region, and we used the same procedure followed by Wolter et al. (2015) to correct the data for detection incompleteness: we used figure 12 from Kim and Fabbiano (2003), where detection probabilities are plotted as a function of source and background counts.

The cumulative XLF of the Cartwheel galaxy is shown in Figure 4.3. It is consistent with the Grimm function for HMXBs, if we assume a 20 $M_{\odot}$ yr^{-1} SFR, as was previously found by Wolter and Trinchieri (2004) with the data of the first *Chandra* observation only, but a flattening at high luminosity may be present. The XLF appears consistent in shape among the three epochs, when we take into account that there is an average error of $\sim 20\%$ on the luminosity, except for the source N10.

Considering that no substantial differences in shape are visible in the XLF among the three *Chandra* epochs, despite the flux variability of the ULXs, we constructed the differential XLF by summing all the sources detected in the three observations, weighting it on SFR. In this way we increased the statistics and we could study in more detail the XLF shape. Here, we describe the procedure used to construct the differential XLF; the luminosities used are in units of 10^{39} erg s^{-1}. We grouped the sources in logarithmic bins equally spaced (using a step: $\log(\Delta) = 0.3$, $x_i = x_0 \times \Delta^i$) to construct a binned differential luminosity function and we obtained six bins. The value of the differential XLF was obtained by the ratio between the number of sources in each bin and the bin width.

First, we used a power-law model to fit the differential LF, applying a maximum likelihood approach. The luminosities were assumed to be distributed as $f = nx^{-\gamma}$, n is the normalization and γ is the power-law index, while x is the luminosity in units of 10^{39} erg s^{-1}. Every bin contains N_i sources and the expected value for each bin is:

$$y_i = \int_{x_i}^{x_{i+1}} nx^{-\gamma} dx = \frac{n}{1-\gamma}(x_{i+1}^{1-\gamma} - x_i^{1-\gamma}) = \frac{n \times (\Delta^{1-\gamma} - 1)}{1-\gamma} x_i^{1-\gamma}; \tag{4.2}$$

dividing by the bin width $l_i = x_{i+1} - x_i$, we obtained the value:

$$\frac{y_i}{l_i} = \frac{n(\Delta^{1-\gamma} - 1)x_i^{-\gamma}}{(1-\gamma)(\Delta - 1)}. \tag{4.3}$$

We introduced

$$\alpha(n, \gamma) = \frac{n(\Delta^{1-\gamma} - 1)}{(1-\gamma)(\Delta - 1)} \tag{4.4}$$

and we obtained the expected value in a more compact form:

$$\frac{y_i}{l_i} = \alpha x_i^{-\gamma} \tag{4.5}$$

In each bin, the sources are distributed following the Poissonian statistics, thus we can write the probability to find N_i sources per bin, given the expected value (y_i), as:

$$P(N_i|y_i) = e^{-y_i}\frac{y_i^{N_i}}{N_i!}. \tag{4.6}$$

The latter is the likelihood function for the single bin; we can neglect the factorial term because it is model independent.

The total probability may be derived as the product of the single bin probabilities. We considered the sum of the logarithms of the probability to simplify the calculation.

$$ln(P_{tot}) = ln(\Pi P(N_i|y_i)) = \Sigma ln(e^{-y_i} y_i^{N_i}) = \Sigma(-y_i + N_i ln(y_i)) \tag{4.7}$$

and, with $\frac{N_i}{l_i}$ and $\frac{y_i}{l_i}$ instead of N_i and y_i, and applying the equations 4.7 and 4.5, the log likelihood results to be:

$$ln(Like) = -\alpha\Sigma x_i^{-\gamma} + ln\alpha\Sigma\frac{N_i}{l_i} - \gamma\Sigma\frac{N_i}{l_i}lnx_i. \tag{4.8}$$

The fit which gives the maximum value for the logarithmic likelihood function, or equivalently the minimum of −ln(Like), is the best fit.

An exponential cut-off power-law, $y = nx^{-\gamma}\ e^{-\frac{x}{x_c}}$, where x_c is the cut-off luminosity, is a better model for the XLF. We followed the same procedure used in the power-law case, and derived the logarithmic likelihood function:

$$ln(Like) = \Sigma[\frac{n}{x_{i+1} - x_i} * p + \frac{N_i}{l_i} ln(\frac{-n}{x_{i+1} - x_i} * p)], \tag{4.9}$$

where

$$p = (x_{i+1}^{1-\gamma})E_\gamma(\frac{x_{i+1}}{x_c}) - (x_i^{1-\gamma})E_\gamma(\frac{x_i}{x_c}), \tag{4.10}$$

E_γ is the exponential integral.

The resulting best-fitting parameters for the power-law model are Γ = 1.51 and included in the 1σ confidence interval [1.30; 1.73] and n = 32.36, included in the interval [21.86; 46.70].

The exponential cut-off model gives Γ = 1.23 [0.88;1.66]; n = 31.55 [21.98;41.55]; x_c = 15.29 [10.29;20.29], corresponding to a luminosity cut-off of 1.53 [1.03;2.03]$\times 10^{40}$ erg s^{-1}.

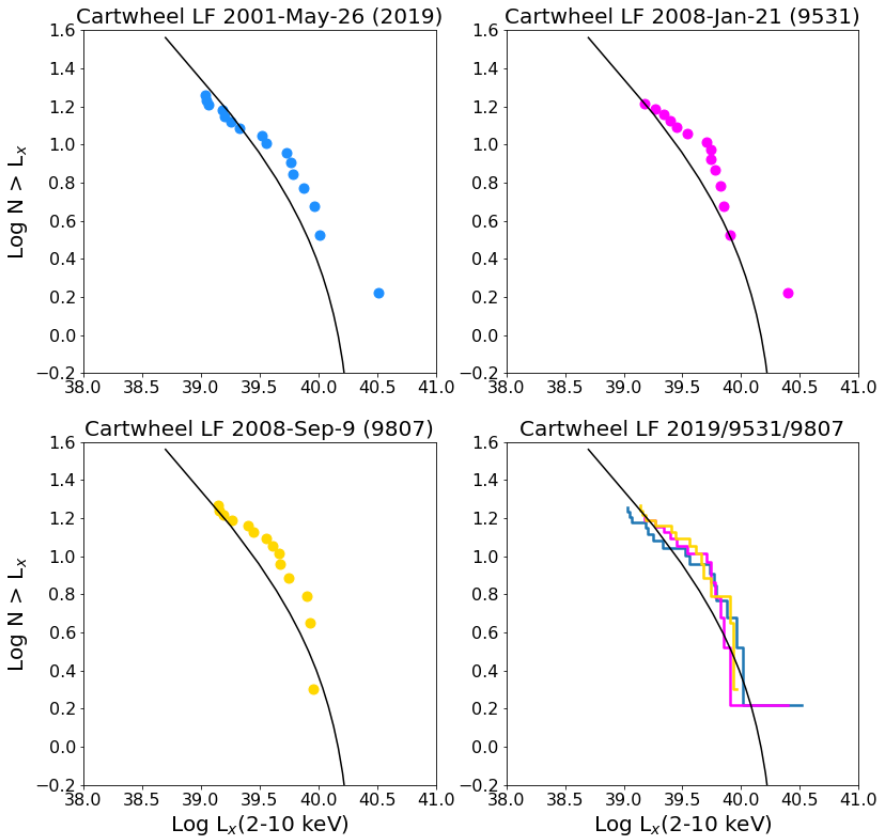

Figure 4.3: upper panels and bottom left: Cartwheel galaxy cumulative XLF, using the three *Chandra* epochs. bottom right panel: XLF of the three *Chandra* epochs plotted together. The black line represents the Grimm function (Grimm et al. 2003) for HMXBs, assuming SFR = $20 M_{\odot} yr^{-1}$, for the Cartwheel galaxy.

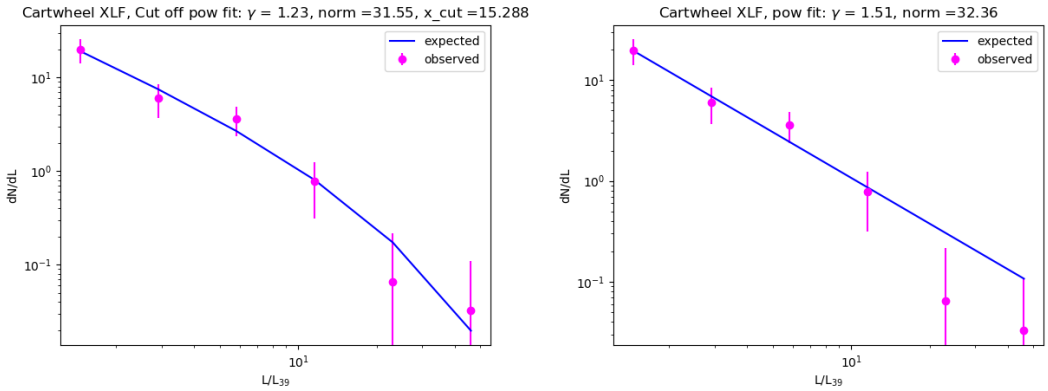

Figure 4.4: Differential XLF. Observed values (magenta); the statistical uncertainties have been derived by using the Gehrels approximation (Gehrels 1986). Left panel: best cut-off power-law fit (solid blue line). Right panel: best power-law fit (solid blue line).

We applied a Kolmogorov-Smirnov test (KS) to evaluate the goodness of the fits. We thus verified if the observed values may be drawn from the same distribution of the expected values, i.e. those expected considering the best-fitting model. The P_{val} of the KS test is about 0.93 for the power-law fit and about 1 for the cut-off power-law fit; the corresponding statistics are respectively ~ 0.33 and ~ 0.17. Both the spectral models are acceptable at more than 2σ significance. The smaller statistics and the larger P_{val} associated to the second model suggest a fit improvement when the cut-off is included in the model.

We compared the derived Γ with the value obtained by Grimm et al. (2003) for HMXBs, who found a Γ value of 1.61 ± 0.12. Our best parameter is smaller and a flattening in the XLF is possible for the Cartwheel, but our value is consistent with the Grimm one within the uncertainties. Grimm et al. fixed the cut-off luminosity at $x_c = 2.1\times10^{40}$ erg s^{-1}, which is a larger value than our best-fitting estimation, but the two results are compatible within the errors. Grimm et al. derived a relation between the SFR and the XLF: $dN/dL_{38} = 3.3SFR\ L^{-1.61}$ for $L<2.1\times10^{40}$ erg s^{-1}. We fit our XLF, excluding all the sources above their cut-off value of 2.1×10^{40} erg s^{-1}, using a power-law with their Γ value, of 1.61, and we compared the derived normalization with 3.3SFR to estimate the Cartwheel SFR. We obtained a SFR of $\sim 17\ M_\odot\ y^{-1}$ for the Cartwheel. This value is similar to the SFR published in the literature: 17.7 $M_\odot$ y^{-1}, derived from FIR (far infrared) data, and 18 $M_\odot$ y^{-1}, derived from L_{H_α} (Mayya et al. 2005).

Because of the change in the limiting *Chandra* flux among the observations, we expect that some sources may be lost in the bin at the lower luminosity. The flatter shape of our XLF, with respect to the Grimm et al. XLF, may be caused by the reduced sensitivity, rather than being a really different trend. If we fit the Cartwheel XLF with a cut-off power-law model, with Γ fixed at the Grimm value (1.61) and leaving the normalization and the cut-off luminosity free, we obtain a cut-off luminosity of $\sim 8.6\times10^{41}$erg s^{-1}. This fit is formally acceptable and its P_{val} (0.93) and fit statistics (0.33) are similar to those associated with the power-law fit without the cut-off. The cut-off value found is larger than the most luminous bin in the XLF and thus it does not influence the fit. To assess the impact of loosing some sources at low luminosity, we found that a good fit with Γ fixed at 1.6 is obtained with six more sources in the first bin, which gives a cut off luminosity of $\sim 4\times10^{40}$ erg s^{-1}. This value is larger if compared to the Grimm analysis and it is easy to explain, considering the higher luminosities of the sources in our sample with respect to the sources analysed by Grimm et al. and this cut-off luminosity is consistent with the one found by Wolter et al. (2018) for a sample of ring galaxies.

4.3.6 Cartwheel galaxy diffuse component and companion galaxies

We have presented a study of the variability of the ULXs in the Cartwheel galaxy and in its companions and we investigated if the flux variability has influenced the XLF shape. We complete the analysis of the *Chandra* data used in this work by considering also the non-variable emission components, both in the Cartwheel and in its companion galaxies.

Cartwheel diffuse emission: In the Cartwheel galaxy, also diffuse emission is present. The analysis of the diffuse emission in *XMM-Newton* data was presented in Crivellari et al. (2009), while Wolter and Trinchieri (2004) considered the diffuse emission in the first *Chandra* epoch. From each *Chandra* image we extracted a spectrum from an elliptical region, whose center was at coordinates RA = 0:37:40.4, Dec = -33:42:59.3; the ellipse major radius was 44.4" and its minor radius was 33.5", which allowed us to include the region inside the galaxy and the ring, but we excluded the detected point-like sources. From previous analysis (Wolter and Trinchieri 2004, Crivellari et al. 2009) we know that the diffuse emission can be attributed to two different components: the emission of unresolved point-like sources and that of a diffuse gas. We grouped the data in bins with at least 2σ significance. As highlighted also in previous analysis (Wolter and Trinchieri 2004), an acceptable fit is given by a power-law, but the addition of another spectral component improves the residuals. Therefore, we used a plasma model (APEC) plus a power-law (POWER-LAW), multiplied by an absorption model (TBABS), to fit the data. We fixed the plasma model abundances at 0.5 times the solar value, because of the low metallicity in the Cartwheel. We modelled the diffuse gas with

Source	Obs	$n_{\rm H}$ 10^{21} (cm^{-2})	Γ	kT (keV)	χ^2/dof	$L_{\rm gas}$ 10^{40} erg s^{-1}	$L_{\rm pow}$
C.		$0.12^{+0.18}_{-0.11}$	$2.3^{+1.3}_{-0.8}$	$0.25^{+0.11}_{-0.06}$	42.18/57	1.3±2.6	3.3±1.9
G1		$2.6^{+4.0}_{-1.3}$	$2.3^{+0.6}_{-0.4}$	$0.2^{+0.4}_{-0.1}$	43.70/43	1.8±0.6	
	1						6.4±0.8
	2						6.6±1.0
	3						5.1±1.1
G2		1.0	$1.4^{+1.3}_{-1.4}$	–	14.24/14	–	0.7±0.4
G3		1.0	$3.3^{+1.2}_{-1.1}$	–	21/30	–	0.7±0.2

Table 4.7: Spectral parameters for the point-like plus diffuse emission (G1 and G3) and for the diffuse emission (Cartwheel galaxy and G2). More details are given on the text. We used a TBABS*(APEC+POW) model in XSPEC. The luminosities are expressed in units of 10^{40} erg s^{-1}. The gas luminosities, i.e. the luminosities from the APEC component, are given in the (0.5-2) keV band; the power-law luminosities are given in (0.5-10) keV. For G1, having considered together both the (constant) diffuse emission and the (variable) point-like emission, we indicate the luminosities in observations 1, 2, 3, respectively the *Chandra* observations 2019, 9531, 9807. For the Cartwheel galaxy, G2 (because we analysed the diffuse component alone) and G3 (because the only point-like source is not significantly variable) we report an average value.

the plasma component and the unresolved point-like sources with the power-law. First, we fit the *Chandra* data, linking the $n_{\rm H}$ among the three epochs, but leaving all the other parameters free. Some differences are found in the best-fitting parameters, suggesting possible spectral variability, but the parameters are consistent within the uncertainties among the observations. Therefore, we linked also the other parameters among the observations to better constrain them. We added to our model a multiplicative constant, which takes into account any differences in flux among the exposures. We report the best fitting parameters in table 4.7. The gas component contributes to the flux just below 2 keV. The power-law instead contributes also above 2 keV. We found a power-law index and a gas temperature similar to those reported by Wolter and Trinchieri (2004), while our best $n_{\rm H}$ value is smaller, causing the flux obtained from the first *Chandra* observation to be lower than the flux derived in the previous analysis, especially for the gas component. The fitting-parameters uncertainties are large and allow also the flux values obtained in the previous analysis. The unabsorbed fluxes are consistent among the epochs within the errors. Their average values are: $F_{pow}^{(0.5-2)keV}$ = 9.8×10^{-15} erg s^{-1} cm^{-2}; $F_{pow}^{(2-10)keV}$ = 7.4×10^{-15} erg s^{-1} cm^{-2}; $F_{gas}^{(0.5-2)keV}$ = 6.9×10^{-15} erg s^{-1} cm^{-2}.

As pointed out by Wolter and Trinchieri (2004) and confirmed also by our spectral analysis including the three *Chandra* epochs, the diffuse emission should include at least two components, compatible with an unresolved X-ray binary population and a diffuse hot gas. Considering the large number of ULXs detected on the ring, it is natural to expect also less luminous binaries generated during the same star formation episode and too faint to be resolved by the current X-ray instrumentation at the Cartwheel distance. Comparing the Cartwheel observations with the results of the simulations of Renaud et al. (2018), the Cartwheel galaxy should be in a phase with the star formation (SF) mainly present in the outer ring. The simulations predicted that the shock-wave, generated by the impact with the intruder galaxy, activated first the SF in the outer ring. Then the gas is expected to flow from the outer ring towards the internal regions through the spokes. As a result, there is an evolution in time of the SF, which moves from the outer to the inner regions of the ring galaxy. This would correspond to a time smaller than 100 < Myr from the impact according to the simulations (Renaud et al. 2018). Other considerations, based on dynamics, suggest an age > 200 Myr (Higdon 1996, Amram et al. 1998). This could imply a longer timescale associated to the real case with respect to the simulations. Should the Cartwheel really be in such a phase, i.e. enhanced SF in the outer ring and not yet started in the inner regions, we would expect both the two diffuse emission components, i.e. unresolved binaries and gas, in the outer ring and just a gas contribution to the diffuse emission of the inner regions. The *Chandra* data have not enough statistics to study the diffuse emission of the inner galaxy regions individually from that of the outer ring, even summing the three

epochs. Crivellari et al. (2009) studied the diffuse emission in these two different regions by using the *XMM-Newton* data, which have a higher statistics also in the region inside the galaxy, thanks to the larger effective area compared to the *Chandra* one. The gas emission detected in the inner galaxy region could not be associated with a particular area – e.g. the nucleus or the inner ring – due to the insufficient angular resolution of *XMM-Newton*. Crivellari et al. (2009) unexpectedly found a power-law component also in the inner regions of the Cartwheel and they suggested that it may be background emission coming from the wings of the PSF of the most bright ring sources. The ideal way to study separately the diffuse emission in the two cited regions would be an instrument which combines the spatial resolution of *Chandra* with the effective area of *XMM-Newton*. To do a more detailed analysis of the diffuse emission in the two distinct regions with the currently active X-ray observatories, a longer *Chandra* exposure (at least 100-200 ks) is needed to obtain enough statistics.

Companion galaxies: Considering the companion galaxies of the Cartwheel, before this work only the point sources detected in the first *Chandra* epoch (Wolter and Trinchieri 2004) and the *XMM-Newton* data (Crivellari et al. 2009) have been published. Here we complete the analysis. The total emission from the companion galaxies includes three components: two come from the emission of the point-like sources, resolved and unresolved, the third is the gas emission. We extracted the spectra from the elliptical regions listed in table 4.8. The spectra have been grouped in 20 counts per bin. The coordinates of the point sources in the companion galaxies are listed with the coordinates of the point like sources in the Cartwheel, in table 4.3.

We studied the spectra of all the three components of G1 by using an absorbed POWER-LAW plus APEC model, to take into account both the point sources, which represent the variable component, and the plasma emission, which we assumed to be stable among the observations. The fitting parameters were consistent, within the errors, among the observations. Therefore we analysed the three spectra together, to better constrain the parameters. The best-fitting parameters are reported in table 4.8, together with the luminosity derived from the flux obtained from the spectral-fitting and the assumed distance of 131 Mpc. By the comparison of the power-law luminosities derived here, which include both the resolved and unresolved point-like emission, and the luminosities of the seven ULXs resolved in G1 (see their coordinates in table 4.3 and their luminosities in table 4.6), we found their relative contribution to the power-law component luminosity. On average, 34% of the power-law emission is accounted for by the unresolved binary population, while 66% of the power-law emission comes from the resolved ULXs.

Most of the emission of G2 can be attributed to source N1, which is also highly variable, thus, we extracted the spectrum of G2 excluding the region of N1, while studying the diffuse emission. The statistics was not enough to use models with two components. We thus fit the data using a power-law model and we linked the parameters among the observations. We fixed the $n_{\rm H}$, which was unconstrained due to the low statistics, at $1{\times}10^{21}$ cm^{-2}, as derived from the fit of the average spectrum of the point-like sources in both the Cartwheel and its companions, while we leaved the power-law index free. See the resulting value and luminosity in table 4.8.

The statistics of G3 is scanty. So we used a single absorbed power-law to model the spectrum of the whole galaxy. We fixed the $n_{\rm H}$ at the value $1{\times}10^{21}$ cm^{-2}, as for G2. The spectral-fitting result is reported in table 4.8.

While for the Cartwheel galaxy and G1 we detected two diffuse components, which can be associated to hot gas emission and a power-law emission coming from the unresolved binary population, G2 and G3 diffuse spectra present just a spectral component, i.e. a power-law. We suggest that also in these galaxies both the components contributes to the diffuse emission, but cannot be individuated because of the scanty statistics.

source	*RA*	*Dec*	major axis	minor axis
G1	0:37:43.19	-33:42:06.94	14.5"	10.9"
G2	0:37:44.93	-33:42:21.25	11.72"	10.83"
G3	0:37:46.11	-33:39:50.48	26.24"	13.57"

Table 4.8: Coordinates of the companion galaxies: G1, G2, G3. The major and minor axis of the elliptical regions used to extract the spectra are listed in column 4 and 5, in arcsec units.

4.4 Summary

We have studied the X-ray emission of the Cartwheel galaxy and of its companions (G1, G2 and G3), with all the available observations taken with *Chandra* and *XMM-Newton* satellites, which observed the galaxies between 2001 and 2008. We wanted to characterize the ULXs variability in a ring galaxy. We detected in total 37 ULXs, 9 never detected before, 28 of them are in the Cartwheel galaxy, which is the largest number of ULXs ever observed in a single galaxy.

We found an absence of short-term variability in most of the sources, but we remark that the low statistics may influence this result. In contrast, we found a significant long-term variability (i.e. with a significance larger than 3σ) in 35% of the sources, a similar behaviour is observed both in the Cartwheel and G1 considered alone. Fourteen ULXs showed a transient behaviour. This suggests that the variability amplitude may be large in many sources. Indeed we found a variability factor larger than 2 in 45% of the ULXs and a F_{var} larger than 30% in 50% of the ULXs (considering both *Chandra* and *XMM-Newton* data).

We also analysed the XLF of the Cartwheel ULXs to verify if the temporal variability may influence the shape of the XLF. We found that the cumulative XLF of the Cartwheel galaxy has a consistent shape among the *Chandra* observations, despite the flux variability of the ULXs. We also compared the Cartwheel XLF with the HMXBs Universal LF (Grimm et al. 2003). We thus constructed the differential XLF, summing the sources detected in the three epochs, and we found a shape flatter than the XLF of the HMXBs, but the two XLFs are consistent within the errors and also with the result of Swartz et al. (2011), who analysed a sample of ULXs in non-ring galaxies. Wolter et al. (2018) obtained the same result for a sample of ULXs in ring galaxies. Both analysis, our and that of Wolter et al. (2018), suggest that more high luminosity objects may be present in ring galaxies than in other types of galaxies.

Future X-ray observatories, such as *Athena* (Nandra et al. 2013), may help to obtain larger statistics data, but less sources will be resolved in the Cartwheel ring because *Chandra* still holds the best angular resolution among the existing and planned X-ray satellites. We thus remark the importance of taking new *Chandra* observations, to improve the study of the ULX population in the Cartwheel and detect new transients.

Chapter 5

Conclusions

5.1 Open questions about Ultraluminous X-ray sources

Despite having been studied since the 80s, there are still many open questions about the ultraluminous X-ray sources and this renders them a particular interesting topic for the current research in astronomy. ULXs are interpreted as accreting compact objects in binary systems (e.g. Kaaret et al. 2017) and, even if there is consensus among the scientific community that many of them host stellar mass compact objects accreting at super-Eddington rates, a detailed description of these sources and of the physical mechanisms responsible for their X-ray emission is still lacking. The most outstanding question about ULXs concerns the nature of the compact object. A group of sources have shown pulsations and thus their neutron star nature has been confirmed (e.g. Bachetti et al. 2014, Israel et al. 2017a). Some authors proposed that the fraction of NSs among the ULX population may be large (e.g. Koliopanos et al. 2017, Pintore et al. 2017) and NSs may even dominate the ULX population, but at the current state of knowledge, we can describe the ULXs as an heterogeneous class of sources containing NSs and stellar mass BHs accreting at super-Eddington rate and possibly a minority of the most luminous objects may host intermediate mass BHs in a sub-Eddington state of accretion. Except for the detection of pulsations, there is not a universal method to determine the compact object mass and thus its nature. In fact, constraints on the mass of the compact object could in principle be found thanks to dynamical studies based on the orbital motion of the compact object and of the companion star. The determination of the mass is based on the construction of velocity curves through the analysis of the optical counterpart emission, which is usually impossible to derive in ULXs because the optical emission is usually dominated by reprocessing of X-rays in the super-critical accretion disc (e.g. Roberts et al. 2011, Fabrika et al. 2021). Some indirect methods may be used to identify candidate NSs, but no methods are currently known to identify a BH in a ULX system. While at first it was thought that the most luminous ULXs may host intermediate mass BHs, we now know that even the most luminous objects can contain a NS (e.g. Israel et al. 2017a): the most luminous PULX, NGC 5907 ULX-1, reaches luminosities of the order of 10^{41} erg s^{-1}.

Also the super-Eddington accretion processes have not yet been completely understood. The most problematic object is NGC 5907 ULX-1 which, with its high luminosity and its NS nature, overcomes the Eddington limit of a factor 500-1000. It should enter the propeller regime before reaching the observed peak luminosity, thus understanding how it is possible is a great challenge for the scientists. In addition, how the transfer of matter happens in such binary systems is still debated. One possibility is an hybrid mechanism between the Roche-Lobe overflow and the wind accretion, a wind Roche-Lobe overflow (El Mellah et al. 2019, Wiktorowicz et al. 2021).

Another question concerns the companion star. Considering that the ULXs are extragalactic objects, observing the companion star is often difficult (e.g. Kaaret et al. 2017). Indeed, the optical emission is consistent to be dominated by light reprocessed by the accretion flow and the contribution to the emission of the companion star is very low (e.g. Fabrika et al. 2015), thus only in few ULXs the companion star has been firmly identified (e.g. Motch et al. 2014, Liu et al. 2013).

Also the variability properties of the ULXs and their possible link to the spectral states or to spectral state transitions are not yet fully understood. About the intra-observation short-term variability, i.e. timescales from minutes to hours, the appearance of the variability seems stochastic (e.g. Heil et al. 2009), but a larger amplitude is usually found in the ULXs spectrally classified in the soft ultraluminous regime with respect to the other spectral regimes (Sutton et al. 2013). The link of the variability with the soft ultraluminous regime has been explained with the compact object seen through a clumpy wind, which stochastically intersects our line of sight producing the observed variability (e.g. Middleton et al. 2011a, 2015a). Furthermore, the short-term variability in ULXs is usually dominated by the hard energy band, which may be explained with the obscuration of the hard inner accretion flow by the clumpy wind (e.g. Sutton et al. 2013, Middleton et al. 2015a).

The inter-observations long-term variability, i.e. timescales of days to years, has not been characterized for many samples of sources and its study was the main subject of this thesis. We report our main findings in the next section.

5.2 Long-term variability in ULXs: summary of our results

With the *Swift*/XRT sample, including 10 spiral galaxies with 25 detected ULXs (including the new candidate transient ULX, NGC 4945 41ULX), we focused on the analysis of the variability of the sources on days timescales, while with the Cartwheel sample we analysed the ULXs behaviour on years timescales.

From the *Swift*/XRT sample, we found that most of the considered sources are significantly variable on timescales of days. Indeed, $\sim$ 71% of the analysed ULXs have shown a variability significance larger than 3σ. We showed that all of them have a variability amplitude $>$ 30% and in half of the sources the F_{var} is larger than 50%. The most luminous sources, which reach a peak luminosity above 10^{40} erg s^{-1} in the *XMM-Newton* data, have large F_{var} ($>$ 60%), with the exception of M101 24ULX, which is luminous but it is the less variable ULX in the *Swift*/XRT data. At smaller luminosities a broad range of F_{var} values is covered. In many ULXs, $\sim$ 53%, the variability is driven by the hard band, as already known at least for the short-term behaviour of the ULXs. In just three cases, M101 16ULX, M101 29ULX and NGC4945 6ULX, the variability is driven by the soft band, while in the remaining cases the variability is similar in the two energy bands. We speculate about the mechanism which can cause this trend on days timescales. The obscuration due to the wind blobs has been estimated to produce variability on timescales of seconds to thousands of seconds in ULXs (e.g. Takeuchi et al. 2013, Middleton et al. 2015a), thus it can no more be an explanation on these days timescales. Therefore, we suggest that the observed days timescale variability may be linked to the propagation through the disc of the fluctuations in the mass accretion rate, a mechanism which can cause variability by up to days timescales (e.g. Middleton et al. 2015a). In addition, the variation imprinted on the soft component would modify also the wind opening angle. Therefore, the wind may be completely or partially along our line of sight in some epochs while we would not see it in other observations. The switching among these different configurations of the wind may produce the additional variability that we have observed in the hard component of many ULXs in the analysed sample on days timescales. Should this hypothesis be confirmed, the long-term variability may be used to study the processes responsible for mass accretion rate variations, such as processes linked to the ejection and properties of the stellar winds of the companion stars or to the transfer mechanism between the two objects in the binary system. The X-ray variability on different timescales has been used in the galactic X-ray binaries to obtain information about the wind of the companion star (e.g. Grinberg et al. 2015, 2020), but the larger distances and the presence of winds emitted in the super-Eddington accretion, which also contribute to the variability, may complicate the situation in ULX systems. The changes in the bolometric luminosity of accretting compact objects are linked to variations in the mass accretion rate, the latter linked to the stellar wind of the companion star or to changes in the transfer of matter, e.g. if the orbit is very eccentric. The estimations of the long-term variability amplitude, derived in this work, may be used as a starting point for future studies to test the amount of the variation in mass accretion rate needed to explain the observed variability and how it can be produced.

Long-term periodicities are found in some ULXs, which usually have a period of months timescales (e.g. Walton et al. 2016, Brightman et al. 2019). We found a similar period in one of the analysed sources, NGC 925 ULX-3 (Salvaggio et al. 2022). This ULX has a flux modulation on a period of about four months, similar to the super-orbital periodicities found in other ULXs (e.g. $\sim$ 39 d in M51 ULX-7, Vasilopoulos et al. 2020, 2021, Brightman et al. 2020; $\sim$ 78 d in NGC 5907 ULX-1, Walton et al. 2016; $\sim$ 115-136 d in NGC 5408 X-1, Foster et al. 2010, An et al. 2016). The orbital period of NGC 925 ULX-3 is not known, thus we cannot exclude that the periodicity is linked to the orbital motion, but given the similarity of the timescale of the periodic variation with that of the confirmed super-orbital periodicity, a super-orbital origin is the most plausible explanation. Considering the older dataset analysed, the periodicity may not always be present in the source or it can be unstable either in phase or duration, supporting the hypothesis of a super-orbital origin, maybe linked to a disc precession (e.g. of a tilted or warped accretion disc). The mechanisms responsible for super-orbital flux modulations in ULXs are still matter of study and with the available data, we could not investigate in detail which one of the processes proposed in literature may explain the flux periodicity in NGC 925 ULX-3.

The *Swift*/XRT light curve of NGC 925 ULX-3 may also be consistent with a propeller phase, which suggests that this ULX may be a PULX. Indeed, between MJD 56165 and MJD 57770 ($\sim$ 4 years) *Swift*/XRT observed the sources only twice, without detections, before the detection with *XMM-Newton* on MJD 57771. In this period, the ULX may have been in a propeller phase, but the flux corresponding to the two upper limits is also consistent with the periodic flux modulation of the source. Another source in the sample, M101 29ULX, can be considered as a candidate PULX. It has been detected only twice during the *Swift*/XRT monitoring and by stacking the upper limits between the detections, we found a flux variation of about an order of magnitude, which may be linked to propeller phases. In addition, we classify the *XMM-Newton* spectrum of this source in the hard ultraluminous regime and the power-law index is low, similar to the values usually found in the PULXs spectra. Both in the *Swift*/XRT and in the *XMM-Newton* images, M101 29ULX is not resolved from other X-ray sources, which may have influenced both our temporal and spectral results. Urquhart et al. (2022), from the analysis of *Chandra* data, also suggest a NS nature for M101 29ULX, but it has to be confirmed. Circinus 4ULX, NGC 4945 4ULX, NGC 925 ULX-3, NGC 5055 1ULX and also two ULXs in the Cartwheel galaxy (P25 and P26) have reached $\sim$ one order of magnitude in their variability factor. Considering the known PULX, they are usually particularly variable among the ULX population, with variability factors larger than one order of magnitude. Thus, based just on their highly variability, these ULXs may be considered a sample where to look for new PULXs. In addition, the PULXs are usually hard sources, which is also observed in Circinus 4ULX (from the hardness ratio) and in NGC 925 ULX-3 (from its average *Swift*/XRT spectrum).

In the analysed sample, we found a possible flaring activity in one source, NGC 5236 58ULX, but a denser monitoring is needed to track the flux rise and decay phases and to constrain the typical duration of a flare.

During the monitoring campaign, also a new transient source with a luminosity in the ultraluminous range switched on in NGC 4945.

From the archival *XMM-Newton* spectra of our *Swift*/XRT sample, we found that the analysed sources are usually well modelled with two thermal components in the 0.3-10 keV band, as expected for stellar mass super-Eddington accretors. In addition, most of the analysed sources for which a spectral classification was possible (13/18, corresponding to $\sim$ 72%), including also a ULS, are classified in a ultraluminous regime of accretion at least in some epochs, confirming that they host stellar mass accretors. For M101 16ULX we found residuals in two observations, with a similar shape to that observed in the ULX showing emission and absorption lines, which suggests the presence of a strong outflow linked to a super-Eddington accretion state. Four sources have a broadened disc shape; three of them have also low luminosities suggesting that they are accreting around their Eddington limit or above it, if the accretor is a NS or a light BH ($M_{BH} < 10\ M_{\odot}$). NGC 4517 1ULX, the fourth ULXs showing a disc shape, has instead a large luminosity in the *XMM-Newton* observation available, $\sim 10^{40}$ erg s^{-1}, thus if it is accreting at about its Eddington limit it should contain a massive stellar mass BH. We notice however that its spectrum is also consistent with a soft

ultraluminous regime, thus it can alternatively contain a light stellar mass BH or even a NS accreting at a high super-Eddington rate. The spectra of Circinus 6ULX, which is not a confirmed ULX and it is usually observed around or below 10^{39} erg s^{-1}, can be fit with just a multicolour blackbody disc with inner temperature kT$_{in}$ $\sim$ 0.7 keV, in most of the observations, which suggests that this source may be in a sub-Eddington accretion state in the considered epochs. The radii of the emitting regions, derived from the spectral fitting normalizations, are all compatible with a stellar mass BH or a NS accretor, suggesting that no IMBH candidates are present in the analysed sample. This confirms the expectation that most of the ULX population is composed of stellar mass compact objects accreting at or above their Eddington limit. From the spectral analysis, we found that some ULXs are variable in their spectral shape and we have found spectral state transitions in four objects. We derived the timescale linked to the spectral state transitions, which is of the order of months and the smaller value found is $\sim$ 5.5 months. Similar timescales are linked to the super-orbital periodicities observed in ULXs, thus it is possible that the state transitions are linked to different phases in the super-orbital period. On the other hand, no periodicities have been found in the ULXs showing the spectral state transitions. Further monitoring is needed to investigate if the state transitions are linked to a (quasi-)periodic process or not.

From the analysis of the Cartwheel sample, we found that many sources, $\sim$ 30%, vary significantly on years timescales. Considering that many sources in the sample have a very low statistics, this percentage has to be considered as a lower limit on the number of ULXs significantly variable. Indeed, fourteen sources showed a transient behaviour (we excluded the sources that have never shown a luminosity larger than $3{\times}10^{39}$ erg s^{-1} and thus may result in an upper limit even with a small change in flux), which suggests that the variability may be large in many sources, which is also confirmed by the large variability factors and fractional variability values found. In some cases, the transient behaviour may be caused by a propeller stage, only possible for a strongly magnetized NS, but the small number of the observations and the low statistics of many sources did not allow us to further investigate this hypothesis. On the other hand, the Cartwheel galaxy contains source N10, which can reach a luminosity of $\sim 10^{41}$ erg s^{-1}. In previous studies of its spectrum (Pizzolato et al. 2010), N10 has been found to be consistent with a massive sMBH accreting at super-Eddington rates, but also an interpretation as a supernova remnant cannot be excluded with the available data. We found no short-term variability in most of the Cartwheel sources.

The Cartwheel XLF is consistent among the three *Chandra* epochs with the same shape within the uncertainties, despite the temporal variability of the ULXs. This result is analogous to the one found for the X-ray point sources in the Antennae (Zezas et al. 2006). The XLF of the Cartwheel is also consistent in shape with the HMXB Universal LF (Grimm et al. 2003) and also with the XLF constructed by Swartz et al. (2011) for a sample of ULXs in non-ring galaxies. The only difference which emerged from our analysis is the possibility that ring galaxies contain a larger number of high luminosity objects. The same trend was previously found by Wolter et al. (2018), for a sample of ring galaxies.

5.3 Final remarks and future perspectives

Temporal variability on different timescales and spectral variability are common features among the ULX population. In this thesis we have confirmed that long-term variability, from days to years timescales, is much diffuse both among the ULXs in spiral galaxies and in ring galaxies. Variability on days timescales is dominated by the hard band in at least half of the sources. We suggest that long-term flux variability may be explained with variations in the mass accretion rate, which produce variability in both the soft and the hard spectral components. The additional variability often found in the hard spectral component may be explained with the wind (soft component) along or out of our line of sight in different epochs, which sometimes obscures the inner accretion flow (hard component), in a super-Eddington accretion scenario. Given the recent findings of Gúrpide et al. (2021a, 2021b) we cannot exclude a link with state transitions among the SUL e SSUL regimes, which would be naturally explained by a different contribution of the wind along our line of sight among the observations.

To improve our knowledge about the long-term properties of the ULXs, more high quality data are needed. Both long exposures, necessary for a detailed spectral modelling (with about 10000 counts we could do a high quality spectral analysis, a detailed timing analysis and a search for pulsations), contemporaneous to long-term monitorings, to derive the long-term variability behaviours, are needed to deepen the long-term study of ULXs. Given the observed timescales of the spectral state transitions and of the super-orbital periodicities, high quality exposures (e.g. with *XMM-Newton*), with a cadence of 1-2 months, simultaneous with a *Swift*/XRT monitoring with a week cadence, may help to test possible correlations among the spectral behaviour and the flux variability, either periodic or aperiodic. Also observations with future X-ray facilities will be a great resource in this direction. With contemporaneous observations it would be possible to improve the results obtained in this work: the study of the variability timescales derived by the long-term light curves together with a simultaneous deep spectral analysis of the sources will allow us to better investigate the origin of the aperiodic long-term variability in ULXs and to confirm whether the fact that it is often driven by the hard spectral component is just due to an obscuring effect, or if the hard component is also intrinsically more variable. In addition, the same data may be used to deepen the study of the super-orbital periodicities in ULXs and to investigate if the fact that they are not always found in the analysed sources, in this thesis we detect a periodicity in just one ULX, is a consequence of no sufficient data quality, e.g. not enough points in the light curves or too sparse sampling, or if super-orbital periodicities are not ubiquitous in ULXs. A possibility is that the super-orbital modulation may have a shorter periodicity in some sources, e.g. few days, instead of the months periodicities usually detected. Therefore, denser monitorings than those obtained with a cadence of 1-2 weeks, usually requested to detect such flux modulations, would be needed. Should different timescales turn out to exist in the super-orbital periodicities in ULXs, they may indicate a different physical origin, maybe linked to the compact object nature or to a different precession mechanism.

From the analysed *Swift*/XRT sample, NGC 925 ULX-3 resulted a particular interesting object. Future studies will help to better characterize the periodicity detected and to investigate the nature of this source in more detail. Other interesting sources, that can be considered for future studies, are the more variable ULXs which may be candidate NSs, i.e. NGC 925 ULX-3, M101 29ULX, NGC 4945 4ULX, Circinus 4ULX and NGC 5055 1ULX. Also NGC 5236 58ULX is worthy of further study, given its flaring behaviour, only rarely observed in ULXs. In this case a dense *Swift*/XRT monitoring with an observation every two days, would be the ideal to track the flaring episodes. At last, future work on the ULXs which have shown state transitions, i.e. Circinus 4ULX, NGC 5236 58ULX, M101 27ULX, NGC 5236 82ULX, would be useful to better characterize the spectral evolution of the ULXs.

The emblematic question I have proposed in the title of this manuscript – Black Hole or Neutron Star? – still remain an open question. Many aspects of the ULXs need further study to reach a complete description of the physical processes in act in these sources and finally characterize the nature of the ULX population, only known for a few sources. Therefore the analysis of samples of sources, like the one proposed here, is fundamental to get closer to the desired answers.

Appendix A

We report the observations of the *Swift*/XRT monitoring and the archival *XMM-Newton* data analysed in this work in the following tables.

	Instr.	Obs.ID	Start time	Stop time	Exposure
			[YYYY-MM-DD hh:mm:ss]		[ks]
1	*Swift*/XRT	00035876002	2019-01-12T02:36:24	2019-01-12T02:53:53	1.0
2	*Swift*/XRT	00032699002	2019-01-18T03:38:01	2019-01-18T14:55:52	2.9
3	*Swift*/XRT	00035876003	2019-01-26T01:19:48	2019-01-26T01:37:41	1.1
4	*Swift*/XRT	00032699003	2019-01-28T00:53:41	2019-01-28T13:56:01	1.7
5	*Swift*/XRT	00032699004	2019-01-31T02:16:04	2019-01-31T02:37:53	1.3
6	*Swift*/XRT	00032699005	2019-02-09T12:40:28	2019-02-09T23:54:52	2.8
7	*Swift*/XRT	00035876004	2019-02-09T15:43:14	2019-02-09T16:00:52	1.1
8	*Swift*/XRT	00032699006	2019-02-17T19:28:11	2019-02-17T21:25:53	2.5
9	*Swift*/XRT	00032699007	2019-03-02T02:57:15	2019-03-02T23:49:53	2.8
10	*Swift*/XRT	00035876006	2019-03-09T18:10:35	2019-03-09T18:28:54	1.1
11	*Swift*/XRT	00035876007	2019-03-23T18:03:00	2019-03-23T18:19:53	1.0
12	*Swift*/XRT	00032699008	2019-04-03T15:23:36	2019-04-06T03:55:52	3.5
13	*Swift*/XRT	00035876008	2019-04-06T13:31:49	2019-04-06T13:49:52	1.1
14	*Swift*/XRT	00032699009	2019-04-14T01:31:02	2019-04-14T08:02:53	3.1
15	*Swift*/XRT	00035876009	2019-04-23T20:17:49	2019-04-23T20:33:52	1.0
16	*Swift*/XRT	00035876010	2019-05-04T17:40:39	2019-05-04T17:41:54	0.1
17	*Swift*/XRT	00032699011	2019-05-05T20:51:17	2019-05-06T01:51:51	2.6
18	*Swift*/XRT	00035876011	2019-05-08T12:12:16	2019-05-08T12:26:53	0.9
19	*Swift*/XRT	00032699012	2019-05-15T00:47:57	2019-05-15T13:11:53	2.7
20	*Swift*/XRT	00035876012	2019-05-18T06:20:02	2019-05-18T06:36:53	1.0
21	*Swift*/XRT	00032699013	2019-05-25T02:26:08	2019-05-25T13:46:53	3.0
22	*Swift*/XRT	00032699014	2019-06-04T03:19:28	2019-06-04T19:18:52	1.5
23	*Swift*/XRT	00035876014	2019-06-05T03:03:52	2019-06-05T04:45:53	1.0
24	*Swift*/XRT	00032699015	2019-06-14T13:52:06	2019-06-14T20:27:53	1.2
25	*Swift*/XRT	00035876015	2019-06-15T20:00:18	2019-06-15T20:15:53	0.9
26	*Swift*/XRT	00032699016	2019-06-24T14:33:46	2019-06-24T21:01:54	2.8
27	*Swift*/XRT	00035876016	2019-06-29T07:23:59	2019-06-29T07:34:53	0.6
28	*Swift*/XRT	00035876017	2019-07-13T09:26:51	2019-07-13T10:43:54	0.8
29	*Swift*/XRT	00035876018	2019-07-24T04:45:34	2019-07-24T05:00:52	0.9
30	*Swift*/XRT	00035876019	2019-08-10T09:59:46	2019-08-10T10:15:54	1.0
31	*Swift*/XRT	00032699017	2019-08-11T03:19:38	2019-08-11T13:14:52	1.7
32	*Swift*/XRT	00032699018	2019-08-16T01:10:45	2019-08-16T22:00:53	1.6
33	*Swift*/XRT	00032699019	2019-08-21T10:18:58	2019-08-21T10:33:53	0.9
34	*Swift*/XRT	00035876020	2019-08-24T02:10:20	2019-08-24T02:24:52	0.9
35	*Swift*/XRT	00032699020	2019-08-26T03:20:19	2019-08-26T03:48:52	1.7

36	*Swift*/XRT	00032699021	2019-08-31T02:59:11	2019-09-01T04:34:52	2.0
37	*Swift*/XRT	00032699022	2019-09-05T06:56:27	2019-09-05T20:13:52	1.7
38	*Swift*/XRT	00035876021	2019-09-07T00:40:56	2019-09-07T00:55:53	0.9
39	*Swift*/XRT	00032699024	2019-09-13T02:58:06	2019-09-13T06:16:52	1.8
40	*Swift*/XRT	00035876022	2019-09-24T13:37:18	2019-09-24T13:52:53	0.9
41	*Swift*/XRT	00032699025	2019-09-25T08:43:53	2019-09-25T21:36:54	1.7
42	*Swift*/XRT	00032699026	2019-09-30T14:33:09	2019-09-30T15:00:54	1.7
43	*Swift*/XRT	00035876023	2019-10-05T07:53:50	2019-10-05T08:06:27	0.8
44	*Swift*/XRT	00032699027	2019-10-05T10:50:54	2019-10-05T11:13:06	1.3
45	*Swift*/XRT	00032699028	2019-10-10T00:38:09	2019-10-10T21:42:53	2.2
46	*Swift*/XRT	00032699029	2019-10-15T08:12:37	2019-10-15T10:02:52	1.8
47	*Swift*/XRT	00035876024	2019-10-19T03:09:43	2019-10-19T03:25:53	1.0
48	*Swift*/XRT	00032699030	2019-10-20T23:27:07	2019-10-20T23:52:54	1.5
49	*Swift*/XRT	00032699031	2019-10-25T00:37:41	2019-10-25T09:03:52	2.0
50	*Swift*/XRT	00032699032	2019-10-30T01:49:29	2019-10-30T03:40:53	1.9
51	*Swift*/XRT	00035876025	2019-11-02T14:10:16	2019-11-02T14:20:53	0.6
52	*Swift*/XRT	00032699033	2019-11-04T02:48:53	2019-11-04T12:30:52	1.5
53	*Swift*/XRT	00035876026	2019-11-16T22:57:41	2019-11-16T23:12:51	0.9
54	*Swift*/XRT	00035876027	2019-11-30T00:30:37	2019-11-30T00:43:54	0.8
55	*Swift*/XRT	00035876028	2019-12-06T18:55:48	2019-12-06T19:10:53	0.9
56	*Swift*/XRT	00035876029	2019-12-13T18:11:08	2019-12-13T18:28:52	1.1
57	*Swift*/XRT	00035876030	2019-12-20T00:03:15	2019-12-20T00:16:54	0.8
58	*Swift*/XRT	00035876031	2019-12-27T13:48:47	2019-12-27T15:29:52	1.0
59	*Swift*/XRT	00035876032	2020-01-10T04:43:15	2020-01-10T04:59:53	1.0
60	*Swift*/XRT	00035876035	2020-01-24T19:00:14	2020-01-24T19:14:54	0.9
61	*Swift*/XRT	00035876036	2020-01-31T21:25:24	2020-01-31T21:36:53	0.7
62	*Swift*/XRT	00035876035	2020-01-24T19:00:14	2020-01-24T19:14:54	0.9
63	*Swift*/XRT	00035876037	2020-02-07T17:29:27	2020-02-07T17:43:52	0.9
64	*Swift*/XRT	00035876038	2020-02-14T11:59:37	2020-02-14T12:11:52	0.7
65	*Swift*/XRT	00035876039	2020-02-28T15:53:16	2020-02-28T16:07:54	0.9
66	*Swift*/XRT	00035876040	2020-03-06T16:45:56	2020-03-06T16:53:53	0.5
67	*Swift*/XRT	00035876041	2020-03-13T09:31:08	2020-03-13T09:46:53	0.9
68	*Swift*/XRT	00035876042	2020-03-20T10:18:04	2020-03-20T10:32:52	0.9
69	*Swift*/XRT	00035876043	2020-03-27T17:52:52	2020-03-27T18:05:54	0.8
70	*Swift*/XRT	00035876044	2020-04-03T05:52:55	2020-04-03T06:08:53	1.0
71	*Swift*/XRT	00035876045	2020-04-17T22:17:38	2020-04-17T22:34:53	1.0
72	*Swift*/XRT	00035876046	2020-04-24T23:15:42	2020-04-24T23:31:52	1.0
73	*Swift*/XRT	00035876047	2020-05-01T20:39:09	2020-05-01T20:53:54	0.9
74	*Swift*/XRT	00035876048	2020-05-08T20:06:08	2020-05-08T20:21:54	0.9
75	*Swift*/XRT	00035876049	2020-05-15T13:05:30	2020-05-15T13:19:52	0.9
76	*Swift*/XRT	00035876050	2020-05-22T04:20:12	2020-05-22T04:30:51	0.6
77	*Swift*/XRT	00035876051	2020-05-29T00:18:10	2020-05-29T00:30:52	0.8
78	*Swift*/XRT	00035876052	2020-06-12T15:21:23	2020-06-12T15:36:53	0.9
79	*Swift*/XRT	00035876053	2020-06-19T16:04:53	2020-06-19T16:19:54	0.9
80	*Swift*/XRT	00035876054	2020-06-26T08:48:53	2020-06-26T09:04:53	1.0
81	*Swift*/XRT	00035876055	2020-07-03T03:30:48	2020-07-03T03:45:53	0.9
82	*Swift*/XRT	00035876056	2020-07-10T08:59:58	2020-07-10T09:13:53	0.8
83	*Swift*/XRT	00035876057	2020-07-17T01:52:44	2020-07-17T02:07:54	0.9
84	*Swift*/XRT	00095729001	2020-07-17T16:16:43	2020-07-17T19:37:53	1.4
85	*Swift*/XRT	00035876058	2020-07-28T15:31:29	2020-07-28T17:14:53	1.0
86	*Swift*/XRT	00095729002	2020-07-31T08:47:49	2020-07-31T13:33:53	1.0
87	*Swift*/XRT	00035876059	2020-07-31T18:29:08	2020-07-31T18:43:53	0.9
88	*Swift*/XRT	00035876060	2020-08-07T15:52:34	2020-08-07T16:08:52	1.0

89	*Swift*/XRT	00035876061	2020-08-14T00:50:30	2020-08-14T01:05:53	0.9
90	*Swift*/XRT	00095729003	2020-08-14T07:29:02	2020-08-14T17:14:53	1.5
91	*Swift*/XRT	00035876062	2020-08-21T03:27:44	2020-08-21T03:43:52	0.7
92	*Swift*/XRT	00035876063	2020-08-28T01:05:12	2020-08-28T01:20:52	0.9
93	*Swift*/XRT	00095729004	2020-08-28T02:32:36	2020-08-28T02:55:52	1.4
94	*Swift*/XRT	00035876064	2020-09-04T19:08:10	2020-09-04T19:22:52	0.9
95	*Swift*/XRT	00095729005	2020-09-07T00:03:00	2020-09-07T03:15:53	1.5
96	*Swift*/XRT	00035876065	2020-09-18T15:08:44	2020-09-18T15:22:52	0.8
97	*Swift*/XRT	00035876066	2020-09-25T03:05:52	2020-09-25T03:23:53	1.1
98	*Swift*/XRT	00095729006	2020-09-25T04:47:43	2020-09-25T05:11:52	1.3
99	*Swift*/XRT	00035876067	2020-10-02T05:47:53	2020-10-02T06:01:53	0.8
100	*Swift*/XRT	00035876068	2020-10-09T04:59:56	2020-10-09T05:15:53	1.0
101	*Swift*/XRT	00095729007	2020-10-09T08:03:36	2020-10-09T08:26:53	1.4
102	*Swift*/XRT	00035876069	2020-10-16T02:17:48	2020-10-16T02:30:52	0.8
103	*Swift*/XRT	00035876070	2020-10-23T03:08:49	2020-10-23T03:19:54	0.7
104	*Swift*/XRT	00095729008	2020-10-23T15:49:39	2020-10-23T16:12:53	1.4
105	*Swift*/XRT	00035876071	2020-10-30T00:49:56	2020-10-30T01:01:53	0.7
106	*Swift*/XRT	00035876072	2020-11-13T19:04:40	2020-11-13T20:49:53	0.9
107	*Swift*/XRT	00095729009	2020-11-20T02:09:54	2020-11-20T02:34:54	1.5
108	*Swift*/XRT	00035876073	2020-11-20T23:03:05	2020-11-20T23:09:22	0.4
109	*Swift*/XRT	00035876074	2020-11-26T20:34:22	2020-11-26T20:46:52	0.8
110	*Swift*/XRT	00035876075	2020-11-27T22:03:08	2020-11-27T22:17:53	0.9
111	*Swift*/XRT	00095729010	2020-12-04T02:09:13	2020-12-04T02:31:55	1.4
112	*Swift*/XRT	00035876077	2020-12-11T17:17:40	2020-12-11T17:31:53	0.9
113	*Swift*/XRT	00035876078	2020-12-18T16:33:36	2020-12-18T16:48:51	0.9
114	*Swift*/XRT	00095729011	2020-12-18T18:08:44	2020-12-18T18:31:54	1.4
115	*Swift*/XRT	00095729012	2021-01-01T15:37:25	2021-01-01T17:27:52	1.6
116	*Swift*/XRT	00095729013	2021-01-15T22:03:57	2021-01-15T22:16:52	0.8
117	*Swift*/XRT	00095729014	2021-01-21T00:38:39	2021-01-21T00:53:52	0.9
118	*Swift*/XRT	00095729015	2021-01-29T13:55:54	2021-01-29T14:17:53	1.3
119	*XMM-Newton*	0111240101	2001-08-06T08:54:51	2001-08-07T15:25:38	109.9
120	*XMM-Newton*	0656580601	2014-03-01T09:55:41	2014-03-01T22:40:41	45.9
121	*XMM-Newton*	0701981001	2013-02-03T07:24:11	2013-02-03T23:46:05	58.9
122	*XMM-Newton*	0824450301	2018-09-16T13:30:41	2018-09-18T03:19:58	136.2
123	*XMM-Newton*	0780950201	2018-02-07T11:55:14	2018-02-08T00:36:54	45.7
124	*XMM-Newton*	0792382701	2016-08-23T16:53:33	2016-08-24T03:10:13	37.0

Table A.1: Log of the observations of Circinus galaxy.

	Instr.	Obs.ID	Start time	Stop time	Exposure
			[YYYY-MM-DD hh:mm:ss]		[ks]
1	*Swift*/XRT	00035892002	2019-01-20T17:29:14	2019-01-20T19:13:53	2.1
2	*Swift*/XRT	00035892003	2019-02-03T00:27:44	2019-02-03T02:08:52	1.2
3	*Swift*/XRT	00035892004	2019-02-17T03:54:56	2019-02-18T21:37:52	2.1
4	*Swift*/XRT	00035892005	2019-03-03T01:03:30	2019-03-03T02:43:52	2.0
5	*Swift*/XRT	00035892006	2019-03-17T07:19:26	2019-03-17T09:08:53	2.1
6	*Swift*/XRT	00035892007	2019-03-31T00:06:53	2019-03-31T01:50:54	1.8
7	*Swift*/XRT	00035892008	2019-04-14T15:58:20	2019-04-14T17:52:53	2.2
8	*Swift*/XRT	00035892009	2019-04-28T13:20:16	2019-04-28T13:24:52	0.3
9	*Swift*/XRT	00035892010	2019-05-12T13:31:40	2019-05-12T15:08:54	0.9
10	*Swift*/XRT	00035892011	2019-05-26T18:30:23	2019-05-26T20:25:53	2.1
11	*Swift*/XRT	00035892012	2019-06-09T06:04:01	2019-06-09T12:15:23	1.5
12	*Swift*/XRT	00035892013	2019-06-23T06:10:11	2019-06-23T07:51:52	2.0
13	*Swift*/XRT	00035892014	2019-07-07T08:29:03	2019-07-07T14:57:53	1.7
14	*Swift*/XRT	00035892015	2019-07-21T13:19:12	2019-07-21T14:55:53	1.0
15	*Swift*/XRT	00035892016	2019-07-24T00:07:10	2019-07-24T06:38:53	0.8
16	*Swift*/XRT	00035892017	2019-08-04T13:32:52	2019-08-04T15:03:52	1.5
17	*Swift*/XRT	00035892018	2019-08-18T04:11:06	2019-08-18T05:58:52	1.1
18	*Swift*/XRT	00035892019	2019-08-20T23:03:22	2019-08-20T23:16:52	0.8
19	*Swift*/XRT	00035892020	2019-09-01T14:07:51	2019-09-01T23:59:53	1.8
20	*Swift*/XRT	00035892021	2019-09-15T12:35:32	2019-09-15T16:17:53	2.1
21	*Swift*/XRT	00035892022	2019-09-29T01:41:12	2019-09-30T06:31:52	1.9
22	*Swift*/XRT	00035892023	2019-10-13T01:48:14	2019-10-13T03:39:53	1.9
23	*Swift*/XRT	00035892024	2019-10-27T02:18:02	2019-10-27T05:42:53	2.1
24	*Swift*/XRT	00035892025	2019-11-10T02:18:47	2019-11-10T04:10:52	2.1
25	*Swift*/XRT	00035892027	2019-12-08T17:20:07	2019-12-08T20:45:41	1.6
26	*XMM-Newton*	0104260101	2002-06-04T02:06:57	2002-06-04T14:09:47	43.4
27	*XMM-Newton*	0164560701	2004-07-23T08:51:10	2004-07-23T20:28:23	41.8
28	*XMM-Newton*	0212480201	2005-01-08T13:42:32	2005-01-08T22:42:45	32.4
29	*XMM-Newton*	0824450501	2018-12-07T06:40:59	2018-12-08T11:25:59	103.5

Table A.2: Log of the observations of M101.

	Instr.	Obs.ID	Start time	Stop time	Exposure
			[YYYY-MM-DD hh:mm:ss]		[ks]
1	*Swift*/XRT	00084359001	2014-07-09T03:54:59	2014-07-09T05:04:10	1.4
2	*Swift*/XRT	00080813001	2015-01-26T14:14:59	2015-01-26T19:56:06	5.1
3	*Swift*/XRT	00080813002	2015-01-29T01:20:58	2015-01-29T05:43:45	1.8
4	*Swift*/XRT	00084359002	2016-07-09T20:25:58	2016-07-09T21:30:29	0.9
5	*Swift*/XRT	00084359003	2016-07-11T06:00:58	2016-07-11T06:57:39	0.2
6	*Swift*/XRT	00084359004	2016-10-11T11:42:57	2016-10-11T12:42:32	0.4
7	*Swift*/XRT	00084359005	2018-05-01T01:46:57	2018-05-01T02:49:04	0.7
8	*Swift*/XRT	00084359006	2018-05-02T17:33:57	2018-05-02T18:35:15	0.7
9	*Swift*/XRT	00084359007	2018-07-09T08:04:57	2018-07-09T09:04:59	0.5
10	*Swift*/XRT	00084359008	2018-10-16T16:34:57	2018-10-16T17:43:45	1.3
11	*Swift*/XRT	00084359009	2018-11-05T22:54:57	2018-11-06T00:01:29	1.0
12	*Swift*/XRT	00084359010	2018-11-07T17:47:57	2018-11-07T19:00:45	1.7
13	*Swift*/XRT	00010979001	2019-01-20T23:57:12	2019-01-21T02:54:52	1.8
14	*Swift*/XRT	00010979002	2019-02-04T09:29:22	2019-02-04T14:41:52	2.0
15	*Swift*/XRT	00010979003	2019-02-21T20:47:45	2019-02-21T22:41:53	1.1
16	*Swift*/XRT	00010979004	2019-03-04T10:01:49	2019-03-04T11:47:52	2.2
17	*Swift*/XRT	00010979005	2019-03-17T13:33:35	2019-03-17T15:15:54	2.0
18	*Swift*/XRT	00010979006	2019-04-01T12:14:09	2019-04-01T16:01:54	1.6
19	*Swift*/XRT	00010979007	2019-04-17T20:25:28	2019-04-17T23:41:52	1.9
20	*Swift*/XRT	00010979008	2019-04-29T09:37:02	2019-04-29T11:17:52	2.1
21	*Swift*/XRT	00010979009	2019-05-14T11:17:48	2019-05-14T14:34:52	2.1
22	*Swift*/XRT	00010979010	2019-05-27T18:23:10	2019-05-28T17:01:53	2.0
23	*Swift*/XRT	00010979011	2019-06-10T15:14:06	2019-06-10T17:06:53	1.9
24	*Swift*/XRT	00010979012	2019-06-24T21:52:40	2019-06-24T23:35:52	2.0
25	*Swift*/XRT	00010979013	2019-07-08T03:03:13	2019-07-08T03:29:53	1.6
26	*Swift*/XRT	00010979014	2019-10-12T14:30:50	2019-10-12T19:38:52	2.1
27	*Swift*/XRT	00010979015	2019-10-25T19:50:50	2019-10-25T23:17:53	2.0
28	*Swift*/XRT	00010979017	2019-11-13T05:05:35	2019-11-13T06:56:53	2.0
29	*Swift*/XRT	00010979018	2019-11-22T04:08:11	2019-11-22T04:34:53	1.6
30	*Swift*/XRT	00084359011	2020-01-12T10:40:52	2020-01-12T10:53:52	0.8
31	*Swift*/XRT	00084359013	2020-10-15T00:42:12	2020-10-15T00:50:53	0.5
32	*Swift*/XRT	00084359014	2020-10-21T12:52:20	2020-10-21T12:55:53	0.2
33	*Swift*/XRT	00084359015	2020-10-22T06:34:13	2020-10-22T06:38:52	0.3
34	*Swift*/XRT	00084359016	2020-10-28T10:52:17	2020-10-28T10:57:53	0.3
35	*Swift*/XRT	00084359017	2020-11-05T12:57:16	2020-11-05T13:07:53	0.6
36	*Swift*/XRT	00084359018	2020-11-07T09:43:41	2020-11-07T09:57:53	0.9

Table A.3: Log of all the *Swift*/XRT observations of NGC 3486 used for the stacked image.

	Instr.	Obs.ID	Start time	Stop time	Exposure
			[YYYY-MM-DD hh:mm:ss]		[ks]
1	*Swift*/XRT	00032765003	2019-01-28T02:29:11	2019-01-28T02:46:51	1.1
2	*Swift*/XRT	00032765004	2019-01-31T19:24:28	2019-01-31T19:39:53	0.9
3	*Swift*/XRT	00032765005	2019-02-11T12:02:38	2019-02-11T13:57:53	2.0
4	*Swift*/XRT	00032765006	2019-02-25T15:39:36	2019-02-25T17:31:52	2.0
5	*Swift*/XRT	00032765007	2019-03-11T04:44:47	2019-03-11T06:27:53	2.0
6	*Swift*/XRT	00032765008	2019-03-25T16:13:44	2019-03-25T17:50:53	2.0
7	*Swift*/XRT	00032765009	2019-04-08T18:22:11	2019-04-08T20:02:52	2.0
8	*Swift*/XRT	00032765010	2019-04-22T05:38:00	2019-04-22T07:28:53	2.1
9	*Swift*/XRT	00032765011	2019-05-06T23:16:54	2019-05-06T23:31:52	0.9
10	*Swift*/XRT	00032765012	2019-05-09T03:57:13	2019-05-09T05:39:52	1.0
11	*Swift*/XRT	00032765013	2019-05-20T09:21:11	2019-05-20T11:13:51	2.0
12	*Swift*/XRT	00032765014	2019-06-03T19:17:38	2019-06-03T21:03:53	1.9
13	*Swift*/XRT	00032765015	2019-06-17T09:44:50	2019-06-17T11:42:53	2.0
14	*Swift*/XRT	00032765016	2019-07-01T14:56:56	2019-07-01T16:28:53	1.4
15	*Swift*/XRT	00032765017	2019-07-15T08:48:02	2019-07-15T09:15:52	1.7
16	*Swift*/XRT	00032765018	2019-10-27T19:36:07	2019-10-27T21:17:53	1.9
17	*Swift*/XRT	00032765019	2019-11-08T03:59:36	2019-11-08T05:53:53	2.0
18	*Swift*/XRT	00032765020	2019-11-23T00:51:35	2019-11-23T01:18:53	1.6
19	*Swift*/XRT	00032765021	2019-12-06T20:19:35	2019-12-06T20:45:52	1.6
20	*Swift*/XRT	00032765022	2019-12-20T03:19:32	2019-12-21T01:56:52	1.8
21	*XMM-Newton*	0082140301	2002-05-22T10:56:57	2002-05-22T20:15:36	33.5

Table A.4: Log of the observations of NGC 3623.

	Instr.	Obs.ID	Start time	Stop time	Exposure
			[YYYY-MM-DD hh:mm:ss]		[ks]
1	*Swift*/XRT	00036578004	2019-01-27T21:44:44	2019-01-27T23:35:53	2.0
2	*Swift*/XRT	00036578005	2019-02-10T05:45:52	2019-02-10T15:37:53	1.9
3	*Swift*/XRT	00036578006	2019-02-24T06:01:25	2019-02-24T22:30:52	2.1
4	*Swift*/XRT	00036578007	2019-03-10T01:31:59	2019-03-10T05:10:53	1.9
5	*Swift*/XRT	00036578008	2019-03-24T11:25:51	2019-03-24T19:35:52	1.9
6	*Swift*/XRT	00036578009	2019-04-07T18:10:46	2019-04-07T19:56:53	2.0
7	*Swift*/XRT	00036578010	2019-04-21T16:58:07	2019-04-21T20:22:53	2.1
8	*Swift*/XRT	00036578011	2019-05-05T09:12:53	2019-05-05T10:47:54	2.1
9	*Swift*/XRT	00036578012	2019-05-19T17:32:32	2019-05-19T19:26:51	2.0
10	*Swift*/XRT	00036578013	2019-06-02T04:57:37	2019-06-02T08:09:52	1.9
11	*Swift*/XRT	00036578014	2019-06-16T17:47:45	2019-06-16T19:31:53	2.0
12	*Swift*/XRT	00036578015	2019-06-30T00:30:32	2019-06-30T02:10:54	1.9
13	*Swift*/XRT	00036578016	2019-07-14T08:54:43	2019-07-14T09:21:53	1.6
14	*Swift*/XRT	00036578017	2019-10-27T00:18:52	2019-10-27T02:11:53	1.9
15	*Swift*/XRT	00036578018	2019-11-09T10:11:32	2019-11-09T12:02:53	1.9
16	*Swift*/XRT	00036578020	2019-12-07T02:41:36	2019-12-07T03:08:53	1.6
17	*Swift*/XRT	00036578021	2019-12-21T00:11:47	2019-12-21T11:23:52	2.1
18	*XMM-Newton*	0093641101	2001-05-26T15:50:25	2001-05-26T18:57:09	11.2

Table A.5: Log of the observations of NGC 3627.

	Instr.	Obs.ID	Start time	Stop time	Exposure
			[YYYY-MM-DD hh:mm:ss]		[ks]
1	*Swift*/XRT	00049859003	2019-01-19T04:52:00	2019-01-19T05:08:52	1.0
2	*Swift*/XRT	00049859004	2019-02-02T14:34:14	2019-02-02T14:50:52	1.0
3	*Swift*/XRT	00049859005	2019-02-16T13:25:18	2019-02-16T13:41:53	1.0
4	*Swift*/XRT	00049859006	2019-03-02T15:14:56	2019-03-02T15:37:53	1.4
5	*Swift*/XRT	00049859007	2019-03-16T15:38:51	2019-03-16T15:53:53	0.9
6	*Swift*/XRT	00049859008	2019-03-30T08:00:13	2019-03-30T08:07:51	0.5
7	*Swift*/XRT	00049859009	2019-04-13T09:41:07	2019-04-13T09:58:53	1.1
8	*Swift*/XRT	00049859012	2019-05-15T16:23:50	2019-05-15T16:39:53	1.0
9	*Swift*/XRT	00049859013	2019-05-25T13:47:52	2019-05-25T14:05:53	1.1
10	*Swift*/XRT	00049859015	2019-06-12T20:05:11	2019-06-12T21:46:53	0.9
11	*Swift*/XRT	00049859016	2019-06-22T11:08:08	2019-06-22T11:26:51	1.1
12	*Swift*/XRT	00049859017	2019-07-06T06:48:24	2019-07-06T07:03:52	0.9
13	*Swift*/XRT	00049859018	2019-07-20T21:12:47	2019-07-20T21:28:52	0.9
14	*Swift*/XRT	00049859019	2019-08-03T10:21:58	2019-08-03T10:39:54	1.1
15	*Swift*/XRT	00049859020	2019-08-17T04:26:19	2019-08-17T04:41:52	0.9
16	*Swift*/XRT	00049859021	2019-08-31T04:37:09	2019-08-31T04:41:02	0.2
17	*Swift*/XRT	00049859022	2019-09-05T02:32:51	2019-09-05T02:45:53	0.8
18	*Swift*/XRT	00049859023	2019-09-14T01:15:31	2019-09-14T01:29:53	0.9
19	*Swift*/XRT	00049859024	2019-09-28T16:23:24	2019-09-28T16:38:52	0.9
20	*Swift*/XRT	00049859025	2019-12-09T18:33:38	2019-12-09T18:47:53	0.9
21	*Swift*/XRT	00049859026	2019-12-16T02:02:41	2019-12-16T02:18:54	1.0
22	*Swift*/XRT	00049859027	2019-12-23T10:58:39	2019-12-23T11:01:52	0.2
23	*Swift*/XRT	00049859028	2019-12-30T14:58:38	2019-12-30T15:14:54	1.0
24	*Swift*/XRT	00049859029	2020-01-06T19:12:36	2020-01-06T19:25:53	0.8
25	*Swift*/XRT	00049859030	2020-01-13T16:53:41	2020-01-13T17:11:52	1.1
26	*Swift*/XRT	00049859031	2020-01-20T17:44:09	2020-01-20T18:02:52	1.1
27	*Swift*/XRT	00049859033	2020-01-30T23:05:20	2020-01-30T23:17:53	0.8
28	*Swift*/XRT	00049859035	2020-02-10T20:24:38	2020-02-10T20:38:53	0.9
29	*Swift*/XRT	00049859036	2020-02-17T21:18:09	2020-02-17T21:32:54	0.9
30	*Swift*/XRT	00049859037	2020-02-24T00:18:32	2020-02-24T00:28:54	0.6
31	*Swift*/XRT	00049859040	2020-03-05T16:36:44	2020-03-05T16:51:54	0.9
32	*Swift*/XRT	00049859041	2020-03-09T00:19:39	2020-03-09T00:30:53	0.7
33	*Swift*/XRT	00049859042	2020-03-16T10:42:48	2020-03-16T10:57:53	0.9
34	*Swift*/XRT	00049859043	2020-03-23T09:56:52	2020-03-23T10:08:54	0.7
35	*Swift*/XRT	00049859044	2020-03-30T06:24:21	2020-03-30T17:18:52	1.0
36	*Swift*/XRT	00049859045	2020-04-06T02:26:53	2020-04-06T02:42:54	1.0
37	*Swift*/XRT	00049859046	2020-04-13T14:18:26	2020-04-13T14:35:51	1.0
38	*Swift*/XRT	00049859047	2020-04-20T21:47:34	2020-04-20T22:02:54	0.9
39	*Swift*/XRT	00049859048	2020-04-27T05:03:25	2020-04-27T05:19:52	1.0
40	*Swift*/XRT	00049859049	2020-05-04T15:49:45	2020-05-04T16:05:52	1.0
41	*Swift*/XRT	00049859050	2020-05-11T16:41:47	2020-05-11T16:56:52	0.9
42	*Swift*/XRT	00049859051	2020-05-18T01:14:31	2020-05-18T01:26:53	0.7
43	*Swift*/XRT	00049859052	2020-05-25T10:24:28	2020-05-25T10:39:53	0.9
44	*Swift*/XRT	00049859053	2020-06-01T14:28:41	2020-06-01T14:43:52	0.9
45	*Swift*/XRT	00049859054	2020-06-08T04:17:11	2020-06-08T04:35:52	1.1
46	*Swift*/XRT	00049859055	2020-06-15T13:20:18	2020-06-15T13:35:54	0.9
47	*Swift*/XRT	00049859056	2020-06-22T12:36:49	2020-06-22T12:52:51	1.0
48	*Swift*/XRT	00049859057	2020-06-29T07:04:46	2020-06-29T07:20:54	1.0
49	*Swift*/XRT	00049859058	2020-07-06T04:36:42	2020-07-06T04:48:52	0.7
50	*Swift*/XRT	00049859059	2020-07-13T02:12:33	2020-07-13T02:28:54	1.0

51	*Swift*/XRT	00049859060	2020-07-20T03:09:28	2020-07-20T03:24:53	0.9
52	*Swift*/XRT	00049859061	2020-07-27T13:39:25	2020-07-27T13:56:53	1.0
53	*Swift*/XRT	00049859062	2020-08-03T10:04:48	2020-08-03T10:19:53	0.9
54	*Swift*/XRT	00049859063	2020-08-10T09:11:12	2020-08-10T09:27:53	1.0
55	*Swift*/XRT	00049859064	2020-08-17T02:24:40	2020-08-17T02:29:53	0.3
56	*Swift*/XRT	00049859065	2020-08-20T04:52:07	2020-08-20T05:06:52	0.9
57	*Swift*/XRT	00049859066	2020-08-24T09:29:24	2020-08-24T09:44:52	0.9
58	*Swift*/XRT	00049859067	2020-08-31T02:20:53	2020-08-31T02:36:54	1.0
59	*Swift*/XRT	00049859068	2020-09-07T02:51:39	2020-09-07T03:07:51	1.0
60	*Swift*/XRT	00013908001	2020-12-14T13:55:27	2020-12-14T15:42:54	2.2
61	*Swift*/XRT	00013908002	2020-12-28T01:20:20	2020-12-28T03:03:54	2.1
62	*Swift*/XRT	00013908003	2021-01-11T03:10:28	2021-01-11T19:08:52	1.8
63	*Swift*/XRT	00013908004	2021-01-25T20:43:13	2021-01-25T22:32:53	1.8
64	*Swift*/XRT	00013908005	2021-02-08T11:14:17	2021-02-08T14:28:51	1.9
65	*Swift*/XRT	00014065001	2021-02-11T20:35:38	2021-02-12T00:05:53	1.2
66	*Swift*/XRT	00014065002	2021-02-17T15:16:04	2021-02-17T15:43:54	1.7
67	*Swift*/XRT	00014065003	2021-02-23T01:59:54	2021-02-23T16:48:53	0.8
68	*Swift*/XRT	00014065004	2021-03-01T06:13:22	2021-03-01T17:50:53	1.2
69	*Swift*/XRT	00013908007	2021-03-08T13:45:47	2021-03-08T23:27:52	2.0
70	*Swift*/XRT	00013908008	2021-03-22T03:52:55	2021-03-22T07:20:52	0.2
71	*Swift*/XRT	00013908009	2021-03-24T03:33:13	2021-03-24T12:04:53	0.8
72	*Swift*/XRT	00013908010	2021-03-25T08:28:31	2021-03-25T08:46:52	1.1
73	*Swift*/XRT	00014065006	2021-03-29T09:36:20	2021-03-29T12:57:52	1.8
74	*Swift*/XRT	00013908011	2021-03-29T14:11:35	2021-03-29T14:28:53	1.0
75	*Swift*/XRT	00014065007	2021-04-05T02:38:43	2021-04-05T02:46:52	0.5
76	*Swift*/XRT	00013908012	2021-04-05T18:27:35	2021-04-05T21:51:53	0.2
77	*Swift*/XRT	00014065008	2021-04-07T05:20:49	2021-04-07T05:24:52	0.2
78	*Swift*/XRT	00013908013	2021-04-09T18:14:57	2021-04-09T19:47:53	1.4
79	*Swift*/XRT	00014065009	2021-04-10T03:43:36	2021-04-10T03:50:39	0.4
80	*Swift*/XRT	00014065010	2021-04-11T19:25:24	2021-04-11T19:27:57	0.2
81	*Swift*/XRT	00014065011	2021-04-16T14:23:59	2021-04-17T01:51:49	1.9
82	*Swift*/XRT	00013908014	2021-04-19T13:50:30	2021-04-19T14:08:53	1.1
83	*Swift*/XRT	00013908015	2021-05-03T13:53:06	2021-05-03T18:41:45	0.8
84	*XMM-Newton*	0112310301	2001-01-21T08:39:22	2001-01-21T15:11:05	23.5
85	*XMM-Newton*	0204870101	2004-01-10T18:28:35	2004-01-11T12:30:35	64.9

Table A.6: Log of the observations of NGC 4945.

	Instr.	Obs.ID	Start time	Stop time	Exposure
			[YYYY-MM-DD hh:mm:ss]		[ks]
1	*Swift*/XRT	00010978001	2019-01-13T08:35:33	2019-01-13T08:50:53	0.9
2	*Swift*/XRT	00010978002	2019-01-27T16:51:29	2019-01-27T17:07:54	1.0
3	*Swift*/XRT	00010978003	2019-02-10T01:18:52	2019-02-10T04:49:54	3.4
4	*Swift*/XRT	00010978004	2019-02-24T03:11:14	2019-02-24T03:27:52	1.0
5	*Swift*/XRT	00010978005	2019-03-10T16:24:51	2019-03-10T16:39:54	0.9
6	*Swift*/XRT	00010978006	2019-03-24T06:46:06	2019-03-24T06:59:53	0.8
7	*Swift*/XRT	00010978007	2019-04-07T15:13:33	2019-04-07T15:30:53	1.0
8	*Swift*/XRT	00010978008	2019-04-21T12:06:07	2019-04-21T13:45:53	1.1
9	*Swift*/XRT	00010978009	2019-05-05T20:34:19	2019-05-05T20:49:54	0.9
10	*Swift*/XRT	00010978010	2019-05-19T09:36:35	2019-05-19T09:52:52	1.0
11	*Swift*/XRT	00010978011	2019-06-02T04:53:20	2019-06-02T08:24:53	1.0
12	*Swift*/XRT	00010978012	2019-06-16T23:01:51	2019-06-16T23:17:51	1.0
13	*Swift*/XRT	00010978013	2019-06-30T16:36:50	2019-06-30T16:53:20	1.0
14	*Swift*/XRT	00010978014	2019-07-14T01:14:07	2019-07-14T01:29:52	0.9
15	*Swift*/XRT	00010978015	2019-07-28T18:52:17	2019-07-28T19:08:52	1.0
16	*Swift*/XRT	00010978016	2019-08-11T06:37:21	2019-08-11T06:52:53	0.9
17	*Swift*/XRT	00010978017	2019-08-25T05:14:06	2019-08-25T05:28:52	0.9
18	*Swift*/XRT	00010978018	2019-09-08T03:51:54	2019-09-08T04:04:52	0.8
19	*Swift*/XRT	00010978019	2019-12-15T21:26:15	2019-12-15T23:12:53	2.0
20	*Swift*/XRT	00010978020	2019-12-22T17:35:33	2019-12-22T19:01:52	1.0
21	*Swift*/XRT	00010978021	2019-12-29T12:05:05	2019-12-29T15:34:54	2.0
22	*Swift*/XRT	00010978022	2020-01-05T03:17:41	2020-01-05T03:44:54	1.6
23	*Swift*/XRT	00010978023	2020-01-12T13:47:17	2020-01-12T15:32:54	2.1
24	*Swift*/XRT	00010978024	2020-01-19T13:03:26	20260-01-19T23:05:54	2.1
25	*Swift*/XRT	00010978025	2020-01-26T17:11:00	2020-01-26T17:35:52	1.5
26	*Swift*/XRT	00010978027	2020-02-09T12:31:09	2020-02-09T12:59:54	1.7
27	*Swift*/XRT	00010978028	2020-02-16T15:03:23	2020-02-16T15:30:53	1.6
28	*Swift*/XRT	00010978029	2020-02-23T01:42:59	2020-02-23T03:38:53	1.9
29	*Swift*/XRT	00010978030	2020-03-01T23:24:29	2020-03-01T23:48:54	1.5
30	*Swift*/XRT	00010978031	2020-03-08T01:59:12	2020-03-08T13:19:52	1.3
31	*Swift*/XRT	00010978033	2020-03-09T22:36:30	2020-03-10T01:45:12	2.0
32	*Swift*/XRT	00010978032	2020-03-11T09:35:22	2020-03-11T11:26:53	1.9
33	*Swift*/XRT	00010978034	2020-03-15T07:35:53	2020-03-15T09:25:54	1.8
34	*Swift*/XRT	00010978035	2020-03-22T13:16:08	2020-03-22T13:42:53	1.6
35	*Swift*/XRT	00010978036	2020-03-29T06:10:04	2020-03-29T06:37:52	1.7
36	*Swift*/XRT	00010978037	2020-04-05T01:00:46	2020-04-05T07:42:53	1.8
37	*Swift*/XRT	00010978038	2020-04-12T06:51:50	2020-04-12T08:22:54	1.9
38	*Swift*/XRT	00010978039	2020-04-19T23:22:29	2020-04-19T23:48:53	1.6
39	*Swift*/XRT	00010978040	2020-04-26T19:46:49	2020-04-26T21:33:52	1.3
40	*Swift*/XRT	00010978041	2020-05-03T10:57:58	2020-05-03T11:24:53	1.6
41	*Swift*/XRT	00010978042	2020-05-10T07:09:26	2020-05-10T12:00:53	1.6
42	*Swift*/XRT	00010978043	2020-05-17T12:42:58	2020-05-17T13:10:53	1.7
43	*Swift*/XRT	00010978044	2020-05-24T12:00:33	2020-05-24T12:27:52	1.6
44	*Swift*/XRT	00010978045	2020-05-31T16:04:55	2020-05-31T16:32:53	1.7
45	*Swift*/XRT	00010978046	2020-06-07T10:42:25	2020-06-07T12:18:52	2.2
46	*Swift*/XRT	00010978047	2020-06-08T20:25:31	2020-06-08T21:53:31	2.0
47	*Swift*/XRT	00010978049	2020-06-10T05:39:24	2020-06-10T07:24:52	1.8
48	*Swift*/XRT	00010978050	2020-06-12T16:36:20	2020-06-12T16:54:53	1.1
49	*Swift*/XRT	00010978051	2020-06-14T11:38:26	2020-06-14T12:00:52	1.3
50	*Swift*/XRT	00010978052	2020-06-21T14:06:54	2020-06-21T14:34:54	1.7

51	*Swift*/XRT	00010978053	2020-06-28T10:11:50	2020-06-28T10:39:53	1.7
52	*Swift*/XRT	00010978054	2020-07-05T03:06:51	2020-07-05T03:34:53	1.7
53	*Swift*/XRT	00010978055	2020-07-12T08:55:42	2020-07-12T16:55:53	1.9
54	*Swift*/XRT	00010978056	2020-07-19T20:47:19	2020-07-19T21:15:54	1.7
55	*Swift*/XRT	00010978057	2020-07-26T20:18:43	2020-07-26T21:51:52	1.8
56	*Swift*/XRT	00010978058	2020-08-02T05:10:19	2020-08-02T05:38:52	1.7
57	*Swift*/XRT	00010978059	2020-08-09T14:06:04	2020-08-09T15:34:55	1.8
58	*XMM-Newton*	0110910201	2003-01-27T10:54:55	2003-01-27T19:26:07	30.7
59	*XMM-Newton*	0503230101	2008-01-16T17:57:33	2008-01-17T04:12:39	36.9
60	*XMM-Newton*	0552080101	2008-08-16T07:50:34	2008-08-16T16:07:28	29.8
61	*XMM-Newton*	0723450101	2013-08-07T16:21:05	2013-08-08T07:04:25	53.0
62	*XMM-Newton*	0723450201	2014-01-11T11:42:19	2014-01-12T03:48:59	58.0
63	*XMM-Newton*	0729561001	2015-02-02T15:42:36	2015-02-03T00:52:36	33.0
64	*XMM-Newton*	0729561201	2014-07-06T17:28:32	2014-07-07T01:45:12	29.8
65	*XMM-Newton*	0761620101	2015-08-07T03:17:34	2015-08-07T20:47:34	63.0
66	*XMM-Newton*	0761620201	2016-01-20T01:26:44	2016-01-20T22:31:44	75.9

Table A.7: Log of the observations of NGC 5236.

	Instr.	Obs.ID	Start time	Stop time	Exposure
			[YYYY-MM-DD hh:mm:ss]		[ks]
1	*Swift*/XRT	00045596019	2019-08-18T16:33:23	2019-08-18T22:55:52	1.3
2	*Swift*/XRT	00045596020	2019-08-21T04:41:38	2019-08-21T05:02:52	1.3
3	*Swift*/XRT	00045596021	2019-08-25T18:33:26	2019-08-25T18:50:51	1.0
4	*Swift*/XRT	00045596022	2019-08-27T05:51:49	2019-08-27T21:57:53	1.5
5	*Swift*/XRT	00045596023	2019-09-01T05:20:20	2019-09-01T16:49:53	1.6
6	*Swift*/XRT	00045596024	2019-09-08T06:00:36	2019-09-09T03:01:52	2.4
7	*Swift*/XRT	00045596025	2019-09-15T13:27:33	2019-09-15T23:14:53	2.7
8	*Swift*/XRT	00045596026	2019-09-22T22:23:05	2019-09-22T22:47:52	1.5
9	*Swift*/XRT	00045596027	2019-09-25T22:05:20	2019-09-25T22:28:54	1.4
10	*Swift*/XRT	00045596028	2019-10-06T02:10:34	2019-10-06T21:28:54	1.2
11	*Swift*/XRT	00045596029	2019-10-09T11:29:11	2019-10-09T19:31:51	1.6
12	*Swift*/XRT	00045596030	2019-10-13T15:26:57	2019-10-13T17:28:52	2.9
13	*Swift*/XRT	00045596031	2019-10-20T06:55:11	2019-10-20T21:41:52	2.1
14	*Swift*/XRT	00045596032	2019-10-27T00:03:15	2019-10-27T22:35:52	2.6
15	*Swift*/XRT	00045596033	2019-11-03T18:17:09	2019-11-03T21:53:52	2.8
16	*Swift*/XRT	00045596034	2019-11-13T12:48:09	2019-11-13T22:33:53	2.8
17	*Swift*/XRT	00045596035	2019-11-17T06:02:31	2019-11-18T10:54:53	2.8
18	*Swift*/XRT	00045596036	2019-11-28T19:07:33	2019-11-28T22:43:54	2.5
19	*Swift*/XRT	00045596037	2019-12-08T03:37:33	2019-12-08T15:12:53	3.3
20	*Swift*/XRT	00089002001	2019-12-13T03:19:50	2019-12-13T05:02:54	1.9
21	*Swift*/XRT	00045596038	2019-12-18T12:12:51	2019-12-18T15:39:53	1.6
22	*Swift*/XRT	00045596039	2019-12-22T19:45:59	2019-12-22T19:53:53	0.5
23	*Swift*/XRT	00045596041	2020-01-02T09:15:03	2020-01-02T14:22:52	3.5
24	*Swift*/XRT	00045596042	2020-01-07T18:45:42	2020-01-07T22:06:52	1.2
25	*Swift*/XRT	00045596044	2020-03-01T21:11:49	2020-03-01T23:08:53	2.4
26	*Swift*/XRT	00045596045	2020-03-08T09:21:10	2020-03-08T11:21:09	2.4
27	*Swift*/XRT	00045596046	2020-03-15T00:37:12	2020-03-15T03:54:52	2.9
28	*Swift*/XRT	00095702001	2020-07-01T01:01:15	2020-07-01T09:06:53	2.1
29	*Swift*/XRT	00095702002	2020-07-11T04:45:24	2020-07-11T06:35:54	2.6
30	*Swift*/XRT	00095702003	2020-07-21T04:02:28	2020-07-21T13:45:53	1.9
31	*Swift*/XRT	00095702004	2020-07-31T17:17:45	2020-07-31T22:10:53	2.1
32	*Swift*/XRT	00095702005	2020-08-10T08:14:50	2020-08-10T10:28:53	2.6
33	*Swift*/XRT	00089004001	2020-08-17T07:32:05	2020-08-17T07:58:52	1.6
34	*Swift*/XRT	00095702006	2020-08-20T00:52:59	2020-08-20T16:55:52	2.8
35	*Swift*/XRT	00095702007	2020-08-30T17:18:07	2020-08-30T19:04:53	2.3
36	*Swift*/XRT	00095702008	2020-09-09T09:58:56	2020-09-09T12:04:52	2.5
37	*Swift*/XRT	00095702009	2020-09-19T10:41:53	2020-09-19T14:05:54	2.4
38	*Swift*/XRT	00095702010	2020-09-29T19:24:34	2020-09-29T21:16:52	2.5
39	*Swift*/XRT	00095702011	2020-10-08T13:35:29	2020-10-09T21:33:53	2.6
40	*Swift*/XRT	00095702012	2020-10-19T12:46:33	2020-10-19T12:48:54	0.1
41	*Swift*/XRT	00095702013	2020-10-22T12:09:32	2020-10-22T13:53:54	2.3
42	*Swift*/XRT	00095702014	2020-10-29T14:49:06	2020-10-29T16:32:52	1.9
43	*Swift*/XRT	00095702015	2020-11-08T10:40:54	2020-11-08T12:28:53	2.5
44	*Swift*/XRT	00095702016	2020-11-18T16:12:05	2020-11-18T22:50:54	1.5
45	*Swift*/XRT	00095702017	2020-11-29T13:15:24	2020-11-29T16:52:53	2.2
46	*Swift*/XRT	00095702018	2020-12-08T05:51:23	2020-12-08T07:48:53	2.0
47	*Swift*/XRT	00095702019	2020-12-18T11:15:01	2020-12-18T17:53:53	1.9
48	*Swift*/XRT	00095702020	2020-12-28T10:18:55	2020-12-28T10:20:26	0.1
49	*Swift*/XRT	00095702021	2021-01-01T06:37:39	2021-01-01T08:25:52	2.4
50	*Swift*/XRT	00095702022	2021-01-07T12:31:39	2021-01-07T16:08:52	2.5

51	*Swift*/XRT	00095702023	2021-01-17T02:01:45	2021-01-17T08:35:54	2.5
52	*Swift*/XRT	00095702025	2021-01-31T10:15:05	2021-01-31T13:37:53	2.3
53	*Swift*/XRT	00095702026	2021-02-06T13:58:46	2021-02-06T15:47:53	2.5
54	*Swift*/XRT	00095702027	2021-02-15T00:28:25	2021-02-16T13:37:54	2.6
55	*Swift*/XRT	00095702028	2021-02-26T01:04:10	2021-02-26T22:07:53	2.3
56	*Swift*/XRT	00095702029	2021-03-08T12:36:39	2021-03-08T14:33:53	2.4
57	*Swift*/XRT	00014387001	2021-06-24T14:22:53	2021-06-24T23:59:53	2.2
58	*Swift*/XRT	00014387002	2021-07-01T00:37:23	2021-07-02T18:26:52	4.2
59	*Swift*/XRT	00014387003	2021-07-08T01:22:21	2021-07-08T01:48:53	1.6
60	*Swift*/XRT	00014387004	2021-07-15T00:40:24	2021-07-15T01:06:54	1.6
61	*Swift*/XRT	00014387005	2021-07-22T11:16:51	2021-07-22T14:47:54	1.8
62	*Swift*/XRT	00014387006	2021-07-29T01:02:01	2021-07-29T13:52:52	2.2
63	*Swift*/XRT	00014387007	2021-08-05T00:34:09	2021-08-05T21:15:52	1.9
64	*Swift*/XRT	00014387008	2021-08-12T13:57:45	2021-08-12T17:17:54	1.8
65	*Swift*/XRT	00014387009	2021-08-19T00:08:53	2021-08-19T19:42:54	1.6
66	*Swift*/XRT	00014387010	2021-08-26T07:38:21	2021-08-26T14:08:54	1.8
67	*Swift*/XRT	00014387011	2021-09-02T21:02:32	2021-09-02T22:59:52	1.8
68	*Swift*/XRT	00014387012	2021-09-09T15:39:37	2021-09-09T20:38:54	1.9
69	*Swift*/XRT	00014387013	2021-09-16T14:48:27	2021-09-16T15:14:52	1.6
70	*Swift*/XRT	00014387014	2021-09-23T18:54:32	2021-09-23T19:14:53	1.2
71	*Swift*/XRT	00014387015	2021-09-28T07:05:47	2021-09-28T18:26:54	0.6
72	*Swift*/XRT	00014387016	2021-09-30T11:53:31	2021-09-30T18:37:52	2.2
73	*Swift*/XRT	00014387017	2021-10-07T03:08:35	2021-10-07T17:41:52	2.0
74	*Swift*/XRT	00014387018	2021-10-14T12:10:11	2021-10-14T15:13:51	1.9
75	*Swift*/XRT	00014387019	2021-10-21T01:26:27	2021-10-21T04:45:54	1.4
76	*Swift*/XRT	00014387020	2021-10-28T10:13:12	2021-10-28T10:37:53	1.5
77	*Swift*/XRT	00014387021	2021-11-04T07:54:52	2021-11-04T08:22:52	1.7
78	*Swift*/XRT	00014387022	2021-11-11T05:43:08	2021-11-11T06:11:53	1.7
79	*Swift*/XRT	00014387023	2021-11-19T15:58:48	2021-11-20T00:11:52	1.7
80	*Swift*/XRT	00014387024	2021-11-24T23:16:06	2021-11-25T07:44:53	1.9
81	*XMM-Newton*	0784510301	2017-01-18T19:45:14	2017-01-19T09:38:34	50.0

Table A.8: Log of the observations of NGC 925.

	Instr.	Obs.ID	Start time	Stop time	Exposure
			[YYYY-MM-DD hh:mm:ss]		[ks]
1	*Swift*/XRT	03110849001	2020-10-21T01:52:56	2020-10-21T22:47:52	0.6
2	*Swift*/XRT	03110849002	2020-10-26T22:12:02	2020-10-26T22:16:53	0.3
3	*Swift*/XRT	03110849003	2020-10-29T17:05:05	2020-10-29T17:23:53	1.1
4	*Swift*/XRT	03110849004	2020-11-13T05:56:00	2020-11-14T02:54:54	2.8
5	*Swift*/XRT	03110849005	2020-11-16T13:28:04	2020-11-16T13:43:29	0.9
6	*Swift*/XRT	03110849006	2020-11-17T13:29:13	2020-11-17T13:44:54	0.9
7	*Swift*/XRT	03110927001	2021-03-02T23:35:24	2021-03-02T23:42:53	0.4
8	*Swift*/XRT	03110927002	2021-03-14T20:49:49	2021-03-14T20:56:52	0.4
9	*Swift*/XRT	03110927003	2021-03-25T08:49:49	2021-03-25T08:56:53	0.4
10	*Swift*/XRT	03110927004	2021-03-31T08:12:19	2021-03-31T08:16:52	0.3
11	*Swift*/XRT	03110927006	2021-05-01T14:06:57	2021-05-01T14:13:53	0.4
12	*Swift*/XRT	03110927007	2021-05-06T04:11:05	2021-05-06T04:16:16	0.3
13	*Swift*/XRT	00014386001	2021-06-23T08:31:28	2021-06-23T10:18:54	1.8
14	*Swift*/XRT	00014386002	2021-06-30T11:04:42	2021-06-30T11:31:52	1.6
15	*Swift*/XRT	00014386003	2021-07-07T04:08:42	2021-07-07T04:32:51	1.4

16	*Swift*/XRT	00014386004	2021-07-14T01:43:45	2021-07-14T02:05:52	1.3
17	*Swift*/XRT	00014386005	2021-07-21T12:05:29	2021-07-21T12:21:52	1.0
18	*Swift*/XRT	00014386006	2021-07-26T07:01:05	2021-07-26T07:01:52	0.1
19	*Swift*/XRT	00014386007	2021-07-28T11:19:37	2021-07-28T11:46:52	1.6
20	*Swift*/XRT	00014386008	2021-08-04T00:57:41	2021-08-04T01:23:53	1.6
21	*Swift*/XRT	00014386009	2021-08-11T01:47:20	2021-08-11T02:13:52	1.6
22	*Swift*/XRT	00014386010	2021-08-18T02:46:12	2021-08-18T03:09:53	1.4
23	*Swift*/XRT	00014386011	2021-08-25T08:28:54	2021-08-25T13:36:52	1.9
24	*Swift*/XRT	00014386012	2021-09-01T12:32:59	2021-09-01T19:18:52	1.8
25	*Swift*/XRT	00014386013	2021-10-06T00:40:39	2021-10-06T01:07:54	1.6
26	*Swift*/XRT	00014386014	2021-10-13T09:38:15	2021-10-13T22:47:53	1.9
27	*Swift*/XRT	03110927009	2021-10-15T23:42:21	2021-10-16T01:31:52	1.5
28	*Swift*/XRT	03110927010	2021-10-17T18:49:17	2021-10-17T18:56:54	0.5
29	*Swift*/XRT	00014386015	2021-10-20T00:53:54	2021-10-20T01:20:39	1.6
30	*Swift*/XRT	03110927011	2021-10-20T12:05:33	2021-10-20T12:23:53	1.1
31	*Swift*/XRT	03110927012	2021-10-21T11:58:33	2021-10-21T13:40:53	0.5
32	*Swift*/XRT	03110927013	2021-10-22T04:05:02	2021-10-23T23:16:52	7.5
33	*Swift*/XRT	03110927014	2021-10-24T14:51:24	2021-10-25T13:30:53	2.3
34	*Swift*/XRT	03110927015	2021-10-26T11:28:29	2021-10-26T11:36:53	0.5
35	*Swift*/XRT	00014386016	2021-10-27T06:20:18	2021-10-27T06:44:52	1.5
36	*Swift*/XRT	03110927016	2021-10-27T08:16:13	2021-10-27T11:40:52	1.6
37	*Swift*/XRT	00014386017	2021-11-03T03:53:30	2021-11-03T04:20:52	1.6
38	*Swift*/XRT	03110927017	2021-11-03T09:09:11	2021-11-03T09:19:53	0.6
39	*Swift*/XRT	03110927018	2021-11-04T08:54:06	2021-11-04T21:33:52	3.5
40	*Swift*/XRT	03110927019	2021-11-06T10:00:06	2021-11-06T21:41:52	5.3
41	*Swift*/XRT	03110927020	2021-11-07T10:01:05	2021-11-08T18:12:53	2.3
42	*Swift*/XRT	03110927022	2021-11-10T01:49:19	2021-11-10T05:17:54	3.5
43	*Swift*/XRT	00014386018	2021-11-10T07:51:23	2021-11-10T08:18:53	1.6
44	*Swift*/XRT	03110927023	2021-11-12T12:29:34	2021-11-13T09:34:52	1.9
45	*Swift*/XRT	03110927024	2021-11-15T17:08:34	2021-11-15T17:21:54	0.8
46	*Swift*/XRT	00014386019	2021-11-17T03:58:23	2021-11-17T23:34:52	2.0
47	*Swift*/XRT	00014386020	2021-11-24T03:11:35	2021-11-24T03:38:52	1.7
48	*Swift*/XRT	00014386021	2021-12-01T04:12:22	2021-12-01T07:37:53	1.7
49	*XMM-Newton*	0405080301	2007-05-28T07:36:12	2007-05-28T21:59:05	51.8
50	*XMM-Newton*	0405080501	2007-06-19T10:03:34	2007-06-19T14:45:26	16.9

Table A.9: Log of the observations of NGC 5055.

	Instr.	Obs.ID	Start time	Stop time	Exposure
			[YYYY-MM-DD hh:mm:ss]		[ks]
1	*Swift*/XRT	00014388001	2021-06-24T08:30:30	2021-06-24T08:58:53	1.7
2	*Swift*/XRT	00014388002	2021-07-01T07:46:19	2021-07-01T08:09:53	1.4
3	*Swift*/XRT	00014388003	2021-07-08T08:47:38	2021-07-08T09:06:52	1.2
4	*Swift*/XRT	00014388004	2021-07-14T03:12:07	2021-07-14T03:40:52	1.7
5	*Swift*/XRT	00014388005	2021-07-22T02:22:03	2021-07-22T02:50:54	1.7
6	*Swift*/XRT	00014388006	2021-07-29T20:43:37	2021-07-29T22:25:52	1.8
7	*Swift*/XRT	00014388007	2021-08-05T15:14:58	2021-08-05T15:42:53	1.7
8	*XMM-Newton*	0203170301	2004-12-25T02:15:13	2004-12-26T09:59:30	114.3

Table A.10: Log of the observations of NGC 4517.

Bibliography

B. P. Abbott and et al. Observation of Gravitational Waves from a Binary Black Hole Merger. *Phys. Rev. Lett.*, 116(6):061102, Feb. 2016. doi: 10.1103/PhysRevLett.116.061102.

B. P. Abbott and et al. GW170817: Observation of Gravitational Waves from a Binary Neutron Star Inspiral. *Phys. Rev. Lett.*, 119(16):161101, Oct. 2017. doi: 10.1103/PhysRevLett.119.161101.

R. Abbott and et al. GW190521: A Binary Black Hole Merger with a Total Mass of 150 $M_{\odot}$. *Phys. Rev. Lett.*, 125(10):101102, Sept. 2020a. doi: 10.1103/PhysRevLett.125.101102.

R. Abbott and et al. Properties and Astrophysical Implications of the 150 $M_{\odot}$ Binary Black Hole Merger GW190521. *ApJ*, 900(1):L13, Sept. 2020b. doi: 10.3847/2041-8213/aba493.

P. Abolmasov. Understanding ULX nebulae in the framework of supercritical accretion. *New Astronomy*, 16(2):138–146, Feb. 2011. doi: 10.1016/j.newast.2010.07.003.

M. A. Abramowicz, B. Czerny, J. P. Lasota, and E. Szuszkiewicz. Slim Accretion Disks. *ApJ*, 332: 646, Sept. 1988. doi: 10.1086/166683.

J. Aird, K. Nandra, E. S. Laird, A. Georgakakis, M. L. N. Ashby, P. Barmby, A. L. Coil, J. S. Huang, A. M. Koekemoer, C. C. Steidel, and C. N. A. Willmer. The evolution of the hard X-ray luminosity function of AGN. *MNRAS*, 401(4):2531–2551, Feb. 2010. doi: 10.1111/j.1365-2966.2009.15829.x.

J. Aleksić, S. Ansoldi, L. A. Antonelli, P. Antoranz, A. Babic, P. Bangale, U. Barres de Almeida, J. A. Barrio, J. Becerra González, W. Bednarek, K. Berger, E. Bernardini, A. Biland, O. Blanch, R. K. Bock, S. Bonnefoy, G. Bonnoli, F. Borracci, T. Bretz, E. Carmona, A. Carosi, D. Carreto Fidalgo, P. Colin, E. Colombo, J. L. Contreras, J. Cortina, S. Covino, P. Da Vela, F. Dazzi, A. De Angelis, G. De Caneva, B. De Lotto, C. Delgado Mendez, M. Doert, A. Domínguez, D. Dominis Prester, D. Dorner, M. Doro, S. Einecke, D. Eisenacher, D. Elsaesser, E. Farina, D. Ferenc, M. V. Fonseca, L. Font, K. Frantzen, C. Fruck, R. J. García López, M. Garczarczyk, D. Garrido Terrats, M. Gaug, G. Giavitto, N. Godinović, A. González Muñoz, S. R. Gozzini, A. Hadamek, D. Hadasch, A. Herrero, D. Hildebrand, J. Hose, D. Hrupec, W. Idec, V. Kadenius, H. Kellermann, M. L. Knoetig, J. Krause, J. Kushida, A. La Barbera, D. Lelas, N. Lewandowska, E. Lindfors, F. Longo, S. Lombardi, M. López, R. López-Coto, A. López-Oramas, E. Lorenz, I. Lozano, M. Makariev, K. Mallot, G. Maneva, N. Mankuzhiyil, K. Mannheim, L. Maraschi, B. Marcote, M. Mariotti, M. Martínez, D. Mazin, U. Menzel, M. Meucci, J. M. Miranda, R. Mirzoyan, A. Moralejo, P. Munar-Adrover, D. Nakajima, A. Niedzwiecki, K. Nilsson, N. Nowak, R. Orito, A. Overkemping, S. Paiano, M. Palatiello, D. Paneque, R. Paoletti, J. M. Paredes, X. Paredes-Fortuny, S. Partini, M. Persic, F. Prada, P. G. Prada Moroni, E. Prandini, S. Preziuso, I. Puljak, R. Reinthal, W. Rhode, M. Ribó, J. Rico, J. RodriguezGarcia, S. Rügamer, A. Saggion, K. Saito, M. Salvati, K. Satalecka, V. Scalzotto, V. Scapin, C. Schultz, T. Schweizer, S. N. Shore, A. Sillanpää, J. Sitarek, I. Snidaric, D. Sobczynska, F. Spanier, V. Stamatescu, A. Stamerra, T. Steinbring, J. Storz, S. Sun, T. Surić, L. Takalo, F. Tavecchio, P. Temnikov, T. Terzić, D. Tescaro, M. Teshima, J. Thaele, O. Tibolla, D. F. Torres, T. Toyama, A. Treves, M. Uellenbeck, P. Vogler, R. M. Wagner,

F. Zandanel, R. Zanin, MAGIC Collaboration, S. Archambault, B. Behera, M. Beilicke, W. Benbow, R. Bird, J. H. Buckley, V. Bugaev, M. Cerruti, X. Chen, L. Ciupik, E. Collins-Hughes, W. Cui, J. Dumm, J. D. Eisch, A. Falcone, S. Federici, Q. Feng, J. P. Finley, H. Fleischhack, P. Fortin, L. Fortson, A. Furniss, S. Griffin, S. T. Griffiths, J. Grube, G. Gyuk, D. Hanna, J. Holder, G. Hughes, T. B. Humensky, C. A. Johnson, P. Kaaret, M. Kertzman, Y. Khassen, D. Kieda, H. Krawczynski, F. Krennrich, S. Kumar, M. J. Lang, G. Maier, S. McArthur, K. Meagher, P. Moriarty, R. Mukherjee, R. A. Ong, A. N. Otte, N. Park, A. Pichel, M. Pohl, A. Popkow, H. Prokoph, J. Quinn, K. Ragan, J. Rajotte, P. T. Reynolds, G. T. Richards, E. Roache, A. C. Rovero, G. H. Sembroski, K. Shahinyan, D. Staszak, I. Telezhinsky, M. Theiling, J. V. Tucci, J. Tyler, A. Varlotta, S. P. Wakely, T. C. Weekes, A. Weinstein, R. Welsing, A. Wilhelm, D. A. Williams, B. Zitzer, VERITAS Collaboration, M. Villata, C. Raiteri, H. D. Aller, M. F. Aller, W. P. Chen, B. Jordan, E. Koptelova, O. M. Kurtanidze, A. Lähteenmäki, B. McBreen, V. M. Larionov, C. S. Lin, M. G. Nikolashvili, E. Angelakis, M. Capalbi, A. Carramiñana, L. Carrasco, P. Cassaro, A. Cesarini, L. Fuhrmann, M. Giroletti, T. Hovatta, T. P. Krichbaum, H. A. Krimm, W. Max-Moerbeck, J. W. Moody, G. Maccaferri, Y. Mori, I. Nestoras, A. Orlati, C. Pace, R. Pearson, M. Perri, A. C. S. Readhead, J. L. Richards, A. C. Sadun, T. Sakamoto, J. Tammi, M. Tornikoski, Y. Yatsu, and A. Zook. The 2009 multiwavelength campaign on Mrk 421: Variability and correlation studies. *A&A*, 576:A126, Apr. 2015. doi: 10.1051/0004-6361/201424216.

V. Allevato, M. Paolillo, I. Papadakis, and C. Pinto. Measuring X-Ray Variability in Faint/Sparsely Sampled Active Galactic Nuclei. *ApJ*, 771(1):9, July 2013. doi: 10.1088/0004-637X/771/1/9.

W. N. Alston, C. Pinto, D. Barret, A. D'Aì, M. Del Santo, H. Earnshaw, A. C. Fabian, F. Fuerst, E. Kara, P. Kosec, M. J. Middleton, M. L. Parker, F. Pintore, A. Robba, T. P. Roberts, R. Sathyaprakash, D. Walton, and E. Ambrosi. Quasi-periodic dipping in the ultraluminous X-ray source, NGC 247 ULX-1. *MNRAS*, 505(3):3722–3729, Aug. 2021. doi: 10.1093/mnras/stab1473.

D. Altamirano, T. Belloni, M. Linares, M. van der Klis, R. Wijnands, P. A. Curran, M. Kalamkar, H. Stiele, S. Motta, T. Muñoz-Darias, P. Casella, and H. Krimm. The Faint "Heartbeats" of IGR J17091-3624: An Exceptional Black Hole Candidate. *ApJ*, 742(2):L17, Dec. 2011. doi: 10.1088/2041-8205/742/2/L17.

P. Amram, C. Mendes de Oliveira, J. Boulesteix, and C. Balkowski. The Hα kinematic of the Cartwheel galaxy. *A&A*, 330:881–893, Feb. 1998.

T. An, X.-L. Lu, and J.-Y. Wang. Temporal evolution of long-timescale periodicities in ULX NGC 5408 X-1. *A&A*, 585:A89, Jan. 2016. doi: 10.1051/0004-6361/201526182.

R. Arcodia, A. Merloni, K. Nandra, J. Buchner, M. Salvato, D. Pasham, R. Remillard, J. Comparat, G. Lamer, G. Ponti, A. Malyali, J. Wolf, Z. Arzoumanian, D. Bogensberger, D. A. H. Buckley, K. Gendreau, M. Gromadzki, E. Kara, M. Krumpe, C. Markwardt, M. E. Ramos-Ceja, A. Rau, M. Schramm, and A. Schwope. X-ray quasi-periodic eruptions from two previously quiescent galaxies. *Nature*, 592(7856):704–707, Apr. 2021. doi: 10.1038/s41586-021-03394-6.

R. Arcodia, G. Miniutti, G. Ponti, J. Buchner, M. Giustini, A. Merloni, K. Nandra, F. Vincentelli, E. Kara, M. Salvato, and D. Pasham. The complex time and energy evolution of quasi-periodic eruptions in eRO-QPE1. *arXiv e-prints*, art. arXiv:2203.11939, Mar. 2022.

K. A. Arnaud. XSPEC: The First Ten Years. In G. H. Jacoby and J. Barnes, editors, *Astronomical Data Analysis Software and Systems V*, volume 101 of *Astronomical Society of the Pacific Conference Series*, page 17, 1996.

E. Athanassoula, I. Puerari, and A. Bosma. Formation of rings in galactic discs by infalling small companions. *MNRAS*, 286:284–302, Apr. 1997. doi: 10.1093/mnras/286.2.284.

E. Bañados, B. P. Venemans, C. Mazzucchelli, E. P. Farina, F. Walter, F. Wang, R. Decarli, D. Stern, X. Fan, F. B. Davies, J. F. Hennawi, R. A. Simcoe, M. L. Turner, H.-W. Rix, J. Yang, D. D. Kelson,

G. C. Rudie, and J. M. Winters. An 800-million-solar-mass black hole in a significantly neutral Universe at a redshift of 7.5. *Nature*, 553(7689):473–476, Jan. 2018. doi: 10.1038/nature25180.

M. Bachetti, V. Rana, D. J. Walton, D. Barret, F. A. Harrison, S. E. Boggs, F. E. Christensen, W. W. Craig, A. C. Fabian, F. Fürst, B. W. Grefenstette, C. J. Hailey, A. Hornschemeier, K. K. Madsen, J. M. Miller, A. F. Ptak, D. Stern, N. A. Webb, and W. W. Zhang. The Ultraluminous X-Ray Sources NGC 1313 X-1 and X-2: A Broadband Study with NuSTAR and XMM-Newton. *ApJ*, 778(2):163, Dec. 2013. doi: 10.1088/0004-637X/778/2/163.

M. Bachetti, F. A. Harrison, D. J. Walton, B. W. Grefenstette, D. Chakrabarty, F. Fürst, D. Barret, A. Beloborodov, S. E. Boggs, F. E. Christensen, W. W. Craig, A. C. Fabian, C. J. Hailey, A. Hornschemeier, V. Kaspi, S. R. Kulkarni, T. Maccarone, J. M. Miller, V. Rana, D. Stern, S. P. Tendulkar, J. Tomsick, N. A. Webb, and W. W. Zhang. An ultraluminous X-ray source powered by an accreting neutron star. *Nature*, 514(7521):202–204, Oct 2014. doi: 10.1038/nature13791.

M. Bachetti, D. Huppenkothen, U. Khan, H. Mishra, S. Sharma, A. Stevens, H. Rashid, E. M. Ribeiro, B. Sipőcz, tappina, A. Desai, J. Swinbank, omargamal8, A. Rasquinha, P. Balm, S. Mumford, R. Campana, N. Garg, A. Tandon, A. Hota, Nick, S. Mishra, A. Smith, M. Mahlke, S. Sachidanand, S. Kumar, R. V. Blanco, S. Kothari, A. Jadhav, and F. Pisanu. Stingraysoftware/stingray: Version 0.2, June 2020. URL `https://doi.org/10.5281/zenodo.3898435`.

R. V. Baluev. Assessing the statistical significance of periodogram peaks. *MNRAS*, 385(3):1279–1285, Apr. 2008. doi: 10.1111/j.1365-2966.2008.12689.x.

J. M. Bardeen and J. A. Petterson. The Lense-Thirring Effect and Accretion Disks around Kerr Black Holes. *ApJ*, 195:L65, Jan. 1975. doi: 10.1086/181711.

S. D. Barthelmy, L. M. Barbier, J. R. Cummings, E. E. Fenimore, N. Gehrels, D. Hullinger, H. A. Krimm, C. B. Markwardt, D. M. Palmer, A. Parsons, G. Sato, M. Suzuki, T. Takahashi, M. Tashiro, and J. Tueller. The Burst Alert Telescope (BAT) on the SWIFT Midex Mission. *Space Sci. Rev.*, 120(3-4):143–164, Oct. 2005. doi: 10.1007/s11214-005-5096-3.

M. M. Basko and R. A. Sunyaev. The limiting luminosity of accreting neutron stars with magnetic fields. *MNRAS*, 175:395–417, May 1976. doi: 10.1093/mnras/175.2.395.

F. E. Bauer, W. N. Brandt, R. M. Sambruna, G. Chartas, G. P. Garmire, S. Kaspi, and H. Netzer. A Chandra Study of the Circinus Galaxy Point-Source Population. *AJ*, 122(1):182–193, July 2001. doi: 10.1086/321123.

K. Belczynski, T. Bulik, C. L. Fryer, A. Ruiter, F. Valsecchi, J. S. Vink, and J. R. Hurley. On the Maximum Mass of Stellar Black Holes. *ApJ*, 714(2):1217–1226, May 2010. doi: 10.1088/0004-637X/714/2/1217.

K. Belczynski, A. Buonanno, M. Cantiello, C. L. Fryer, D. E. Holz, I. Mandel, M. C. Miller, and M. Walczak. The Formation and Gravitational-wave Detection of Massive Stellar Black Hole Binaries. *ApJ*, 789(2):120, July 2014. doi: 10.1088/0004-637X/789/2/120.

A. Belfiore, P. Esposito, F. Pintore, G. Novara, R. Salvaterra, A. De Luca, A. Tiengo, P. Caraveo, F. Fürst, G. L. Israel, D. Magistrali, M. Marelli, S. Mereghetti, A. Papitto, G. A. Rodríguez Castillo, C. Salvaggio, L. Stella, D. J. Walton, A. Wolter, and L. Zampieri. Diffuse X-ray emission around an ultraluminous X-ray pulsar. *Nature Astronomy*, page 475, Oct 2019. doi: 10.1038/s41550-019-0903-z.

A. Belfiore, P. Esposito, F. Pintore, G. Novara, R. Salvaterra, A. De Luca, A. Tiengo, P. Caraveo, F. Fürst, G. L. Israel, D. Magistrali, M. Marelli, S. Mereghetti, A. Papitto, G. A. Rodríguez Castillo, C. Salvaggio, L. Stella, D. J. Walton, A. Wolter, and L. Zampieri. Diffuse X-ray emission around an ultraluminous X-ray pulsar. *Nature Astronomy*, 4:147–152, Feb. 2020. doi: 10.1038/s41550-019-0903-z.

T. Belloni, M. Klein-Wolt, M. Méndez, M. van der Klis, and J. van Paradijs. A model-independent analysis of the variability of GRS 1915+105. *A&A*, 355:271–290, Mar. 2000.

T. M. Belloni. *States and Transitions in Black Hole Binaries*, volume 794, page 53. 2010. doi: 10.1007/978-3-540-76937-8_3.

C. T. Berghea, K. A. Weaver, E. J. M. Colbert, and T. P. Roberts. Testing the Paradigm that Ultraluminous X-Ray Sources as a Class Represent Accreting Intermediate-Mass Black Holes. *ApJ*, 687(1):471–487, Nov. 2008. doi: 10.1086/591722.

M. C. i. Bernadich, A. D. Schwope, K. Kovlakas, A. Zezas, and I. Traulsen. An expanded ultraluminous X-ray source catalogue. *arXiv e-prints*, art. arXiv:2110.14562, Oct. 2021.

B. Binder, J. Gross, B. F. Williams, M. Eracleous, T. J. Gaetz, P. P. Plucinsky, and E. D. Skillman. The Effect of Variability on X-Ray Binary Luminosity Functions: Multiple-epoch Observations of NGC 300 with Chandra. *ApJ*, 834(2):128, Jan 2017. doi: 10.3847/1538-4357/834/2/128.

J. M. Blondin. The Shadow Wind in High-Mass X-Ray Binaries. *ApJ*, 435:756, Nov. 1994. doi: 10.1086/174853.

J. M. Blondin, I. R. Stevens, and T. R. Kallman. Enhanced Winds and Tidal Streams in Massive X-Ray Binaries. *ApJ*, 371:684, Apr. 1991. doi: 10.1086/169934.

V. Braito, J. N. Reeves, G. C. Dewangan, I. George, R. E. Griffiths, A. Markowitz, K. Nandra, D. Porquet, A. Ptak, T. J. Turner, T. Yaqoob, and K. Weaver. Relativistic Iron K Emission and Absorption in the Seyfert 1.9 Galaxy MCG -5-23-16. *ApJ*, 670(2):978–991, Dec. 2007. doi: 10.1086/521916.

M. Brightman. A new ultraluminous X-ray source in NGC 4945. *The Astronomer's Telegram*, 14380: 1, Feb. 2021.

M. Brightman, F. Harrison, D. J. Walton, F. Fuerst, A. Hornschemeier, A. Zezas, M. Bachetti, B. Grefenstette, A. Ptak, S. Tendulkar, and M. Yukita. Spectral and Temporal Properties of the Ultraluminous X-Ray Pulsar in M82 from 15 years of Chandra Observations and Analysis of the Pulsed Emission Using NuSTAR. *ApJ*, 816(2):60, Jan. 2016a. doi: 10.3847/0004-637X/816/2/60.

M. Brightman, F. A. Harrison, D. Barret, S. W. Davis, F. Fürst, K. K. Madsen, M. Middleton, J. M. Miller, D. Stern, L. Tao, and D. J. Walton. A Broadband X-Ray Spectral Study of the Intermediate-mass Black Hole Candidate M82 X-1 with NuSTAR, Chandra, and Swift. *ApJ*, 829(1):28, Sept. 2016b. doi: 10.3847/0004-637X/829/1/28.

M. Brightman, F. A. Harrison, F. Fürst, M. J. Middleton, D. J. Walton, D. Stern, A. C. Fabian, M. Heida, D. Barret, and M. Bachetti. Magnetic field strength of a neutron-star-powered ultraluminous X-ray source. *Nature Astronomy*, 2:312–316, Feb. 2018. doi: 10.1038/s41550-018-0391-6.

M. Brightman, H. Earnshaw, F. Fürst, F. A. Harrison, M. Heida, G. Israel, S. Pike, D. Stern, and D. J. Walton. Swift monitoring of M51: A 38-day super-orbital period for the pulsar ULX7 and a new transient ULX. *arXiv e-prints*, art. arXiv:1912.04431, Dec 2019.

M. Brightman, H. Earnshaw, F. Fürst, F. A. Harrison, M. Heida, G. Israel, S. Pike, D. Stern, and D. J. Walton. Swift Monitoring of M51: A 38 day Superorbital Period for the Pulsar ULX7 and a New Transient Ultraluminous X-Ray Source. *ApJ*, 895(2):127, June 2020. doi: 10.3847/1538-4357/ab7e2a.

M. Brightman, M. Bachetti, H. Earnshaw, F. Fürst, M. Heida, G. L. Israel, S. Pike, D. Stern, and D. J. Walton. Evolution of the spin, spectrum and super-orbital period of the ultraluminous X-ray pulsar M51 ULX7. *arXiv e-prints*, art. arXiv:2111.05342, Nov. 2021.

M. Brightman, M. Bachetti, H. Earnshaw, F. Fürst, M. Heida, G. L. Israel, S. Pike, D. Stern, and D. J. Walton. Evolution of the Spin, Spectrum and Superorbital Period of the Ultraluminous X-Ray Pulsar M51 ULX7. *ApJ*, 925(1):18, Jan. 2022. doi: 10.3847/1538-4357/ac3829.

D. N. Burrows, J. E. Hill, J. A. Nousek, J. A. Kennea, A. Wells, J. P. Osborne, A. F. Abbey, A. Beardmore, K. Mukerjee, A. D. T. Short, G. Chincarini, S. Campana, O. Citterio, A. Moretti, C. Pagani, G. Tagliaferri, P. Giommi, M. Capalbi, F. Tamburelli, L. Angelini, G. Cusumano, H. W. Bräuninger, W. Burkert, and G. D. Hartner. The Swift X-Ray Telescope. *Space Sci. Rev.*, 120 (3-4):165–195, Oct. 2005. doi: 10.1007/s11214-005-5097-2.

M. D. Caballero-García, T. Belloni, and L. Zampieri. Quasi-periodic oscillations and energy spectra from the two brightest Ultra-Luminous X-ray sources in M82. *MNRAS*, 436(4):3262–3270, Dec. 2013. doi: 10.1093/mnras/stt1807.

M. Cappi, F. Tombesi, S. Bianchi, M. Dadina, M. Giustini, G. Malaguti, L. Maraschi, G. G. C. Palumbo, P. O. Petrucci, G. Ponti, C. Vignali, and T. Yaqoob. X-ray evidence for a mildly relativistic and variable outflow in the luminous Seyfert 1 galaxy Mrk 509. *A&A*, 504(2):401–407, Sept. 2009. doi: 10.1051/0004-6361/200912137.

S. Carpano, F. Haberl, C. Maitra, and G. Vasilopoulos. Discovery of pulsations from NGC 300 ULX1 and its fast period evolution. *MNRAS*, 476(1):L45–L49, May 2018. doi: 10.1093/mnrasl/sly030.

W. Cash. Parameter estimation in astronomy through application of the likelihood ratio. *ApJ*, 228: 939–947, Mar 1979. doi: 10.1086/156922.

E. J. M. Colbert and R. F. Mushotzky. The Nature of Accreting Black Holes in Nearby Galaxy Nuclei. *ApJ*, 519(1):89–107, July 1999. doi: 10.1086/307356.

E. J. M. Colbert and A. F. Ptak. A Catalog of Candidate Intermediate-Luminosity X-Ray Objects. *ApJS*, 143(1):25–45, Nov. 2002. doi: 10.1086/342507.

E. Crivellari, A. Wolter, and G. Trinchieri. The Cartwheel galaxy with XMM-Newton. *A&A*, 501: 445–453, July 2009. doi: 10.1051/0004-6361/200810707.

D. Cseh, S. Corbel, P. Kaaret, C. Lang, F. Grisé, Z. Paragi, A. Tzioumis, V. Tudose, and H. Feng. Black Hole Powered Nebulae and a Case Study of the Ultraluminous X-Ray Source IC 342 X-1. *ApJ*, 749(1):17, Apr. 2012. doi: 10.1088/0004-637X/749/1/17.

D. Cseh, P. Kaaret, S. Corbel, F. Grise, C. Lang, E. Kording, H. Falcke, P. G. Jonker, J. C. A. Miller-Jones, S. Farrell, Y. J. Yang, Z. Paragi, and S. Frey. Unveiling recurrent jets of the ULX Holmberg II X-1: evidence for a massive stellar-mass black hole? *MNRAS*, 439:L1–L5, Mar. 2014. doi: 10.1093/mnrasl/slt166.

D. Cseh, J. C. A. Miller-Jones, P. G. Jonker, F. Grisé, Z. Paragi, S. Corbel, H. Falcke, S. Frey, P. Kaaret, and E. Körding. The evolution of a jet ejection of the ultraluminous X-ray source Holmberg II X-1. *MNRAS*, 452(1):24–31, Sept. 2015. doi: 10.1093/mnras/stv1308.

K. C. Dage, S. E. Zepf, M. B. Peacock, A. Bahramian, O. Noroozi, A. Kundu, and T. J. Maccarone. X-ray spectral variability of ultraluminous X-ray sources in extragalactic globular clusters. *MNRAS*, 485(2):1694–1707, May 2019. doi: 10.1093/mnras/stz479.

K. C. Dage, S. E. Zepf, E. Thygesen, A. Bahramian, A. Kundu, T. J. Maccarone, M. B. Peacock, and J. Strader. X-ray spectroscopy of newly identified ULXs associated with M87's globular cluster population. *MNRAS*, 497(1):596–608, Sept. 2020. doi: 10.1093/mnras/staa1963.

A. D'Aì, R. Iaria, T. Di Salvo, A. Riggio, L. Burderi, and N. R. Robba. Chandra X-ray spectroscopy of a clear dip in GX 13+1. *A&A*, 564:A62, Apr. 2014. doi: 10.1051/0004-6361/201322044.

A. D'Aì, C. Pinto, M. Del Santo, F. Pintore, R. Soria, A. Robba, E. Ambrosi, W. Alston, D. Barret, A. C. Fabian, F. Fürst, E. Kara, P. Kosec, M. Middleton, T. Roberts, G. Rodriguez-Castillo, and D. J. Walton. The Chameleon on the branches: spectral state transition and dips in NGC 247 ULX-1. *MNRAS*, 507(4):5567–5579, Nov. 2021. doi: 10.1093/mnras/stab2427.

D. S. Davis and R. F. Mushotzky. XMM-Newton Observations of an Intermediate X-Ray Object in NGC 2276. *ApJ*, 604(2):653–661, Apr. 2004. doi: 10.1086/381929.

A. De Luca, R. Salvaterra, A. Tiengo, D. D'Agostino, M. G. Watson, F. Haberl, and J. Wilms. Science with the EXTraS Project: Exploring the X-Ray Transient and Variable Sky. In N. R. Napolitano, G. Longo, M. Marconi, M. Paolillo, and E. Iodice, editors, *The Universe of Digital Sky Surveys*, volume 42 of *Astrophysics and Space Science Proceedings*, page 291, Jan. 2016. doi: 10.1007/978-3-319-19330-4_46.

A. De Luca, R. Salvaterra, A. Belfiore, S. Carpano, D. D'Agostino, F. Haberl, G. L. Israel, D. Law-Green, G. Lisini, M. Marelli, G. Novara, A. M. Read, G. Rodriguez-Castillo, S. R. Rosen, D. Salvetti, A. Tiengo, G. Vianello, M. G. Watson, C. Delvaux, T. Dickens, P. Esposito, J. Greiner, H. Hämmerle, A. Kreikenbohm, S. Kreykenbohm, M. Oertel, D. Pizzocaro, J. P. Pye, S. Sandrelli, B. Stelzer, J. Wilms, and F. Zagaria. The EXTraS project: Exploring the X-ray transient and variable sky. *A&A*, 650:A167, June 2021. doi: 10.1051/0004-6361/202039783.

B. De Marco, G. Ponti, G. Miniutti, T. Belloni, M. Cappi, M. Dadina, and T. Muñoz-Darias. Time lags in the ultraluminous X-ray source NGC 5408 X-1: implications for the black hole mass. *MNRAS*, 436(4):3782–3791, Dec. 2013. doi: 10.1093/mnras/stt1853.

R. Della Ceca, F. J. Carrera, A. Caccianiga, P. Severgnini, L. Ballo, V. Braito, A. Corral, A. Del Moro, S. Mateos, A. Ruiz, and M. G. Watson. Exploring the active galactic nuclei population with extreme X-ray-to-optical flux ratios (f_x/f_o > 50). *MNRAS*, 447(4):3227–3242, Mar. 2015. doi: 10.1093/mnras/stu2665.

M. Díaz Trigo, A. N. Parmar, L. Boirin, C. Motch, A. Talavera, and S. Balman. Variations in the dip properties of the low-mass X-ray binary XB 1254-690 observed with XMM-Newton and INTEGRAL. *A&A*, 493(1):145–157, Jan. 2009. doi: 10.1051/0004-6361:200810154.

D. Donato, S. B. Cenko, S. Covino, E. Troja, T. Pursimo, C. C. Cheung, O. Fox, A. Kutyrev, S. Campana, D. Fugazza, H. Landt, and N. R. Butler. A Tidal Disruption Event in a nearby Galaxy Hosting an Intermediate Mass Black Hole. *ApJ*, 781(2):59, Feb. 2014. doi: 10.1088/0004-637X/781/2/59.

H. P. Earnshaw, T. P. Roberts, and R. Sathyaprakash. Searching for propeller-phase ULXs in the XMM-Newton Serendipitous Source Catalogue. *MNRAS*, 476(3):4272–4277, May 2018. doi: 10.1093/mnras/sty501.

H. P. Earnshaw, B. W. Grefenstette, M. Brightman, D. J. Walton, D. Barret, F. Fürst, F. A. Harrison, M. Heida, S. N. Pike, D. Stern, and N. A. Webb. A Broadband Look at the Old and New ULXs of NGC 6946. *ApJ*, 881(1):38, Aug. 2019a. doi: 10.3847/1538-4357/ab20cd.

H. P. Earnshaw, T. P. Roberts, M. J. Middleton, D. J. Walton, and S. Mateos. A new, clean catalogue of extragalactic non-nuclear X-ray sources in nearby galaxies. *MNRAS*, 483(4):5554–5573, Mar. 2019b. doi: 10.1093/mnras/sty3403.

H. P. Earnshaw, M. Heida, M. Brightman, F. Fürst, F. A. Harrison, A. Jaodand, M. J. Middleton, T. P. Roberts, R. Sathyaprakash, D. Stern, and D. J. Walton. The (Re)appearance of NGC 925 ULX-3, a New Transient ULX. *ApJ*, 891(2):153, Mar. 2020. doi: 10.3847/1538-4357/ab77b8.

R. Edelson, T. J. Turner, K. Pounds, S. Vaughan, A. Markowitz, H. Marshall, P. Dobbie, and R. Warwick. X-Ray Spectral Variability and Rapid Variability of the Soft X-Ray Spectrum Seyfert 1 Galaxies Arakelian 564 and Ton S180. *ApJ*, 568(2):610–626, Apr 2002. doi: 10.1086/323779.

R. Edgar. A review of Bondi-Hoyle-Lyttleton accretion. *New Astronomy Reviews*, 48(10):843–859, Sept. 2004. doi: 10.1016/j.newar.2004.06.001.

I. El Mellah, J. O. Sundqvist, and R. Keppens. Wind Roche lobe overflow in high-mass X-ray binaries. A possible mass-transfer mechanism for ultraluminous X-ray sources. *A&A*, 622:L3, Feb. 2019. doi: 10.1051/0004-6361/201834543.

P. A. Evans, A. P. Beardmore, K. L. Page, J. P. Osborne, P. T. O'Brien, R. Willingale, R. L. C. Starling, D. N. Burrows, O. Godet, L. Vetere, J. Racusin, M. R. Goad, K. Wiersema, L. Angelini, M. Capalbi, G. Chincarini, N. Gehrels, J. A. Kennea, R. Margutti, D. C. Morris, C. J. Mountford, C. Pagani, M. Perri, P. Romano, and N. Tanvir. Methods and results of an automatic analysis of a complete sample of Swift-XRT observations of GRBs. *MNRAS*, 397(3):1177–1201, Aug. 2009. doi: 10.1111/j.1365-2966.2009.14913.x.

G. Fabbiano. X-rays from normal galaxies. *ARA&A*, 27:87–138, Jan. 1989. doi: 10.1146/annurev.aa.27.090189.000511.

G. Fabbiano, A. Zezas, A. R. King, T. J. Ponman, A. Rots, and F. Schweizer. The Time-variable Ultraluminous X-Ray Sources of "The Antennae". *ApJ*, 584(1):L5–L8, Feb 2003. doi: 10.1086/368174.

A. C. Fabian and M. J. Rees. SS 433: a double jet in action? *MNRAS*, 187:13P–16, Apr. 1979. doi: 10.1093/mnras/187.1.13P.

S. Fabrika. The jets and supercritical accretion disk in SS433. *Astrophys. Space Phys. Res.*, 12: 1–152, Jan. 2004.

S. Fabrika, Y. Ueda, A. Vinokurov, O. Sholukhova, and M. Shidatsu. Supercritical accretion disks in ultraluminous X-ray sources and SS 433. *Nature Physics*, 11(7):551–553, July 2015. doi: 10.1038/nphys3348.

S. N. Fabrika. The Supercritical Accretion Disk of SS 433. *Ap&SS*, 252:439–450, Jan. 1997. doi: 10.1023/A:1000885810366.

S. N. Fabrika, K. E. Atapin, A. S. Vinokurov, and O. N. Sholukhova. Ultraluminous X-Ray Sources. *Astrophysical Bulletin*, 76(1):6–38, Jan. 2021. doi: 10.1134/S1990341321010077.

X. Fan, M. A. Strauss, D. P. Schneider, R. H. Becker, R. L. White, Z. Haiman, M. Gregg, L. Pentericci, E. K. Grebel, V. K. Narayanan, Y.-S. Loh, G. T. Richards, J. E. Gunn, R. H. Lupton, G. R. Knapp, Ž. Ivezić, W. N. Brandt, M. Collinge, L. Hao, D. Harbeck, F. Prada, J. Schaye, I. Strateva, N. Zakamska, S. Anderson, J. Brinkmann, N. A. Bahcall, D. Q. Lamb, S. Okamura, A. Szalay, and D. G. York. A Survey of z>5.7 Quasars in the Sloan Digital Sky Survey. II. Discovery of Three Additional Quasars at z>6. *AJ*, 125(4):1649–1659, Apr. 2003. doi: 10.1086/368246.

S. A. Farrell, N. A. Webb, D. Barret, O. Godet, and J. M. Rodrigues. An intermediate-mass black hole of over 500 solar masses in the galaxy ESO243-49. *Nature*, 460(7251):73–75, July 2009. doi: 10.1038/nature08083.

R. P. Fender, T. M. Belloni, and E. Gallo. Towards a unified model for black hole X-ray binary jets. *MNRAS*, 355(4):1105–1118, Dec. 2004. doi: 10.1111/j.1365-2966.2004.08384.x.

H. Feng and P. Kaaret. Spectral State Transitions of the Ultraluminous X-Ray Sources X-1 and X-2 in NGC 1313. *ApJ*, 650(1):L75–L78, Oct. 2006. doi: 10.1086/508613.

H. Feng and P. Kaaret. Identification of the X-ray Thermal Dominant State in an Ultraluminous X-ray Source in M82. *ApJ*, 712(2):L169–L173, Apr. 2010. doi: 10.1088/2041-8205/712/2/L169.

H. Feng and R. Soria. Ultraluminous X-ray sources in the Chandra and XMM-Newton era. *New Astronomy Reviews*, 55(5):166–183, Nov. 2011. doi: 10.1016/j.newar.2011.08.002.

H. Feng, L. Tao, P. Kaaret, and F. Grisé. Nature of the Soft ULX in NGC 247: Super-Eddington Outflow and Transition between the Supersoft and Soft Ultraluminous Regimes. *ApJ*, 831(2):117, Nov. 2016. doi: 10.3847/0004-637X/831/2/117.

L. Ferrarese and H. Ford. Supermassive Black Holes in Galactic Nuclei: Past, Present and Future Research. *Space Sci. Rev.*, 116(3-4):523–624, Feb. 2005. doi: 10.1007/s11214-005-3947-6.

L. Foschini, G. Di Cocco, L. C. Ho, L. Bassani, M. Cappi, M. Dadina, F. Gianotti, G. Malaguti, F. Panessa, E. Piconcelli, J. B. Stephen, and M. Trifoglio. XMM-Newton observations of ultraluminous X-ray sources in nearby galaxies. *A&A*, 392:817–825, Sept. 2002. doi: 10.1051/0004-6361:20020950.

D. L. Foster, P. A. Charles, and K. Holley-Bockelmann. Interpretation of the 115 Day Periodic Modulation in the X-ray Flux of NGC 5408 X-1. *ApJ*, 725(2):2480–2484, Dec. 2010. doi: 10.1088/0004-637X/725/2/2480.

A. Fruscione, J. C. McDowell, G. E. Allen, N. S. Brickhouse, D. J. Burke, J. E. Davis, N. Durham, M. Elvis, E. C. Galle, D. E. Harris, D. P. Huenemoerder, J. C. Houck, B. Ishibashi, M. Karovska, F. Nicastro, M. S. Noble, M. A. Nowak, F. A. Primini, A. Siemiginowska, R. K. Smith, and M. Wise. CIAO: Chandra's data analysis system. In *Proc. SPIE*, volume 6270 of *Society of Photo-Optical Instrumentation Engineers (SPIE) Conference Series*, page 62701V, Jun 2006. doi: 10.1117/12.671760.

F. Fürst, D. J. Walton, F. A. Harrison, D. Stern, D. Barret, M. Brightman, A. C. Fabian, B. Grefenstette, K. K. Madsen, M. J. Middleton, J. M. Miller, K. Pottschmidt, A. Ptak, V. Rana, and N. Webb. Discovery of Coherent Pulsations from the Ultraluminous X-Ray Source NGC 7793 P13. *ApJ*, 831(2):L14, Nov 2016. doi: 10.3847/2041-8205/831/2/L14.

F. Fürst, D. J. Walton, D. Stern, M. Bachetti, D. Barret, M. Brightman, F. A. Harrison, and V. Rana. Spectral Changes in the Hyperluminous Pulsar in NGC 5907 as a Function of Super-orbital Phase. *ApJ*, 834(1):77, Jan. 2017. doi: 10.3847/1538-4357/834/1/77.

F. Fürst, D. J. Walton, M. Heida, F. A. Harrison, D. Barret, M. Brightman, A. C. Fabian, M. J. Middleton, C. Pinto, V. Rana, F. Tramper, N. Webb, and P. Kretschmar. A tale of two periods: determination of the orbital ephemeris of the super-Eddington pulsar NGC 7793 P13. *A&A*, 616: A186, Sept. 2018. doi: 10.1051/0004-6361/201833292.

D. K. Galloway, A. N. Ajamyan, J. Upjohn, and M. Stuart. Intermittent dipping in a low-mass X-ray binary. *MNRAS*, 461(4):3847–3853, Oct. 2016. doi: 10.1093/mnras/stw1576.

Y. Gao, Q. D. Wang, P. N. Appleton, and R. A. Lucas. Nonnuclear Hyper/Ultraluminous X-Ray Sources in the Starbursting Cartwheel Ring Galaxy. *ApJ*, 596(2):L171–L174, Oct 2003. doi: 10.1086/379598.

N. Gehrels. Confidence Limits for Small Numbers of Events in Astrophysical Data. *ApJ*, 303:336, Apr. 1986. doi: 10.1086/164079.

N. Gehrels, G. Chincarini, P. Giommi, K. O. Mason, J. A. Nousek, A. A. Wells, N. E. White, S. D. Barthelmy, D. N. Burrows, L. R. Cominsky, K. C. Hurley, F. E. Marshall, P. Mészáros, P. W. A. Roming, L. Angelini, L. M. Barbier, T. Belloni, S. Campana, P. A. Caraveo, M. M. Chester, O. Citterio, T. L. Cline, M. S. Cropper, J. R. Cummings, A. J. Dean, E. D. Feigelson, E. E. Fenimore, D. A. Frail, A. S. Fruchter, G. P. Garmire, K. Gendreau, G. Ghisellini, J. Greiner, J. E. Hill, S. D. Hunsberger, H. A. Krimm, S. R. Kulkarni, P. Kumar, F. Lebrun, N. M. Lloyd-Ronning, C. B. Markwardt, B. J. Mattson, R. F. Mushotzky, J. P. Norris, J. Osborne, B. Paczynski, D. M. Palmer, H. S. Park, A. M. Parsons, J. Paul, M. J. Rees, C. S. Reynolds, J. E. Rhoads, T. P. Sasseen, B. E. Schaefer, A. T. Short, A. P. Smale, I. A. Smith, L. Stella, G. Tagliaferri, T. Takahashi, M. Tashiro, L. K. Townsley, J. Tueller, M. J. L. Turner, M. Vietri, W. Voges, M. J. Ward, R. Willingale, F. M. Zerbi, and W. W. Zhang. The Swift Gamma-Ray Burst Mission. *ApJ*, 611(2):1005–1020, Aug. 2004. doi: 10.1086/422091.

S. Gezari. Tidal Disruption Events. *ARA&A*, 59, Sept. 2021. doi: 10.1146/annurev-astro-111720-030029.

T. Ghosh, V. Rana, and M. Bachetti. Hard X-ray flares and spectral variability in NGC 4395 ULX1. *arXiv e-prints*, art. arXiv:2202.01432, Feb. 2022.

J. C. Gladstone and T. P. Roberts. The ultraluminous X-ray source population of NGC 4485/4490. *MNRAS*, 397(1):124–134, Jul 2009. doi: 10.1111/j.1365-2966.2009.14937.x.

J. C. Gladstone, T. P. Roberts, and C. Done. The ultraluminous state. *MNRAS*, 397(4):1836–1851, Aug 2009. doi: 10.1111/j.1365-2966.2009.15123.x.

J. C. Gladstone, C. Copperwheat, C. O. Heinke, T. P. Roberts, T. F. Cartwright, A. J. Levan, and M. R. Goad. Optical Counterparts of the Nearest Ultraluminous X-Ray Sources. *ApJS*, 206(2):14, June 2013. doi: 10.1088/0067-0049/206/2/14.

A. C. Gonçalves and R. Soria. On the weakness of disc models in bright ULXs. *MNRAS*, 371(2): 673–683, Sept. 2006. doi: 10.1111/j.1365-2966.2006.10687.x.

S. A. Grebenev. The nature of the bimodal luminosity distribution of ultraluminous X-ray pulsars. *Astronomy Letters*, 43(7):464–471, Jul 2017. doi: 10.1134/S1063773717050012.

J. E. Greene, J. Strader, and L. C. Ho. Intermediate-Mass Black Holes. *ARA&A*, 58:257–312, Aug. 2020. doi: 10.1146/annurev-astro-032620-021835.

H.-J. Grimm, M. Gilfanov, and R. Sunyaev. High-mass X-ray binaries as a star formation rate indicator in distant galaxies. *MNRAS*, 339:793–809, Mar. 2003. doi: 10.1046/j.1365-8711.2003.06224.x.

V. Grinberg, M. A. Leutenegger, N. Hell, K. Pottschmidt, M. Böck, J. A. García, M. Hanke, M. A. Nowak, J. O. Sundqvist, R. H. D. Townsend, and J. Wilms. Long term variability of Cygnus X-1. VII. Orbital variability of the focussed wind in Cyg X-1/HDE 226868 system. *A&A*, 576:A117, Apr. 2015. doi: 10.1051/0004-6361/201425418.

V. Grinberg, M. A. Nowak, and N. Hell. Color-color diagrams as tools for assessment of the variable absorption in high mass X-ray binaries. *A&A*, 643:A109, Nov. 2020. doi: 10.1051/0004-6361/202039183.

F. Grisé, P. Kaaret, H. Feng, J. J. E. Kajava, and S. A. Farrell. X-ray Spectral State is not Correlated with Luminosity in Holmberg II X-1. *ApJ*, 724(2):L148–L152, Dec. 2010. doi: 10.1088/2041-8205/724/2/L148.

F. Grisé, P. Kaaret, S. Corbel, D. Cseh, and H. Feng. A long-term X-ray monitoring of the ultraluminous X-ray source NGC 5408 X-1 with Swift reveals the presence of dips but no orbital period. *MNRAS*, 433(2):1023–1038, Aug. 2013. doi: 10.1093/mnras/stt783.

A. Gúrpide, O. Godet, F. Koliopanos, N. Webb, and J. F. Olive. Long-term X-ray spectral evolution of ultraluminous X-ray sources: implications on the accretion flow geometry and the nature of the accretor. *A&A*, 649:A104, May 2021a. doi: 10.1051/0004-6361/202039572.

A. Gúrpide, O. Godet, G. Vasilopoulos, N. A. Webb, and J. F. Olive. Discovery of a recurrent spectral evolutionary cycle in the ultra-luminous X-ray sources Holmberg II X-1 and NGC 5204 X-1. *A&A*, 654:A10, Oct. 2021b. doi: 10.1051/0004-6361/202140781.

F. A. Harrison, W. W. Craig, F. E. Christensen, C. J. Hailey, W. W. Zhang, S. E. Boggs, D. Stern, W. R. Cook, K. Forster, P. Giommi, B. W. Grefenstette, Y. Kim, T. Kitaguchi, J. E. Koglin, K. K. Madsen, P. H. Mao, H. Miyasaka, K. Mori, M. Perri, M. J. Pivovaroff, S. Puccetti, V. R. Rana, N. J. Westergaard, J. Willis, A. Zoglauer, H. An, M. Bachetti, N. M. Barrière, E. C. Bellm, V. Bhalerao, N. F. Brejnholt, F. Fuerst, C. C. Liebe, C. B. Markwardt, M. Nynka, J. K. Vogel, D. J. Walton, D. R. Wik, D. M. Alexander, L. R. Cominsky, A. E. Hornschemeier, A. Hornstrup, V. M. Kaspi,

G. M. Madejski, G. Matt, S. Molendi, D. M. Smith, J. A. Tomsick, M. Ajello, D. R. Ballantyne, M. Baloković, D. Barret, F. E. Bauer, R. D. Blandford, W. N. Brandt, L. W. Brenneman, J. Chiang, D. Chakrabarty, J. Chenevez, A. Comastri, F. Dufour, M. Elvis, A. C. Fabian, D. Farrah, C. L. Fryer, E. V. Gotthelf, J. E. Grindlay, D. J. Helfand, R. Krivonos, D. L. Meier, J. M. Miller, L. Natalucci, P. Ogle, E. O. Ofek, A. Ptak, S. P. Reynolds, J. R. Rigby, G. Tagliaferri, S. E. Thorsett, E. Treister, and C. M. Urry. The Nuclear Spectroscopic Telescope Array (NuSTAR) High-energy X-Ray Mission. *ApJ*, 770(2):103, June 2013. doi: 10.1088/0004-637X/770/2/103.

A. Heger and S. E. Woosley. The Nucleosynthetic Signature of Population III. *ApJ*, 567(1):532–543, Mar. 2002. doi: 10.1086/338487.

A. Heger, C. L. Fryer, S. E. Woosley, N. Langer, and D. H. Hartmann. How Massive Single Stars End Their Life. *ApJ*, 591(1):288–300, July 2003. doi: 10.1086/375341.

M. Heida, P. G. Jonker, M. A. P. Torres, E. Kool, M. Servillat, T. P. Roberts, P. J. Groot, D. J. Walton, D. S. Moon, and F. A. Harrison. Near-infrared counterparts of ultraluminous X-ray sources. *MNRAS*, 442(2):1054–1067, Aug. 2014. doi: 10.1093/mnras/stu928.

M. Heida, M. A. P. Torres, P. G. Jonker, M. Servillat, S. Repetto, T. P. Roberts, D. J. Walton, D. S. Moon, and F. A. Harrison. Discovery of a red supergiant counterpart to RX J004722.4-252051, a ULX in NGC 253. *MNRAS*, 453(4):3510–3518, Nov. 2015. doi: 10.1093/mnras/stv1853.

M. Heida, P. G. Jonker, M. A. P. Torres, T. P. Roberts, D. J. Walton, D. S. Moon, D. Stern, and F. A. Harrison. Keck/MOSFIRE spectroscopy of five ULX counterparts. *MNRAS*, 459(1):771–778, June 2016. doi: 10.1093/mnras/stw695.

M. Heida, R. M. Lau, B. Davies, M. Brightman, F. Fürst, B. W. Grefenstette, J. A. Kennea, F. Tramper, D. J. Walton, and F. A. Harrison. Discovery of a Red Supergiant Donor Star in SN2010da/NGC 300 ULX-1. *ApJ*, 883(2):L34, Oct. 2019. doi: 10.3847/2041-8213/ab4139.

L. M. Heil and S. Vaughan. The linear rms-flux relation in an ultraluminous X-ray source. *MNRAS*, 405(1):L86–L89, June 2010. doi: 10.1111/j.1745-3933.2010.00864.x.

L. M. Heil, S. Vaughan, and T. P. Roberts. A systematic study of variability in a sample of ultraluminous X-ray sources. *MNRAS*, 397(2):1061–1072, Aug 2009. doi: 10.1111/j.1365-2966.2009.15068.x.

L. Hernández-García, S. Vaughan, T. P. Roberts, and M. Middleton. X-ray time lags and non-linear variability in the ultraluminous X-ray sources NGC 5408 X-1 and NGC 6946 X-1. *MNRAS*, 453 (3):2877–2884, Nov. 2015. doi: 10.1093/mnras/stv1830.

J. L. Higdon. Wheels of Fire. I. Massive Star Formation in the Cartwheel Ring Galaxy. *ApJ*, 455: 524, Dec. 1995. doi: 10.1086/176602.

J. L. Higdon. Wheels of Fire. II. Neutral Hydrogen in the Cartwheel Ring Galaxy. *ApJ*, 467:241, Aug. 1996. doi: 10.1086/177599.

R. Hirai and I. Mandel. Conditions for accretion disc formation and observability of wind-accreting X-ray binaries. , 38:e056, Nov. 2021. doi: 10.1017/pasa.2021.53.

J. A. Hoffman, H. L. Marshall, and W. H. G. Lewin. Dual character of the rapid burster and a classification of X-ray bursts. *Nature*, 271(5646):630–633, Feb. 1978. doi: 10.1038/271630a0.

C.-P. Hu, K. L. Li, A. K. H. Kong, C. Y. Ng, and L. C.-C. Lin. Swift Detection of a 65 Day X-Ray Period from the Ultraluminous Pulsar NGC 7793 P13. *ApJ*, 835(1):L9, Jan. 2017. doi: 10.3847/2041-8213/835/1/L9.

C.-P. Hu, Y. Ueda, and T. Enoto. Possible Periodic Dips in the Pulsating Ultraluminous X-Ray Source M51 ULX-7. *ApJ*, 909(1):5, Mar. 2021. doi: 10.3847/1538-4357/abd7a5.

D. Huppenkothen, M. Bachetti, A. Stevens, S. Migliari, P. Balm, O. Hammad, U. M. Khan, H. Mishra, H. Rashid, S. Sharma, E. M. Ribeiro, and R. V. Blanco. stingray: A modern python library for spectral timing. *Journal of Open Source Software*, 4(38):1393, 2019a. doi: 10.21105/joss.01393. URL `https://doi.org/10.21105/joss.01393`.

D. Huppenkothen, M. Bachetti, A. L. Stevens, S. Migliari, P. Balm, O. Hammad, U. M. Khan, H. Mishra, H. Rashid, S. Sharma, E. Martinez Ribeiro, and R. Valles Blanco. Stingray: A Modern Python Library for Spectral Timing. *ApJ*, 881(1):39, Aug. 2019b. doi: 10.3847/1538-4357/ab258d.

A. F. Illarionov and R. A. Sunyaev. Why the Number of Galactic X-ray Stars Is so Small? *A&A*, 39: 185, Feb. 1975.

K. Inayoshi, R. Nakatani, D. Toyouchi, T. Hosokawa, R. Kuiper, and M. Onoue. Rapid growth of seed black holes during early bulge formation. *arXiv e-prints*, art. arXiv:2110.10693, Oct. 2021.

A. R. Ingram and S. E. Motta. A review of quasi-periodic oscillations from black hole X-ray binaries: Observation and theory. *New Astronomy Reviews*, 85:101524, Sept. 2019. doi: 10.1016/j.newar.2020.101524.

A. Iovino. Detecting Fainter Compact Groups: Results from a New Automated Algorithm. *AJ*, 124: 2471–2489, Nov. 2002. doi: 10.1086/343059.

J. A. Irwin, A. E. Athey, and J. N. Bregman. X-Ray Spectral Properties of Low-Mass X-Ray Binaries in Nearby Galaxies. *ApJ*, 587(1):356–366, Apr. 2003. doi: 10.1086/368179.

N. Isobe, A. Kubota, K. Makishima, P. Gand hi, R. E. Griffiths, G. C. Dewangan, T. Itoh, and T. Mizuno. Discovery of a Bright Transient Ultraluminous X-Ray Source, Suzaku J1305-4931 in NGC4945. *PASJ*, 60:S241, Jan. 2008. doi: 10.1093/pasj/60.sp1.S241.

G. L. Israel, A. Belfiore, L. Stella, P. Esposito, P. Casella, A. De Luca, M. Marelli, A. Papitto, M. Perri, S. Puccetti, G. A. R. Castillo, D. Salvetti, A. Tiengo, L. Zampieri, D. D'Agostino, J. Greiner, F. Haberl, G. Novara, R. Salvaterra, R. Turolla, M. Watson, J. Wilms, and A. Wolter. An accreting pulsar with extreme properties drives an ultraluminous x-ray source in NGC 5907. *Science*, 355(6327):817–819, Feb 2017a. doi: 10.1126/science.aai8635.

G. L. Israel, A. Papitto, P. Esposito, L. Stella, L. Zampieri, A. Belfiore, G. A. Rodríguez Castillo, A. De Luca, A. Tiengo, F. Haberl, J. Greiner, R. Salvaterra, S. Sandrelli, and G. Lisini. Discovery of a 0.42-s pulsar in the ultraluminous X-ray source NGC 7793 P13. *MNRAS*, 466(1):L48–L52, Mar 2017b. doi: 10.1093/mnrasl/slw218.

G. L. Israel, G. A. Rodriguez Castillo, and UNSEEN Collaboration. The extragalactic population of neutron stars: the ULX paradigm revolution . *Mem. Soc. Astron. Italiana*, 90:216, Jan. 2019.

F. Jansen, D. Lumb, B. Altieri, J. Clavel, M. Ehle, C. Erd, C. Gabriel, M. Guainazzi, P. Gondoin, R. Much, R. Munoz, M. Santos, N. Schartel, D. Texier, and G. Vacanti. XMM-Newton observatory. I. The spacecraft and operations. *A&A*, 365:L1–L6, Jan. 2001. doi: 10.1051/0004-6361:20000036.

M. Jaroszynski, M. A. Abramowicz, and B. Paczynski. Supercritical accretion disks around black holes. *Acta Astronomica*, 30(1):1–34, Jan. 1980.

V. Jithesh. Spectral and temporal properties of ultra-luminous X-ray source NGC 55 ULX1. *MNRAS*, 509(4):5166–5178, Feb. 2022. doi: 10.1093/mnras/stab3307.

P. Kaaret and H. Feng. X-ray Monitoring of Ultraluminous X-ray Sources. *ApJ*, 702(2):1679–1682, Sept. 2009. doi: 10.1088/0004-637X/702/2/1679.

P. Kaaret, M. G. Simet, and C. C. Lang. A 62 Day X-Ray Periodicity and an X-Ray Flare from the Ultraluminous X-Ray Source in M82. *ApJ*, 646(1):174–183, July 2006. doi: 10.1086/504830.

P. Kaaret, H. Feng, and T. P. Roberts. Ultraluminous X-Ray Sources. *ARA&A*, 55(1):303–341, Aug 2017. doi: 10.1146/annurev-astro-091916-055259.

P. M. W. Kalberla, W. B. Burton, D. Hartmann, E. M. Arnal, E. Bajaja, R. Morras, and W. G. L. Poeppel. VizieR Online Data Catalog: Leiden/Argentine/Bonn (LAB) Survey of Galactic HI (Kalberla+ 2005). *VizieR Online Data Catalog*, art. VIII/76, Jul 2005.

E. Kara, C. Pinto, D. J. Walton, W. N. Alston, M. Bachetti, D. Barret, M. Brightman, C. R. Canizares, H. P. Earnshaw, A. C. Fabian, F. Fürst, P. Kosec, M. J. Middleton, T. P. Roberts, R. Soria, L. Tao, and N. A. Webb. Discovery of a soft X-ray lag in the ultraluminous X-ray source NGC 1313 X-1. *MNRAS*, 491(4):5172–5178, Feb. 2020. doi: 10.1093/mnras/stz3318.

S. Karino, K. Nakamura, and A. Taani. Stellar wind accretion and accretion disk formation: Applications to neutron star high-mass X-ray binaries. *PASJ*, 71(3):58, June 2019. doi: 10.1093/pasj/psz034.

T. Kawashima, K. Ohsuga, S. Mineshige, T. Yoshida, D. Heinzeller, and R. Matsumoto. Comptonized Photon Spectra of Supercritical Black Hole Accretion Flows with Application to Ultraluminous X-Ray Sources. *ApJ*, 752(1):18, June 2012. doi: 10.1088/0004-637X/752/1/18.

D.-W. Kim and G. Fabbiano. Chandra X-Ray Observations of NGC 1316 (Fornax A). *ApJ*, 586(2): 826–849, Apr 2003. doi: 10.1086/367930.

A. King and J.-P. Lasota. ULXs: Neutron stars versus black holes. *MNRAS*, 458(1):L10–L13, May 2016. doi: 10.1093/mnrasl/slw011.

A. King, J.-P. Lasota, and W. Kluźniak. Pulsing ULXs: tip of the iceberg? *MNRAS*, 468(1):L59–L62, June 2017. doi: 10.1093/mnrasl/slx020.

A. R. King. Accretion rates and beaming in ultraluminous X-ray sources. *MNRAS*, 385(1):L113–L115, Mar. 2008. doi: 10.1111/j.1745-3933.2008.00444.x.

A. R. King. Masses, beaming and Eddington ratios in ultraluminous X-ray sources. *MNRAS*, 393 (1):L41–L44, Feb. 2009. doi: 10.1111/j.1745-3933.2008.00594.x.

A. R. King and K. A. Pounds. Black hole winds. *MNRAS*, 345(2):657–659, Oct. 2003. doi: 10.1046/j.1365-8711.2003.06980.x.

A. R. King, M. B. Davies, M. J. Ward, G. Fabbiano, and M. Elvis. Ultraluminous X-Ray Sources in External Galaxies. *ApJ*, 552(2):L109–L112, May 2001. doi: 10.1086/320343.

W. Kluzniak and J. P. Lasota. An ultraluminous nascent millisecond pulsar. *MNRAS*, 448:L43–L47, Mar. 2015. doi: 10.1093/mnrasl/slu200.

F. Koliopanos, G. Vasilopoulos, O. Godet, M. Bachetti, N. A. Webb, and D. Barret. ULX spectra revisited: Accreting, highly magnetized neutron stars as the engines of ultraluminous X-ray sources. *A&A*, 608:A47, Dec. 2017. doi: 10.1051/0004-6361/201730922.

E. Körding, H. Falcke, and S. Markoff. Population X: Are the super-Eddington X-ray sources beamed jets in microblazars or intermediate mass black holes? *A&A*, 382:L13–L16, Jan. 2002. doi: 10.1051/0004-6361:20011776.

P. Kosec, C. Pinto, A. C. Fabian, and D. J. Walton. Searching for outflows in ultraluminous X-ray sources through high-resolution X-ray spectroscopy. *MNRAS*, 473(4):5680–5697, Feb. 2018a. doi: 10.1093/mnras/stx2695.

P. Kosec, C. Pinto, D. J. Walton, A. C. Fabian, M. Bachetti, M. Brightman, F. Fürst, and B. W. Grefenstette. Evidence for a variable Ultrafast Outflow in the newly discovered Ultraluminous Pulsar NGC 300 ULX-1. *MNRAS*, 479(3):3978–3986, Sept. 2018b. doi: 10.1093/mnras/sty1626.

P. Kosec, C. Pinto, C. S. Reynolds, M. Guainazzi, E. Kara, D. J. Walton, A. C. Fabian, M. L. Parker, and I. Valtchanov. Ionised Emission and Absorption in a Large Sample of Ultraluminous X-ray Sources. *arXiv e-prints*, art. arXiv:2109.14683, Sept. 2021.

C. Kouveliotou, J. van Paradijs, G. J. Fishman, M. S. Briggs, J. Kommers, B. A. Harmon, C. A. Meegan, and W. H. G. Lewin. A new type of transient high-energy source in the direction of the Galactic Centre. *Nature*, 379(6568):799–801, Feb. 1996. doi: 10.1038/379799a0.

K. Kovlakas, A. Zezas, J. J. Andrews, A. Basu-Zych, T. Fragos, A. Hornschemeier, B. Lehmer, and A. Ptak. A census of ultraluminous X-ray sources in the local Universe. *MNRAS*, 498(4): 4790–4810, Nov. 2020. doi: 10.1093/mnras/staa2481.

A. Kubota, Y. Tanaka, K. Makishima, Y. Ueda, T. Dotani, H. Inoue, and K. Yamaoka. Evidence for a Black Hole in the X-Ray Transient GRS 1009-45. *PASJ*, 50:667–673, Dec. 1998. doi: 10.1093/pasj/50.6.667.

A. Kubota, T. Mizuno, K. Makishima, Y. Fukazawa, J. Kotoku, T. Ohnishi, and M. Tashiro. Discovery of Spectral Transitions from Two Ultraluminous Compact X-Ray Sources in IC 342. *ApJ*, 547(2): L119–L122, Feb 2001. doi: 10.1086/318903.

V. La Parola, A. D'Aí, G. Cusumano, and T. Mineo. Swift-XRT six-year monitoring of the ultraluminous X-ray source M33 X-8. *A&A*, 580:A71, Aug. 2015. doi: 10.1051/0004-6361/201425384.

M. A. Lara-López, I. A. Zinchenko, L. S. Pilyugin, M. L. P. Gunawardhana, O. López-Cruz, S. P. O. Sullivan, A. Feltre, M. Rosado, M. Sánchez-Cruces, J. Chevallard, M. E. De Rossi, S. Dib, J. Fritz, I. Fuentes-Carrera, L. E. Garduño, and E. Ibar. Metal-THINGS: On the Metallicity and Ionization of ULX Sources in NGC 925. *ApJ*, 906(1):42, Jan. 2021. doi: 10.3847/1538-4357/abc892.

J. P. Lasota, T. Alexander, G. Dubus, D. Barret, S. A. Farrell, N. Gehrels, O. Godet, and N. A. Webb. The Origin of Variability of the Intermediate-mass Black-hole ULX System HLX-1 in ESO 243-49. *ApJ*, 735(2):89, July 2011. doi: 10.1088/0004-637X/735/2/89.

D. Lin, J. Strader, E. R. Carrasco, D. Page, A. J. Romanowsky, J. Homan, J. A. Irwin, R. A. Remillard, O. Godet, N. A. Webb, H. Baumgardt, R. Wijnands, D. Barret, P.-A. Duc, J. P. Brodie, and S. D. J. Gwyn. A luminous X-ray outburst from an intermediate-mass black hole in an off-centre star cluster. *Nature Astronomy*, 2:656–661, June 2018. doi: 10.1038/s41550-018-0493-1.

L. C.-C. Lin, C.-P. Hu, A. K. H. Kong, D. C.-C. Yen, J. Takata, and Y. Chou. Long-term X-ray variability of ultraluminous X-ray sources. *MNRAS*, 454(2):1644–1657, Dec. 2015. doi: 10.1093/mnras/stv2025.

L. C.-C. Lin, C.-P. Hu, K.-L. Li, J. Takata, D. C.-C. Yen, K. Kwak, Y.-M. Kim, and A. K. H. Kong. Investigation of X-ray timing and spectral properties of ESO 243-49 HLX-1 with long-term Swift monitoring. *MNRAS*, 491(4):5682–5692, Feb. 2020. doi: 10.1093/mnras/stz3372.

V. M. Lipunov and N. I. Shakura. Interaction of the accretion disk with the magnetic field of a neutron star. *Soviet Astronomy Letters*, 6:14–17, Feb. 1980.

J.-F. Liu and J. N. Bregman. Ultraluminous X-Ray Sources in Nearby Galaxies from ROSAT High Resolution Imager Observations I. Data Analysis. *ApJS*, 157(1):59–125, Mar. 2005. doi: 10.1086/427170.

J.-F. Liu, J. N. Bregman, Y. Bai, S. Justham, and P. Crowther. Puzzling accretion onto a black hole in the ultraluminous X-ray source M 101 ULX-1. *Nature*, 503(7477):500–503, Nov 2013. doi: 10.1038/nature12762.

Q. Z. Liu and I. F. Mirabel. A catalogue of ultraluminous X-ray sources in external galaxies. *A&A*, 429:1125–1129, Jan. 2005. doi: 10.1051/0004-6361:20041878.

N. R. Lomb. Least-Squares Frequency Analysis of Unequally Spaced Data. *Ap&SS*, 39(2):447–462, Feb. 1976. doi: 10.1007/BF00648343.

K. S. Long, S. Dodorico, P. A. Charles, and M. A. Dopita. Observations of the X-ray sources in the nearby SC galaxy M 33. *ApJ*, 246:L61–L64, June 1981. doi: 10.1086/183553.

W. Luangtip, T. P. Roberts, and C. Done. The X-ray spectral evolution of the ultraluminous X-ray source Holmberg IX X-1. *MNRAS*, 460(4):4417–4432, Aug. 2016. doi: 10.1093/mnras/stw1282.

R. Lucke, D. Yentis, H. Friedman, G. Fritz, and S. Shulman. Discovery of X-ray pulsations in SMC X-1. *ApJ*, 206:L25–L28, May 1976. doi: 10.1086/182125.

O. L. Lupie and K. H. Nordsieck. Visible and Infrared Continuum Spectropolarimetric Observations of Ten OB Supergiant and O Emission-Line Stars. *AJ*, 93:214, Jan. 1987. doi: 10.1086/114302.

R. Lynds and A. Toomre. On the interpretation of ring galaxies: the binary ring system II Hz 4. *ApJ*, 209:382–388, Oct. 1976. doi: 10.1086/154730.

Y. E. Lyubarskii and R. A. Syunyaev. Accretion Column Structure. *Soviet Astronomy Letters*, 14: 390, Sept. 1988.

K. K. Madsen, A. P. Beardmore, K. Forster, M. Guainazzi, H. L. Marshall, E. D. Miller, K. L. Page, and M. Stuhlinger. IACHEC Cross-calibration of Chandra, NuSTAR, Swift, Suzaku, XMM-Newton with 3C 273 and PKS 2155-304. *AJ*, 153(1):2, Jan. 2017. doi: 10.3847/1538-3881/153/1/2.

K. Makishima, A. Kubota, T. Mizuno, T. Ohnishi, M. Tashiro, Y. Aruga, K. Asai, T. Dotani, K. Mitsuda, Y. Ueda, S. Uno, K. Yamaoka, K. Ebisawa, Y. Kohmura, and K. Okada. The Nature of Ultraluminous Compact X-Ray Sources in Nearby Spiral Galaxies. *ApJ*, 535(2):632–643, Jun 2000. doi: 10.1086/308868.

W. P. Maksym, M. P. Ulmer, M. C. Eracleous, L. Guennou, and L. C. Ho. A tidal flare candidate in Abell 1795. *MNRAS*, 435(3):1904–1927, Nov. 2013. doi: 10.1093/mnras/stt1379.

M. Mapelli, B. Moore, L. Giordano, L. Mayer, M. Colpi, E. Ripamonti, and S. Callegari. Intermediate-mass black holes and ultraluminous X-ray sources in the Cartwheel ring galaxy. *MNRAS*, 383(1): 230–246, Jan 2008. doi: 10.1111/j.1365-2966.2007.12534.x.

M. Mapelli, M. Colpi, and L. Zampieri. Low metallicity and ultra-luminous X-ray sources in the Cartwheel galaxy. *MNRAS*, 395(1):L71–L75, May 2009. doi: 10.1111/j.1745-3933.2009.00645.x.

M. Mapelli, E. Ripamonti, L. Zampieri, M. Colpi, and A. Bressan. Ultra-luminous X-ray sources and remnants of massive metal-poor stars. *MNRAS*, 408(1):234–253, Oct. 2010. doi: 10.1111/j.1365-2966.2010.17048.x.

B. Margon and S. F. Anderson. Ten Years of SS 433 Kinematics. *ApJ*, 347:448, Dec. 1989. doi: 10.1086/168132.

Y. D. Mayya, D. Bizyaev, R. Romano, J. A. Garcia-Barreto, and E. I. Vorobyov. The Detection of Nonthermal Radio Continuum Spokes and the Study of Star Formation in the Cartwheel. *ApJ*, 620 (1):L35–L38, Feb. 2005. doi: 10.1086/428400.

M. J. Middleton, T. P. Roberts, C. Done, and F. E. Jackson. Challenging times: a re-analysis of NGC 5408 X-1. *MNRAS*, 411(1):644–652, Feb. 2011a. doi: 10.1111/j.1365-2966.2010.17712.x.

M. J. Middleton, A. D. Sutton, and T. P. Roberts. X-ray spectral evolution in the ultraluminous X-ray source M33 X-8. *MNRAS*, 417(1):464–471, Oct. 2011b. doi: 10.1111/j.1365-2966.2011.19285.x.

M. J. Middleton, D. J. Walton, T. P. Roberts, and L. Heil. Broad absorption features in wind-dominated ultraluminous X-ray sources? *MNRAS*, 438(1):L51–L55, Feb. 2014. doi: 10.1093/mnrasl/slt157.

M. J. Middleton, L. Heil, F. Pintore, D. J. Walton, and T. P. Roberts. A spectral-timing model for ULXs in the supercritical regime. *MNRAS*, 447(4):3243–3263, Mar. 2015a. doi: 10.1093/mnras/stu2644.

M. J. Middleton, D. J. Walton, A. Fabian, T. P. Roberts, L. Heil, C. Pinto, G. Anderson, and A. Sutton. Diagnosing the accretion flow in ultraluminous X-ray sources using soft X-ray atomic features. *MNRAS*, 454(3):3134–3142, Dec 2015b. doi: 10.1093/mnras/stv2214.

M. J. Middleton, D. J. Walton, A. Fabian, T. P. Roberts, L. Heil, C. Pinto, G. Anderson, and A. Sutton. Diagnosing the accretion flow in ultraluminous X-ray sources using soft X-ray atomic features. *MNRAS*, 454(3):3134–3142, Dec 2015c. doi: 10.1093/mnras/stv2214.

M. J. Middleton, P. C. Fragile, M. Bachetti, M. Brightman, Y. F. Jiang, W. C. G. Ho, T. P. Roberts, A. R. Ingram, T. Dauser, C. Pinto, D. J. Walton, F. Fuerst, A. C. Fabian, and N. Gehrels. Lense-Thirring precession in ULXs as a possible means to constrain the neutron star equation of state. *MNRAS*, 475(1):154–166, Mar. 2018. doi: 10.1093/mnras/stx2986.

M. J. Middleton, P. C. Fragile, A. Ingram, and T. P. Roberts. The Lense-Thirring timing-accretion plane for ULXs. *MNRAS*, 489(1):282–296, Oct. 2019. doi: 10.1093/mnras/stz2005.

M. J. Middleton, D. J. Walton, W. Alston, T. Dauser, S. Eikenberry, Y. F. Jiang, A. C. Fabian, F. Fuerst, M. Brightman, H. Marshall, M. Parker, C. Pinto, F. A. Harrison, M. Bachetti, D. Altamirano, A. J. Bird, G. Perez, J. Miller-Jones, P. Charles, S. Boggs, F. Christensen, W. Craig, K. Forster, B. Grefenstette, C. Hailey, K. Madsen, D. Stern, and W. Zhang. NuSTAR reveals the hidden nature of SS433. *MNRAS*, 506(1):1045–1058, Sept. 2021. doi: 10.1093/mnras/stab1280.

M. C. Miller and D. P. Hamilton. Production of intermediate-mass black holes in globular clusters. *MNRAS*, 330(1):232–240, Feb. 2002. doi: 10.1046/j.1365-8711.2002.05112.x.

S. Mineo, M. Gilfanov, and R. Sunyaev. X-ray emission from star-forming galaxies - I. High-mass X-ray binaries. *MNRAS*, 419(3):2095–2115, Jan. 2012. doi: 10.1111/j.1365-2966.2011.19862.x.

S. Mineo, S. Rappaport, A. Levine, D. Pooley, B. Steinhorn, and J. Homan. A Comprehensive X-Ray and Multiwavelength Study of the Colliding Galaxy Pair NGC 2207/IC 2163. *ApJ*, 797(2):91, Dec. 2014. doi: 10.1088/0004-637X/797/2/91.

G. Miniutti, R. D. Saxton, M. Giustini, K. D. Alexander, R. P. Fender, I. Heywood, I. Monageng, M. Coriat, A. K. Tzioumis, A. M. Read, C. Knigge, P. Gandhi, M. L. Pretorius, and B. Agís-González. Nine-hour X-ray quasi-periodic eruptions from a low-mass black hole galactic nucleus. *Nature*, 573(7774):381–384, Sept. 2019. doi: 10.1038/s41586-019-1556-x.

K. Mitsuda, H. Inoue, K. Koyama, K. Makishima, M. Matsuoka, Y. Ogawara, N. Shibazaki, K. Suzuki, Y. Tanaka, and T. Hirano. Energy spectra of low-mass binary X-ray sources observed from Tenma. *PASJ*, 36:741–759, Jan. 1984.

S. Mondal, K. Belczyński, G. Wiktorowicz, J.-P. Lasota, and A. R. King. The connection between merging double compact objects and the ultraluminous X-ray sources. *MNRAS*, 491(2):2747–2759, Jan. 2020a. doi: 10.1093/mnras/stz3227.

S. Mondal, A. Różańska, E. V. Lai, and B. De Marco. An extreme ultraluminous X-ray source X-1 in NGC 5055. *A&A*, 642:A94, Oct. 2020b. doi: 10.1051/0004-6361/202038684.

S. Mondal, A. Różańska, P. Bagińska, A. Markowitz, and B. De Marco. Spectral state transitions in Circinus ULX5. *A&A*, 651:A54, July 2021a. doi: 10.1051/0004-6361/202140459.

S. Mondal, A. Różańska, B. De Marco, and A. Markowitz. Evidence for Fe K_α line and soft X-ray lag in NGC 7456 ultraluminous X-ray source-1. *MNRAS*, 505(1):L106–L111, July 2021b. doi: 10.1093/mnrasl/slab061.

A. Moretti, S. Campana, D. Lazzati, and G. Tagliaferri. The Resolved Fraction of the Cosmic X-Ray Background. *ApJ*, 588(2):696–703, May 2003. doi: 10.1086/374335.

E. H. Morgan, R. A. Remillard, and J. Greiner. RXTE Observations of QPOs in the Black Hole Candidate GRS 1915+105. *ApJ*, 482(2):993–1010, June 1997. doi: 10.1086/304191.

C. Motch, M. W. Pakull, R. Soria, F. Grisé, and G. Pietrzyński. A mass of less than 15 solar masses for the black hole in an ultraluminous X-ray source. *Nature*, 514(7521):198–201, Oct. 2014. doi: 10.1038/nature13730.

S. E. Motta, T. Munoz-Darias, A. Sanna, R. Fender, T. Belloni, and L. Stella. Black hole spin measurements through the relativistic precession model: XTE J1550-564. *MNRAS*, 439:L65–L69, Mar. 2014. doi: 10.1093/mnrasl/slt181.

S. E. Motta, M. Marelli, F. Pintore, P. Esposito, R. Salvaterra, A. De Luca, G. L. Israel, A. Tiengo, and G. A. R. Castillo. The Slow Heartbeats of an Ultraluminous X-Ray Source in NGC 3621. *ApJ*, 898(2):174, Aug. 2020. doi: 10.3847/1538-4357/ab9b81.

P. Mucciarelli, P. Casella, T. Belloni, L. Zampieri, and P. Ranalli. A variable Quasi-Periodic Oscillation in M82 X-1. Timing and spectral analysis of XMM-Newton and RossiXTE observations. *MNRAS*, 365(4):1123–1130, Feb. 2006. doi: 10.1111/j.1365-2966.2005.09754.x.

A. A. Mushtukov, V. F. Suleimanov, S. S. Tsygankov, and J. Poutanen. On the maximum accretion luminosity of magnetized neutron stars: connecting X-ray pulsars and ultraluminous X-ray sources. *MNRAS*, 454(3):2539–2548, Dec. 2015. doi: 10.1093/mnras/stv2087.

A. A. Mushtukov, V. F. Suleimanov, S. S. Tsygankov, and A. Ingram. Optically thick envelopes around ULXs powered by accreating neutron stars. *MNRAS*, 467(1):1202–1208, May 2017. doi: 10.1093/mnras/stx141.

A. A. Mushtukov, A. Ingram, M. Middleton, D. I. Nagirner, and M. van der Klis. Timing properties of ULX pulsars: optically thick envelopes and outflows. *MNRAS*, 484(1):687–697, Mar. 2019. doi: 10.1093/mnras/sty3525.

S. Naik, B. Paul, and Z. Ali. X-Ray Spectroscopy of the High-mass X-Ray Binary Pulsar Centaurus X-3 over Its Binary Orbit. *ApJ*, 737(2):79, Aug. 2011. doi: 10.1088/0004-637X/737/2/79.

K. Nandra, I. M. George, R. F. Mushotzky, T. J. Turner, and T. Yaqoob. ASCA Observations of Seyfert 1 Galaxies. I. Data Analysis, Imaging, and Timing. *ApJ*, 476(1):70–82, Feb. 1997. doi: 10.1086/303600.

K. Nandra, D. Barret, X. Barcons, A. Fabian, J.-W. den Herder, L. Piro, M. Watson, C. Adami, J. Aird, J. M. Afonso, D. Alexander, C. Argiroffi, L. Amati, M. Arnaud, J.-L. Atteia, M. Audard, C. Badenes, J. Ballet, L. Ballo, A. Bamba, A. Bhardwaj, E. Stefano Battistelli, W. Becker, M. De Becker, E. Behar, S. Bianchi, V. Biffi, L. Bîrzan, F. Bocchino, S. Bogdanov, L. Boirin, T. Boller, S. Borgani, K. Borm, N. Bouché, H. Bourdin, R. Bower, V. Braito, E. Branchini, G. Branduardi-Raymont, J. Bregman, L. Brenneman, M. Brightman, M. Brüggen, J. Buchner, E. Bulbul, M. Brusa, M. Bursa, A. Caccianiga, E. Cackett, S. Campana, N. Cappelluti, M. Cappi, F. Carrera, M. Ceballos, F. Christensen, Y.-H. Chu, E. Churazov, N. Clerc, S. Corbel, A. Corral, A. Comastri, E. Costantini, J. Croston, M. Dadina, A. D'Ai, A. Decourchelle, R. Della Ceca, K. Dennerl, K. Dolag, C. Done, M. Dovciak, J. Drake, D. Eckert, A. Edge, S. Ettori, Y. Ezoe, E. Feigelson, R. Fender, C. Feruglio, A. Finoguenov, F. Fiore, M. Galeazzi, S. Gallagher, P. Gandhi, M. Gaspari, F. Gastaldello, A. Georgakakis, I. Georgantopoulos, M. Gilfanov, M. Gitti, R. Gladstone, R. Goosmann, E. Gosset, N. Grosso, M. Guedel, M. Guerrero, F. Haberl, M. Hardcastle, S. Heinz, A. Alonso Herrero, A. Hervé, M. Holmstrom, K. Iwasawa, P. Jonker, J. Kaastra, E. Kara, V. Karas, J. Kastner, A. King, D. Kosenko, D. Koutroumpa, R. Kraft, I. Kreykenbohm, R. Lallement, G. Lanzuisi, J. Lee, M. Lemoine-Goumard, A. Lobban, G. Lodato, L. Lovisari, S. Lotti, I. McCharthy, B. McNamara, A. Maggio, R. Maiolino, B. De Marco, D. de Martino, S. Mateos,

G. Matt, B. Maughan, P. Mazzotta, M. Mendez, A. Merloni, G. Micela, M. Miceli, R. Mignani, J. Miller, G. Miniutti, S. Molendi, R. Montez, A. Moretti, C. Motch, Y. Nazé, J. Nevalainen, F. Nicastro, P. Nulsen, T. Ohashi, P. O'Brien, J. Osborne, L. Oskinova, F. Pacaud, F. Paerels, M. Page, I. Papadakis, G. Pareschi, R. Petre, P.-O. Petrucci, E. Piconcelli, I. Pillitteri, C. Pinto, J. de Plaa, E. Pointecouteau, T. Ponman, G. Ponti, D. Porquet, K. Pounds, G. Pratt, P. Predehl, D. Proga, D. Psaltis, D. Rafferty, M. Ramos-Ceja, P. Ranalli, E. Rasia, A. Rau, G. Rauw, N. Rea, A. Read, J. Reeves, T. Reiprich, M. Renaud, C. Reynolds, G. Risaliti, J. Rodriguez, P. Rodriguez Hidalgo, M. Roncarelli, D. Rosario, M. Rossetti, A. Rozanska, E. Rovilos, R. Salvaterra, M. Salvato, T. Di Salvo, J. Sanders, J. Sanz-Forcada, K. Schawinski, J. Schaye, A. Schwope, S. Sciortino, P. Severgnini, F. Shankar, D. Sijacki, S. Sim, C. Schmid, R. Smith, A. Steiner, B. Stelzer, G. Stewart, T. Strohmayer, L. Strüder, M. Sun, Y. Takei, V. Tatischeff, A. Tiengo, F. Tombesi, G. Trinchieri, T. G. Tsuru, A. Ud-Doula, E. Ursino, L. Valencic, E. Vanzella, S. Vaughan, C. Vignali, J. Vink, F. Vito, M. Volonteri, D. Wang, N. Webb, R. Willingale, J. Wilms, M. Wise, D. Worrall, A. Young, L. Zampieri, J. In't Zand, S. Zane, A. Zezas, Y. Zhang, and I. Zhuravleva. The Hot and Energetic Universe: A White Paper presenting the science theme motivating the Athena+ mission. *arXiv e-prints*, art. arXiv:1306.2307, June 2013.

W. W. Ober, M. F. El Eid, and K. J. Fricke. Evolution of Massive Pregalactic Stars - Part Two - Nucleosynthesis in Pair Creation Supernovae and Pregalactic Enrichment. *A&A*, 119:61, Mar. 1983.

K. Ohsuga and S. Mineshige. Why Is Supercritical Disk Accretion Feasible? *ApJ*, 670(2):1283–1290, Dec. 2007. doi: 10.1086/522324.

K. Ohsuga and S. Mineshige. Global Structure of Three Distinct Accretion Flows and Outflows around Black Holes from Two-dimensional Radiation-magnetohydrodynamic Simulations. *ApJ*, 736(1):2, July 2011. doi: 10.1088/0004-637X/736/1/2.

K. Ohsuga, S. Mineshige, M. Mori, and Y. Kato. Global Radiation-Magnetohydrodynamic Simulations of Black-Hole Accretion Flow and Outflow: Unified Model of Three States. *PASJ*, 61(3): L7–L11, June 2009. doi: 10.1093/pasj/61.3.L7.

M. Orlandini, V. Doroshenko, L. Zampieri, E. Bozzo, A. Baykal, P. Blay, M. Chernyakova, R. Corbet, A. D'Aì, T. Enoto, C. Ferrigno, M. Finger, D. Klochkov, I. Kreykenbohm, S. C. Inam, P. Jenke, J. C. Leyder, N. Masetti, A. Manousakis, T. Mihara, B. Paul, K. Postnov, P. Reig, P. Romano, A. Santangelo, N. Shakura, R. Staubert, J. M. Torrejón, R. Walter, J. Wilms, and C. Wilson-Hodge. Probing stellar winds and accretion physics in high-mass X-ray binaries and ultra-luminous X-ray sources with LOFT. *arXiv e-prints*, art. arXiv:1501.02777, Jan. 2015.

P. Padovani, D. M. Alexander, R. J. Assef, B. De Marco, P. Giommi, R. C. Hickox, G. T. Richards, V. Smolčić, E. Hatziminaoglou, V. Mainieri, and M. Salvato. Active galactic nuclei: what's in a name? *A&A Rev.*, 25(1):2, Aug. 2017. doi: 10.1007/s00159-017-0102-9.

M. W. Pakull and L. Mirioni. Optical Counterparts of Ultraluminous X-Ray Sources. *arXiv e-prints*, art. astro-ph/0202488, Feb. 2002.

M. W. Pakull and L. Mirioni. Bubble Nebulae around Ultraluminous X-Ray Sources. In J. Arthur and W. J. Henney, editors, *Revista Mexicana de Astronomia y Astrofisica Conference Series*, volume 15 of *Revista Mexicana de Astronomia y Astrofisica Conference Series*, pages 197–199, Jan. 2003.

M. W. Pakull, R. Soria, and C. Motch. A 300-parsec-long jet-inflated bubble around a powerful microquasar in the galaxy NGC 7793. *Nature*, 466(7303):209–212, Jul 2010. doi: 10.1038/nature09168.

A. N. Parmar, N. E. White, P. Giommi, and M. Gottwald. The Discovery of 3.8 Hour Periodic Intensity Dips and Eclipses from the Transient Low-Mass X-Ray Binary EXO 0748-676. *ApJ*, 308:199, Sept. 1986. doi: 10.1086/164490.

D. R. Pasham, T. E. Strohmayer, and R. F. Mushotzky. A 400-solar-mass black hole in the galaxy M82. *Nature*, 513(7516):74–76, Sept. 2014. doi: 10.1038/nature13710.

W. D. Pence, S. L. Snowden, K. Mukai, and K. D. Kuntz. Chandra X-Ray Sources in M101. *ApJ*, 561(1):189–202, Nov. 2001. doi: 10.1086/323240.

C. Pinto, M. J. Middleton, and A. C. Fabian. Resolved atomic lines reveal outflows in two ultraluminous X-ray sources. *Nature*, 533(7601):64–67, May 2016. doi: 10.1038/nature17417.

C. Pinto, W. Alston, R. Soria, M. J. Middleton, D. J. Walton, A. D. Sutton, A. C. Fabian, H. Earnshaw, R. Urquhart, E. Kara, and T. P. Roberts. From ultraluminous X-ray sources to ultraluminous supersoft sources: NGC 55 ULX, the missing link. *MNRAS*, 468(3):2865–2883, July 2017. doi: 10.1093/mnras/stx641.

C. Pinto, R. Soria, D. J. Walton, A. D'Aì, F. Pintore, P. Kosec, W. N. Alston, F. Fuerst, M. J. Middleton, T. P. Roberts, M. Del Santo, D. Barret, E. Ambrosi, A. Robba, H. Earnshaw, and A. C. Fabian. XMM-Newton campaign on the ultraluminous X-ray source NGC 247 ULX-1: outflows. *MNRAS*, 505(4):5058–5074, Aug. 2021. doi: 10.1093/mnras/stab1648.

F. Pintore and L. Zampieri. Six years of XMM-Newton observations of NGC 1313 X-1 and X-2. *Astronomische Nachrichten*, 332(4):337, May 2011. doi: 10.1002/asna.201011494.

F. Pintore, L. Zampieri, A. Wolter, and T. Belloni. Ultraluminous X-ray sources: a deeper insight into their spectral evolution. *MNRAS*, 439(4):3461–3475, Apr. 2014. doi: 10.1093/mnras/stu195.

F. Pintore, P. Esposito, L. Zampieri, S. Motta, and A. Wolter. Spectral variability in Swift and Chandra observations of the ultraluminous source NGC 55 ULX1. *MNRAS*, 448(2):1153–1161, Apr. 2015. doi: 10.1093/mnras/stv028.

F. Pintore, L. Zampieri, A. D. Sutton, T. P. Roberts, M. J. Middleton, and J. C. Gladstone. The ultraluminous X-ray source NGC 5643 ULX1: a large stellar mass black hole accreting at super-Eddington rates? *MNRAS*, 459(1):455–466, June 2016. doi: 10.1093/mnras/stw669.

F. Pintore, L. Zampieri, L. Stella, A. Wolter, S. Mereghetti, and G. L. Israel. Pulsator-like Spectra from Ultraluminous X-Ray Sources and the Search for More Ultraluminous Pulsars. *ApJ*, 836(1): 113, Feb. 2017. doi: 10.3847/1538-4357/836/1/113.

F. Pintore, A. Belfiore, G. Novara, R. Salvaterra, M. Marelli, A. De Luca, M. Rigoselli, G. Israel, G. Rodriguez, S. Mereghetti, A. Wolter, D. J. Walton, F. Fuerst, E. Ambrosi, L. Zampieri, A. Tiengo, and C. Salvaggio. A new ultraluminous X-ray source in the galaxy NGC 5907. *MNRAS*, 477(1):L90–L95, Jun 2018a. doi: 10.1093/mnrasl/sly048.

F. Pintore, L. Zampieri, S. Mereghetti, A. Wolter, G. Rodríguez, G. L. Israel, P. Esposito, S. Paiano, G. Trinchieri, and P. Ochner. The two ultraluminous X-ray sources in the galaxy NGC 925. *MNRAS*, 479(3):4271–4277, Sept. 2018b. doi: 10.1093/mnras/sty1766.

F. Pintore, M. Marelli, R. Salvaterra, G. L. Israel, G. A. Rodríguez Castillo, P. Esposito, A. Belfiore, A. De Luca, A. Wolter, S. Mereghetti, L. Stella, M. Rigoselli, H. P. Earnshaw, C. Pinto, T. P. Roberts, D. J. Walton, F. Bernardini, F. Haberl, C. Salvaggio, A. Tiengo, L. Zampieri, M. Bachetti, M. Brightman, P. Casella, D. D'Agostino, S. Dall'Osso, F. Fürst, F. A. Harrison, M. Mapelli, A. Papitto, and M. Middleton. The Ultraluminous X-Ray Sources Population of the Galaxy NGC 7456. *ApJ*, 890(2):166, Feb. 2020. doi: 10.3847/1538-4357/ab6ffd.

F. Pintore, S. Motta, C. Pinto, M. G. Bernardini, G. Rodriguez-Castillo, R. Salvaterra, G. L. Israel, P. Esposito, E. Ambrosi, C. Salvaggio, L. Zampieri, and A. Wolter. The rare X-ray flaring activity of the ultraluminous X-ray source NGC 4559 X7. *MNRAS*, 504(1):551–564, June 2021. doi: 10.1093/mnras/stab913.

F. Pizzolato, A. Wolter, and G. Trinchieri. Chandra observations of the ULX N10 in the Cartwheel galaxy. *MNRAS*, 406:1116–1124, Aug. 2010. doi: 10.1111/j.1365-2966.2010.16735.x.

S. F. Portegies Zwart and S. L. W. McMillan. The Runaway Growth of Intermediate-Mass Black Holes in Dense Star Clusters. *ApJ*, 576(2):899–907, Sept. 2002. doi: 10.1086/341798.

J. Poutanen, G. Lipunova, S. Fabrika, A. G. Butkevich, and P. Abolmasov. Supercritically accreting stellar mass black holes as ultraluminous X-ray sources. *MNRAS*, 377:1187–1194, May 2007. doi: 10.1111/j.1365-2966.2007.11668.x.

A. Ptak, E. Colbert, R. P. van der Marel, E. Roye, T. Heckman, and B. Towne. Optical Counterparts of Ultraluminous X-Ray Sources Identified from Archival HST WFPC2 Images. *ApJS*, 166(1): 154–187, Sept. 2006. doi: 10.1086/505218.

J. Puls, J. S. Vink, and F. Najarro. Mass loss from hot massive stars. *A&A Rev.*, 16(3-4):209–325, Dec. 2008. doi: 10.1007/s00159-008-0015-8.

Y. Qiu, R. Soria, S. Wang, G. Wiktorowicz, J. Liu, Y. Bai, A. Bogomazov, R. Di Stefano, D. J. Walton, and X. Xu. CG X-1: An Eclipsing Wolf-Rayet ULX in the Circinus Galaxy. *ApJ*, 877(1): 57, May 2019. doi: 10.3847/1538-4357/ab16e7.

E. Quintin, N. A. Webb, A. Gúrpide, M. Bachetti, and F. Fürst. A new candidate pulsating ULX in NGC 7793. *MNRAS*, 503(4):5485–5494, June 2021. doi: 10.1093/mnras/stab814.

R. C. Reis and J. M. Miller. On the Size and Location of the X-Ray Emitting Coronae around Black Holes. *ApJ*, 769(1):L7, May 2013. doi: 10.1088/2041-8205/769/1/L7.

R. A. Remillard and J. E. McClintock. X-Ray Properties of Black-Hole Binaries. *ARA&A*, 44(1): 49–92, Sept. 2006. doi: 10.1146/annurev.astro.44.051905.092532.

F. Renaud, E. Athanassoula, P. Amram, A. Bosma, F. Bournaud, P.-A. Duc, B. Epinat, J. Fensch, K. Kraljic, V. Perret, and C. Struck. Morphology and enhanced star formation in a Cartwheel-like ring galaxy. *MNRAS*, 473:585–602, Jan. 2018. doi: 10.1093/mnras/stx2360.

A. Robba, C. Pinto, D. J. Walton, R. Soria, P. Kosec, F. Pintore, T. P. Roberts, W. N. Alston, M. Middleton, G. Cusumano, H. P. Earnshaw, F. Fürst, R. Sathyaprakash, E. Kyritsis, and A. C. Fabian. Broadband X-ray spectral variability of the pulsing ULX NGC 1313 X-2. *A&A*, 652: A118, Aug. 2021. doi: 10.1051/0004-6361/202140884.

T. P. Roberts. X-ray observations of ultraluminous X-ray sources. *Ap&SS*, 311(1-3):203–212, Oct 2007. doi: 10.1007/s10509-007-9547-z.

T. P. Roberts and E. J. M. Colbert. Chandra reveals a black hole X-ray binary within the ultraluminous supernova remnant MF 16. *MNRAS*, 341(4):L49–L54, June 2003. doi: 10.1046/j.1365-8711.2003.06670.x.

T. P. Roberts and R. S. Warwick. A ROSAT High Resolution Imager survey of bright nearby galaxies. *MNRAS*, 315(1):98–114, June 2000. doi: 10.1046/j.1365-8711.2000.03384.x.

T. P. Roberts, R. E. Kilgard, R. S. Warwick, M. R. Goad, and M. J. Ward. Chandra monitoring observations of the ultraluminous X-ray source NGC 5204 X-1. *MNRAS*, 371(4):1877–1890, Oct. 2006. doi: 10.1111/j.1365-2966.2006.10821.x.

T. P. Roberts, J. C. Gladstone, A. D. Goulding, A. M. Swinbank, M. J. Ward, M. R. Goad, and A. J. Levan. (No) dynamical constraints on the mass of the black hole in two ULXs. *Astronomische Nachrichten*, 332(4):398, May 2011. doi: 10.1002/asna.201011508.

G. A. Rodriguez Castillo and G. L. Israel. Digging out the neutron stars extragalactic population - INAF-CINECA MoU report. *Mem. Soc. Astron. Italiana*, 91:336, Jan. 2020.

G. A. Rodríguez Castillo, G. L. Israel, A. Belfiore, F. Bernardini, P. Esposito, F. Pintore, A. De Luca, A. Papitto, L. Stella, A. Tiengo, L. Zampieri, M. Bachetti, M. Brightman, P. Casella, D. D'Agostino, S. Dall'Osso, H. P. Earnshaw, F. Fürst, F. Haberl, F. A. Harrison, M. Mapelli, M. Marelli, M. Middleton, C. Pinto, T. P. Roberts, R. Salvaterra, R. Turolla, D. J. Walton, and A. Wolter. Discovery of a 2.8 s pulsar in a 2 d orbit High-Mass X-ray Binary powering the Ultraluminous X-ray source ULX-7 in M51. *arXiv e-prints*, art. arXiv:1906.04791, Jun 2019.

G. A. Rodríguez Castillo, G. L. Israel, A. Belfiore, F. Bernardini, P. Esposito, F. Pintore, A. De Luca, A. Papitto, L. Stella, A. Tiengo, L. Zampieri, M. Bachetti, M. Brightman, P. Casella, D. D'Agostino, S. Dall'Osso, H. P. Earnshaw, F. Fürst, F. Haberl, F. A. Harrison, M. Mapelli, M. Marelli, M. Middleton, C. Pinto, T. P. Roberts, R. Salvaterra, R. Turolla, D. J. Walton, and A. Wolter. Discovery of a 2.8 s Pulsar in a 2 Day Orbit High-mass X-Ray Binary Powering the Ultraluminous X-Ray Source ULX-7 in M51. *ApJ*, 895(1):60, May 2020. doi: 10.3847/1538-4357/ab8a44.

P. W. A. Roming, T. E. Kennedy, K. O. Mason, J. A. Nousek, L. Ahr, R. E. Bingham, P. S. Broos, M. J. Carter, B. K. Hancock, H. E. Huckle, S. D. Hunsberger, H. Kawakami, R. Killough, T. S. Koch, M. K. McLelland, K. Smith, P. J. Smith, J. C. Soto, P. T. Boyd, A. A. Breeveld, S. T. Holland, M. Ivanushkina, M. S. Pryzby, M. D. Still, and J. Stock. The Swift Ultra-Violet/Optical Telescope. *Space Sci. Rev.*, 120(3-4):95–142, Oct. 2005. doi: 10.1007/s11214-005-5095-4.

C. Salvaggio, A. Wolter, F. Pintore, C. Pinto, E. Ambrosi, G. L. Israel, A. Marino, R. Salvaterra, L. Zampieri, and A. Belfiore. Investigating the nature of the ultraluminous X-ray sources in the galaxy NGC 925. *MNRAS*, Mar. 2022. doi: 10.1093/mnras/stac559.

R. Sathyaprakash, T. P. Roberts, D. J. Walton, F. Fuerst, M. Bachetti, C. Pinto, W. N. Alston, H. P. Earnshaw, A. C. Fabian, M. J. Middleton, and R. Soria. The discovery of weak coherent pulsations in the ultraluminous X-ray source NGC 1313 X-2. *MNRAS*, 488(1):L35–L40, Sep 2019. doi: 10.1093/mnrasl/slz086.

J. D. Scargle. Studies in astronomical time series analysis. II. Statistical aspects of spectral analysis of unevenly spaced data. *ApJ*, 263:835–853, Dec. 1982. doi: 10.1086/160554.

B. Schleicher, A. Arbet-Engels, D. Baack, M. Balbo, A. Biland, M. Blank, T. Bretz, K. Bruegge, M. Bulinski, J. Buss, M. Doerr, D. Dorner, D. Elsaesser, S. Grischagin, D. Hildebrand, L. Linhoff, K. Mannheim, S. A. Mueller, D. Neise, A. Neronov, M. Noethe, A. Paravac, W. Rhode, F. Schulz, K. Sedlaczek, A. Shukla, V. Sliusar, E. v. Willert, and R. Walter. Fractional Variability—A Tool to Study Blazar Variability. *Galaxies*, 7(2):62, May 2019. doi: 10.3390/galaxies7020062.

M. Servillat, S. A. Farrell, D. Lin, O. Godet, D. Barret, and N. A. Webb. X-Ray Variability and Hardness of ESO 243-49 HLX-1: Clear Evidence for Spectral State Transitions. *ApJ*, 743(1):6, Dec. 2011. doi: 10.1088/0004-637X/743/1/6.

N. I. Shakura and R. A. Sunyaev. Reprint of 1973A&A....24..337S. Black holes in binary systems. Observational appearance. *A&A*, 500:33–51, June 1973.

T. Shimura and F. Takahara. On the Spectral Hardening Factor of the X-Ray Emission from Accretion Disks in Black Hole Candidates. *ApJ*, 445:780, June 1995. doi: 10.1086/175740.

G. K. Skinner, D. K. Bedford, R. F. Elsner, D. Leahy, M. C. Weisskopf, and J. Grindlay. Discovery of 69 ms periodic X-ray pulsations in A0538 - 66. *Nature*, 297(5867):568–570, June 1982. doi: 10.1038/297568a0.

X. Song, D. J. Walton, G. B. Lansbury, P. A. Evans, A. C. Fabian, H. Earnshaw, and T. P. Roberts. The hunt for pulsating ultraluminous X-ray sources. *MNRAS*, 491(1):1260–1277, Jan. 2020. doi: 10.1093/mnras/stz3036.

R. Soria and A. Kong. Revisiting the ultraluminous supersoft source in M 101: an optically thick outflow model. *MNRAS*, 456(2):1837–1858, Feb. 2016. doi: 10.1093/mnras/stv2671.

R. Soria, M. Cropper, M. Pakull, R. Mushotzky, and K. Wu. The star-forming environment of an ultraluminous X-ray source in NGC4559: an optical study. *MNRAS*, 356(1):12–28, Jan. 2005. doi: 10.1111/j.1365-2966.2004.08438.x.

R. Soria, K. Wu, and Z. Kunic. Characteristic temperatures and spectral appearance of ULX disks. In S. Carpano, M. Ehle, and W. Pietsch, editors, *X-rays From Nearby Galaxies*, pages 48–51, Feb. 2008.

R. Soria, K. D. Kuntz, P. F. Winkler, W. P. Blair, K. S. Long, P. P. Plucinsky, and B. C. Whitmore. The Birth of an Ultraluminous X-Ray Source in M83. *ApJ*, 750(2):152, May 2012. doi: 10.1088/0004-637X/750/2/152.

R. Soria, A. Musaeva, K. Wu, L. Zampieri, S. Federle, R. Urquhart, E. van der Helm, and S. Farrell. Outbursts of the intermediate-mass black hole HLX-1: a wind-instability scenario. *MNRAS*, 469 (1):886–905, July 2017. doi: 10.1093/mnras/stx888.

A. M. Stobbart, T. P. Roberts, and R. S. Warwick. A dipping black hole X-ray binary candidate in NGC 55. *MNRAS*, 351(3):1063–1070, July 2004. doi: 10.1111/j.1365-2966.2004.07848.x.

A. M. Stobbart, T. P. Roberts, and J. Wilms. XMM-Newton observations of the brightest ultraluminous X-ray sources. *MNRAS*, 368(1):397–413, May 2006. doi: 10.1111/j.1365-2966.2006.10112.x.

O. Straub, O. Godet, N. Webb, M. Servillat, and D. Barret. Investigating the mass of the intermediate mass black hole candidate HLX-1 with the slimbh model. *A&A*, 569:A116, Sept. 2014. doi: 10.1051/0004-6361/201423874.

T. E. Strohmayer and R. F. Mushotzky. Evidence for an Intermediate-mass Black Hole in NGC 5408 X-1. *ApJ*, 703(2):1386–1393, Oct. 2009. doi: 10.1088/0004-637X/703/2/1386.

C. Struck, P. N. Appleton, K. D. Borne, and R. A. Lucas. Hubble Space Telescope Imaging of Dust Lanes and Cometary Structures in the Inner Disk of the Cartwheel Ring Galaxy. *AJ*, 112:1868, Nov. 1996. doi: 10.1086/118148.

A. D. Sutton, T. P. Roberts, and M. J. Middleton. The ultraluminous state revisited: fractional variability and spectral shape as diagnostics of super-Eddington accretion. *MNRAS*, 435(2):1758–1775, Oct. 2013. doi: 10.1093/mnras/stt1419.

A. D. Sutton, T. P. Roberts, and M. J. Middleton. X-Ray Spectral Residuals in NGC 5408 X-1: Diffuse Emission from Star Formation, or the Signature of a Super-Eddington Wind? *ApJ*, 814 (1):73, Nov. 2015. doi: 10.1088/0004-637X/814/1/73.

D. A. Swartz, K. K. Ghosh, A. F. Tennant, and K. Wu. The Ultraluminous X-Ray Source Population from the Chandra Archive of Galaxies. *ApJS*, 154(2):519–539, Oct. 2004. doi: 10.1086/422842.

D. A. Swartz, A. F. Tennant, and R. Soria. Ultraluminous X-Ray Source Correlations with Star-Forming Regions. *ApJ*, 703(1):159–168, Sept. 2009. doi: 10.1088/0004-637X/703/1/159.

D. A. Swartz, R. Soria, A. F. Tennant, and M. Yukita. A Complete Sample of Ultraluminous X-ray Source Host Galaxies. *ApJ*, 741(1):49, Nov 2011. doi: 10.1088/0004-637X/741/1/49.

S. Takeuchi, K. Ohsuga, and S. Mineshige. Clumpy Outflows from Supercritical Accretion Flow. *PASJ*, 65:88, Aug. 2013. doi: 10.1093/pasj/65.4.88.

L. Tao, H. Feng, F. Grisé, and P. Kaaret. Compact Optical Counterparts of Ultraluminous X-Ray Sources. *ApJ*, 737(2):81, Aug. 2011. doi: 10.1088/0004-637X/737/2/81.

Y. Terashima and A. S. Wilson. The Luminous X-Ray Source Population in M51 Observed with Chandra. *ApJ*, 601(2):735–758, Feb 2004. doi: 10.1086/380505.

J. Timmer and M. Koenig. On generating power law noise. *A&A*, 300:707, Aug. 1995.

F. Tombesi, M. Cappi, J. N. Reeves, and V. Braito. Evidence for ultrafast outflows in radio-quiet AGNs - III. Location and energetics. *MNRAS*, 422(1):L1–L5, May 2012. doi: 10.1111/j.1745-3933.2012.01221.x.

J. A. Tomsick, K. Yamaoka, S. Corbel, P. Kaaret, E. Kalemci, and S. Migliari. Truncation of the Inner Accretion Disk Around a Black Hole at Low Luminosity. *ApJ*, 707(1):L87–L91, Dec. 2009. doi: 10.1088/0004-637X/707/1/L87.

L. J. Townsend, J. A. Kennea, M. J. Coe, V. A. McBride, D. A. H. Buckley, P. A. Evans, and A. Udalski. The 2016 super-Eddington outburst of SMC X-3: X-ray and optical properties and system parameters. *MNRAS*, 471(4):3878–3887, Nov. 2017. doi: 10.1093/mnras/stx1865.

S. S. Tsygankov, A. A. Mushtukov, V. F. Suleimanov, and J. Poutanen. Propeller effect in action in the ultraluminous accreting magnetar M82 X-2. *MNRAS*, 457(1):1101–1106, Mar 2016. doi: 10.1093/mnras/stw046.

S. S. Tsygankov, V. Doroshenko, A. A. Lutovinov, A. A. Mushtukov, and J. Poutanen. SMC X-3: the closest ultraluminous X-ray source powered by a neutron star with non-dipole magnetic field. *A&A*, 605:A39, Sept. 2017. doi: 10.1051/0004-6361/201730553.

R. B. Tully, L. Rizzi, E. J. Shaya, H. M. Courtois, D. I. Makarov, and B. A. Jacobs. The Extragalactic Distance Database. *AJ*, 138(2):323–331, Aug. 2009. doi: 10.1088/0004-6256/138/2/323.

R. B. Tully, H. M. Courtois, A. E. Dolphin, J. R. Fisher, P. Héraudeau, B. A. Jacobs, I. D. Karachentsev, D. Makarov, L. Makarova, S. Mitronova, L. Rizzi, E. J. Shaya, J. G. Sorce, and P.-F. Wu. Cosmicflows-2: The Data. *AJ*, 146(4):86, Oct. 2013. doi: 10.1088/0004-6256/146/4/86.

R. B. Tully, H. M. Courtois, and J. G. Sorce. Cosmicflows-3. *AJ*, 152(2):50, Aug. 2016. doi: 10.3847/0004-6256/152/2/50.

R. Urquhart and R. Soria. Optically thick outflows in ultraluminous supersoft sources. *MNRAS*, 456 (2):1859–1880, Feb. 2016a. doi: 10.1093/mnras/stv2293.

R. Urquhart and R. Soria. Two Eclipsing Ultraluminous X-Ray Sources in M51. *ApJ*, 831(1):56, Nov. 2016b. doi: 10.3847/0004-637X/831/1/56.

R. T. Urquhart, R. Soria, R. Di Stefano, K. Cui, P. Esposito, G. L. Israel, S. Kumar, S. Motta, F. Pintore, and G. Riva. Quasi periodic whispers from a transient ULX in M\,101: signatures of a fast-spinning neutron star? *arXiv e-prints*, art. arXiv:2201.07252, Jan. 2022.

F. Vagnetti, R. Middei, M. Antonucci, M. Paolillo, and R. Serafinelli. Ensemble X-ray variability of active galactic nuclei. II. Excess variance and updated structure function. *A&A*, 593:A55, Sept. 2016. doi: 10.1051/0004-6361/201629057.

J. T. VanderPlas. Understanding the Lomb-Scargle Periodogram. *ApJS*, 236(1):16, May 2018. doi: 10.3847/1538-4365/aab766.

G. Vasilopoulos, M. Petropoulou, F. Koliopanos, P. S. Ray, C. B. Bailyn, F. Haberl, and K. Gendreau. NGC 300 ULX1: spin evolution, super-Eddington accretion, and outflows. *MNRAS*, 488(4): 5225–5231, Oct. 2019. doi: 10.1093/mnras/stz2045.

G. Vasilopoulos, S. K. Lander, F. Koliopanos, and C. D. Bailyn. M51 ULX-7: superorbital periodicity and constraints on the neutron star magnetic field. *MNRAS*, 491(4):4949–4959, Feb. 2020. doi: 10.1093/mnras/stz3298.

G. Vasilopoulos, F. Koliopanos, F. Haberl, H. Treiber, M. Brightman, H. P. Earnshaw, and A. Gúrpide. Chandra Probes the X-Ray Variability of M51 ULX-7: Evidence of Propeller Transition and X-Ray Dips on Orbital Periods. *ApJ*, 909(1):50, Mar. 2021. doi: 10.3847/1538-4357/abda49.

S. Vaughan, R. Edelson, R. S. Warwick, and P. Uttley. On characterizing the variability properties of X-ray light curves from active galaxies. *MNRAS*, 345(4):1271–1284, Nov. 2003. doi: 10.1046/j.1365-2966.2003.07042.x.

E. Vesperini, S. L. W. McMillan, A. D'Ercole, and F. D'Antona. Intermediate-mass Black Holes in Early Globular Clusters. *ApJ*, 713(1):L41–L44, Apr. 2010. doi: 10.1088/2041-8205/713/1/L41.

K. Vierdayanti, K.-Y. Watarai, and S. Mineshige. On Black Hole Mass Estimation from X-Ray Spectra of Ultraluminous X-Ray Sources. *PASJ*, 60:653, June 2008. doi: 10.1093/pasj/60.3.653.

J. S. Vink. The theory of stellar winds. *Ap&SS*, 336(1):163–167, Nov. 2011. doi: 10.1007/s10509-011-0636-7.

A. Vinokurov, S. Fabrika, and K. Atapin. Ultra-luminous X-ray sources as supercritical accretion disks: Spectral energy distributions. *Astrophysical Bulletin*, 68(2):139–153, Apr. 2013. doi: 10.1134/S1990341313020028.

M. Volonteri. Formation of supermassive black holes. *A&A Rev.*, 18(3):279–315, July 2010. doi: 10.1007/s00159-010-0029-x.

M. Volonteri and M. J. Rees. Rapid Growth of High-Redshift Black Holes. *ApJ*, 633(2):624–629, Nov. 2005. doi: 10.1086/466521.

M. Volonteri, F. Haardt, and P. Madau. The Assembly and Merging History of Supermassive Black Holes in Hierarchical Models of Galaxy Formation. *ApJ*, 582(2):559–573, Jan. 2003. doi: 10.1086/344675.

D. J. Walton, T. P. Roberts, S. Mateos, and V. Heard. 2XMM ultraluminous X-ray source candidates in nearby galaxies. *MNRAS*, 416(3):1844–1861, Sept. 2011. doi: 10.1111/j.1365-2966.2011.19154.x.

D. J. Walton, F. Fuerst, F. Harrison, D. Stern, M. Bachetti, D. Barret, F. Bauer, S. E. Boggs, F. E. Christensen, W. W. Craig, A. C. Fabian, B. W. Grefenstette, C. J. Hailey, K. K. Madsen, J. M. Miller, A. Ptak, V. Rana, N. A. Webb, and W. W. Zhang. An Extremely Luminous and Variable Ultraluminous X-Ray Source in the Outskirts of Circinus Observed with NuSTAR. *ApJ*, 779(2):148, Dec 2013. doi: 10.1088/0004-637X/779/2/148.

D. J. Walton, M. J. Middleton, V. Rana, J. M. Miller, F. A. Harrison, A. C. Fabian, M. Bachetti, D. Barret, S. E. Boggs, F. E. Christensen, W. W. Craig, F. Fuerst, B. W. Grefenstette, C. J. Hailey, K. K. Madsen, D. Stern, and W. Zhang. NuSTAR, XMM-Newton, and Suzaku Observations of the Ultraluminous X-Ray Source Holmberg II X-1. *ApJ*, 806(1):65, June 2015. doi: 10.1088/0004-637X/806/1/65.

D. J. Walton, F. Fürst, M. Bachetti, D. Barret, M. Brightman, A. C. Fabian, N. Gehrels, F. A. Harrison, M. Heida, M. J. Middleton, V. Rana, T. P. Roberts, D. Stern, L. Tao, and N. Webb. A 78 Day X-Ray Period Detected from NGC 5907 ULX1 by Swift. *ApJ*, 827(1):L13, Aug. 2016. doi: 10.3847/2041-8205/827/1/L13.

D. J. Walton, M. Bachetti, F. Fürst, D. Barret, M. Brightman, A. C. Fabian, B. W. Grefenstette, F. A. Harrison, M. Heida, J. Kennea, P. Kosec, R. M. Lau, K. K. Madsen, M. J. Middleton, C. Pinto, J. F. Steiner, and N. Webb. A Potential Cyclotron Resonant Scattering Feature in the Ultraluminous X-Ray Source Pulsar NGC 300 ULX1 Seen by NuSTAR and XMM-Newton. *ApJ*, 857(1):L3, Apr. 2018a. doi: 10.3847/2041-8213/aabadc.

D. J. Walton, F. Fürst, F. A. Harrison, D. Stern, M. Bachetti, D. Barret, M. Brightman, A. C. Fabian, M. J. Middleton, A. Ptak, and L. Tao. Super-Eddington accretion on to the neutron star NGC 7793 P13: Broad-band X-ray spectroscopy and ultraluminous X-ray sources. *MNRAS*, 473(4): 4360–4376, Feb. 2018b. doi: 10.1093/mnras/stx2650.

D. J. Walton, F. Fürst, M. Heida, F. A. Harrison, D. Barret, D. Stern, M. Bachetti, M. Brightman, A. C. Fabian, and M. J. Middleton. Evidence for Pulsar-like Emission Components in the Broadband ULX Sample. *ApJ*, 856(2):128, Apr. 2018c. doi: 10.3847/1538-4357/aab610.

D. J. Walton, C. Pinto, M. Nowak, M. Bachetti, R. Sathyaprakash, E. Kara, T. P. Roberts, R. Soria, M. Brightman, C. R. Canizares, H. P. Earnshaw, F. Fürst, M. Heida, M. J. Middleton, D. Stern, L. Tao, N. Webb, W. N. Alston, D. Barret, A. C. Fabian, F. A. Harrison, and P. Kosec. The unusual broad-band X-ray spectral variability of NGC 1313 X-1 seen with XMM-Newton, Chandra, and NuSTAR. *MNRAS*, 494(4):6012–6029, June 2020. doi: 10.1093/mnras/staa1129.

D. J. Walton, A. D. A. Mackenzie, H. Gully, N. R. Patel, T. P. Roberts, H. P. Earnshaw, and S. Mateos. A Multi-Mission Catalogue of Ultraluminous X-ray Source Candidates. *arXiv e-prints*, art. arXiv:2110.07625, Oct. 2021.

D. J. Walton, A. D. A. Mackenzie, H. Gully, N. R. Patel, T. P. Roberts, H. P. Earnshaw, and S. Mateos. A multimission catalogue of ultraluminous X-ray source candidates. *MNRAS*, 509(2):1587–1604, Jan. 2022. doi: 10.1093/mnras/stab3001.

S. Wang, Y. Qiu, J. Liu, and J. N. Bregman. Chandra ACIS Survey of X-Ray Point Sources in Nearby Galaxies. II. X-Ray Luminosity Functions and Ultraluminous X-Ray Sources. *ApJ*, 829(1):20, Sept. 2016. doi: 10.3847/0004-637X/829/1/20.

S. Wang, R. Soria, R. Urquhart, and J. Liu. Discovery of two eclipsing X-ray binaries in M 51. *MNRAS*, 477(3):3623–3645, July 2018. doi: 10.1093/mnras/sty872.

K.-y. Watarai and S. Mineshige. Model for Relaxation Oscillations of a Luminous Accretion Disk in GRS 1915+105: Variable Inner Edge. *ApJ*, 596(1):421–428, Oct. 2003. doi: 10.1086/377576.

K.-y. Watarai, J. Fukue, M. Takeuchi, and S. Mineshige. Galactic Black-Hole Candidates Shining at the Eddington Luminosity. *PASJ*, 52:133, Feb. 2000. doi: 10.1093/pasj/52.1.133.

M. C. Weisskopf, H. D. Tananbaum, L. P. Van Speybroeck, and S. L. O'Dell. Chandra X-ray Observatory (CXO): overview. In J. E. Truemper and B. Aschenbach, editors, *X-Ray Optics, Instruments, and Missions III*, volume 4012 of *Society of Photo-Optical Instrumentation Engineers (SPIE) Conference Series*, pages 2–16, July 2000. doi: 10.1117/12.391545.

S.-S. Weng and H. Feng. Evidence for Precession due to Supercritical Accretion in Ultraluminous X-Ray Sources. *ApJ*, 853(2):115, Feb. 2018. doi: 10.3847/1538-4357/aaa45c.

N. E. White and S. S. Holt. Accretion disk coronae. *ApJ*, 257:318–337, June 1982. doi: 10.1086/159991.

N. E. White and J. H. Swank. The periodic absorption events from 4U 1915-05. *ApJ*, 253:L61–L66, Feb. 1982. doi: 10.1086/183737.

G. Wiktorowicz, J.-P. Lasota, K. Belczynski, Y. Lu, J. Liu, and K. Iłkiewicz. Wind-powered Ultraluminous X-ray Sources. *ApJ*, 918(2):60, Sept. 2021. doi: 10.3847/1538-4357/ac0cf7.

C. A. Wilson-Hodge, C. Malacaria, P. A. Jenke, G. K. Jaisawal, M. Kerr, M. T. Wolff, Z. Arzoumanian, D. Chakrabarty, J. P. Doty, K. C. Gendreau, S. Guillot, W. C. G. Ho, B. LaMarr, C. B. Markwardt, F. Özel, G. Y. Prigozhin, P. S. Ray, M. Ramos-Lerate, R. A. Remillard, T. E. Strohmayer, M. L. Vezie, K. S. Wood, and NICER Science Team. NICER and Fermi GBM Observations of the First Galactic Ultraluminous X-Ray Pulsar Swift J0243.6+6124. *ApJ*, 863(1):9, Aug. 2018. doi: 10.3847/1538-4357/aace60.

L. M. Winter, R. F. Mushotzky, and C. S. Reynolds. XMM-Newton Archival Study of the Ultraluminous X-Ray Population in Nearby Galaxies. *ApJ*, 649(2):730–752, Oct. 2006. doi: 10.1086/506579.

A. Wolter and G. Trinchieri. A thorough study of the intriguing X-ray emission from the Cartwheel ring. *A&A*, 426, 2004. doi: 10.1051/0004-6361:20047110.

A. Wolter, G. Trinchieri, and A. Iovino. High energy phenomena in the Cartwheel's ring. *A&A*, 342: 41–46, Feb. 1999.

A. Wolter, G. Trinchieri, and M. Colpi. On the compact nature of the most luminous ULX in the Cartwheel ring. *MNRAS*, 373:1627–1632, Dec. 2006. doi: 10.1111/j.1365-2966.2006.11116.x.

A. Wolter, P. Esposito, M. Mapelli, F. Pizzolato, and E. Ripamonti. NGC 2276: a remarkable galaxy with a large number of ultraluminous X-ray sources. *MNRAS*, 448(1):781–791, Mar 2015. doi: 10.1093/mnras/stv054.

A. Wolter, A. Fruscione, and M. Mapelli. The X-Ray Luminosity Function of Ultraluminous X-Ray Sources in Collisional Ring Galaxies. *ApJ*, 863(1):43, Aug 2018. doi: 10.3847/1538-4357/aacb34.

H. Wolter. Spiegelsysteme streifenden Einfalls als abbildende Optiken für Röntgenstrahlen. *Annalen der Physik*, 445(1):94–114, Jan. 1952. doi: 10.1002/andp.19524450108.

L. Zampieri and T. P. Roberts. Low-metallicity natal environments and black hole masses in ultraluminous X-ray sources. *MNRAS*, 400(2):677–686, Dec. 2009. doi: 10.1111/j.1365-2966.2009.15509.x.

L. Zampieri, P. Mucciarelli, R. Falomo, P. Kaaret, R. Di Stefano, R. Turolla, M. Chieregato, and A. Treves. The Ultraluminous X-Ray Source NGC 1313 X-2 (MS 0317.7-6647) and Its Environment. *ApJ*, 603(2):523–530, Mar. 2004. doi: 10.1086/381541.

L. Zampieri, D. Impiombato, R. Falomo, F. Grisé, and R. Soria. Searching for the orbital period of the ultraluminous X-ray source NGC 1313 X-2. *MNRAS*, 419(2):1331–1337, Jan. 2012. doi: 10.1111/j.1365-2966.2011.19790.x.

A. Zezas and G. Fabbiano. Chandra Observations of "The Antennae" Galaxies (NGC 4038/4039). IV. The X-Ray Source Luminosity Function and the Nature of Ultraluminous X-Ray Sources. *ApJ*, 577(2):726–737, Oct. 2002. doi: 10.1086/342135.

A. Zezas, G. Fabbiano, A. H. Rots, and S. S. Murray. Chandra Observations of "The Antennae" Galaxies (NGC 4038/4039). II. Detection and Analysis of Galaxian X-Ray Sources. *ApJS*, 142(2): 239–260, Oct. 2002. doi: 10.1086/342010.

A. Zezas, G. Fabbiano, A. Baldi, F. Schweizer, A. R. King, T. J. Ponman, and A. H. Rots. Chandra Monitoring Observations of The Antennae Galaxies. I. Catalog of Source Properties. *ApJS*, 166: 211–248, Sept. 2006. doi: 10.1086/501526.

A. Zezas, G. Fabbiano, A. Baldi, F. Schweizer, A. R. King, A. H. Rots, and T. J. Ponman. Chandra Monitoring Observations of the Antennae Galaxies. II. X-Ray Luminosity Functions. *ApJ*, 661 (1):135–148, May 2007. doi: 10.1086/513091.

M. Zhang and W.-B. Liu. Innermost stable circular orbits of charged spinning test particles. *Physics Letters B*, 789:393–398, Feb. 2019. doi: 10.1016/j.physletb.2018.12.051.